

ANNUAL REPORT 2014



DAVID J. BRENNER
Director

SALLY A. AMUNDSON
Editor

HOWARD B. LIEBERMAN
Co-Editor



COLUMBIA UNIVERSITY
College of Physicians and Surgeons



Table of Contents

CONTENTS.....	1
COLLABORATING DEPARTMENTS AND INSTITUTIONS	4
ACKNOWLEDGEMENT OF SUPPORT.....	5
RELATED WEB SITES	5
A NOTE FROM OUR DIRECTOR.....	6
STAFF NEWS	7
THE WELDON MEMORIAL PRIZE.....	8
LABORATORY COLLOQUIA AND SEMINARS	9
STAFF LISTING	10
STAFF PHOTO	11
RESEARCH REPORTS	
<i>MICROBEAM DEVELOPMENT AND SINGLE CELL STUDIES</i>	
Development of the Super Microbeam at RARAF	
Gerhard Randers-Pehrson, Andrew D. Harken, Guy Garty, and David J. Brenner	13
Super Resolution Stimulated Emission Depletion Microscopy at the RARAF Microbeam	
Andrew D. Harken, Gerhard Randers-Pehrson, and David J. Brenner.....	14
Flow Cytometry for Microfluidic Fluorescence-Activated Cell Sorting (microFACS) at RARAF	
Andrew D. Harken, David Welch, Gerhard Randers-Pehrson, and David J. Brenner	15
Analyses of Microbeam-induced ROS in Single Cells	
Brian Ponnaiya, Manuela Buonanno, Alan Bigelow, and Doug Spitz	16
A Bead-based Microfluidic Approach to Integrated Single-cell Gene Expression Analysis	
Hao Sun, Jing Zhu, Tim Olsen, Jianguo Tao, Brian Ponnaiya, Sally A. Amundson, David J. Brenner, and Qiao Lin.....	19
Radiation-induced Differential Expression of p53 Responsive Genes is Influenced by their Cellular Localization: A Single-cell Study	
Brian Ponnaiya, Manuela Buonanno, Sally A. Amundson, and David J. Brenner.....	21
Targeted Cytoplasmic Irradiation and Autophagy	
Jinhua Wu, Bo Zhang, Mercy M. Davidson, and Tom K. Hei	24
<i>BYSTANDER STUDIES</i>	
Glioblastoma Stem Cells: Radiation Response and Radiation-induced Bystander Signaling Effects	
Vladimir N. Ivanov and Tom K. Hei	27
An Application of a Mouse Orthotopic Prostate Cancer Model for Radiation-induced Non-targeted Response	
Hongning Zhou, Enyuan Shang, Kevin M. Hopkins, and Tom K. Hei	30
RAD9 Deficiency Enhances Bystander Signaling in Human Prostate Cancer Cells	
Sunil K. Panigrahi, Constantinos G. Broustas, and Howard B. Lieberman	31
Radiation Bystander Effect on Gene Expression in RAD9 Deficient Cells	
Shanaz A. Gandhi, Kevin M. Hopkins, Sunil K. Panigrahi, Howard B. Lieberman, and Sally A. Amundson	34
<i>CELLULAR AND MOLECULAR STUDIES</i>	
The Importance of Filters for Biological Applications of Far-UVC Excilamps	
Manuela Buonanno, Alan W. Bigelow, Gerhard Randers-Pehrson, and David J. Brenner.....	36

Effects of Radiation Type and Delivery Mode on the Radioresistant Eukaryote <i>Cryptococcus neoformans</i> Igor Shuryak, Ruth A. Bryan, Jack Broitman, Stephen A. Marino, Alfred Morgenstern, Christos Apostolidis, and Ekaterina Dadachova.....	38
Antitumor Activity of Pamidronate in a Breast Cancer Model by Targeting Rho-A Gene Expression Richard Ponce-Cusia and Gloria M. Calaf	41
High Dose Gamma Radiation and the Human Endothelial Barrier: Collapse of Live Vessels Preety Sharma and Peter Grabham	44
RAD9 Silencing Suppresses Prostatosphere Formation Constantinos G. Broustas and Howard B. Lieberman	46
RAD9 Modulates Secretion of the Tissue Inhibitors of Metalloproteinases (TIMP) in Prostate Cancer Cells Constantinos G. Broustas and Howard B. Lieberman	49
RAD9 Enhances Base Excision Repair by Regulating Neil1 Glycosylase Sunil K. Panigrahi, Kevin M. Hopkins, and Howard B. Lieberman	51
Effects of BET Bromodomain Inhibitor JQ1 on Radiosensitivity of Prostate Cancer Cell Lines Enyuan Shang, Hongning Zhou, and Tom K. Hei.....	55
Knockdown of DNA Repair Gene Expression in Mouse Embryonic Stem Cells Proficient or Deficient in mRad9 Li Wang, Kevin M. Hopkins, and Howard B. Lieberman.....	57
Expression and Purification of the hRAD9(1-272 aa) Flag –hHUS1-hRAD1 Protein Complex Li Wang and Howard B. Lieberman.....	58
Regulation of Death in Human Melanoma Cells Carrying Stem Cell Biomarkers: Apoptosis versus Necroptosis Vladimir N. Ivanov and Tom K. Hei	60
<u>TRANSLATIONAL STUDIES</u>	
High-Dose and Fractionation Effects in Stereotactic Radiation Therapy: Analysis of Tumor Control Data from 2,965 Patients Igor Shuryak, David J. Carlson, J. Martin Brown, and David J. Brenner	65
Far UVC (~200 nm) as a Safe and Low-cost Tool for Reducing Surgical Site Infections: In Vivo Studies Manuela Buonanno, Alan W. Bigelow, Gerhard Randers-Pehrson, Henry M. Spotnitz, and David J. Brenner.....	68
Determining Key Pathways Sensitizing Lung Cancer to Combined Chemoradiation Therapy by Exploiting Synthetic Lethal Relationships in an RNAi High-throughput Screen Kunal R Chaudhary and Simon Cheng.....	70
<u>CENTER FOR HIGH-THROUGHPUT MINIMALLY-INVASIVE RADIATION BIODOSIMETRY</u>	
Anatomically Accurate Mouse Phantoms for Radiation Dosimetry Studies David Welch, Andrew Harken, Gerhard Randers-Pehrson, and David J. Brenner	72
First Irradiations with a Novel Capillary Irradiator Guy Garty, Helen C. Turner, Maria Taveras, and David J. Brenner	74
Accelerator-Based Biological Irradiation Facility Simulating Neutron Exposure from an Improved Nuclear Device Yanping Xu, Gerhard Randers-Pehrson, Stephen A. Marino, Guy Garty, Andrew Harken, and David J. Brenner.....	76

Depletion and Recovery Kinetics of Long-term and Short-term Hematopoietic Stem Cells in C57BL/6 Mice Irradiated with γ-rays	
Erik F. Young and Lubomir B. Smilenov.....	78
Automated FISH on the RABiT System	
Mikhail Repin, Sergey Pampou, Helen C. Turner, Guy Garty, and David J. Brenner.....	80
Automated Scoring of Dicentric Chromosomes	
Guy Garty, Mikhail Repin, and David J. Brenner.....	81
Development of an Automated High-throughput System for Detection of Intrachromosomal Rearrangements	
Alan W. Bigelow, Guy Garty, Adayabalam S. Balajee, Yanping Xu, Charles R. Geard, and David J. Brenner.....	83
Analysis of Partial Body Irradiation using γ-H2AX Foci	
Guy Garty, Manuela Buonanno, and David J. Brenner.....	86
γ-H2AX Kinetic Profile in Mouse Lymphocytes Exposed to the Internal Emitters Cesium-137 and Strontium-90	
Helen C. Turner, Igor Shuryak, Waylon Weber, Melanie Doyle-Eisele, Raymond Guilmette, Dunstana Melo, Sally A. Amundson, and David J. Brenner.....	87
Assaying Hematopoietic Responses of Mice Following Partial Body Irradiation	
Brian Ponnaiya, Jay Perrier, Lubomir Smilenov, and David J. Brenner.....	90
Whole Blood Immunoassay using Gamma-H2AX Phosphorylation with Minimal Sample Preparation	
Erik F. Young, Matthew L. Johnston, and Kenneth L. Shepard.....	91
Human Pattern of Radiation-induced Gene Expression Restored in Humanized Mice	
Sally A. Amundson, Shanaz A. Ghandhi, Mashkura Chowdhury, Erik Young, and Lubomir B. Smilenov.....	93
Gene Expression Effects of Neutron Irradiation on Human Whole Blood	
Shanaz A. Ghandhi, Yanping Xu, Guy Garty, Lubomir B. Smilenov, and Sally A. Amundson.....	95
Correlation of Radiation-induced Micronuclei and Radiosensitivity among Inbred Mouse Strains	
Brian Ponnaiya, Jay Perrier, and David J. Brenner.....	96
THE RADIOLOGICAL RESEARCH ACCELERATOR FACILITY – an NIH-Supported Resource Center	
Dir., David J. Brenner, PhD, DSc; Assoc. Dir. Gerhard Randers-Pehrson, PhD; Mgr., Stephen A. Marino, MS	
Research using RARAF.....	98
Development of Facilities.....	101
Singletron Utilization and Operation.....	105
Training.....	105
Dissemination.....	107
Personnel.....	108
Recent Publications of Work Performed at RARAF.....	108
PUBLICATIONS.....	109

Collaborating Institutions

Individuals from the following departments and institutions collaborated with the Center's faculty and staff in the research reports included in this year's publication (for individual attributions see specific reports):

Collaborating Columbia University Departments:

- Department of Radiation Oncology
- Department of Surgery
- Department of Mechanical Engineering
- Department of Systems Biology
- Department of Electrical Engineering

Collaborating Institutions:

- Department of Radiation Oncology, University of Iowa, Iowa City, IA
- Department of Radiology, Albert Einstein College of Medicine, Bronx, NY
- Department of Mechatronics Engineering, Harbin Institute of Technology, Harbin, Heilongjiang, China
- Department of Microbiology and Immunology, Albert Einstein College of Medicine, Bronx, NY
- European Commission, Joint Research Centre, Institute for Transuranium Elements, Karlsruhe, Germany
- Institute for Advanced Research, Tarapacá University, Arica, Chile
- Department of Therapeutic Radiology, Yale University School of Medicine, New Haven, CT.
- Department of Radiation Oncology, Stanford University School of Medicine, Stanford, CA.
- Lovelace Biomedical and Environmental Research Institute, Lovelace Respiratory Research Institute, Albuquerque, NM. ■



Gary Johnson was presented with the annual College of Physicians and Surgeons Award for Excellence in a formal ceremony in January. (l to r): Gary Johnson; David Brenner and Gary Johnson; Dean Lee Goldman, David Brenner, and Gary Johnson.

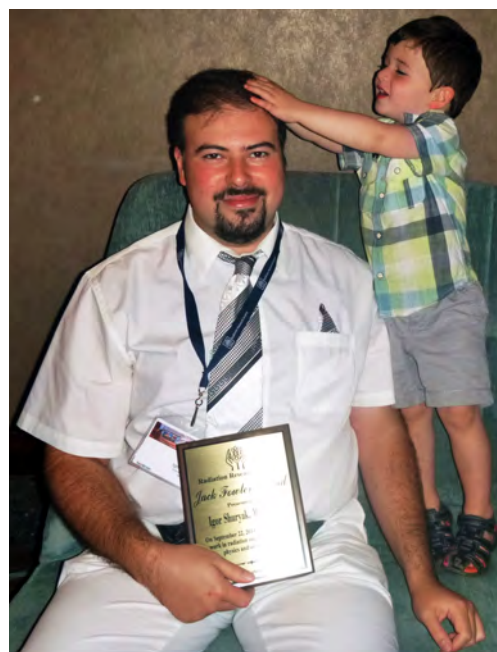
Acknowledgement of Support

In 2014 the Center for Radiological Research was supported by competitively awarded grants from the following agencies:

- Department of Health and Human Services
 - Biomedical Advanced Research and Development Authority
 - National Institutes of Health:
 - National Cancer Institute [Program Project (P01) and Individual Research Grants (R01s)]
 - National Institute of Biomedical Imaging and Bio-engineering (P41)
 - National Institute of Allergy and Infectious Disease (U19)
- National Institute of Environmental Health and Safety (R01s and R21)
- National Institute of General Medical Sciences (R01)
- Gardner Capital Corporation
- National Aeronautics and Space Administration
- Wallace H. Coulter Foundation

Websites

Center for Radiological Research.....www.cumc.columbia.edu/crr/
Radiological Research Accelerator Facility.....www.raraf.org
Center for High-Throughput Minimally-Invasive Radiation Biodosimetry.....cmcr.columbia.edu
Mechanisms of Bystander Effects.....www.radiation-bystander.columbia.edu
Web-Rad-Train.....www.web-rad-train.org
Department of Radiation Oncology.....www.cumc.columbia.edu/dept/radoncology
CRR Annual Reports (1999-present)..... www.cumc.columbia.edu/crr/events/annual-reports



Left: Elvis was sighted presenting the Jack Fowler Award to Igor Shuryak at the Radiation Research Society Meeting in Las Vegas. Or it was that Radiation Research Society president Frank Cucinotta? Right: Igor and Al Shuryak.

A Note from Our Director

Our Center continues to thrive. One very pleasing event this year was being awarded another five years of funding from the NIH for our "Center for High-Throughput Minimally-Invasive Radiation Biodosimetry". This project represents one of our more translationally oriented programs, applying our cytogenetics, transcriptomics and metabolomics expertise to current issues of homeland security. Over its history our Center has always maintained a balance between basic radiation research and translational applications to current-day problems.

And speaking of our history, we approach our Centenary! The original founder of our Center, Gioacchino Failla graduated with a Bachelors degree in Electrical Engineering from Columbia University in 1915, and started research in 1916 in what would become the Memorial Hospital Biophysics Laboratory (which would subsequently become the Columbia University Radiological Research Laboratory and then the Center for Radiological Research). There will be more of our history in the next Annual Report, and a variety of events are being planned for our centenary, so stay tuned!

Failla was the archetypal translational radiation researcher, studying the mechanisms of how radiation interacts with matter and then applying these concepts both to develop the fundamentals of radiation dosimetry, and to apply them to the then new field of radiation therapy. Failla was inspired in this by his PhD Supervisor, Marie Curie, who very much saw her basic research as leading to practical applications, both in radiotherapy and in radiology. Some nice illustrations of both of these themes are illustrated below. On the left is a clipping from the New York Times (May 12 1921), describing Marie Curie's visit to New York (and her graduate student Failla), with the Times reporting that she hoped to "end all cancers" with radium therapy. On the right is Mme. Curie driving one of the "Little Curie" ambulances that she designed during World War 1, each containing a portable x-ray machine.

These themes of translational radiation research both for radiation oncology and for radiology, continue to dominate our thinking, 100 years on.... ■

The New York Times.

MME. CURIE PLANS TO END ALL CANCERS

Says Radium Is Sure Cure, Even in Deep-Rooted Cases, if Properly Treated.

GETS TRIBUTE ON ARRIVAL

Motherly Looking Scientist in Plain Black Frock Gives Thanks to Americans.

Bringing the message that radium could cure even the most deep-rooted cancer, Mme. Marie Curie, whose husband, the late Professor Pierre Curie, gave her the major part of the credit for their joint discovery of radium, arrived yesterday on the Olympic of the White Star Line. Mme. Curie came at the invitation of a group of women who have raised more than \$100,000 to present her with a gram of radium.



Staff News

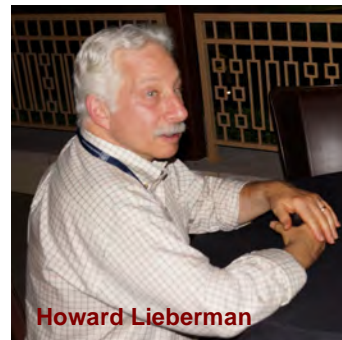
Dr. David Brenner continued as a member of the National Academy of Sciences Nuclear and Radiation Studies Board, and was a member of a NAS study on “Research Directions in Human Biological Effects of Low Level Ionizing Radiation.” He was also a member of the New York City Radiological Advisory Committee (RAC), which is an interagency committee comprised of local NYC representatives supplemented with national expertise from state, federal, and the private sector. Dr. Brenner continued to serve as an Associate Editor of the journal *Radiation and Environmental Biophysics*.



Dr. Tom Hei completed his six year term as a Distinguished Visiting Scientist at the National Institute of Radiological Sciences (NIRS) in Chiba, Japan and served as an external examiner of the Hiroshima University Phoenix Leader Education Program. He holds an Adjunct Professorship at the Chinese Academy of Sciences and a Chair Professorship at Soochow University. He serves as Editor in Chief of *Life Sciences in Space Research*, and as an Associate Editor of the *Journal of Radiation Research* and of *Translational Cancer Research*. In October, Dr. Hei began a six year term on the NIH Cancer Etiology Study Section.



Dr. Howard Lieberman was a member of the Israel Cancer Research Fund Scientific Advisory Board. He continued to serve as Associate Editor for both *Radiation Research* and the *Journal of Cellular Physiology*.



Dr. Sally Amundson continued to serve on the National Council for Radiation Protection and Measurements (NCRP), chaired a NCRP commentary on basic science and epidemiology integration for low dose radiation exposures, and served on a National Academies of Science committee on backscatter x-ray machines for airport passenger screening. In addition, Dr. Amundson continued to serve on the Governing Council of the Radiation Research Society and as an Associate Editor of *Radiation Research*, and completed her service on the Scientific Advisory Committee of the Radiation Effects Research Foundation (RERF) in Hiroshima, Japan.



During the year, Angela Lugo was promoted to Business Manager, Annerys Rodriguez was promoted to Junior Accountant, and Margaret German was promoted to Senior Clerk. Mr. Gary Johnson received the College of Physicians and Surgeons Award for Excellence (p. 4), and Dr. Igor Shuryak won the Jack Fowler Award of the Radiation Research Society (p. 5).

Several visiting scientists also performed research in the Center during 2014. Dr. Christine Hellweg of the Germany Aerospace Center joined the Center as a Visiting Scientist for six months, working with Dr. Tom Hei's team. Dr. Lisa Herr of Marco Durante's laboratory at GSI Helmholtz Center (Darmstadt, Germany) came to the Center to work on a project with Dr. David Brenner's team. Ms. Sherry Yin, a fourth year P&S

medical student, took a year off to do research with Drs. Simon Cheng and Tom Hei. She received the AMA seed grant, the P&S Dean's Fellowship, and the AOA Carolyn L. Kuckein Student Research Fellowship for this work. Finally, Dr. Chi Zhang, a senior radiation oncology resident at CUMC, also worked in Dr. Tom Hei's laboratory. He received the Radiological Research Society of North America (RSNA) Resident's Research Award for 2014.

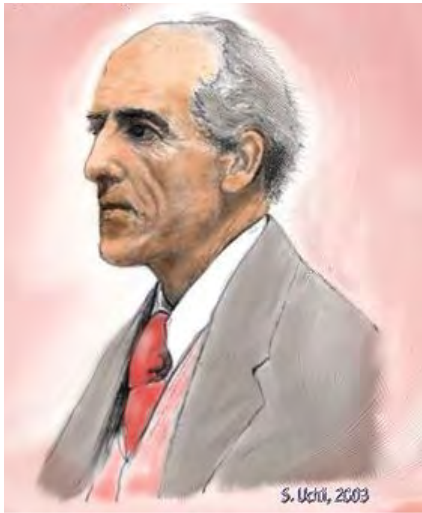
Mr. Stephen Marino, who served as the RARAF administrator for many years, retired at the end of the year. Drs. Sureshkumar and Ana Vasileva also left the center in 2014. We wish them all well in the future. ■

The Weldon Memorial Prize

It has been announced that our Director, David Brenner, will be awarded the next Weldon Memorial Prize, which is given annually by the University of Oxford. The prize is awarded *"without regard to nationality or membership of any University to the person who, in the judgment of the electors, has, in the ten years next preceding the date of the award, published the most noteworthy contribution to the development of mathematical or statistical methods applied to problems in biology"*.

The prize is named in honor of Walter Weldon (1860-1906), who famously rolled a set of twelve dice 26,306 times "to judge whether the differences between a series of group frequencies and a theoretical law, taken as a whole, were or were not more than might be attributed to the chance fluctuations of random sampling." Weldon's dice data were used by Karl Pearson in his pioneering 1900 paper on the chi-squared statistic.

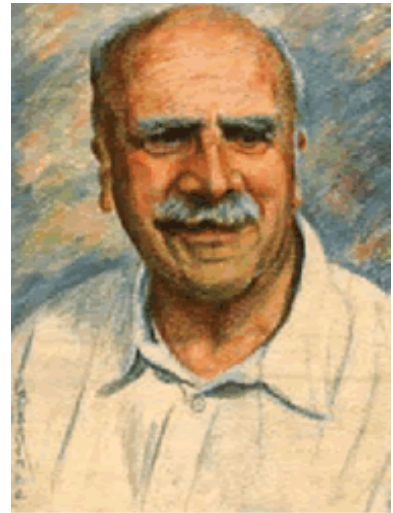
A few of the past recipients of the Weldon Prize are shown below: ■



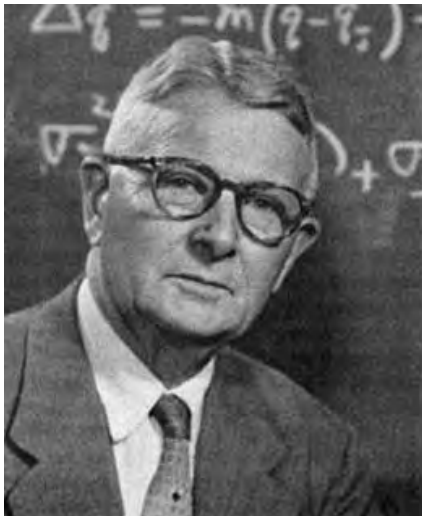
Karl Pearson (1912)



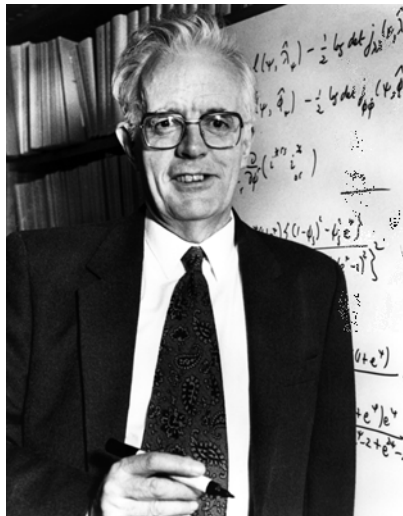
Ronald Fisher (1930)



JBS Haldane (1938)



Sewall Wright (1947)



David Cox (1983)



Richard Peto (2003)

Laboratory Colloquia and Seminars

Approximately every four months, the Center organizes morning-long colloquium sessions featuring presentations of recent work by Center researchers and guest speakers. These colloquia are attended by Center professional and technical staff and graduate students, as well as by physicians and scientists from other departments at CUMC. They serve as a forum for discussions and forging future collaborations. The 2014 Colloquium Series was organized and coordinated by Dr. Lubomir Smilenov.

January Colloquium:

- Dr. Emily Chen, Department of Pharmacology, CUMC: “Shotgun proteomics – from phenotypes to hypotheses.”
- Dr. Guy Garty, CRR: “Microbeam-coupled capillary electrophoresis: Measuring the processing of reactive oxygen species in single irradiated cells.”
- Dr. Chi Zhang, Department of Radiation Oncology, CUMC: “Treat glioblastomas like HIV – Multi-targeted therapy.”

July Colloquium:

- Dr. Vladimir Ivanov, CRR: “Radiation-induced crosstalk of human glioblastoma cells and neural stem cells (NSC) regulates viability and differentiation of NSC.”
- Dr. Nobuyuki Hamada, Central Research Institute of Electric Power Industry (CRIEPI), Japan:

“Ionizing irradiation stimulates proliferation of human lens epithelial cells.”

- Dr. Sunil Panigrahi, CRR: “Rad9 regulates the base excision repair gene Neil1.”

December Colloquium:

- Dr. Shanaz Ghandhi, CRR: “Effect of ⁹⁰Sr internal emitter on gene expression in mouse blood.”
- Prof. Howard Lieberman, CRR: “Tracing Darwin’s steps: A trip to the Galapagos.”
- Prof. Oliver Hobert, Dept. of Biochemistry / Molecular Biophysics, CUMC: “Memory of Things Past.”

In addition to our colloquium series, we have also welcomed a number of distinguished guest speakers from around the country and around the world. Guest speakers during 2014 included the following:

- Dr. Vilhelm A. Bohr, Laboratory of Molecular Gerontology, NIH: “Nuclear and Mitochondrial DNA Repair Aspects of Neurodegeneration.”
- Prof. John W. Hopewell, The Particle Therapy Cancer Research Institute at the University of Oxford: “Biological Effective Dose in Radiosurgery: does it matter, should we care?”
- Dr. Jingsong Yuan, MD Anderson Cancer Center: “DNA damage response pathways in cancer development and therapy” ■



Final preparation of the CMCR renewal proposal took over the conference room in September.

Faculty and Staff

Faculty:

DAVID J. BRENNER, Ph.D., D.Sc.

➤ *Director*

➤ *RARAF Director*

Higgins Professor of Radiation Biophysics
Professor of Radiation Oncology
Professor of Environmental Health Sciences

TOM K. HEI, Ph.D.

➤ *Associate Director*

➤ *Vice-Chairman, Dept. of Radiation Oncology*

Professor of Radiation Oncology
Professor of Environmental Health Sciences

ERIC J. HALL, D.Phil., D.Sc., FACR, FRCR, FASTRO

Higgins Professor Emeritus,
Special Lecturer in Radiation Oncology,
Special Research Scientist

CHARLES R. GEARD, Ph.D.

Professor Emeritus of Clinical Radiation Oncology

HOWARD B. LIEBERMAN, Ph.D.

Professor of Radiation Oncology
Professor of Environmental Health Sciences

SALLY A. AMUNDSON, Sc.D.

Associate Professor of Radiation Oncology

GUY GARTY, Ph.D.

Associate Professor of Radiation Oncology (in the
CRR) at the Columbia University Medical Center

PETER GRABHAM, Ph.D.

Assistant Professor of Radiation Oncology (in the
CRR) at the Columbia University Medical Center

LUBOMIR SMILENOV, Ph.D.

Assistant Professor of Radiation Oncology (in the
CRR) at the Columbia University Medical Center

YONGLIANG ZHAO, Ph.D.

Adjunct Assistant Professor

Research Staff:

GERHARD RANDERS-PEHRSON, Ph.D.

Senior Research Scientist

ADAYABALAM BALAJEE, Ph.D.

Research Scientist

VLADIMIR IVANOV, Ph.D.

Research Scientist

HONGNING ZHOU, M.D.

Research Scientist

ALAN BIGELOW, Ph.D.

Associate Research Scientist

CONSTANTINOS BROUSTAS, Ph.D.

Associate Research Scientist

GLORIA CALAF, Ph.D.

Adj. Associate Research Scientist

CONGJU CHEN, Ph.D.

Associate Research Scientist

SHANAZ GHANDHI, Ph.D.

Associate Research Scientist

ANDREW HARKEN, Ph.D.

Associate Research Scientist

PREETY SHARMA, Ph.D.

Associate Research Scientist

M.A. SURESHKUMAR, Ph.D.

Associate Research Scientist

SUNIL PANIGRAHI, Ph.D.

Associate Research Scientist

BRIAN PONNAIYA, Ph.D.

Associate Research Scientist

MIKHAIL REPIN, Ph.D.

Associate Research Scientist

IGOR SHURYAK, M.D., Ph.D.

Associate Research Scientist

HELEN TURNER, Ph.D.

Associate Research Scientist

ANA VASILEVA, Ph.D.

Associate Research Scientist

LI WANG, Ph.D.

Associate Research Scientist

YANPING XU, Ph.D.

Associate Research Scientist

ERIK YOUNG, Ph.D.

Associate Research Scientist

KEVIN M. HOPKINS, M.S., Senior Staff Associate

STEPHEN A. MARINO, M.S., Senior Staff Associate

M. HASEEB DURRANI, M.S., Staff Associate

DENNIS FARRELL, Staff Associate

JAY PERRIER, Staff Associate

RADOSLAW PIENIAZEK, Staff Associate

MARIA TAVERAS, R.N., Research Nurse

Post-Doctoral Research Scientists:

MANUELA BUONANNO, Ph.D.

STANLEY LUE, Ph.D.

DAVID WELCH, Ph.D.

JINHUA WU, Ph.D.

Design & Instrument Shop:

GARY W. JOHNSON, A.A.S., Senior Staff Associate

➤ *Design & Instrument Shop Director*

DAVID CUNIBERTI, B.A., Instrument Maker

DENNIS KEAVENEY, Instrument Maker

ROBERT C. MORTON, Instrument Maker

Technical Staff:

CUI-XIA KUAN, Technical Assistant

MASHKURA CHOWDHURY, Technician B

Administrative & Secretarial Staff:

ERICA PENA, B.A., Center Administrator

MARGARET ZHU, M.A., Center Administrator

ANGELA LUGO, B.A., Business Manager

ANNERYS RODRIGUEZ, Junior Accountant

MARGARET GERMAN, Senior Clerk

Faculty and Staff



Front Row (l-r): Dr. Gerhard Randers-Pehrson, Dr. Sally Amundson, Dr. Eric Hall, Dr. David Brenner, Dr. Tom Hei, Dr. Howard Lieberman, Ms. Margaret Zhu.

2nd Row: Mr. Gary Johnson, Dr. Constantinos Broustas, Dr. Charles Geard, Ms. Sherry Yin, Dr. Li Wang, Ms. Mashkura Chowdhury, Dr. Preety Sharma, Dr. Jinhua (Dannis) Wu, Dr. Shanaz Ghandhi, Ms. Cui-Xia Kuan, Dr. Stanley Lue, Ms. Maria Taveras, Dr. Helen Turner, Ms. Margaret German, Dr. Peter Grabham, Mr. Dennis Keaveney, Ms. Angela Lugo, Dr. Lubomir Smilenov.

Back Row: Youping Sun (Radiation Oncology), Mr. Dennis Farrell, Mr. Robert Morton, Dr. Sunil Panigrahi, Mr. David Cuniberti, Dr. Mikhail Repin, Dr. Kunal Chaudhary (Radiation Oncology), Dr. Andrew Harkin, Mr. Stephen Marino, Dr. Igor Shuryak, Dr. Guy Garty, Mr. Kevin Hopkins, Dr. Alan Bigelow, Dr. Yanping Xu, Dr. Manuella Buonanno, Dr. Brian Ponnaiya, Mr. Haseeb Durrani.

Not Pictured: Dr. Yongliang Zhao, Dr. Adayabalam Balajee, Dr. Vladimir Ivanov, Dr. Hongning Zhou, Dr. Gloria Calaf, Dr. Congju (Maggie) Chen, Dr. M.A. Sureshkumar, Dr. Ana Vasileva, Dr. Erik Young, Mr. Jay Perrier, Mr. Radek Pieniazek, Dr. David Welch, Ms. Erica Pena, Ms. Annerys Rodriguez.



Top (l to r): Dennis Keaveney, Igor Shuryak; Howard Lieberman; Karen Schleif. Second Row (l to r): Charles Geard, Tom Hei; Shanaz Gandhi, Vladimir Ivanov. Third Row (l to R): Dennis Keaveney, David Cuniberti, Gary Johnson, David Brenner, Rob Morton, Sally Amundson, Gerhard Randers-Pehrson, Steve Marino; Manuela Buonanno. Bottom Row (l to r): Tom Hei, Kumiko and Kenshi Komatsu (a visiting scientist with Drs. Hall and Hei from 1987 to 1989); Helen Turner; Yvette Acevedo, Eric Hall.

Development of the Super Microbeam at RARAF

Gerhard Randers-Pehrson, Andrew D. Harken, Guy Garty, and David J. Brenner

The Super Microbeam will use a super-conducting solenoid particle focusing system to focus our charged-particle microbeam down to a 75 nm beam spot size. This new system will replace our electrostatic microbeam, which has a current beam spot size of 400 nm. The design and construction of the Super Microbeam is proceeding in two phases: first, the design, purchase and installation of the super-conducting solenoid, then second, the installation of an electrostatic first element lens to reduce the beam to the ultimate 75 nm spot size.

In the past year, we have begun the construction of the Super-Microbeam, with funding support from our renewed P41 Biotechnology Resource Grant from NIBIB. We have finalized the magnetic parameters of the solenoid working with Cryomagnetics, Inc. (Oak Ridge,

TN, USA) and have ordered the solenoid based on the agreed specifications. The design includes two steel plates added for magnetic shielding to the top and bottom of the magnet housing to protect electronics and detectors that we will need to place at the endstation. The placement of these shields and the resulting magnetic fields are shown in Figure 1. With this magnetic field, the magnet will be able to focus 11 MeV alpha particles, our magnetically most difficult particle to focus.

We have also made a significant design change for the system in the second phase of this project. The original plan was to manufacture a single quadrupole triplet to use as the first stage of the compound lens. We have now concluded that we can reconfigure our present double triplet system to use the first two stages of what will now become a three-stage compound lens as shown in Figure 2. The advantages of this design are twofold. Firstly, the system has a higher demagnification, allowing us to sacrifice some of that in exchange for a somewhat longer working distance above the solenoid. Secondly, reusing the present lenses removes the need for time-consuming and expensive manufacture of new lenses.

This super microbeam will, in combination with imaging provided by the Super Resolution STED microscope, allow us to target and irradiate sub-resolution objects that cannot be irradiated with the current electrostatic microbeam. We anticipate that we will be taking possession of the new solenoid in the spring of 2015, and assembling of the Super Microbeam throughout the summer. We plan to have the completed Super-Microbeam system available for biology experiments by the Spring of 2016.

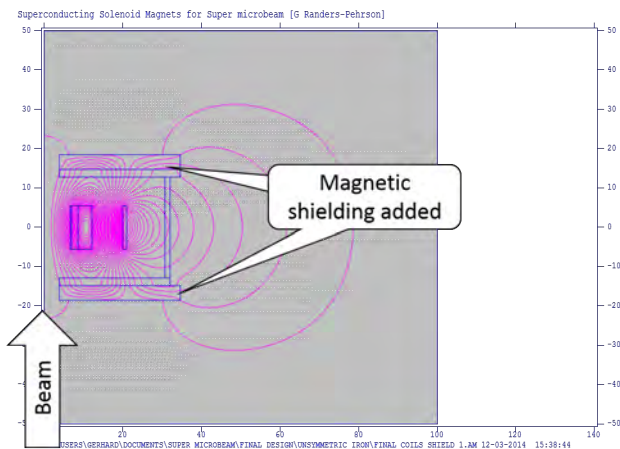


Figure 1. Magnetic field map of the solenoid provided by Cryomagnetics, Inc. This is a slice of the symmetric field around the beam axis indicated at the left.

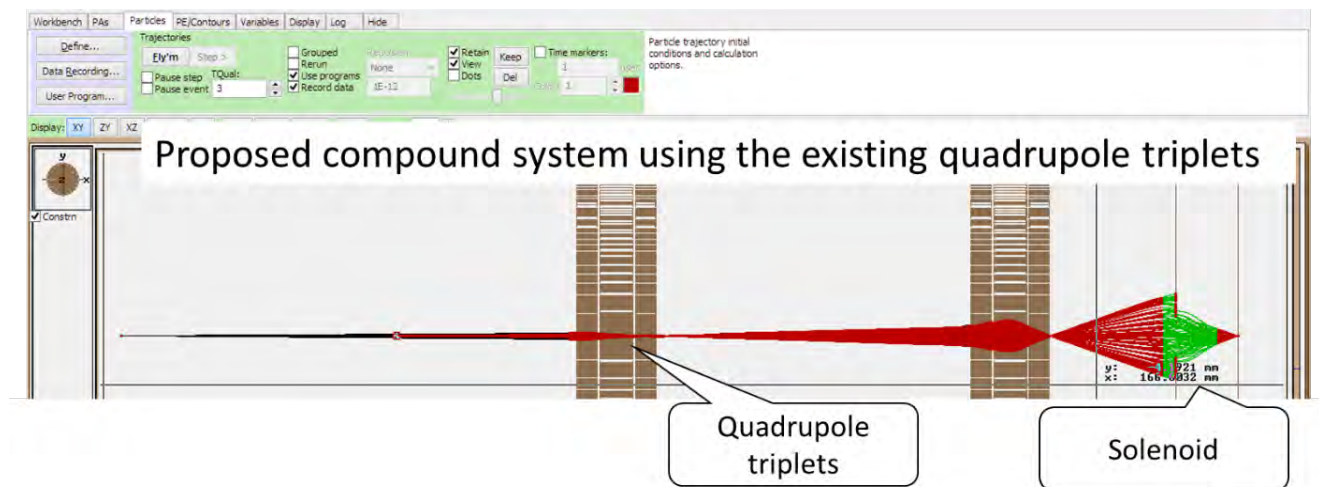


Figure 2. The new design of the compound system consisting of two electrostatic quadrupole triplets preceding the solenoid. Voltages are adjusted to obtain two point crossovers to avoid errors from rotational misalignment. The triplet positions were chosen to approximately balance spherical aberrations.

Super Resolution Stimulated Emission Depletion Microscopy at the RARAF Microbeam

Andrew D. Harken, Gerhard Randers-Pehrson, and David J. Brenner

Introduction

As we have developed better charged-particle microbeam focusing, we have concurrently developed better imaging techniques to work with our new capabilities [1]. As previously reported, we are developing a “Super Microbeam” with a sub-100 nm beam spot size [2].

Current imaging capabilities, based on standard diffraction limited imaging, are sufficient for our present beam size of 0.5 microns. For sub-100 nm targets we will require new imaging techniques – super resolution imaging. We have chosen Stimulated Emission Depletion (STED) as it is compatible with our ends for rapid imaging and can be built leveraging off our existing microbeam imaging technologies.

Presented here is the construction of our STED microscopy system as integrated with our multi-photon microscope on our microbeam endstation.

STED Theory

Stimulated emission depletion super resolution microscopy is based on the principle that an excited fluorophore can be de-excited by stimulating it to emit at a longer wavelength than the standard fluorescence wavelength. By localization of where this stimulated emission occurs, it is possible to deplete the excited fluorophores around the edge of an excitation spot leaving a sub-diffraction, sub-100 nm spot where fluorescence is possible. This depletion ‘donut’ and effective spot are shown schematically in Fig. 1.

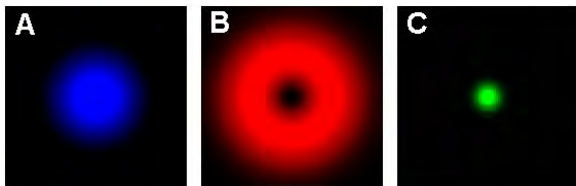


Figure 1. A) Excitation laser spot. B) Depletion ‘donut’ that is centered on the excitation spot. C) The effective fluorescence detected by the imaging system.

By scanning the excitation spot and the STED ‘donut’ across a sample as a combined pair, it is possible to form an image through correlation of spot location and fluorescent signal detection.

STED at RARAF

The implementation of STED at RARAF will be leveraging off our previous development of a multi-photon microscope on our microbeam endstation. The multi-photon microscope will provide the excitation laser

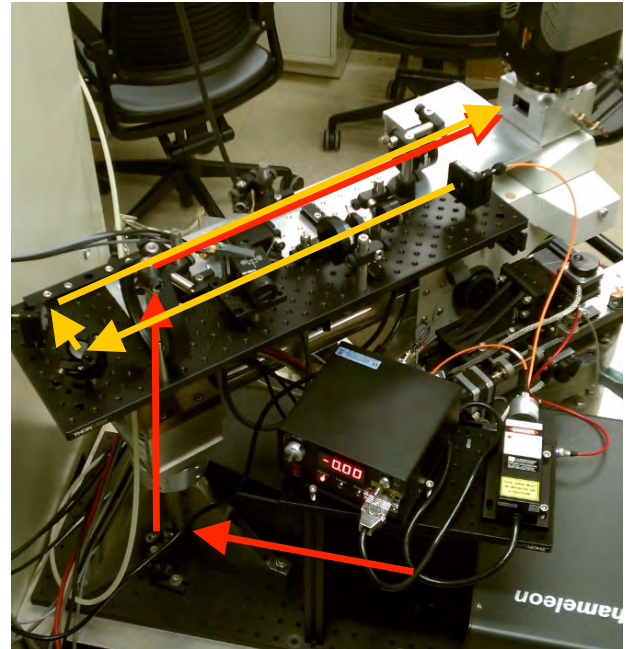


Figure 2. STED optics platform combined with the multi-photon microscope on the back of the microbeam endstation. Arrows show light pathways for the multi-photon laser (red) and the STED laser (yellow).

for our STED system. This existing microscope has all of the optics needed for introducing laser illumination into the optical focusing system of our endstation microscope.

We have constructed the STED microscope and are now proceeding with laser co-alignment. Figure 2 shows the microbeam endstation with the newly added optics bench for the STED laser introduction pathway. We have updated the design by moving the required optical components into this free space configuration at the endstation rather than housing them remotely with the STED laser source. We are currently using a low power diode-pumped solid-state laser, allowing us to co-align the lasers without the safety concerns of using the high power STED depletion laser. The STED depletion laser will be housed remotely and will be brought in at the optical fiber input as per the right side of Fig. 2.

Summary

Super resolution STED microscopy will allow us to image sub-100 nm targets of interest for RARAF users working with the new super microbeam. We have completed initial construction of the STED system and have begun final co-alignment of the lasers. We look forward to offering this new tool to our users in the coming year.

References

1. Bigelow A, Garty G, Funayama T, Randers-Pehrson G, Brenner D, Geard C. *Expanding the question-answering potential of single-cell microbeams at*

RARAF, USA. J Radiat Res (Tokyo). 2009;50 Suppl A:A21-8.

2. Randers-Pehrson G. *Design of a Super Microbeam*, Center for Radiological Research Annual Report 2011. 2012; pp. 26-27. ■

Flow Cytometry for Microfluidic Fluorescence-Activated Cell Sorting (microFACS) at RARAF

Andrew D. Harken, David Welch, Gerhard Randers-Pehrson, and David J. Brenner

Introduction

We have designed a microfluidic fluorescence-activated cell sorting (microFACS) system at RARAF. The microFACS system is designed to fit within the endstation geometry of the RARAF microbeam irradiator and ultimately to be coupled directly to our microfluidic cell handling and irradiation tools.

This development will allow RARAF users to sort cells based on fluorescent markers immediately prior to or following irradiation. The overall design of the microFACS is a sorting system that can be used as a standalone bench top unit or integrated with the other microfluidic systems at RARAF.

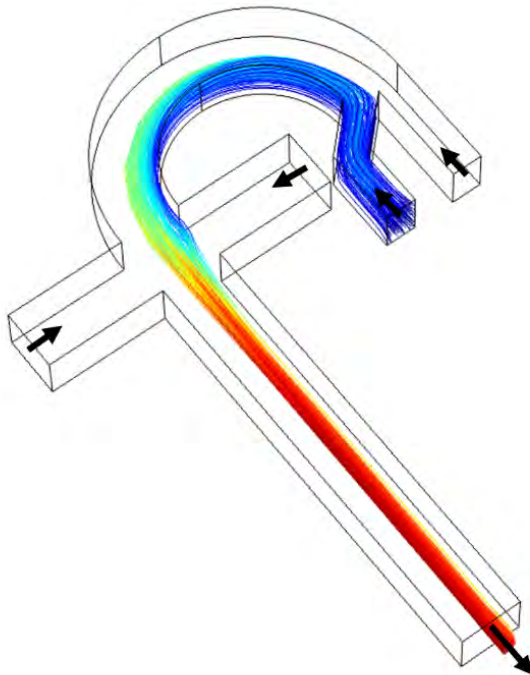


Figure 1. COMSOL model showing the Dean flow focusing of the sample input using the new 180° bend. The color of the trajectories corresponds to the velocity: slower (blue) to faster (red). The arrows denote flow directions. The column diameter at the exit is 60 μm .

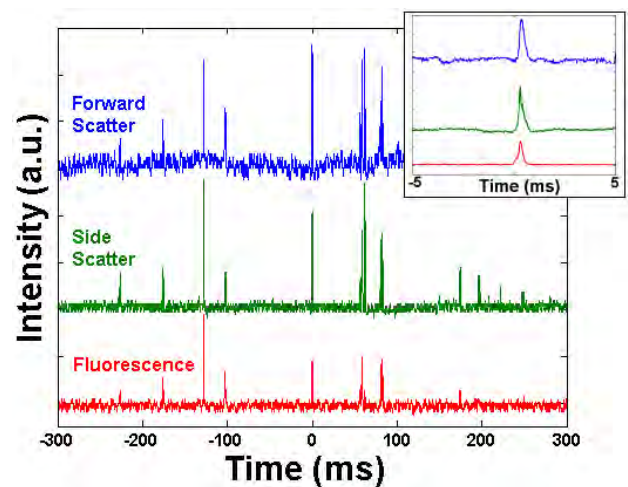


Figure 2. Oscilloscope traces of single-cell detection events (peaks) in the microfluidic flow cytometer channel. Forward scatter (blue), side scatter (green), and CellTracker Orange fluorescence (red) signals are acquired simultaneously. Inset is a blow up showing all three signals for a single-cell detection event at time zero. Traces are scaled to the forward scatter intensity for visibility.

Reported here is the continued refinement of the microfluidics flow cytometry section of the microFACS system.

Flow Cytometry

The flow cytometry section of the microFACS is responsible for sample introduction and for detection of the sample using laser fluorescence. The microfluidics uses Dean vortexing, based on the work of Mao, et. al., [1] to sheath flow focus the sample into a small column in the center of the flow channel. This focusing allows for more even illumination and detection of the samples. Figure 1 is the model of the focusing system using COMSOL Multiphysics software.

This design has been refined to use a 180° bend vs the 90° bend used in our previous design. This refinement has allowed the flow rate to be reduced by a factor of 5,

without loss of sheath flow focusing or detection fidelity, which makes the microFACS more compatible with our other microfluidic systems with regard to sample flow rates [2].

Sample detection

We have performed tests of this flow cytometry section using AG 1522 cells labeled with CellTracker orange at 500 nM for 30 minutes. Figure 2 shows oscilloscope traces of cell detection events in the three output channels: forward scatter (blue), side scatter (green) and fluorescence (red). The inset is the single event detection at time zero. All three signals are acquired simultaneously and scaled to the forward scatter intensity for visibility.

Conclusion

We have designed a new microfluidics fluorescence-activated cell sorting (microFACS) system. This work

demonstrates the ability of the flow cytometry section to detect cells labeled with a method previously used at RARAF. With refinement of our microfluidic flow focusing system, the microFACS is now more compatible with the flow rates of our other microfluidic devices. The continued testing and integration of the whole system is ongoing and we look forward to offering this technology to our users.

References

1. Mao X, Waldeisen JR, Huang TJ. "Microfluidic drifting" - implementing three-dimensional hydrodynamic focusing with a single-layer planar microfluidic device. *Lab on a Chip*. 2007;7:1260-2.
2. Garty G, Grad M, Jones BK, Xu Y, Xu J, Randers-Pehrson G, Attinger D, Brenner DJ. *Design of a novel flow-and-shoot microbeam*. *Radiation Protection Dosimetry*. 2011;143:344-8 PMID: PMC3108275. ■

Analyses of Microbeam-induced ROS in Single Cells

Brian Ponnaiya, Manuela Buonanno, Alan Bigelow, and Doug Spitz^a

Ionizing radiation-induced reactive oxygen species (ROS) are thought to contribute to genomic instability and ultimately to cancer [1-3]. Previous microbeam studies have demonstrated that cytoplasmic irradiations result in increased levels of ROS within the irradiated cell [4, 5]. Increased ROS from damaged mitochondria could mediate the late effects of high-LET radiation, such as cancer induction and normal tissue damage. The experiments discussed here were designed to compare the generation of ROS species following nuclear and cytoplasmic irradiation.

Individual Sirt3^{-/-} MEFs were microbeam irradiated with 1 or 10 particles through the nucleus, or 2 or 20 particles through the cytoplasm (1 or 10 particles in each of two sites, 2 μm away from the nucleus along the long axis of the cell). Immediately following the irradiation of cells on a dish, 10 μM DHE (in PBS with 5 mM Pyruvate) was added and the dish was returned to the incubator. Cells were imaged at 5, 15, 30 and 60 minutes post-irradiation. Images were acquired using a 40X air objective and an exposure time of 1 second (constant across all dishes and across all experiments). Mean nuclear fluorescence intensities of individual nuclei were measured using Image ProPlus.

The responses observed after nuclear and cytoplasmic irradiations are presented in figure 1. At the earliest time point assayed, 5 minutes post-irradiation, there were significantly increased fluorescence in the cells irradiated

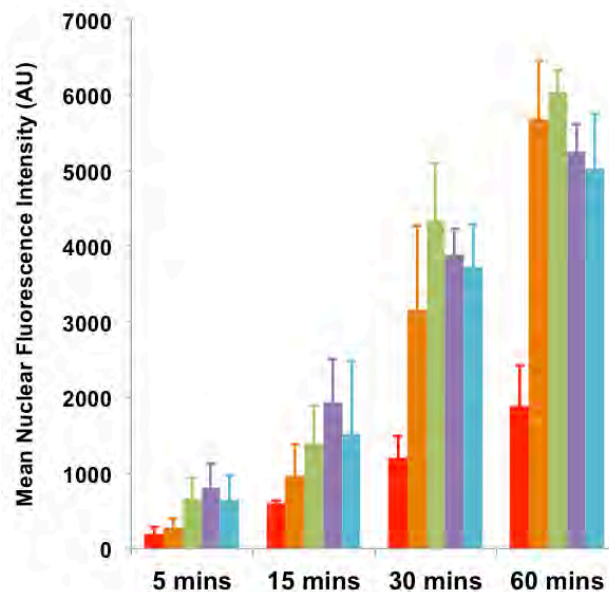


Fig 1. MitoSOX fluorescence in nuclei of control cells (red) and cells microbeam irradiated through either the nucleus [1 α-particle (orange) or 10 α-particles (green)] and cytoplasm [2 α-particles (purple) or 20 α-particles (blue)]. Data are expressed as the mean ± SD from 3 separate experiments.

^aDepartment of Radiation Oncology, University of Iowa, Iowa City, IA, USA.

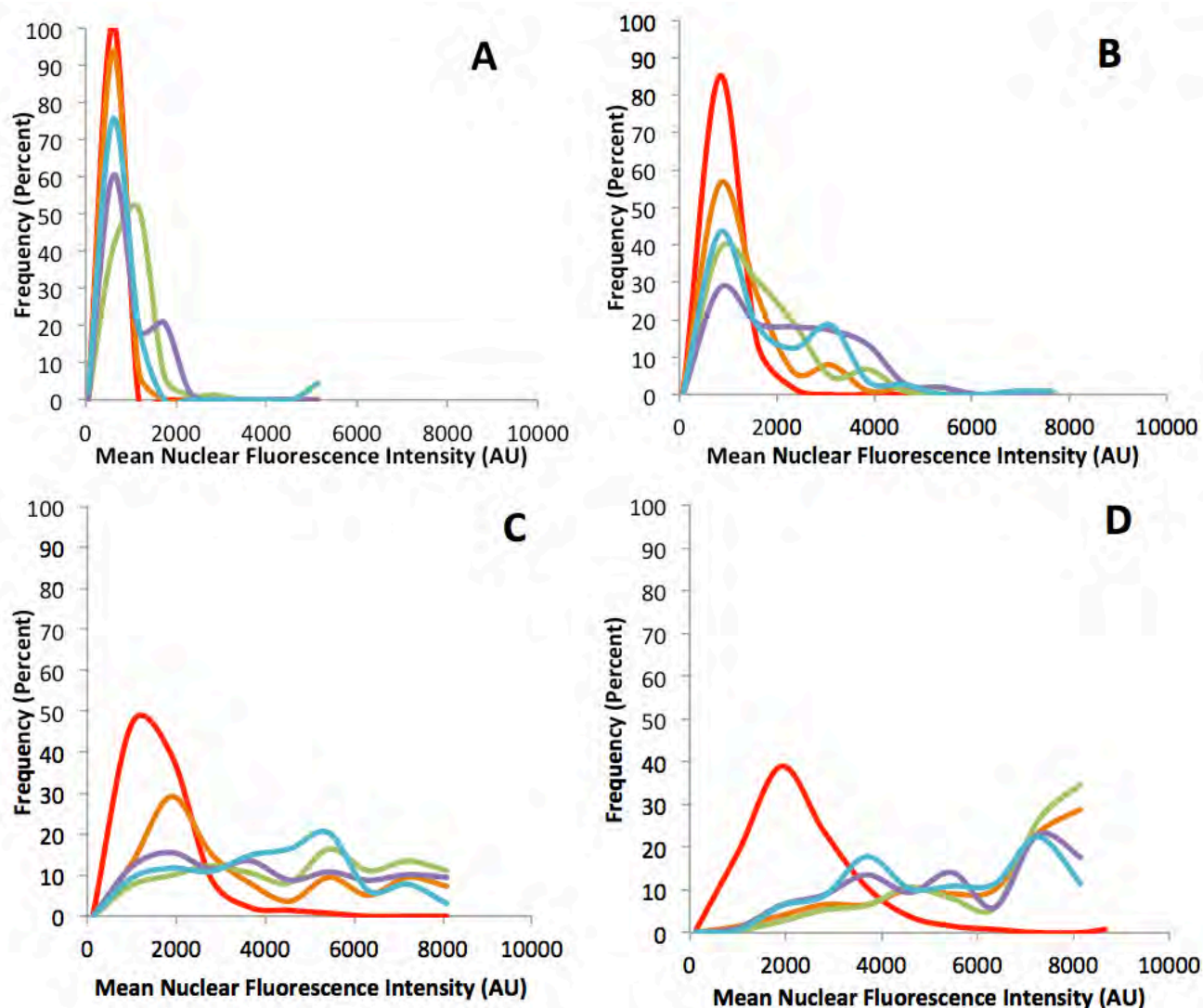


Fig. 2. Frequency distribution of MitoSOX fluorescence in nuclei of individual control cells (red) and cells microbeam irradiated through either the nucleus [1 α -particle (orange) or 10 α -particles (green)] and cytoplasm [2 α -particles (purple) or 20 α -particles (blue)], at 5, 15, 30 and 60 minutes post irradiation (Panels A, B, C and D respectively).

with 10 particles through the nucleus and both 2 and 20 particles through the cytoplasm. While there was a gradual increase in fluorescence in the control cells with increasing time post irradiation, at all subsequent time points there were significantly enhanced fluorescence intensities in all irradiated populations. While elevated levels of ROS in the nucleus might be expected following nuclear irradiations, this was true of cytoplasmic irradiations as well.

When analyzed as individual cell responses, (figure 2), there were increased fluorescence responses at the earliest time point assayed (5 minutes) in only some cells under all irradiation conditions (10 alpha particles through the nucleus being the most effective). These increases were significantly increased at 30 and 60 minutes post-irradiation. The kinetics of the response appears to be dose dependent to some extent - i.e. the 10 α -nuclear irradiated cells were quicker to respond than the 1 α -nuclear irradiated ones. Again, as in figure 1, with time a

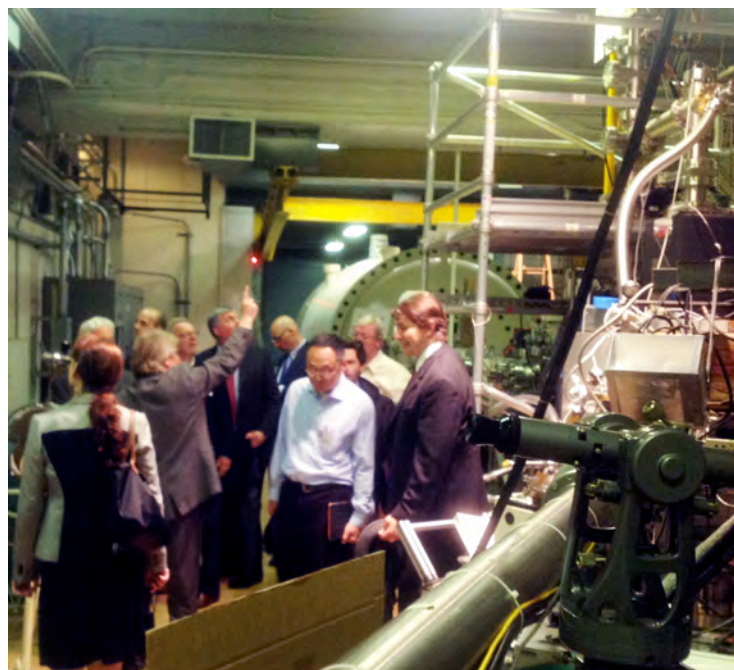
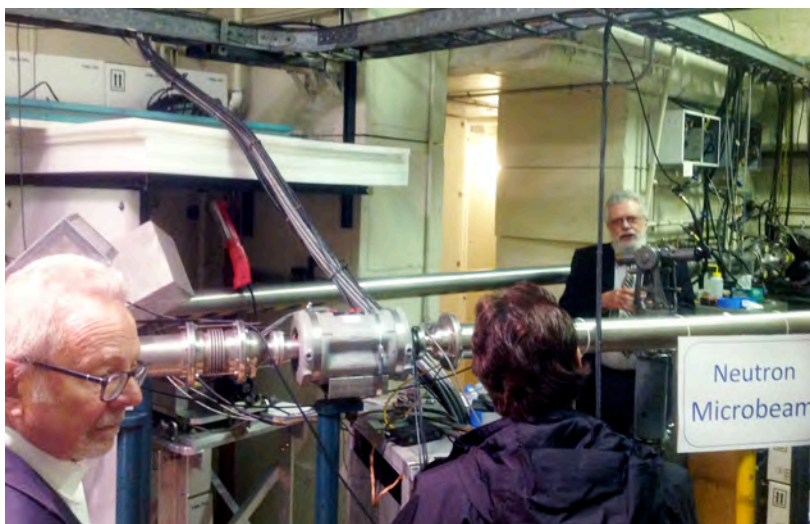
gradual increase in fluorescence in the control cells was observed.

In summary, it was observed that both nuclear and cytoplasmic irradiations resulted in elevated nuclear fluorescence as early as 5 min post irradiation. The elevated nuclear signals were observed up to 24 hours later (data not shown). Studies are ongoing to elucidate the signaling pathways involved in the generation of ROS in the nucleus following microbeam-targeted cytoplasmic damage.

References

1. Dayal D, Martin SM, Owens KM, Aykin-Burns N, Zhu Y, Boominathan A, Pain D, Limoli CL, Goswami PC, Domann FE, Spitz DR. Mitochondrial complex II dysfunction can contribute significantly to genomic instability after exposure to ionizing radiation. *Radiation research*. 2009;172(6):737-45. PubMed Central PMCID: PMC2793528.

2. Dayal D, Martin SM, Limoli CL, Spitz DR. Hydrogen peroxide mediates the radiation-induced mutator phenotype in mammalian cells. *The Biochemical journal*. 2008;413(1):185-91. PubMed Central PMCID: PMC2677991.
3. Ralph SJ, Rodriguez-Enriquez S, Neuzil J, Saavedra E, Moreno-Sanchez R. The causes of cancer revisited: "mitochondrial malignancy" and ROS-induced oncogenic transformation - why mitochondria are targets for cancer therapy. *Molecular aspects of medicine*. 2010;31(2):145-70. PubMed PMID: 20206201.
4. Hei TK, Zhou H, Ivanov VN, Hong M, Lieberman HB, Brenner DJ, Amundson SA, Geard CR. Mechanism of radiation-induced bystander effects: a unifying model. *J Pharm Pharmacol*. 2008;60(8):943-50. PubMed Central PMCID: PMC4410683.
5. Zhou H, Ivanov VN, Gillespie J, Geard CR, Amundson SA, Brenner DJ, Yu Z, Lieberman HB, Hei TK. Mechanism of radiation-induced bystander effect: role of the cyclooxygenase-2 signaling pathway. *Proceedings of the National Academy of Sciences of the United States of America*. 2005;102(41):14641-6. PubMed Central PMCID: PMC1253564. ■



Members of the CRR Advisory Council on a tour of RARAF. Clockwise from upper left: Eric Goldstone, C.J. DeSantis, Alan Jakimo, and Gerhard Randers-Pehrson; Chip Cameron and Gerhard Randers-Pehrson; Paul Locke, Alan Jakimo, David Brenner, and Gerhard Randers-Pehrson; Andrew Harkin, Gerald Chan, and other council members examine the beam lines exiting the accelerator.

A Bead-based Microfluidic Approach to Integrated Single-cell Gene Expression Analysis

Hao Sun^{a,b}, Jing Zhu^a, Tim Olsen^a, Jianguo Tao^b, Brian Ponnaiya, Sally A. Amundson, David J. Brenner, and Qiao Lin^a

A major challenge in gene expression profiling is the ubiquitous heterogeneity existing in biological samples [1, 2]. Conventionally, gene expression measurements are focused on groups of cells from organs, tissues or cell culture as the measurement technologies have been limited by accuracy, sensitivity, and dynamic range. While cells may appear morphologically identical, recent evidence reveals that gene expression levels in individual cells in a population can vary due to cellular

heterogeneity [3]. Thus, gene expression studies using groups of cells can fail to detect differences in the molecular composition of individual cells [1, 4].

We have developed a microbead-based approach that integrates all steps for genetic analysis of a single cell [5], including immobilization and lysis of the cell, as well as purification, reverse transcription (RT) and quantitative real-time PCR (qPCR) of messenger RNA (mRNA) (Figure 1). All biochemical reactions in the multi-step

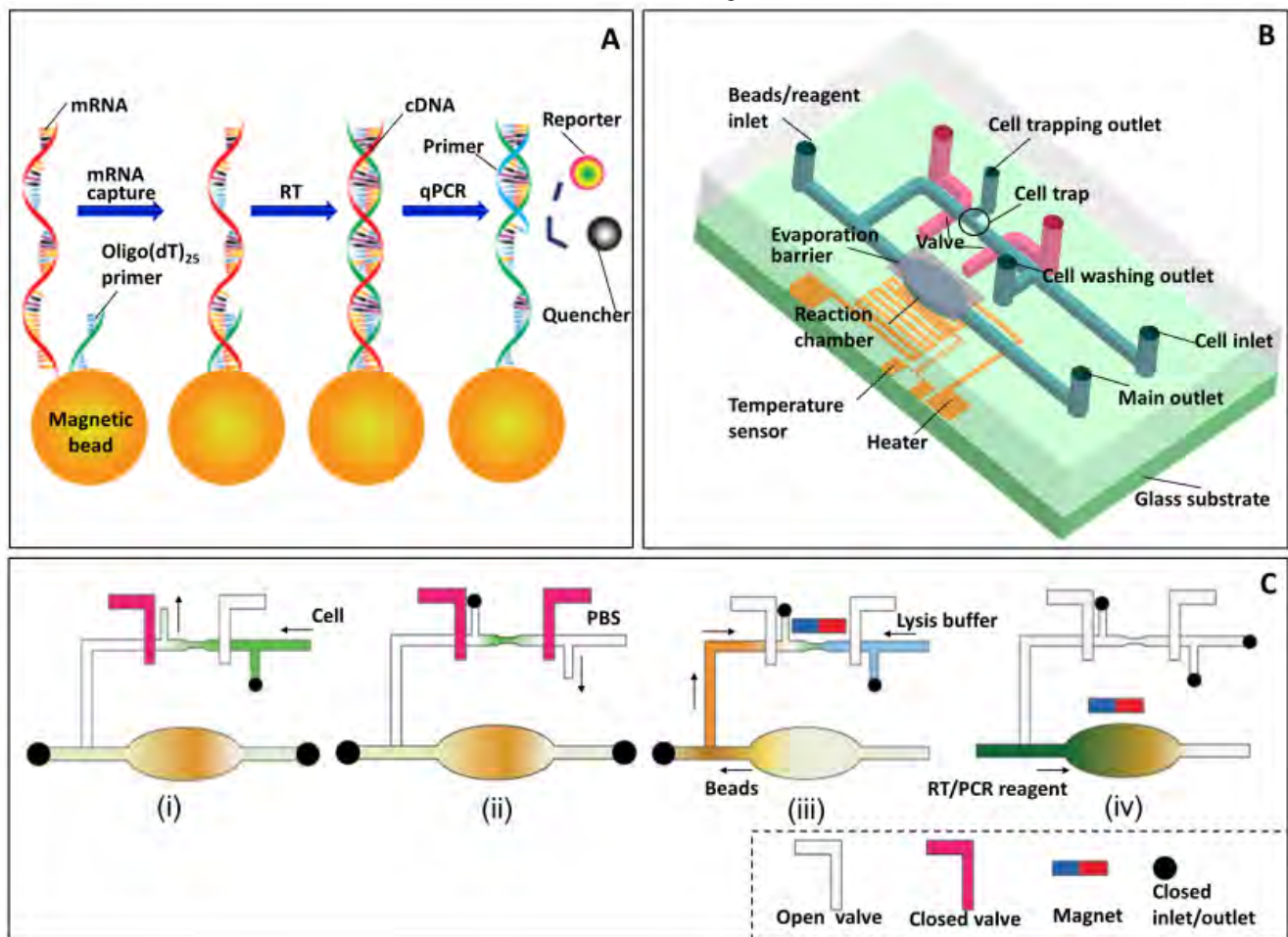


Figure 1. The microfluidic RT-qPCR device: (A) Bead-based RT-qPCR principle. Each Oligo(dT)₂₅ bead ($2.8 \pm 0.2 \mu\text{m}$) is composed of a superparamagnetic particle and a polymer shell. The beads specifically target polyA tails and can capture mRNA molecules from virtually any crude sample, eliminating the need to purify total RNA when the desired information-bearing nucleic acid is mRNA. (B) Schematic of the device. (C) Operation of the device.

^aDepartment of Mechanical Engineering, Columbia University, New York, NY, USA.

^bDepartment of Mechatronics Engineering, Harbin Institute of Technology, Harbin, Heilongjiang, China

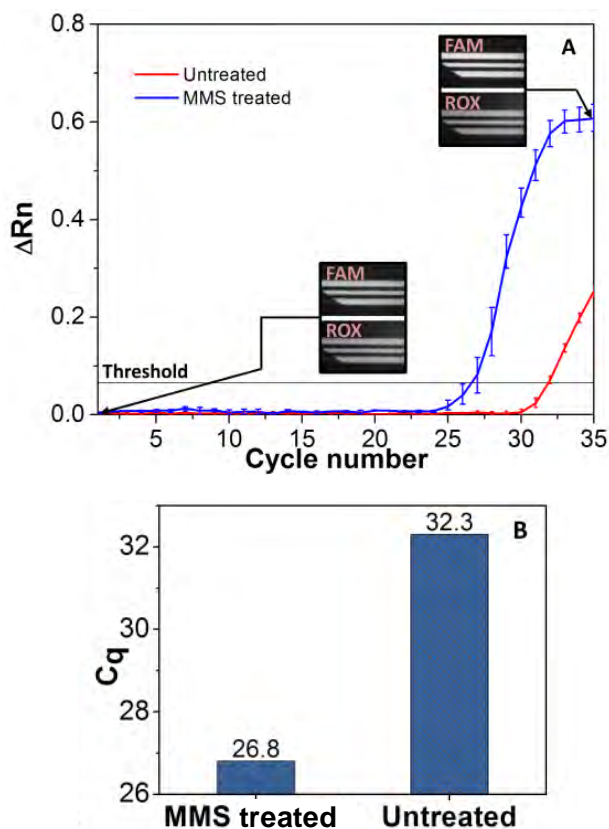


Figure 2. Fully integrated on-chip single-cell RT-qPCR. (A) Amplification curves of MMS treated and untreated single cell RT-qPCR. (B) C_q values for integrated RT-qPCR in treated and untreated single cells. All error bars correspond to standard deviation of five repeated experiments.

assay are completed on microbeads in a single chamber. This eliminates labor-intensive and error-prone manual transfer of the analyte and reagents between the reactions while simplifying the device design, fabrication and operation. As such, the device eliminates the potential for loss or cross-contamination of analytes and drastically improves assay efficiency especially at low mRNA abundance, thereby enabling rapid, sensitive and reliable single-cell gene expression analysis.

Preliminary experiments using the chip examined CDKN1A expression levels in single cells assayed following Methyl methanesulfonate (MMS) treatment

(Figure 2). The mean C_q value (the threshold cycle where fluorescence, indicating amplification, becomes detectable) of MMS treated single MCF-7 cells was 5.48 cycles lower than the value for untreated single cells. This means that after 2.5 h of MMS treatment, the amount of CDKN1A templates in individual MCF-7 cells was about 45-fold higher than in untreated single cells. After the MMS treatment, the transcript levels of the CDKN1A gene had been upregulated significantly in individual cells, and were easily detected in the microchip.

The results presented here demonstrate that our device is capable of detecting alterations in gene expression levels of single cells. In addition, the chip has the flexibility to be used as a preprocessing device for commercial systems that require reverse transcribed input (eg. Digital PCR machines) or pre-amplified material (eg. The NanoString nCounter).

References

- [1] Q. F. Wills, K. J. Livak, A. J. Tipping, A. J. Tipping, T. Enver, A. J. Goldson, D. W. Sexton, C. Holmes, Single-cell gene expression analysis reveals genetic associations masked in whole-tissue experiments. *Nature Biotechnology*, 2013, 31(8): 748-752.
- [2] R. Sandberg, Entering the era of single-cell transcriptomics in biology and medicine [J]. *Nature Methods*, 2014, 11(1): 22-24.
- [3] K.H. Narsinh, N. Sun, V. Sanchez-Freire, A.S. Lee, P. Almeida, et al., Single cell transcriptional profiling reveals heterogeneity of human induced pluripotent stem cells, *Journal of Clinical Investigation*, 2011, (121): 1217-1221.
- [4] D. W. M. Tan, K.B. Jensen, M.W.B. Trotter, J.T. Connelly, S. Broad, F.M. Watt, Single-cell gene expression profiling reveals functional heterogeneity of undifferentiated human epidermal cells, *Development*, 2013, (140): 1433-1444.
- [5] Sun H, Olsen T, Zhu J, Tao JG, Ponnaiya B, Amundson SA, Brenner DJ and Lin Q, A bead-based microfluidic approach to integrated single-cell gene expression analysis by quantitative RT-PCR. *RSC Advances*, 2015. 5(7): p. 4886-4893. NIHMSID 650011. ■



David Brenner and Steve Marino



Mashkura Chowdhury and Sally Amundson



Andrew Harkin and Eric Hall

Radiation-induced Differential Expression of p53 Responsive Genes is Influenced by their Cellular Localization: A Single-cell Study

Brian Ponnaiya, Manuela Buonanno, Sally A. Amundson, and David J. Brenner

Studies of cell-to-cell variability in gene expression are emerging in research areas such as cancer [1], stem cells [2], and immunology [3], for their potential to reveal new mechanistic insights within individual cells and to correlate them to cellular functions [4].

We have previously reported on the variability of alterations in gene expression in individual irradiated cells using a traditional RT-PCR approach [5] and Taqman Low-Density Arrays [6]. Here we present results of gene

expression alterations in single control and irradiated cells using the NanoString nCounter protocols [7]. This technology is attractive given the minimal amplification required and the possibility of examining a very large number of gene products (up to 800) in a single cell. It is sensitive and reproducible and also allows quantitative measurements of low abundance mRNAs [8, 9].

Early passage (population doubling < 35) IMR-90 human lung fibroblasts (Coriell Cell Repository, Camden, NJ) were maintained in a density-inhibited state for one

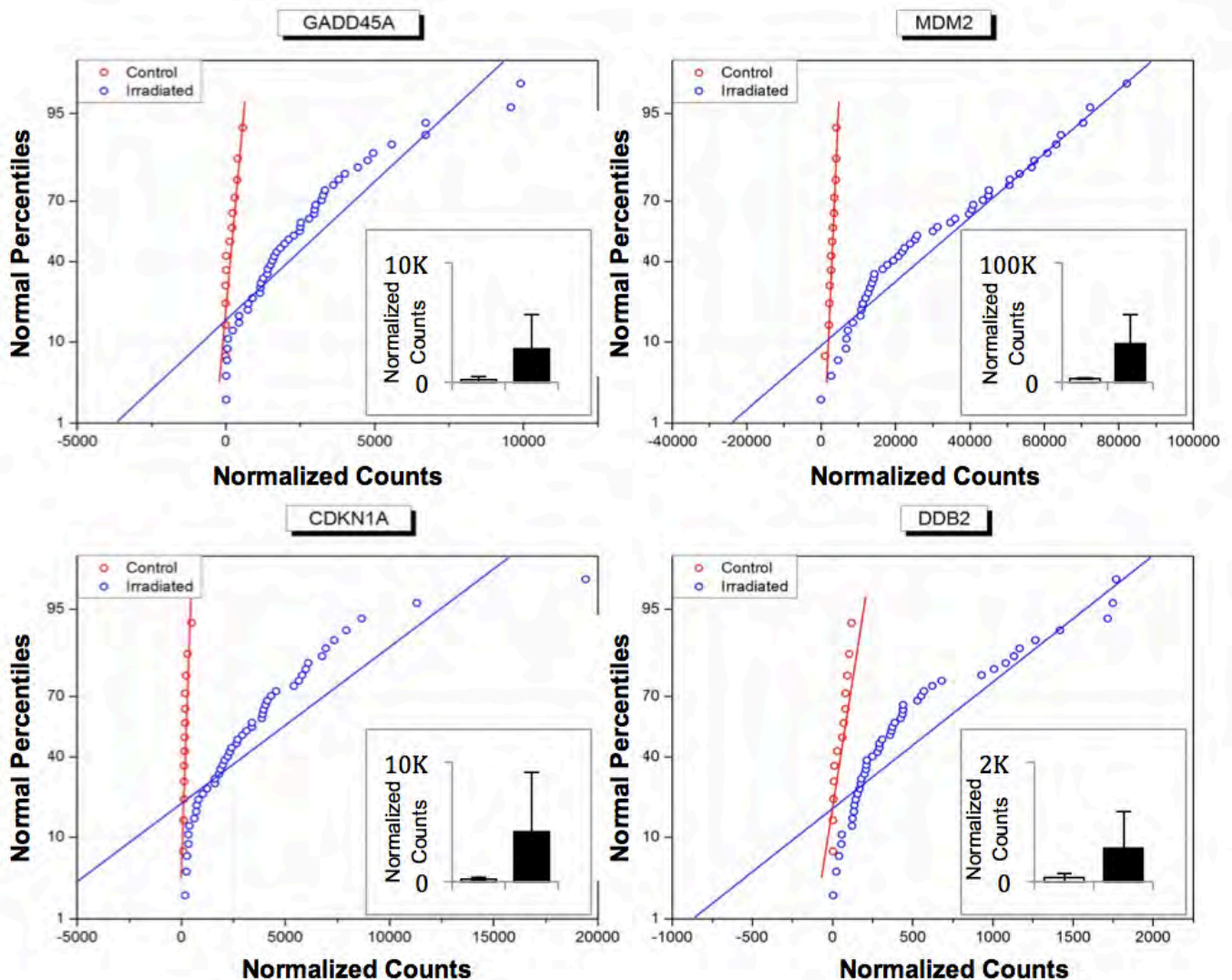


Fig. 1. Expression of p53-responsive genes coding for proteins localized to the nucleus. Probability plots of expression levels in 14 control (red symbols) and 48 irradiated (blue symbols) single cells. Insets are mean values for pooled counts of all control cells (clear bars) or all irradiated cells (filled bars) \pm SD.

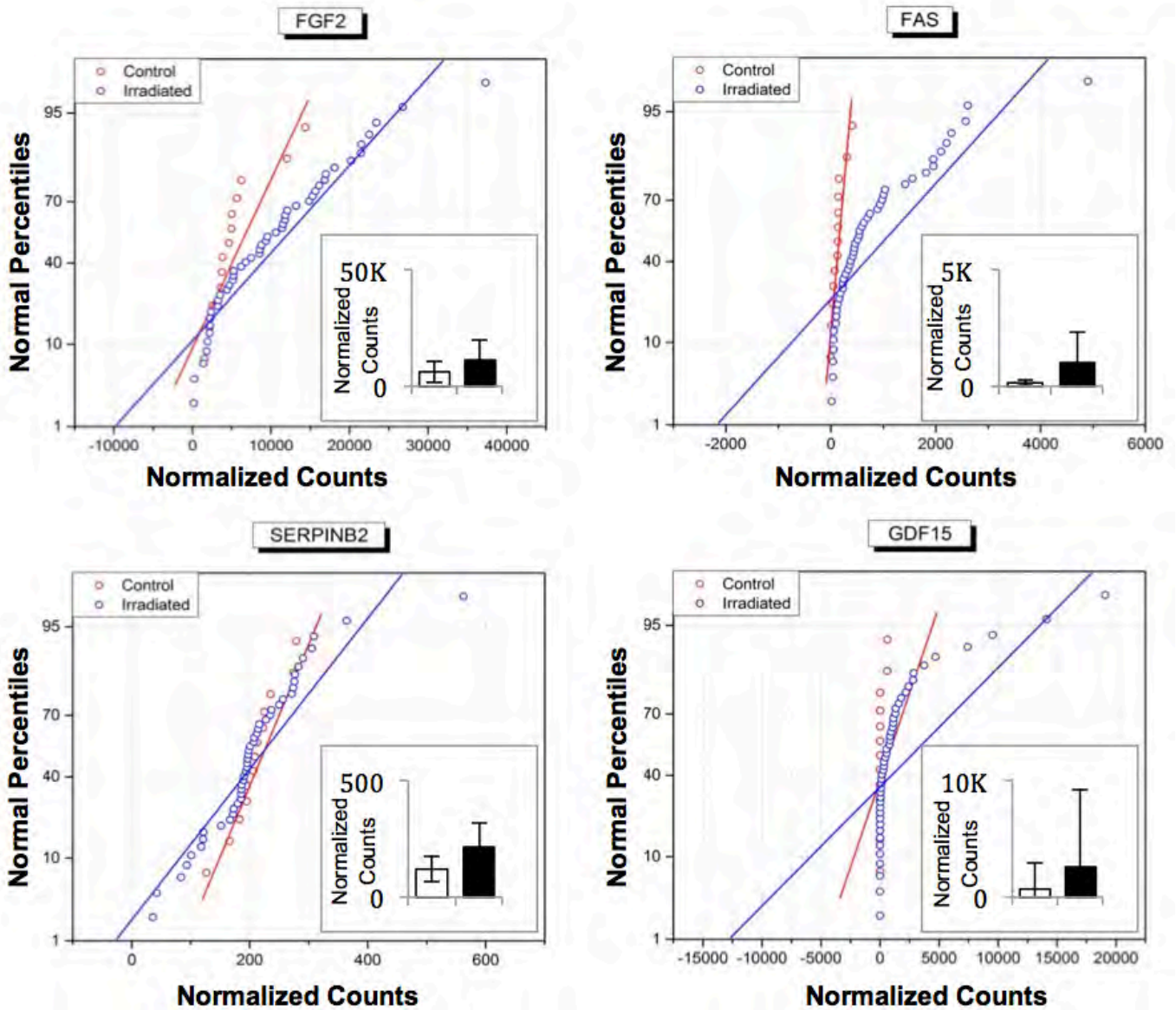


Fig. 2. Expression of p53-responsive genes coding for proteins localized to the cytoplasm or nuclear membrane. Probability plots of expression levels in 14 control and 48 irradiated single cells. Insets are mean values for pooled counts of all control cells (clear bars) or all irradiated cells (filled bars) \pm SD.

week to ensure that >90% of the population was in G0/G1 phase of the cell cycle [10]. Confluent cultures were exposed to a 4 Gy dose of γ rays (0.8 Gy/minute) using a Gammacell-40 ^{137}Cs irradiator (AECL, Ontario, Canada). Control cells were sham-treated and handled in parallel with the test cultures. Four hours after irradiation, the cells were harvested and resuspended at 1×10^6 cells/ml in 1% BSA in PBS (Sigma-Aldrich Corp., St. Louis, MO). One hundred, ten, or individual control and irradiated cells were sorted into wells of 96-well plates using a flow cytometer (FACSARIA, BD Biosciences, San Jose, CA) at the HICCC Flow Cytometry Shared Resource. The NanoString nCounter was then used to assay a 20-gene set in 14 non-irradiated and 48 irradiated single cells using a customized nCounter CodeSet. This custom panel included 4 endogenous control genes, B2M, PPIA and GAPDH and RPLPO, that have previously been shown to

be stably expressed across individual IMR-90 cells [6] as well as 16 genes that have been previously demonstrated to be highly radiation responsive in IMR-90 cells [11]. Raw counts for each gene were normalized using GAPDH and single cell profiles were analyzed as described below.

As a first step, expression profiles of p53-responsive genes were compared as a function of the cellular localization of their protein products. Results of genes coding for proteins localized in the nucleus, i.e. GADD45A, MDM2, CDKN1A and DDB2, are presented in Figure 1. For this set of genes there was very little variation in counts among control cells, as can be seen from the steep slopes in the probability plots and small deviation in the pooled data (inserts). In contrast, irradiated cells had a wider range of counts, with a large fraction of the cells demonstrating counts higher than those of the controls. This was also observed when the

two populations were compared, with increased mean counts in the irradiated pool of cells.

When expression profiles of p53-responsive genes that encode extra-nuclear proteins were compared in the same control and irradiated cells, a different pattern was observed (Figure 2). In control cells, expression levels for FGF2, FAS, SERPINB2 and GDF15 were, for the most part, more variable than those of transcripts coding for nuclear proteins. In addition, counts in a majority of the irradiated cells fell within the range of the control, non-irradiated cells. As can be seen from the figure, while there was an elevation of the mean counts in the irradiated pool of cells when compared to the controls, this increase was driven by only a small number of the irradiated cells.

In conclusion, these data demonstrate that when examined at the single cell level, alterations in expression of p53-responsive genes correlate with the cellular location of the corresponding protein. Expression of genes coding for nuclear proteins appeared to be more uniformly regulated among cells, and was increased in a majority of the irradiated cells, while only a small number of the same cells had increased numbers of transcripts for extra-nuclear proteins. This in turn points to the usefulness of single cell analyses, in particular, the quantification of multiple genes within the same individual cell.

References

1. Navin N, Hicks J. Future medical applications of single-cell sequencing in cancer. *Genome Med.* 2011; 3(5):31. Epub 2011/06/03. PMID: PMC3219072.
2. Narsinh KH, Sun N, Sanchez-Freire V, Lee AS, Almeida P, Hu S, Jan T, Wilson KD, Leong D, Rosenberg J, Yao M, Robbins RC, Wu JC. Single cell transcriptional profiling reveals heterogeneity of human induced pluripotent stem cells. *J Clin Invest.* 2011; 121(3):1217-21. PMID: PMC3049389.
3. Flatz L, Roychoudhuri R, Honda M, Filali-Mouhim A, Goulet JP, Kettaf N, Lin M, Roederer M, Haddad EK, Sekaly RP, Nabel GJ. Single-cell gene-expression profiling reveals qualitatively distinct CD8 T cells elicited by different gene-based vaccines. *Proc Natl Acad Sci U S A.* 2011; 108(14): 5724-9. PMID: PMC3078363.
4. Raj A, van Oudenaarden A. Nature, nurture, or chance: stochastic gene expression and its consequences. *Cell.* 2008; 135(2):216-26. Epub 2008/10/30. PMID: PMC3118044.
5. Ponnaiya B, Jenkins-Baker G, Randers-Pherson G, Geard CR. Quantifying a bystander response following microbeam irradiation using single-cell RT-PCR analyses. *Exp Hematol.* 2007; 35(4 Suppl 1):64-8. Epub 2007/03/24.
6. Ponnaiya B, Amundson SA, Ghandhi SA, Smilenov LB, Geard CR, Buonanno M, Brenner DJ. Single-cell responses to ionizing radiation. *Radiation and environmental biophysics.* 2013; 52(4):523-30. PubMed Central PMID: PMC3812812.
7. Geiss GK, Bumgarner RE, Birditt B, Dahl T, Dowidar N, Dunaway DL, Fell HP, Ferree S, George RD, Grogan T, James JJ, Maysuria M, Mitton JD, Oliveri P, Osborn JL, Peng T, Ratcliffe AL, Webster PJ, Davidson EH, Hood L, Dimitrov K. Direct multiplexed measurement of gene expression with color-coded probe pairs. *Nat Biotechnol.* 2008; 26(3):317-25.
8. Hastie ND, Bishop JO. The expression of three abundance classes of messenger RNA in mouse tissues. *Cell.* 1976; 9(4 PT 2):761-74. Epub 1976/12/01.
9. Velculescu VE, Madden SL, Zhang L, Lash AE, Yu J, Rago C, Lal A, Wang CJ, Beaudry GA, Ciriello KM, Cook BP, Dufault MR, Ferguson AT, Gao Y, He TC, Hermeking H, Hiraldo SK, Hwang PM, Lopez MA, Luderer HF, Mathews B, Petroziello JM, Polyak K, Zawel L, Kinzler KW, et al. Analysis of human transcriptomes. *Nat Genet.* 1999 ;23(4):387-8. Epub 1999/12/02.
10. Terasima T, Tolmach LJ. Changes in x-ray sensitivity of HeLa cells during the division cycle. *Nature.* 1961; 190: 1210-1211.
11. Ghandhi SA, Yaghoubian B, Amundson SA. Global gene expression analyses of bystander and alpha particle irradiated normal human lung fibroblasts: synchronous and differential responses. *BMC medical genomics.* 2008; 1:63. PMID: PMC2627914. ■



David Brenner and Howard Lieberman



Sunil Panigrahi



Hongning Zhou and Tom Hei

Targeted Cytoplasmic Irradiation and Autophagy

Jinhua Wu, Bo Zhang, Mercy M. Davidson^a, Tom K. Hei

The effect of ionizing irradiation on cytoplasmic organelles is often underestimated because the general dogma considers direct DNA damage in the nuclei to be the primary cause of radiation induced toxicity. Using a precision microbeam irradiator, we examined the changes in mitochondrial dynamics and functions triggered by targeted cytoplasmic irradiation with α -particles. Mitochondrial dysfunction induced by targeted cytoplasmic irradiation led to activation of autophagy, which degraded dysfunctional mitochondria in order to maintain cellular energy homeostasis. The activation of autophagy was cytoplasmic irradiation specific and was not detected in nuclear irradiated cells. The autophagy was oxyradical-dependent and required the activity of the mitochondrial fission protein dynamin related protein 1 (DRP1). Inhibition of autophagy resulted in prolonged DNA damage repair and decreased cell viability, supporting the cytoprotective function of autophagy. Our results reveal a novel mode by which dysfunctional mitochondria are degraded by autophagy to protect cells from cytoplasmic radiation-induced toxicity.

We examined the biological consequences of dysfunctional mitochondria induced by targeted cytoplasmic irradiation in human small airway epithelial (SAE) cells. Using LC3B immunofluorescence staining [1], we detected an increase in autophagy as early as 30 minutes post-irradiation. The formation of LC3B puncta reached a maximum by 4 hours, and returned to basal level by 24 hours post-irradiation (Figure 1A). Interestingly, the activation of autophagy was only observed in cytoplasmically irradiated SAE cells, not in nuclear irradiated cells (Figure 1B), suggesting a unique biological consequence of targeted cytoplasmic irradiation that may be overridden when direct nuclear damage is also present. Consistent with our previous findings that reactive radical species play an important role in modulating the biological response induced by cytoplasmic irradiation [2], short term pretreatment of cells with dimethyl sulfoxide (DMSO) at 0.5%, which functions as a free radical scavenger, prevented the induction of autophagy in cytoplasmically irradiated cells (Figure 1C).

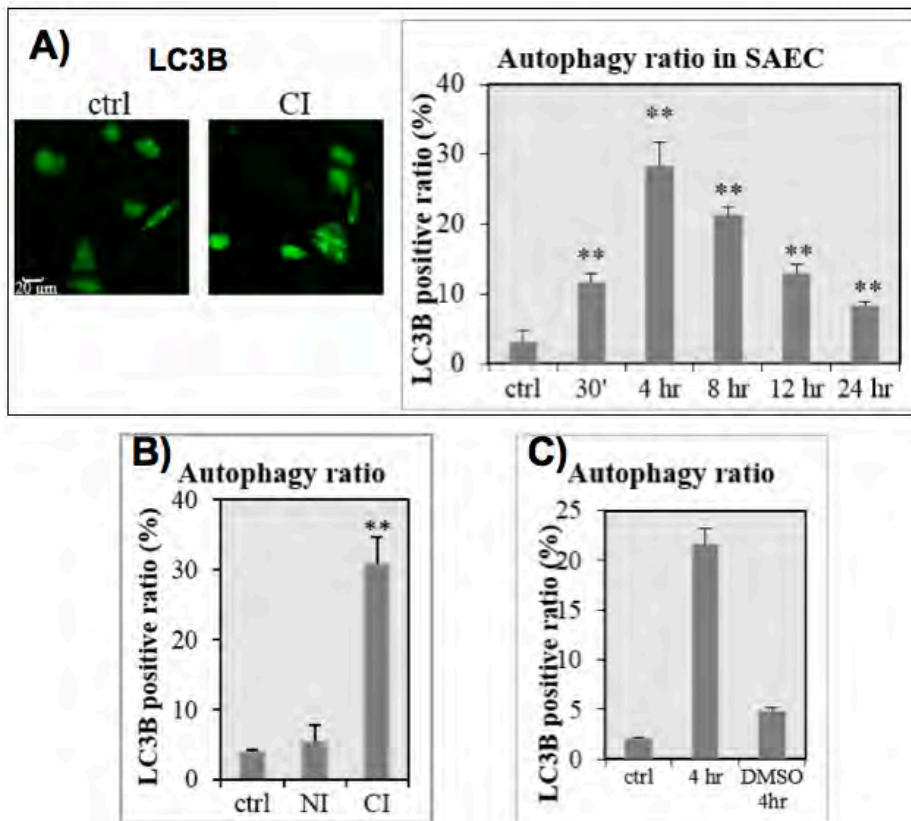


Figure 1. Cytoplasmic irradiation induces autophagy in SAE. A) LC3B immunofluorescent staining showed an increase in LC3B puncta after cytoplasmic irradiation (CI). B) Comparison of radiation sites. SAE cells were irradiated with 5 α -particles in the nucleus (NI) or cytoplasm (CI) and autophagy levels were evaluated by the ratio of cells positive for LC3B puncta 4 hours post irradiation. C) DMSO (0.5%) was used as a free-radical scavenger 30 minutes before irradiation. LC3B staining showed a significant decrease of autophagy with DMSO treatment.

^aDepartment of Radiation Oncology, Columbia University, New York, NY

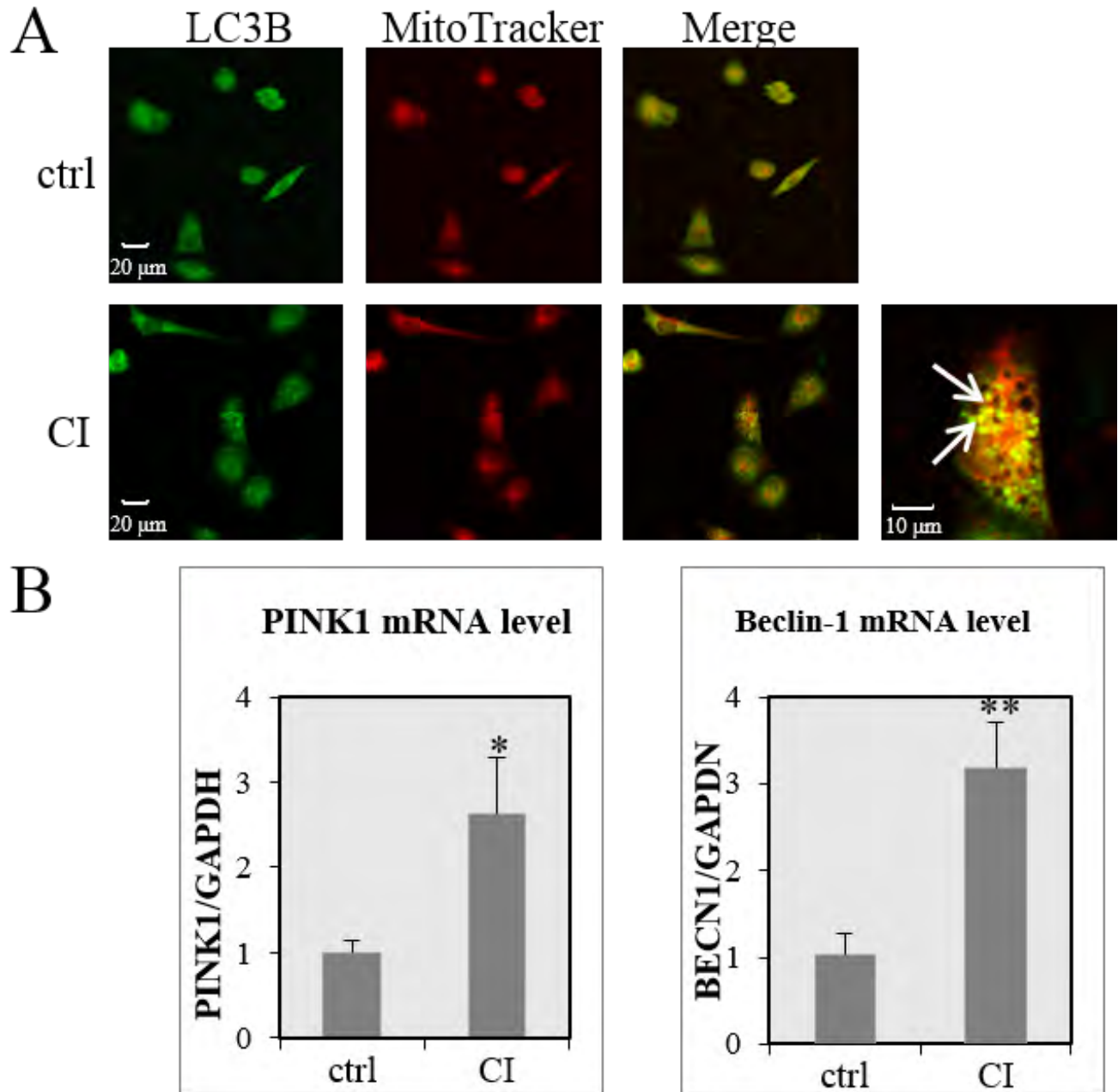


Figure 2. Mitophagy and non-selective autophagy mediated by cytoplasmic irradiation. A) Co-localization of autophagosome (LC3B labeled in green) and mitochondria (MitoTrackerRed) after cytoplasmic irradiation (4 hr). B) mRNA level of mitophagy marker PINK1 and non-selective autophagy marker beclin-1 increased by targeted cytoplasmic irradiation (30 min). ctrl, control. CI, cytoplasmically irradiated.

To elucidate the correlation between mitochondrial dysfunction and autophagy, we labeled mitochondria with MitoTracker Red and stained the SAE cells with LC3B to visualize autophagosomes after targeted cytoplasmic irradiation. Co-localization of mitochondria inside of autophagosomes was detected 4 hours post-irradiation (Figure 2A).

To further confirm the presence of autophagy and mitochondrial selective autophagy (mitophagy), we determined the mRNA and protein levels of the

autophagy marker Beclin1 and mitophagy marker PINK1 in SAE cells. Increased expression of both mRNA and protein of Beclin1 and PINK1 was detected in SAE cells as early as 30 minutes after irradiation (Figure 2B). Interestingly, using mdivi-1 [3], a small molecule inhibitor of the key mitochondrial fission protein DRP1, on SAE cells (Figure 3A) or knockdown of DRP1 in HCT116 colon carcinoma cells (Figure 3B) both abolished autophagy after cytoplasmic irradiation. These results suggest a key role of DRP1, a promoter of

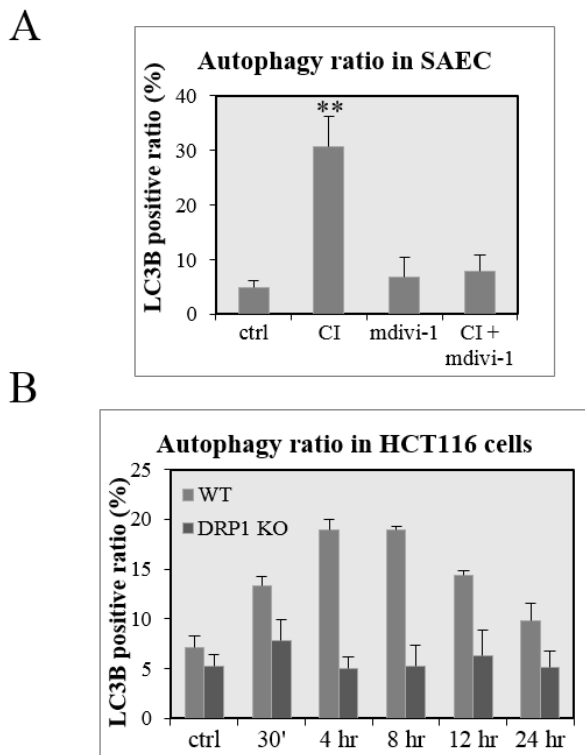


Figure 3. Cytoplasmic irradiation induces autophagy in a DRP1 dependent manner. A) DRP1 inhibitor mdivi-1 inhibits cytoplasmic irradiation mediated autophagy. LC3B staining showed reduced foci formation in the presence of mdivi-1 (4 hr). B) A DRP1 knockout in HCT116 cells showed reduced levels of autophagy.

mitochondrial fission, in regulating autophagy induced by cytoplasmic irradiation.

The biological consequences of inhibiting autophagy in cytoplasmically irradiated SAE cells were determined by using the autophagy inhibitors Chloroquine (CQ) and 3-methyladenine (3-MA). Cytoplasmic irradiation is known to induce formation of γ -H2AX foci, indicating an induction of DNA double strand breaks. Thirty minutes after cytoplasmic irradiation either with or without the autophagy inhibitors, there was no significant difference in induction of DSB in SAE cells as measured by γ -H2AX foci. By 24 hours after irradiation, the γ -H2AX positive ratio of cytoplasmically irradiated SAE cells had returned to background levels. However, in cells irradiated in the presence of autophagy inhibitors, DSB levels remained high (Figure 4A). These data suggested a delayed DSB repair in the absence of functional autophagy. Consistent with previous studies, cytoplasmic irradiation resulted in little or no cytotoxicity as determined by the dye exclusion assay. In contrast, cells treated with CQ exhibited a 19% reduction in cell viability within 48 hours after treatment (Figure 4B).

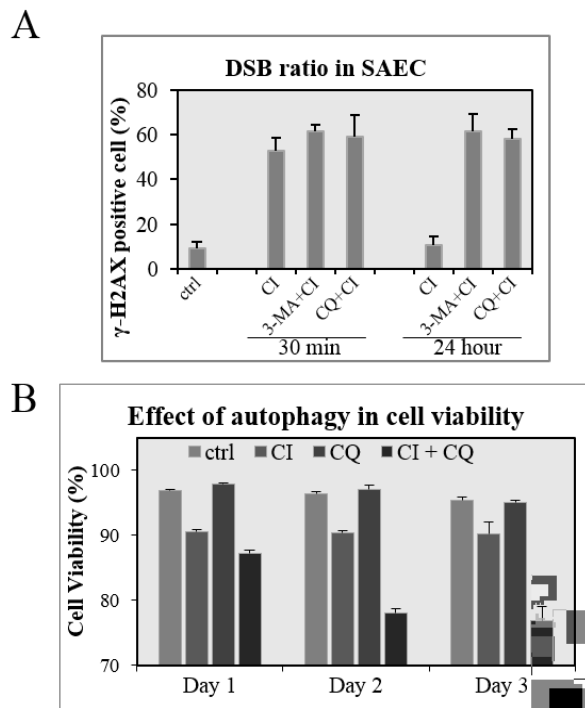


Figure 4. Cytoprotective role of autophagy. A) Inhibition of autophagy led to delayed DSB repair. B) Inhibition of autophagy increased cell killing 48 and 72 hours after cytoplasmic irradiation.

These data suggested autophagy played a cytoprotective role during cytoplasmic irradiation and mitochondrial fragmentation.

Acknowledgements

The authors thank members of the Radiological Research Accelerator Facility for their assistance with the microbeam irradiations (Drs. Guy Garty, Andrew Harkins, Alan Bigelow, and Yanping Xu). This research was supported by the NIH grants 5P01-CA49062-22 and 5R01-ES12888-07. The Radiological Research Accelerator Facility is an NIH sponsored Resource Center through grant EB-002033 (National Institute of Biomedical Imaging and Bioengineering).

References

1. Klionsky, D.J., et al., Guidelines for the use and interpretation of assays for monitoring autophagy. *Autophagy*, 2012. **8**(4): p. 445-544.
2. Zhang, B., et al., Cytoplasmic irradiation results in mitochondrial dysfunction and DRP1-dependent mitochondrial fission. *Cancer Res*, 2013. **73**(22): p. 6700-10.
3. Tanaka, A. and R.J. Youle, A chemical inhibitor of DRP1 uncouples mitochondrial fission and apoptosis. *Mol Cell*, 2008. **29**(4): p. 409-10. ■

Glioblastoma Stem Cells: Radiation Response and Radiation-induced Bystander Signaling Effects

Vladimir N. Ivanov and Tom K. Hei

Although the precise origin of glioblastoma (GBM) cells is not known, the current hypothesis is that glioma-initiating cells, which have characteristics of cancer stem-like cells, might give rise to GBM (Singh et al., 2003). To directly assess the intercellular communication between glioblastoma stem-like cells (GSC) and normal human neural stem cells (NSC) after ionizing irradiation of GSC, experiments were performed with direct irradiation of a GBM subpopulation enriched with GSC and evaluated for the induction of a bystander response in non-targeted NSC.

U87MG human glioblastoma cells were used in the present study. A U87MG neurosphere population

enriched for GSC was established after 15 passages of U87MG cells in serum-free NSC medium supplemented with insulin, EGF and FGF2 (Fig. 1A-D), as previously described (Ashizawa et al., 2013). Immunostaining demonstrated that the vast majority of neurospheres after 15 passages were GFAP⁺ (glial marker), SOX2⁺ (stem cell pluripotency marker) and CD133⁺ (glioma stem cell marker) (Fig. 1B).

FACS analysis further confirmed that approximately 65% of cells in the neurospheres were CD133⁺. The percentage of CD133⁺ cells dropped 24 h after irradiation, reflecting, probably, a change in CD133 surface expression on GSC and/or death of a fraction of CD133⁺

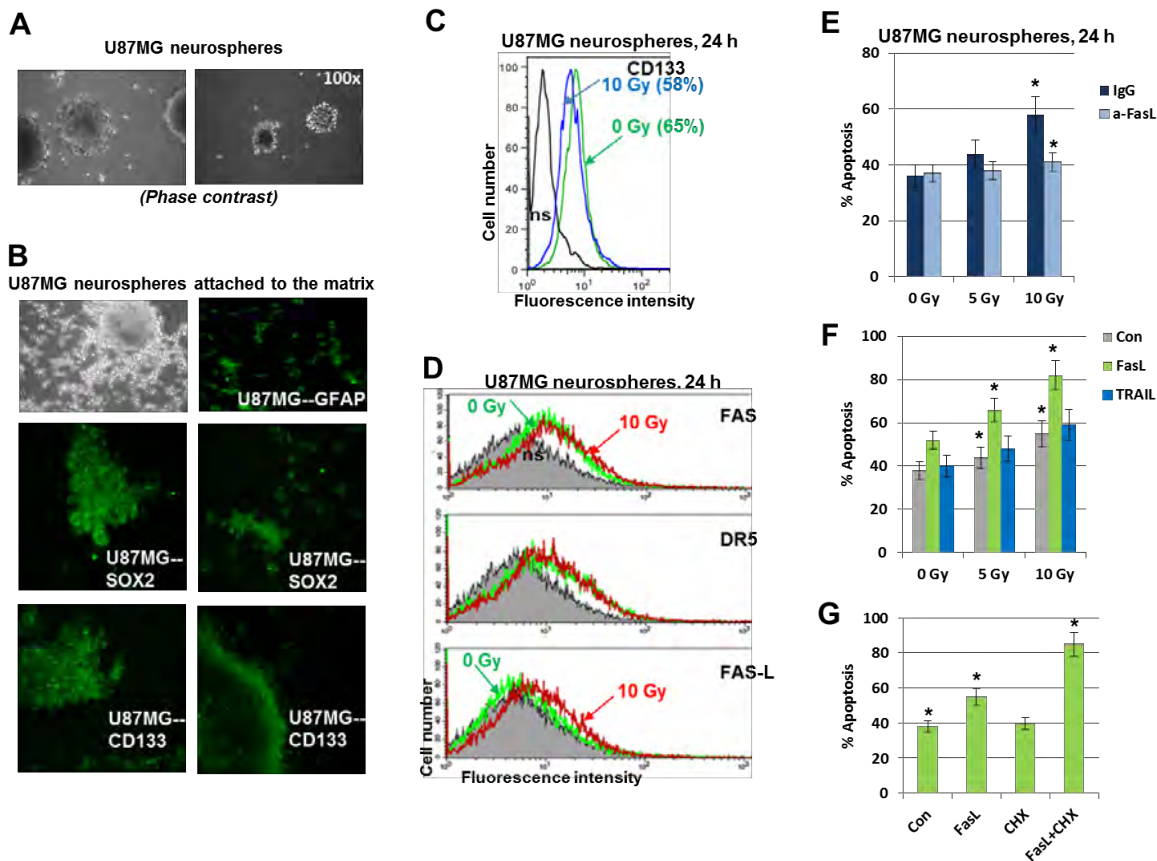


Figure 1. Establishing an enriched population of glioma stem-like cells among U87MG neurospheres. (A and B) U87MG neurosphere culture was established after 15 passages in serum-free media with EGF and FGF2. Immunostaining of neurospheres attached to the fibronectin matrix revealed numerous CD133⁺ and SOX2⁺ U87MG cells; furthermore, all cells were GFAP⁺. (C and D) Immunostaining and FACS analysis of U87MG neurosphere cultures. Surface expression levels of CD133, FAS, DR5 and FAS-L were determined before and 24 h after irradiation (10 Gy). The fraction of CD133⁺ dropped from 65% to 58% after irradiation at 10 Gy. (E) Effects of anti-FasL Ab on apoptotic levels of U87MG neurospheres before and after irradiation. Anti-FasL Ab (5 µg/ml) and normal IgG were added to the media before irradiation. Apoptotic levels were determined 24 h after irradiation using propidium iodide staining and FACS analysis. (F) Additional effects of exogenous FasL and TRAIL (40 ng/ml) on radiation-induced apoptosis of U87MG neurospheres. Death ligands were added 4 h after irradiation. (G) FasL-induced apoptosis of U87MG neurospheres with and without cyclohexamide (CHX).

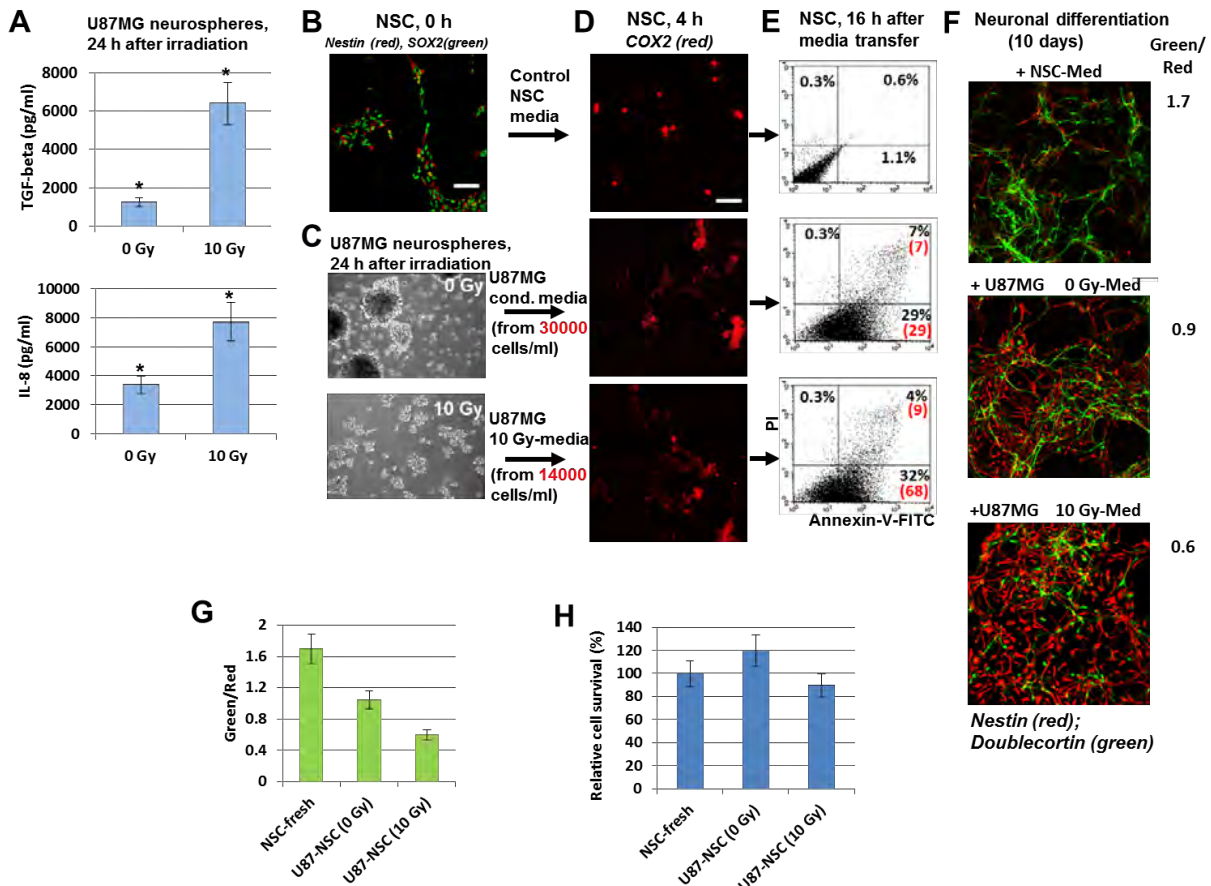


Figure 2. Cytokine secretion, apoptosis and bystander effects in bystander NSC after media transfer from non-treated and γ -irradiated U87MG neurospheres. (A) TGF β 1 and IL8 secretion before and after irradiation. (B-H) Media transfer experiments. Control NSC were stained for Nestin (red) and SOX2 (green) (panel B). U87MG neurospheres 24 h after irradiation are shown in panel C. Up-regulation of COX2 protein levels in NSC (panel D) was induced by exposure to media (4 h) transferred from non-irradiated and irradiated U87MG. Apoptosis of NSC (panel E) was induced by exposure to media (16 h) that were transfer from non-irradiated and irradiated U87MG neurospheres. Apoptosis was detected using Annexin-V-FITC+PI staining. Normalized levels of apoptosis are shown in brackets (panel E). (F-H) U87MG neurospheres were cultured in the NSC serum-free media. Effects of media transfer from non-treated (U87MG 0 Gy-M) and irradiated (U87MG 10 Gy-M) neurospheres with 8-h pretreatment of NSC on the subsequent neuronal differentiation of NSC (10 days). Differentiation of the native NSC in NSC-media (NSC-Med) was used as a reference. Immunostaining was performed ten days after initiation of differentiation. Bar = 50 μ m. The ratio of green/red cells reflects the degree of neuronal differentiation (panel G). Relative cell survival is shown in panel H.

cells (Fig. 1C). Furthermore, notable fractions of the U87MG neurosphere population were positive for the apoptosis markers FAS or DR5. Radiation induced moderate expression of the endogenous membrane FAS-L, but did not affect levels of TRAIL (Fig. 1D and data not shown). Interestingly, gamma-irradiation (10 Gy) of U87MG neurospheres induced apoptosis that was partially blocked by anti-FasL antibody (Fig. 1E). On the other hand, addition of exogenous recombinant FasL 4 h after irradiation significantly upregulated (+30%) apoptosis in GSC, while exogenous TRAIL exhibited only marginal effects (Fig. 1F). Relatively high basal percentages (35-38%) of sub-G1 cells reflected the permanent presence of contaminating dead cells in the core of non-adherent spheroids during cell culturing. Taken together, these results highlight a notable role of FasL/Fas and a marginal role of TRAIL/DR5 for radiation-induced apoptosis of U87MG neurospheres.

Using ELISA, we observed dramatic up-regulation of TGF β 1 and IL8 production 24 h after irradiation of glioblastoma neurospheres (Fig. 2A). GSC produced relatively similar levels of IL8, but substantially higher levels of TGF β 1, especially after irradiation, compared to non-stem GB cells (data not shown). A critical role TGF β in self-renewal of GSC is well established (Hardee et al., 2012; Penuelas et al., 2009).

Media transfer experiments from non-treated and irradiated neurospheres to the naïve NSC were performed for evaluation of non-targeted bystander effects. Of note, the same NSC-media (serum-free, with EGF and FGF2) was used for culture of both neurospheres and NSC. Media transfer experiments from neurospheres to the naïve NSC elicited cyclooxygenase-2 (COX2) induction in NSC (Fig. 2B-D) and notable up-regulation of NSC apoptosis, especially after irradiated media transfer. Levels of apoptosis were detected using Annexin-V-

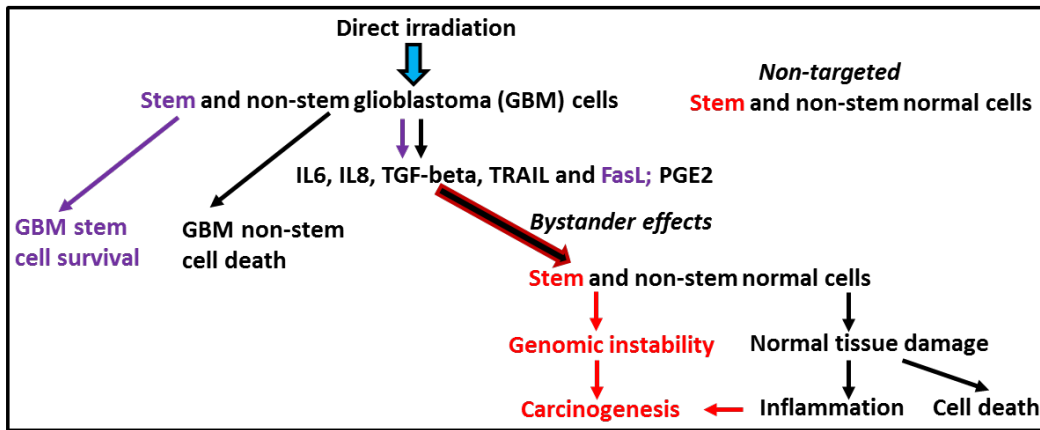


Figure 3. Direct irradiation of stem and non-stem glioblastoma cells and the induction of bystander effects in non-targeted stem (including NSC) and non-stem normal cells. Direct irradiation kills GBM non-stem cells while GBM stem cells can survive. Furthermore, direct irradiation induces bystander signaling resulting in the secretion of cytokines, death ligands, and prostaglandin E2. These signaling molecules can induce damage and/or suppress differentiation of normal cells, while upregulating genomic instability and inducing/accelerating secondary carcinogenesis among normal stem/progenitor cells.

FITC+PI staining of NSC and FACS analysis (Fig. 2E). Apoptotic levels in NSC were normalized to the number of glioblastoma cells used for secretion into the conditioned culture media (Fig. 2C and E). Immunostaining with antibody against the cleaved (active) fragment of caspase-8 further confirmed caspase-8-mediated apoptosis in NSC induced by media from glioblastoma neurospheres (data not shown).

Levels of neuronal differentiation before and after pretreatment with irradiated media were evaluated using the ratio of Doublecortin (a marker of neuronal differentiation) to Nestin, an early neuroprogenitor marker. We observed that media generated after irradiation of neurospheres at 10 Gy substantially suppressed neuronal differentiation of NCS (Fig 2F and G), reminiscent of the effects of media transfer experiments using non-stem U87MG glioblastoma cells with high radiation-induced secretion of IL8 and TGFβ. The absence of negative effects for the control NSC by pretreatment with fresh serum-free culture medium should be highlighted, in comparison with the small negative effects of the fresh GB media pretreatment described above. This makes the media transfer experiments from irradiated neurospheres to non-targeted bystander NSC very convincing. We detected relatively small effects of gamma-irradiation on survival of U87 neurospheres (Fig. 2F).

Taken together, our study demonstrated induction of bystander responses in non-targeted NSC after media transfer from irradiated glioblastoma cells that significantly exceeded effects of conditioned media

transfer. A graphical summary of the results obtained is shown in Fig. 3, which also highlights a probable difference in bystander responses between normal stem and non-stem cells. A role of bystander response of normal stem cells in carcinogenesis is under active investigation.

References

- Ashizawa, T., Miyata, H., Iizuka, A., Komiyama, M., Oshita, C., Kume, A., Nogami, M., Yagoto, M., Ito, I., Oishi, T., *et al.* (2013). Effect of the STAT3 inhibitor STX-0119 on the proliferation of cancer stem-like cells derived from recurrent glioblastoma. *International journal of oncology* 43, 219-227.
- Hardee, M.E., Marciscano, A.E., Medina-Ramirez, C.M., Zagzag, D., Narayana, A., Lonning, S.M., and Barcellos-Hoff, M.H. (2012). Resistance of glioblastoma-initiating cells to radiation mediated by the tumor microenvironment can be abolished by inhibiting transforming growth factor-beta. *Cancer Res* 72, 4119-4129.
- Penuelas, S., Anido, J., Prieto-Sanchez, R.M., Folch, G., Barba, I., Cuartas, I., Garcia-Dorado, D., Poca, M.A., Sahuquillo, J., Baselga, J., *et al.* (2009). TGF-beta increases glioma-initiating cell self-renewal through the induction of LIF in human glioblastoma. *Cancer Cell* 15, 315-327.
- Singh, S.K., Clarke, I.D., Terasaki, M., Bonn, V.E., Hawkins, C., Squire, J., and Dirks, P.B. (2003). Identification of a cancer stem cell in human brain tumors. *Cancer Res* 63, 5821-5828. ■

An Application of a Mouse Orthotopic Prostate Cancer Model for Radiation-induced Non-targeted Response

Hongning Zhou, Enyuan Shang, Kevin M. Hopkins, and Tom K. Hei

Radiation is an important modality in the treatment of many types of human cancers. On the other hand, radiation is also a well-known human carcinogen and therapy-induced secondary cancers have become a matter of concern among long-term survivors, particularly among pediatric patients. The increased development of brain tumors in genetically susceptible mice [1], as well as mutation induction in out of field lung tissues [2] have been reported in partially irradiated mice. These findings raise an interesting opportunity: establishing a mouse model to mimic radiation therapy for investigating the clinical relevance of radiation-induced non-targeted response.

Prostate cancer is a leading cause of illness and death among men in the western world. In addition, certain similarities between the mouse and human prostate gland support the use of mouse models for elucidation of alterations that accompany prostate development and progress. The orthotopic prostate cancer model will provide the ideal model to mimic a clinical therapy scenario for radiation-induced non-targeted response, especially when used together with an image-guided Small Animal Radiation Research Platform (SARRP).

Before starting development of this model, the first question we asked was what is the contribution of the immune system to radiation-induced non-targeted response? Using athymic nude mice, we found that partial body irradiation can increase cyclooxygenase-2 (COX2) expression and induce γ H2AX formation in out of field lung tissues (Figure 1) in a manner similar to those

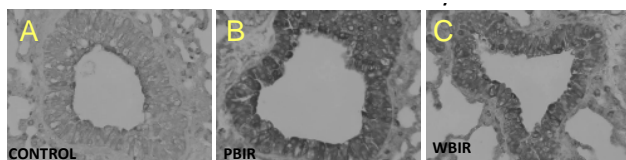


Figure 1. Immunohistochemical staining of COX2 in lung tissues of A) control athymic nude mice, B) animals irradiated in the lower abdominal area with a single 5 Gy dose of X-rays and, C) mice exposed to 5 Gy whole body X-irradiation.

reported recently using an inbred mouse strain [2]. These findings suggest the suitability of using nude mice in radiation induced non-targeted response studies.

As a continuation of this study, human PC3 prostate cancer cells tagged with luciferase were orthotopically injected into the mouse dorsal glands, and tumor growth was monitored using bioluminescence (Figure 2). Mice were irradiated with focused X-ray beams using the

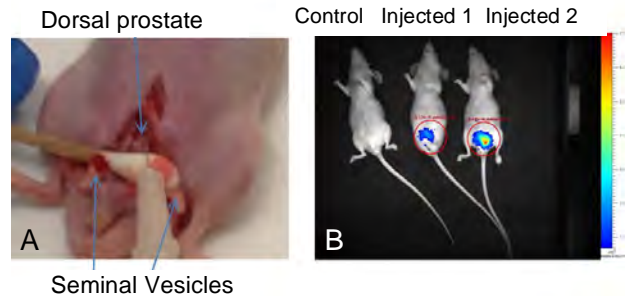


Figure 2. A) Orthotopic injection of prostate cancer cells into the dorsal gland of male athymic nude mice. B) Two weeks after injection, animals were imaged using in vivo bioluminescent imaging. The color scale indicates the intensity of luminescence, and is indicative of tumor uptake and growth in the prostate.

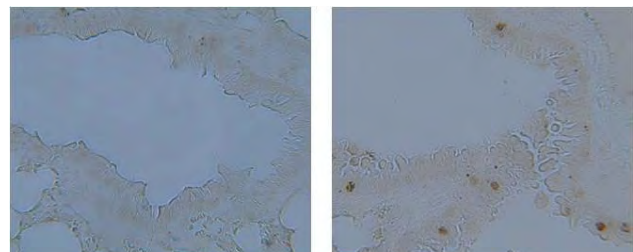


Figure 3. Immunohistochemical staining of γ H2AX foci in lung tissues of control athymic nude mice (left), and animals irradiated with 12 Gy of X-rays (4 fractions, 3Gy each) using the SARRP 200 (right).

SARRP about three weeks after tumor cell injection, and after confirmation of tumor growth by bioluminescence imaging. As shown in Figure 3, nude mice demonstrated robust bystander/ out-of-field γ H2AX foci formation in the lung 24 hours after 4 fractions of irradiation. In contrast, there were few or no γ H2AX foci in the control lung tissue. The experiments are ongoing, and more results will be available soon. Endpoints including induction of COX2, 8-OHdG, γ H2AX foci, and secondary tumor occurrence will continue to be examined in out-of-field areas, including brain, lung, liver and bone at different times after irradiation.

References

1. Mancuso M, Pasquali E, Leonardi S, Tanori M, Rebessi S, Di Majo V, Pazzaglia S, Toni MP, Pimpinella M, Covelli V and Saran A (2008) Oncogenic bystander radiation effects in Patched heterozygous mouse cerebellum. *Proc Natl Acad Sci U S A* **105**: 12445-12450.

2. Chai Y, Calaf GM, Zhou H, Ghandhi SA, Elliston CD, Wen G, Nohmi T, Amundson SA and Hei TK (2013) Radiation induced COX-2 expression and

mutagenesis at non-targeted lung tissues of gpt delta transgenic mice. *Br J Cancer* **108**: 91-98. ■

RAD9 Deficiency Enhances Bystander Signaling in Human Prostate Cancer Cells

Sunil K. Panigrahi, Constantinos G. Broustas, and Howard B. Lieberman

Introduction

Non-targeted effects of radiation on geographical neighbors or descendants of irradiated cells might play a major role in potential health consequences of radiation exposures, particularly in the induction of malignancy and resistance to anticancer therapies [1]. Previously, it has been reported that DNA damage is not restricted to directly irradiated cells but is observed in neighboring cells as well as in descendant populations. Effects can be categorized as follows 1) radiation-induced genomic instability; signals from irradiated cells are inherited by succeeding cell generations; and 2) radiation-induced bystander effect; signals from irradiated cells are

transferred to neighboring cells either by direct cell-cell contact, or indirectly through chemokines/cytokines or oxisomes in shared media [2, 3]. Cells deficient in DNA repair genes have shown enhanced radiation-induced bystander effects, relative to repair proficient cells [4, 5], whereas stem cells or cells with high telomerase activity have shown a decrease in bystander signaling [6]. It has also been reported that bystander signaling depends upon the phenotype or genotype of both the irradiated and the recipient cells [6].

In our previous studies, we reported that RAD9 deficiency makes the cells more sensitive to DNA

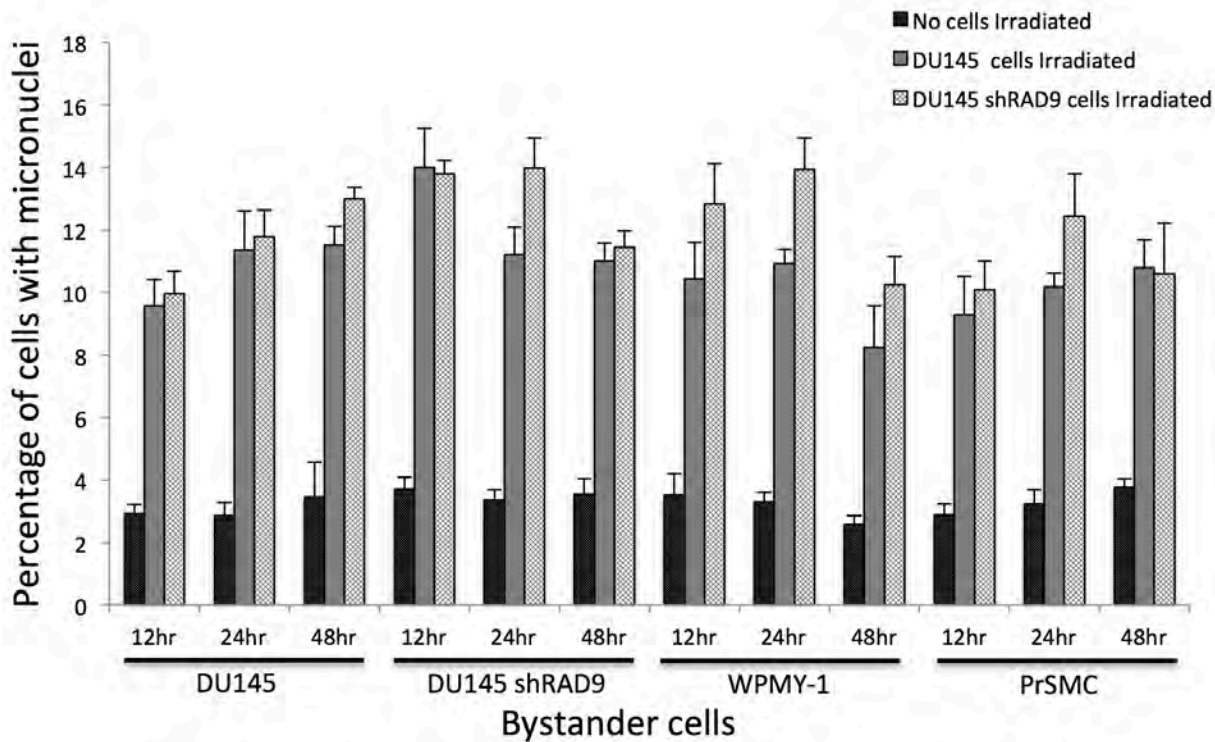


Figure 1. RAD9 deficiency enhances micronuclei formation. DU145 and DU145-shRAD9 cells were irradiated with 1 Gy of gamma rays. After exposure, cells were incubated for 30 minutes followed by transfer of conditioned medium to unirradiated cells (DU145, DU145-shRAD9, WPMY-1, & PrSMC). The bystander cells (cells receiving media from irradiated cells) were incubated for the indicated time periods (12, 24 and 48 hrs), followed by addition of cytochalasin B and micronuclei scoring. Micronuclei per total scored cells X100 (MN percentage) was plotted and error bars represent the standard deviation of three independent experiments.

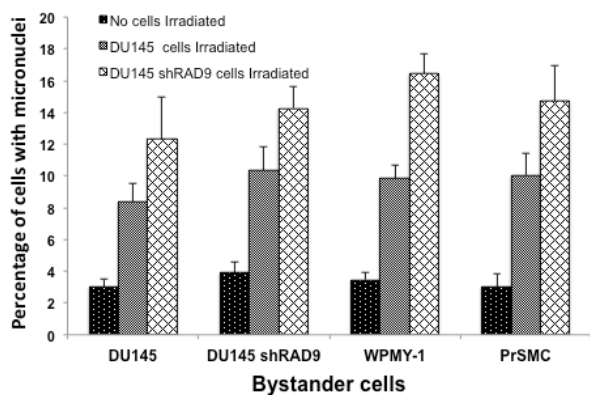


Figure 2. Rad9 knock down enhances bystander signaling both in donor and recipient cells. DU145 and DU145-shRAD9 cells were irradiated with ⁴He ions (LET 123 keV/μm) from a 5.5 MV Singletron accelerator, using the track segment mode at the Radiological Research Accelerator Facility. After irradiation, dishes containing unirradiated cells (DU145, DU145-shRAD9, WPMY-1, & PrSMC) were inserted into the track segment dishes. Dishes containing both irradiated and bystander cells were co-cultured for 24 hrs. The rest of the procedure is as Figure 1. Micronuclei per total scored cells X100 (MN percentage) was plotted and error bars represent the standard deviation of three independent experiments.

damaging agents, including ionizing radiation. Also, we found that RAD9 ablation or knockdown enhanced the radiation induced bystander response in mouse embryonic stem cells and H1299 human lung cancer cells, respectively [5, 7]. RAD9 also plays a significant role in prostate cancer progression and metastasis. One of our recent studies demonstrates that RAD9 enhances radioresistance of prostate cancer cells [8]. Here we show RAD9-dependent enhancement of the bystander response in prostate cancer cells as well as in prostate stromal cells.

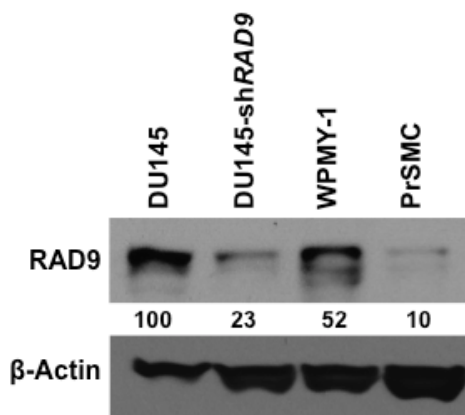


Figure 3. DU145 cells have higher RAD9 expression as compared to primary and immortalized cells. RAD9 protein levels were detected in DU145, DU145-shRAD9, WPMY-1 and PrSMC cell lysates. β-Actin was used as the loading control. The numbers below each lane represent percent abundance of RAD9 compared to β-actin and relative to DU145 cells.

Results and discussion

Based on the above observations, we wanted to know whether RAD9 has any role in the bystander process in human prostate cancer cells. Two approaches included: 1) transfer of conditioned medium to non-irradiated cells; and 2) co-culture non-irradiated cells growing in Transwell inserts with irradiated cells growing in track segment dishes. Primary human prostate stromal cells (PrSMC), immortalized prostate smooth muscle cells (WPMY-1), the human prostate cancer cell line DU145 and the latter expressing shRNA against RAD9 were used in this study.

In brief, the procedure for approach 1 is: DU145 and DU145-shRAD9 cells were irradiated with 1 Gy using a Gammacell 40 ¹³⁷Cs irradiator (0.8Gy/min). After irradiation, cells were incubated for 30 minutes, followed by transfer of conditioned medium to non-irradiated cells (DU145, DU145-shRAD9, WPMY-1, and PrSMC). The non-irradiated cells were grown in conditioned media for 12, 24 or 48 hrs.

For the second approach, recipient cells (DU145, DU145-shRAD9, WPMY-1, and PrSMC) were grown in specialized Transwell plates (Corning # 3491), and cells to be irradiated were grown in Mylar-bottomed track segment dishes as described previously [7]. DU145 and DU145-shRAD9 cells were irradiated with ⁴He ions (LET 123 keV/μm) from a 5.5 MV Singletron accelerator, using the track segment mode at the Radiological Research Accelerator Facility of Columbia University. After irradiation, cells in Transwells were inserted into the track segment dishes and co-cultured for 24 hrs. At indicated times post-irradiation, cells were fixed with methanol, stained with SYBR-green, and micronuclei (MN) were counted using a fluorescence microscope. MN percentage was calculated as the number of micronuclei per 100 binucleated cells.

A higher MN percentage was observed in all bystander cells receiving conditioned media from DU145-shRAD9 irradiated cells (Figure 1). By comparing micronuclei counts among the three time intervals, a peak bystander response was obtained at 24 hr post-irradiation, which decreased at 48 hrs (Figure 1). For the ⁴He ion experiment, a similar result was obtained, showing an increase in MN percentage in cells inserted into DU145-shRAD9 irradiated dishes compared to those inserted into DU145 irradiated dishes (Figure 2).

An increase in MN percentage was also observed in DU145-shRAD9, WPMY-1 and PrSMC cells compared to parental DU145 cells when all received conditioned medium from either DU145 cells or DU145 cells containing shRNA against RAD9 (Figure 2). Although all these cells have different genotypes, one similarity is that they have lower RAD9 levels compared to DU145 cells (Figure 3). This indicates that RAD9 functions to reduce bystander signaling.

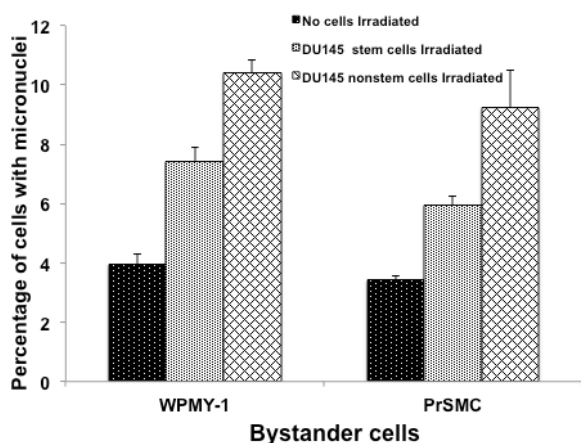


Figure 4. Stem like prostate cancer cells exhibit decreased bystander signaling. Stem cells and non stem cells from the DU145 cell line were sorted by FACS and were irradiated with 1 Gy gamma rays, then incubated for 30 minutes followed by media transfer to unirradiated cells (WPMY-1 & PrSMC). The bystander cells (cells receiving media from the irradiated cells) were incubated for 24 hrs followed by addition of cytochalasin B and micronuclei counting. Micronuclei per total cells scored X100 (MN percentage) was plotted and error bars represent the standard deviation of three independent experiments.

Further we asked whether stemness of cancer cells has a role in the bystander process. To address this, we isolated cancer stem cells from DU145 cells using FACS as described [9]. In brief, live DU145 cells were double-stained with fluorescently conjugated CD44 and CD133 antibodies and stem cell populations were isolated by FACS. The bystander response was measured by scoring micronuclei in WPMY-1 and PrSMC cells 24 hr after transferring conditioned medium from irradiated stem and non-stem cell populations. Micronuclei percentage increased after receipt of conditioned medium from DU145 non-stem cells relative to DU145 stem cells (Figure 4). Though the recipient cell populations have different genetic backgrounds, and represent immortalized versus primary cells, they showed no difference in their bystander responses when they received signal from the same DU145 cells (Figure 4). Interestingly, both recipient cell types had low RAD9 expression (Figure 3), which indicates RAD9 might play a more important role in transmitting a bystander signal than in responding to the bystander signal in these cells.

Our ongoing studies will delineate downstream factors and mechanisms of the bystander process in prostate

cancer cells. These results might provide information to formulate novel therapeutics strategies to treat patients with prostate cancer.

References

1. Mothersill, C. and Seymour, C. (2003) Radiation-induced bystander effects, carcinogenesis and models. *Oncogene*, 22, 7028-7033.
2. Morgan, W.F. (2003) Non-targeted and delayed effects of exposure to ionizing radiation: II. Radiation-induced genomic instability and bystander effects in vivo, clastogenic factors and transgenerational effects. *Radiat Res*, 159, 581-596.
3. Morgan, W.F. (2003) Non-targeted and delayed effects of exposure to ionizing radiation: I. Radiation-induced genomic instability and bystander effects in vitro. *Radiat Res*, 159, 567-580.
4. Nagasawa, H. and Little, J.B. (2002) Bystander effect for chromosomal aberrations induced in wild-type and repair deficient CHO cells by low fluences of alpha particles. *Mutat Res*, 508, 121-129.
5. Zhu, A., Zhou, H., Leloup, C., Marino, S.A., Geard, C.R., Hei, T.K. and Lieberman, H.B. (2005) Differential impact of mouse Rad9 deletion on ionizing radiation-induced bystander effects. *Radiat Res*, 164, 655-661.
6. Cogan, N., Baird, D.M., Phillips, R., Crompton, L.A., Caldwell, M.A., Rubio, M.A., Newson, R., Lyng, F. and Case, C.P. (2010) DNA damaging bystander signalling from stem cells, cancer cells and fibroblasts after Cr(VI) exposure and its dependence on telomerase. *Mutat Res*, 683, 1-8.
7. Ghandhi, S.A., Ponnaiya, B., Panigrahi, S.K., Hopkins, K.M., Cui, Q., Hei, T.K., Amundson, S.A. and Lieberman, H.B. (2014) RAD9 deficiency enhances radiation induced bystander DNA damage and transcriptomal response. *Radiat Oncol*, 9, 206.
8. Broustas, C.G. and Lieberman, H.B. (2014) RAD9 enhances radioresistance of human prostate cancer cells through regulation of ITGB1 protein levels. *Prostate*, 74, 1359-1370.
9. Dubrovskaya, A., Kim, S., Salamone, R.J., Walker, J.R., Maira, S.M., Garcia-Echeverria, C., Schultz, P.G. and Reddy, V.A. (2009) The role of PTEN/Akt/PI3K signaling in the maintenance and viability of prostate cancer stem-like cell populations. *Proc Natl Acad Sci U S A*, 106, 268-273. ■

Radiation Bystander Effect on Gene Expression in RAD9 Deficient Cells

Shanaz A. Ghandhi, Kevin M. Hopkins, Sunil K. Panigrahi, Howard B. Lieberman, and Sally A. Amundson

Introduction

We studied the effect of radiation and bystander response in cells that expressed reduced levels of the human RAD9 protein. This is of interest because RAD9 is known to have a role in signaling after DNA damage

and in cell cycle checkpoint control [1]. A role for RAD9 in bystander signaling has also already been established [2], and we were interested in the effect of RAD9 on gene expression as part of the bystander response.

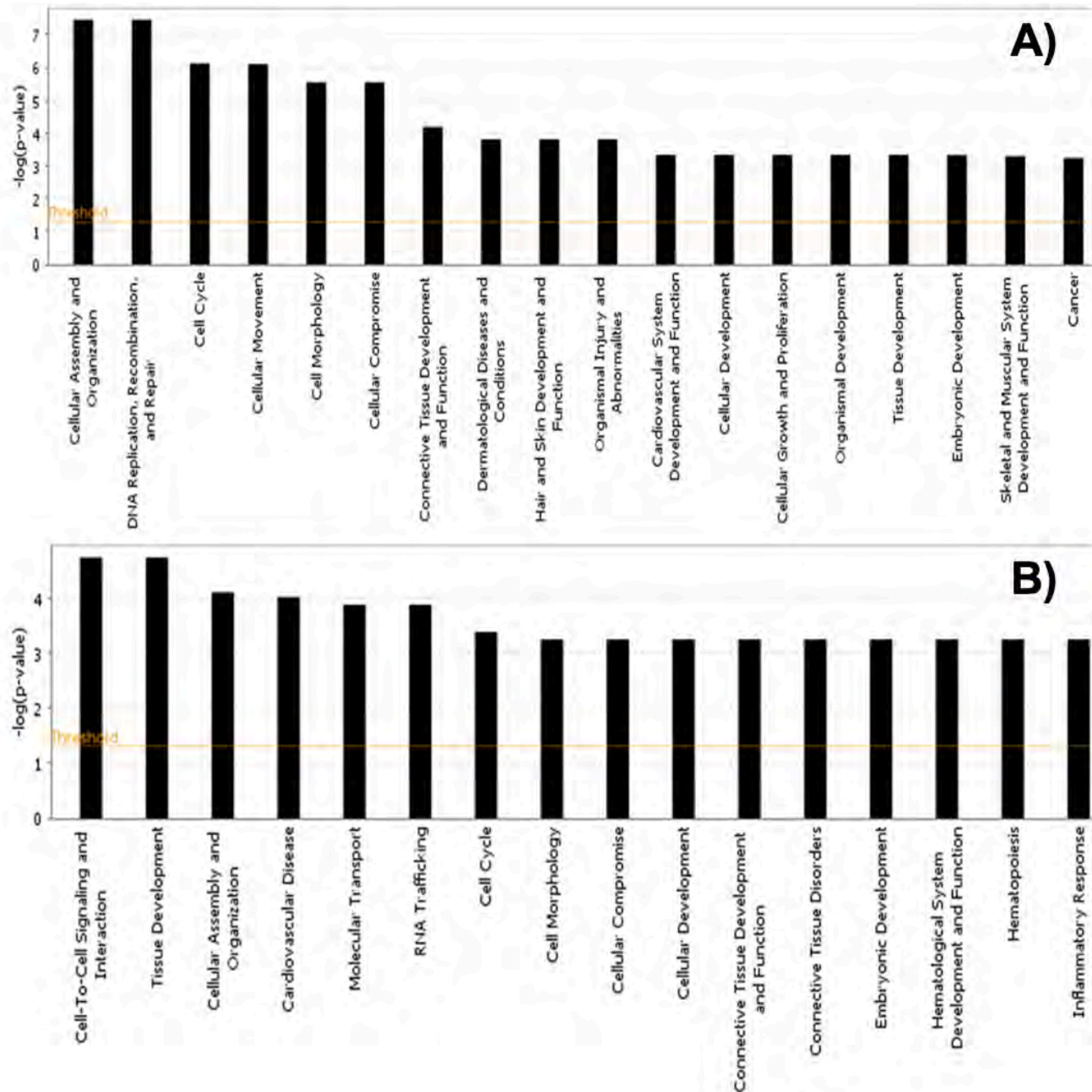


Figure 1. IPA generated list of top biological processes in directly irradiated (A) and bystander (B) cells. Each biological process was ranked by significance based on a p-value for the number of significantly differentially expressed genes associated with that biological process compared against the IPA database.

Methods

H1299 cells with reduced RAD9 levels were irradiated with 1 Gy α particles and RNA was extracted 4 hours later. We studied the effect of direct irradiation and bystander response using whole genome expression profiling [3].

Results and Discussion

Gene expression analyses revealed that 572 genes were significantly differentially expressed in directly irradiated cells, and 254 genes in the bystander cells. We compared the gene expression response in directly irradiated and bystander cells using Ingenuity Pathway Analysis biological processes. We found that among the 572 genes responding to direct irradiation top processes were cell cycle, DNA repair and cellular structure and movement (Figure 1A). Among the bystander responding genes top processes were cell-to-cell signaling, cellular assembly and RNA trafficking (Figure 1B). Cell cycle, cell morphology and inflammatory response were also significantly affected biological processes in the bystander cell response, but were less strongly implicated

than cellular signaling and interaction. Using a gene expression approach to understand the bystander response in RAD9 deficient cells confirmed that both the direct and bystander radiation response of cells appears to be generally conserved at the level of biological processes in the absence of normal levels of RAD9 protein.

References

1. Zhou BB and Bartek J (2004) Targeting the checkpoint kinases: chemosensitization versus chemoprotection. *Nat Rev Cancer*, 4:216–225.
2. Zhu A, Zhou H, Leloup C, Marino SA, Geard CR, Hei TK, Lieberman HB (2005) Differential impact of mouse Rad9 deletion on ionizing radiation induced bystander effects. *Radiat Res*, 164:655–661.
3. Ghandhi SA, Ponnaiya B, Panigrahi SK, Hopkins KM, Cui Q, Hei TK, Amundson SA, Lieberman HB. (2014) RAD9 deficiency enhances radiation induced bystander DNA damage and transcriptomal response. *Radiat Oncol*, 9:206. ■



Clockwise from upper left: Yanping Xu, Manuela Buonanno, Sally Amundson, Guy Garty, Andrew Harkin, Brian Ponnaiya, Mikhail Repin, and Helen Turner; David Horowitz; Simon Cheng and Sherry Yin; Guy Garty; Presentations at the video site visit for the P41 resubmission.

The Importance of Filters for Biological Applications of Far-UVC Excilamps

Manuela Buonanno, Alan W. Bigelow, Gerhard Randers-Pehrson, and David J. Brenner

Introduction

Despite improvements in operating room practices, surgical site infections (SSI) result in substantial morbidity, prolonged hospital stays, and increased direct patient costs [1]. This is due to the increasing number of SSIs that are attributable to antibiotic-resistant pathogens as well as viruses.

UV radiation is an effective method to inactivate microbes, however, conventional germicidal lamps are both carcinogenic and cataractogenic due to their high penetration in human cells. As a safer alternative to reduce SSI, we have used UV lamps that emit single wavelengths (around 200 nm), defined by the gas mixture they contain. Such single-wavelength lamps, based on UV emitted from an excited molecular complex (an exciplex), are called excimer lamps, or excilamps [2]. In our preliminary studies, we have shown that 207 nm light from krypton-bromine (KrBr) excilamps can be highly cytotoxic to bacteria, while being minimally cytotoxic to human cells [3].

It follows that such far-UVC excimer lamps have considerable promise to be safe and inexpensive tools for SSI reduction, while potentially sharing with conventional UV germicidal lamps the major advantage of being

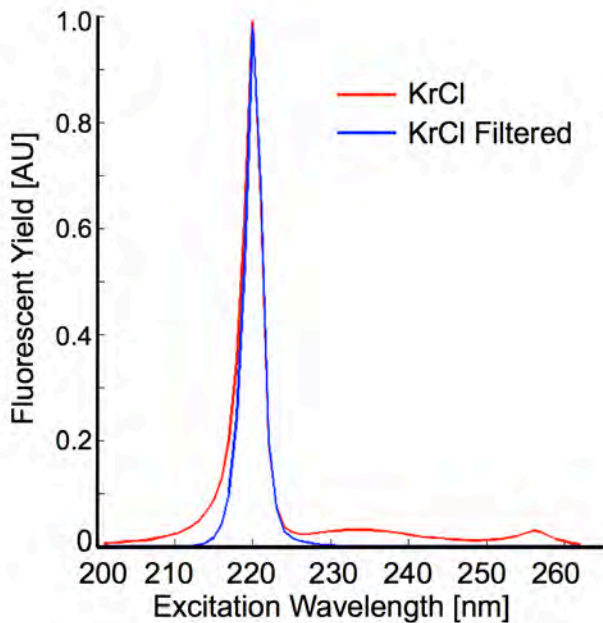


Figure 1. Emission spectra of the KrCl excilamp either unfiltered (red), or with appropriate filtration resulting in the emission of the single 222 nm wavelength (blue).

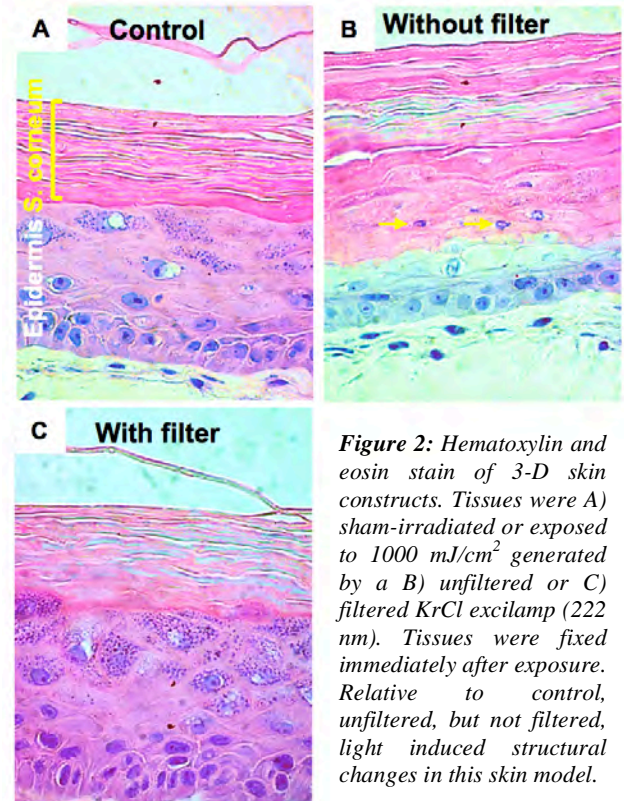


Figure 2: Hematoxylin and eosin stain of 3-D skin constructs. Tissues were A) sham-irradiated or exposed to 1000 mJ/cm² generated by a B) unfiltered or C) filtered KrCl excilamp (222 nm). Tissues were fixed immediately after exposure. Relative to control, unfiltered, but not filtered, light induced structural changes in this skin model.

equally effective on drug-resistant and drug-sensitive bacteria. However, to achieve this goal the excilamp has to be appropriately filtered. As an example, Figure 1 shows the emission spectra of a krypton-chlorine (KrCl) excilamp (red) that, appropriately filtered, emits the single 222 nm wavelength (blue).

Removal of higher and therefore more penetrating wavelength components is critical in the context of the induction of biological damage. Figure 2 shows hematoxylin and eosin staining of full thickness MatTek® skin tissues exposed to a filtered or unfiltered KrCl excilamp. The tissues were exposed to 1000 mJ/cm², fixed 4 days later and stained for histological analysis. We observed that compared to control (Fig. 2A) and the filtered lamp (Fig. 2C), the unfiltered light (Fig. 2B) induced hyperkeratosis (an increased thickness of the stratum corneum), a reduction in epidermal thickness, and parakeratosis, nuclear debris remaining trapped in the stratum corneum (yellow arrows in Fig. 2B).

Damage induced by the higher wavelength components was also detected as DNA photodamage (Fig. 3). MatTek® skin tissues were exposed to 150 mJ/cm²

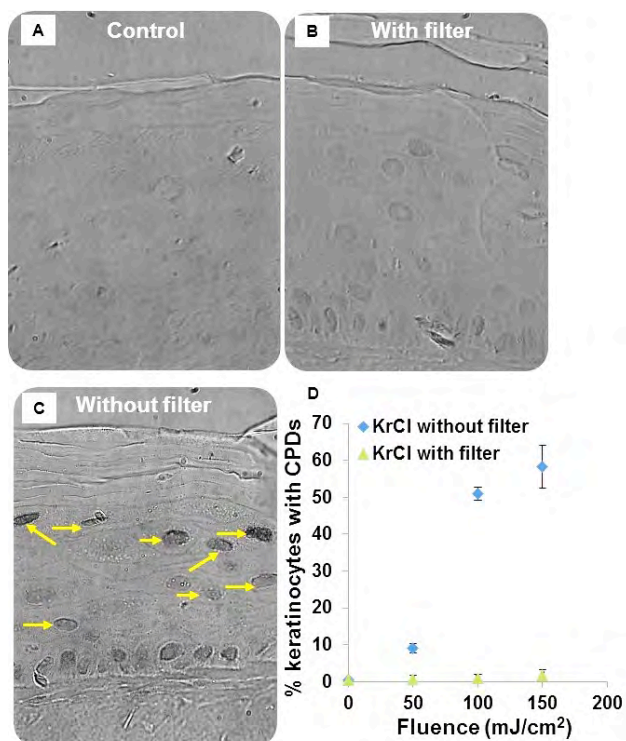


Figure 3: Immunohistochemical analysis of CPDs (appearing as black nuclei) in the epidermis of 3-D skin constructs that were A) sham-irradiated or exposed to 150 mJ/cm² generated by a B) unfiltered or C) filtered KrCl excilamp (222 nm). D) Quantification of the induced photodamage. Relative to control and to filtered 222-nm light, unfiltered UV induced an increase in the percentage of epidermal cells carrying DNA photodamage.

from a filtered or unfiltered KrCl excilamp and fixed immediately afterwards. Immunohistochemical analysis of cyclobutane pyrimidine dimers (CPDs) (Fig. 3), the most abundant pre-mutagenic DNA lesions induced by UV light, revealed that unfiltered 222-nm light induced an increase in the number of epidermal cells showing CPDs (indicated by yellow arrows in Fig. 3C), compared to control (Fig. 3A). Tissue exposed to filtered light looked (Fig. 3B) similar to controls (Fig. 3A); the induced DNA photodamage is quantified in Fig. 3D.

In conclusion, appropriately filtered far-UVC excilamps represent an inexpensive and safer alternative to conventional UV lamps, while remaining effective at inactivating microbes.

References

1. Klevens, R.M., et al., *Estimating health care-associated infections and deaths in U.S. hospitals, 2002*. Public Health Rep, 2007. **122**(2): p. 160-6.
2. Sosnin, E.A., Oppenlander, T. and Tarasenko, F.V., *Applications of capacitive and barrier discharge excilamps in photoscience*. J Photochem Photobiol, 2006. **C**(7): p. 145-163.
3. Buonanno, M., et al., *207-nm UV light - a promising tool for safe low-cost reduction of surgical site infections. I: in vitro studies*. PLoS One, 2013. **8**(10): p. e76968. ■



Top (l to r): Alan Bigelow and Guy Garty; Lee Goldman and David Brenner. Bottom (l to r): Alan Bigelow and Guy Garty; Howard Lieberman and David Brenner; Lubomir Smilenov.

Effects of Radiation Type and Delivery Mode on the Radioresistant Eukaryote *Cryptococcus neoformans*

Igor Shuryak, Ruth A. Bryan^a, Jack Broitman^b, Stephen A. Marino, Alfred Morgenstern^c, Christos Apostolidis^c, and Ekaterina Dadachova^{a,b}

Radioresistant organisms can survive large doses of ionizing radiation (e.g. hundreds or thousands of Gy) without losing reproductive potential. Radioresistance is probably an evolutionary by-product of other properties (e.g. resistance to desiccation and/or to other genotoxic agents), which are important for the organism's survival in its natural environment [1-2].

Many fungi tolerate large radiation doses not only under laboratory conditions, but also survive (or even gain a competitive advantage) in environments heavily contaminated by radioisotopes [3-4]. Overcoming the radioresistance of pathogenic fungi is important for medical purposes, and fungus-specific radioimmunotherapy (RIT) shows considerable promise in accomplishing this. For example, it has resulted in successful eradication of fungal pathogens in vitro and in vivo [5-6].

So far, most research on radioresistant fungi, particularly on human pathogens, has involved sparsely ionizing radiation (e.g. gamma-rays). Here we employed *Cryptococcus neoformans* as a model organism. This fungus is an important human pathogen, especially in immunocompromised individuals affected by human immunodeficiency virus (HIV). It is a particularly interesting model system because it is highly resistant to sparsely-ionizing radiation from external sources, but is susceptible to densely-ionizing radiation delivered by radiolabeled monoclonal antibodies specific to fungal antigens in vitro and in vivo [5-6].

To elucidate and quantify the effects of radiation type and delivery mode on clonogenic survival of *C. neoformans*, we compared the effects of densely-ionizing particles (⁴He ions delivered either by external beam at RARAF (Fig. 1), which we call external-beam alpha-particles for convenience, or alpha-particles produced by ²¹³Bi radiolabeled antibodies) and sparsely-ionizing ¹³⁷Cs gamma-rays. Our goals were: (1) estimate alpha-particle doses to the cell nucleus (and to the cell body) from

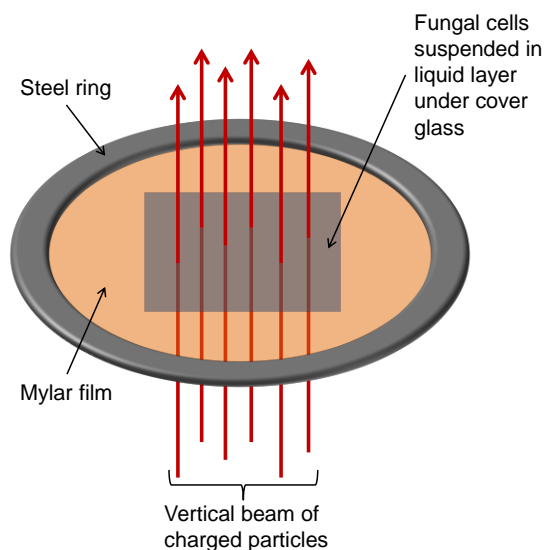


Figure 1. Schematic, rotated depiction of external-beam alpha-particle irradiation of *C. neoformans* cells in Mylar-bottom dishes at RARAF.

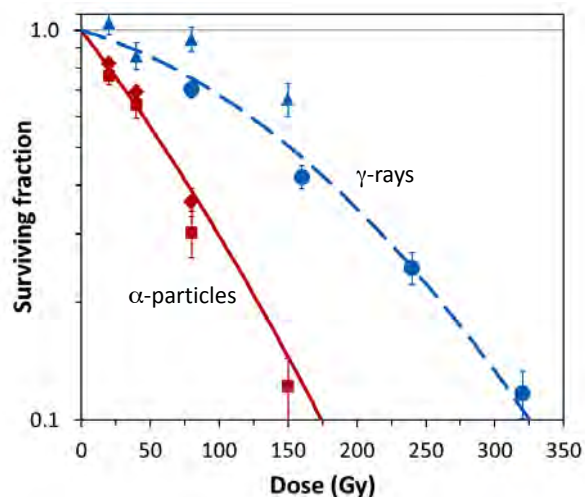


Figure 2. *C. neoformans* clonogenic survival curves for external-beam alpha-particles and gamma-rays. Different symbol types of each color represent separate repeat experiments. Curves represent best-fit linear-quadratic dose responses with parameters discussed in the main text. Error bars are 95% confidence intervals.

^aDepartment of Radiology, Albert Einstein College of Medicine, Bronx, NY.

^bDepartment of Microbiology and Immunology, Albert Einstein College of Medicine, Bronx, NY.

^cEuropean Commission, Joint Research Centre, Institute for Transuranium Elements, Karlsruhe, Germany

Table 1. Estimated cellular doses to *C. neoformans* from ^{213}Bi radiolabeled antibodies.

Experimental Stage	α -particle dose (Gy) from decays on antibodies bound to target cell surface		α -particle dose (Gy) from decays on antibodies bound to other cells or suspended in medium				Total α -particle dose (Gy)		β -particle dose (Gy)
	Nucleus	Cell Body	Contribution from initial 50 μm of α -particle track		Contribution from terminal 35 μm of α -particle track (Bragg peak region)		Nucleus	Cell Body	
			Nucleus	Cell Body	Nucleus	Cell Body			
Incubation	4.83	5.49	3.64	3.67	4.85	4.85	13.31	14.01	0.48
Pellet	1.60	1.82	21.45	21.62	28.57	28.58	51.62	52.03	0.11
Post-pellet	0.91	1.04	0.28	0.28	0.37	0.37	1.56	1.69	0.33
Total	7.34	8.35	25.37	25.57	33.79	33.80	66.50	67.72	0.92

radiolabeled antibodies; (2) using these estimates, clarify from a dosimetric perspective how radiolabeled antibodies can produce sufficient radiation doses to kill radioresistant *C. neoformans* cells by developing analytic approaches for alpha-particle dosimetry appropriate for the current experiments; (3) estimate the linear-quadratic (LQ) parameters for *C. neoformans* cell survival after exposure to gamma-rays and to external-beam alpha-particles and determine to what extent the radioresistance of *C. neoformans* applies to densely ionizing radiation; (4) estimate alpha-particle RBE for *C. neoformans*; (5) compare the cytotoxic effectiveness (per unit of alpha-particle dose) of radiolabeled antibodies with the effectiveness of external-beam alpha-particles; and (6) assess how the responses of *C. neoformans* to different radiation types conform to patterns observed in mammalian cell radiobiology.

The standard LQ formalism provided reasonable fits to *C. neoformans* clonogenic cell survival curves for both γ -rays and external-beam α -particles (Fig. 2). The best-fit LQ parameter values ($\alpha = 0.24 \times 10^{-2} \text{ Gy}^{-1}$ for gamma-rays and $1.07 \times 10^{-2} \text{ Gy}^{-1}$ for external-beam alpha-particles, and $\beta = 1.44 \times 10^{-5} \text{ Gy}^{-2}$ for both radiation types) are approximately two orders of magnitude smaller than those typical for mammalian cells. These numbers translated into predictions that 91% of *C. neoformans* cells survive 1 traversal through the nucleus, and 11% survive 20 traversals, suggesting that *C. neoformans* is more radioresistant than mammalian cells even when differences in the size of the nucleus are taken into consideration.

The relative biological effectiveness (RBE) for alpha-particles vs gamma-rays, estimated for low radiation doses using the ratio of linear dose response components (alpha values), was 4.47 for *C. neoformans*. At an alpha-particle dose of 59.8 Gy, which was predicted to produce 50% cell survival, the RBE decreased to 2.53. At an alpha-particle dose of 304.9 Gy, which was predicted to produce 1% cell survival, the RBE decreased further to 1.60. These RBE values are within the range reported for mammalian cells at comparable levels of cell survival [7-

8]. These results suggest that in *C. neoformans*, as in mammalian cell lines, repair of alpha-particle induced damage, e.g. complex DNA double strand breaks (DSBs), is more difficult than repair of gamma-ray induced damage (e.g. simpler DSBs).

The estimated α -particle doses to the *C. neoformans* cell nucleus, or to the cell body, from the highest tested concentration of ^{213}Bi -labeled capsule-specific antibody are shown in Table 1. The total physical α -particle dose to the nucleus was 66.5 Gy. The Bragg peak region of the α -particle track accounted for about 51% of this dose (33.8 Gy). The best-fit value for the Bragg peak RBE, relative to the initial portion of the α -particle track, was 1.71 (95% CI: 1.46, 1.98). Relative to γ -rays, the Bragg peak RBE was 7.66 (95% CI: 6.32, 9.04). This RBE value is reasonable, considering that maximum LET in the Bragg peak was >3-fold higher than in the initial part of the ^{213}Po alpha-particle track.

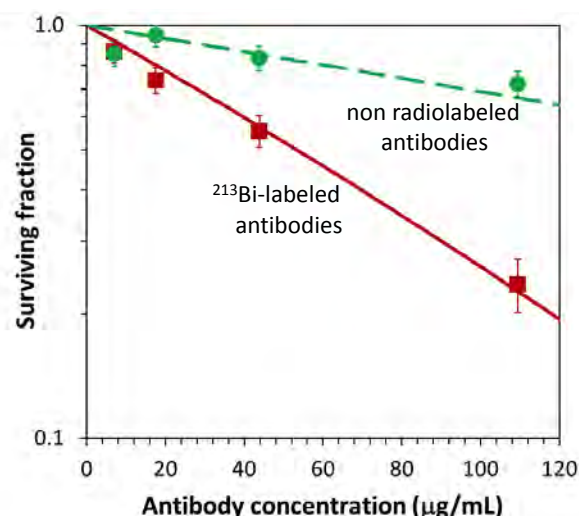


Figure 3. The effects of ^{213}Bi radiolabeled antibodies, and non-radiolabeled antibodies, on clonogenic survival of *C. neoformans*. Curves represent best-fit dose responses. The values of the linear-quadratic radiation-related parameters used to generate the predicted survival curve for ^{213}Bi radiolabeled antibodies are the same as those estimated for external-beam alpha-particles. Error bars are 95% confidence intervals.

When the Bragg peak RBE was taken into consideration, the “biologically-effective alpha-particle dose” from radiolabeled antibodies became $(66.5 - 33.8) + 33.8 \times 1.71 = 90.6$ Gy. This high value does emphasize the inherent effectiveness of alpha-emitter radiolabeled antibodies, and their ability to kill even highly radioresistant pathogens.

When the increased RBE of the alpha-particle Bragg peak was taken into consideration, observed cell survival of radiolabeled antibody-treated *C. neoformans* was consistent with predictions based on the alpha-particle dose to the cell nucleus and the linear-quadratic parameters estimated for external-beam α -particles (Fig. 3). However, non-radiological cytotoxic effects of antibodies were also present and accounted for up to 23% of *C. neoformans* cell death.

Thus, our modeling formalism, which assumed that the dose responses for α -particles delivered by external beam, and by ^{213}Bi radiolabeled antibodies, could be described by the same set of linear-quadratic parameters, and that radiological and non-radiological antibody effects were strictly additive, demonstrated reasonable agreement with the data. This result, which suggests that the radiobiological effectiveness of alpha-particles on *C. neoformans* depends mainly on the dose to vulnerable cell structures, rather than on delivery mode (e.g. external-beam or radiolabeled antibodies), is generally consistent with data on mammalian cells.

These results quantify the degree of *C. neoformans* resistance to densely-ionizing radiations, and show how this resistance can be overcome with fungus-specific radiolabeled antibodies.

References

1. Zahradka K, Slade D, Bailone A, Sommer S,

Averbeck D, Petranovic M, et al. Reassembly of shattered chromosomes in *Deinococcus radiodurans*. *Nature* 2006;443:569-73.

2. Daly MJ. Death by protein damage in irradiated cells. *DNA Repair (Amst)* 2012;11:12-21.

3. Dighton J, Tugay T, and Zhdanova N. Fungi and ionizing radiation from radionuclides. *FEMS Microbiol Lett* 2008;281:109-20.

4. Dadachova E and Casadevall A. Ionizing radiation: how fungi cope, adapt, and exploit with the help of melanin. *Curr Opin Microbiol* 2008;11:525-31.

5. Dadachova E, Howell RW, Bryan RA, Frenkel A, Nosanchuk JD, and Casadevall A. Susceptibility of the human pathogenic fungi *Cryptococcus neoformans* and *Histoplasma capsulatum* to gamma-radiation versus radioimmunotherapy with alpha- and beta-emitting radioisotopes. *Journal of Nuclear Medicine* 2004;45:313-20.

6. Bryan RA, Jiang ZW, Howell RC, Morgenstern A, Bruchertseifer F, Casadevall A, et al. Radioimmunotherapy Is More Effective than Antifungal Treatment in Experimental Cryptococcal Infection. *Journal of Infectious Diseases* 2010;202:633-7.

7. Franken NA, ten Cate R, Krawczyk PM, Stap J, Haveman J, Aten J, et al. Comparison of RBE values of high-LET alpha-particles for the induction of DNA-DSBs, chromosome aberrations and cell reproductive death. *Radiat Oncol* 2011;6:64.

8. Howell RW, Goddu SM, Narra VR, Fisher DR, Schenter RE, and Rao DV. Radiotoxicity of gadolinium-148 and radium-223 in mouse testes: relative biological effectiveness of alpha-particle emitters in vivo. *Radiat Res* 1997;147:342-8. ■



Left (l to r): Alan Bigelow, Chris Marino, Manuela Buonanno, Gerhard Randers-Pehrson, Steve Marino, Andrew Harkin, and David Welch. Above, first row (l to r): Kara Pinaud, Tom Hei, Eric Hall, Cliff Chao, Simon Cheng, Eileen Connolly, Sally Amundson. Back row (l to r): Karen Schleif, Cheng-Shie Wu, Anshu Jain, Anand Shah, David Horowitz, Chi Zhang, Ted Yanagihara, Dan Carrier.

Antitumor Activity of Pamidronate in a Breast Cancer Model by Targeting *Rho-A* Gene Expression

Richard Ponce-Cusi^a and Gloria M. Calaf^a

Breast cancer is one of the most common types of cancer in women. We have developed an *in vitro* breast cancer model by exposing the immortalized human breast epithelial cell line MCF-10F to low doses of high LET (linear energy transfer) α particle radiation (150 keV/ μ m) and subsequently treating the cells with 17 β -estradiol (10^{-8} M) [1]. This model consists of human breast epithelial cells in different stages of transformation: i) a control cell line, MCF-10F, ii); a non-malignant cell line, Alpha3 iii) a malignant and tumorigenic cell line, Alpha5 and iv) Tumor2, which was derived from cells from a tumor recovered after injection of the Alpha5 cell line into nude mice.

In the present study, we evaluated the antitumor activity of pamidronate in the series of transformed human breast epithelial cells described above. Pamidronate is a member of the nitrogen-containing bisphosphonates, potent antiresorptive drugs used in the treatment of metabolic bone disease. Pamidronate is used specifically for the treatment of bone metastasis of breast and prostate cancer. It has been reported that pamidronate has an apoptotic effect in breast cancer cell lines [2] through inactivation of the Ras/ERK pathway [3]. Others [4, 5] have reported that pamidronate preferentially decreased cell proliferation in myeloma and breast cancer cells overexpressing c-Ha-ras. Ras is an important signal transducing protein for growth factor activated pathways, and approximately 20-30% of human breast tumors contain mutated versions of Ras proteins.

Cell viability and LD₅₀ were determined using the 3-(4, 5-dimethylthiazol-2-yl)-2, 5-diphenyltetrazolium bromide (MTT) assay (Figure 1A). The mean LD₅₀ in MCF-10F was 10 μ M after 48 hours. Treatment with 10 μ M pamidronate for 48 hours significantly inhibited the invasive capabilities of the Alpha5 cell line, as measured using a Matrigel-invasion assay (Figure 1B). The same treatment also significantly inhibited migration of both the Alpha5 and Tumor2 cell lines as measured using a scratch wound assay (Figure 1C).

Rho-A, a member of the Ras superfamily, is a small GTPase protein known to regulate cell morphology through the actin cytoskeleton in the formation of stress fibers [6, 7], and it is generally distributed in the nuclei of cancer cells. We used quantitative real-time RT-PCR to measure expression of the *Rho-A* gene. Data were

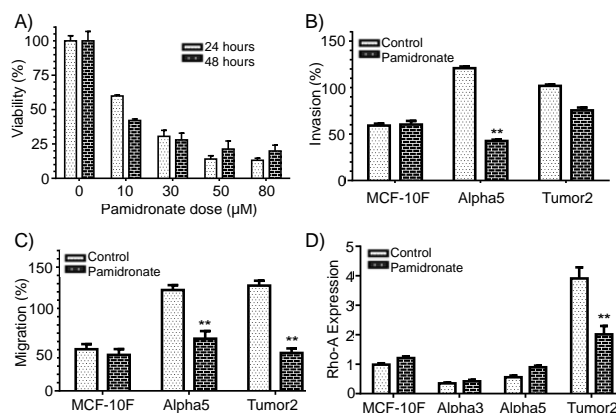


Figure 1. A) Effect of pamidronate on cell viability. The MCF-10F cell line was treated with different doses of pamidronate (from 0 to 80 μ M) and incubated for 24 and 48h. Viability was determined by using the MTT assay and an automated cell counter. The effect of pamidronate (10 μ M/48h) on B) cell invasion and C) migration in the MCF-10F, Alpha5, and Tumor2 cell lines was quantified by microscopy (40x magnification). These experiments were carried out as described previously [15]. Bars represent the mean \pm S.E.M. of three independent experiments; **p<0.01 vs. control group. D) The effect of pamidronate (10 μ M/48h) on expression of the *Rho-A* gene was evaluated in MCF-10F, Alpha3, Alpha5, and Tumor2 cell lines by RT-qPCR. β -Actin was used as an endogenous control gene to normalize *Rho-A* expression. Bars represent the mean \pm S.E.M. of three independent experiments; **p<0.01 vs. controls.

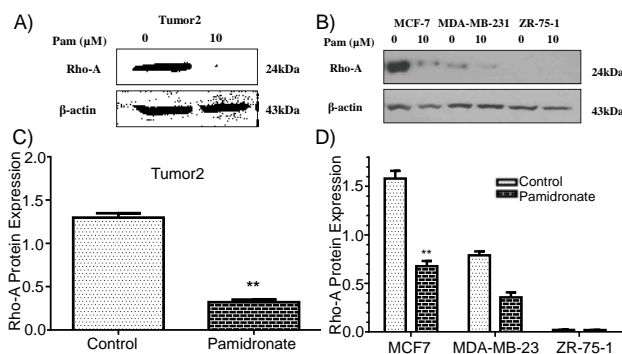


Figure 2. *Rho-A* protein expression: Effect of pamidronate (10 μ M/48h) in the Tumor2 cell line (A-B); MCF-7, MDA-MB-231 and ZR-75-1 (C-D) determined by Western blot analyses. β -Actin was used as a control for loading. Band density of the specific protein was analyzed with Adobe Photoshop and the results were expressed as average density normalized to β -Actin. Bars represent the mean \pm S.E.M. of three independent experiments. **p<0.01 vs control.

expressed as the average \pm standard error of the mean (SEM). Comparison between treated groups and controls was carried out by ANOVA and Dunnet's test. Treatment

^a Institute for Advanced Research, Tarapacá University, Arica, Chile.

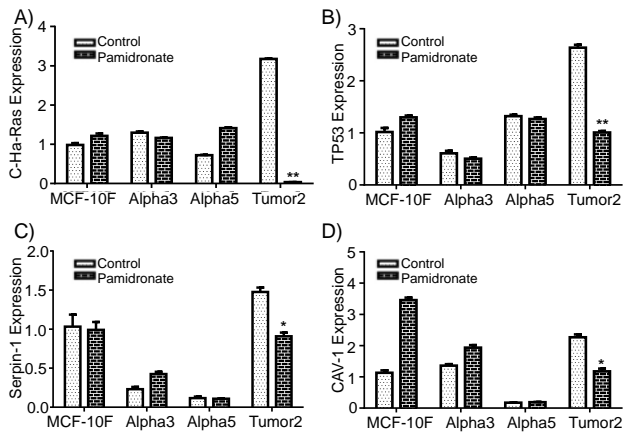


Figure 3. Effect of pamidronate (10 μ M/48h) on A) c-Ha-ras, B) TP53 C) Serpin-1 and D) CAV-1 gene expression measured by RT-qPCR in MCF-10F, Alpha3, Alpha5 and Tumor2 cell lines. β -Actin was used as an endogenous control gene. Bars represent the mean \pm S.E.M. of three independent experiments; * $p < 0.05$, ** $p < 0.01$ vs. controls.

with 10 μ M pamidronate for 48h decreased *Rho-A* gene (Figure 1D) and protein (Figure 2A and B) expression in Tumor2 in comparison with the untreated controls.

Similar decreases in protein expression were also seen in the breast cancer cell lines MCF7 and MDA-MB-231 (Figure 2C and D).

We next used analysis by real-time PCR to monitor the effect of pamidronate treatment on several additional genes implicated in breast cancer and apoptosis.

The p53 gene, known as the guardian of the genome, [8] responds to stress signals and activates the transcription of downstream target genes involved in important cellular mechanisms like cell cycle control, DNA repair and apoptosis. Among downstream p53 effector genes are the serpins, serine protease inhibitors that are structurally conserved across nearly all branches of life [9]. Among newly characterized serpin functions, regulation of cellular proliferation through apoptosis modulation and proteasome disturbance seem to play major roles. Indeed, apoptosis dysregulation is likely to be a cornerstone of tumorigenesis, since uncontrolled cellular viability results in tumor proliferation, while inefficient disposal of apoptotic debris may favor the rescue of auto-reactive immune cells. Accordingly, several serpins have been found to be over-expressed in

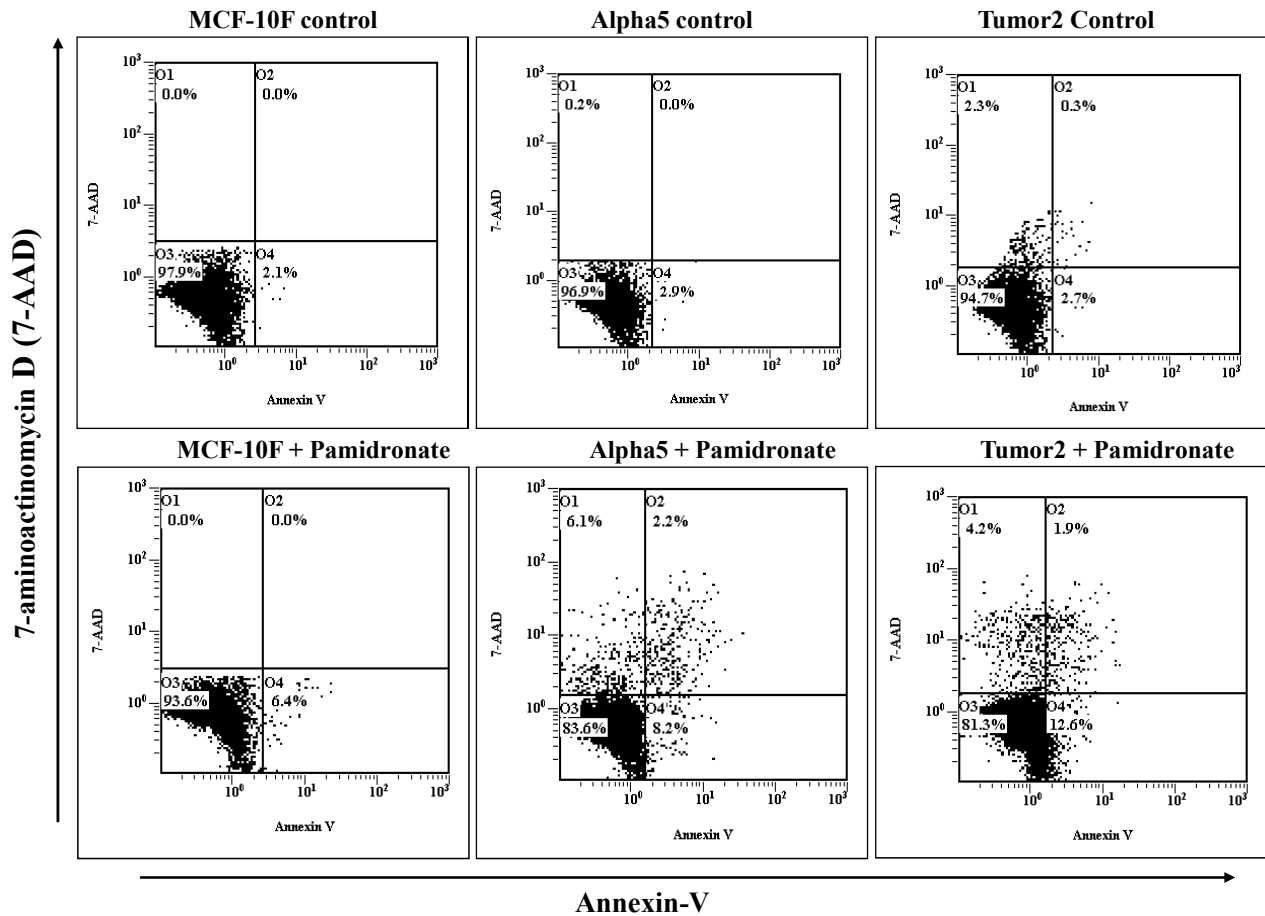


Figure 4. Flow cytometric analysis of apoptosis in breast cancer cells. Apoptotic effects of pamidronate (10 μ M/48h) were evaluated in MCF-10F, Alpha5, and Tumor2 cell lines compared to untreated controls. The upper left quadrant (O1) contains cells undergoing necrosis; the upper right quadrant (O2), cells at the end stage of apoptosis; the lower left quadrant (O3), viable cells with no measurable apoptosis; and the lower right quadrant (O4), cells undergoing apoptosis. The percentage of the cells in apoptosis was determined using CXP analysis software.

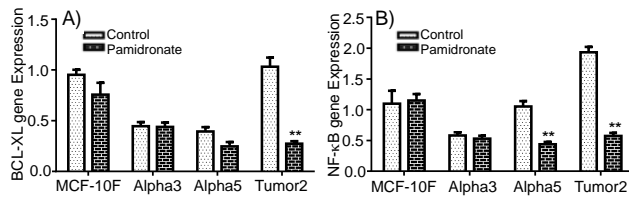


Figure 5. Effect of pamidronate (10 μ M/48h) on A) BCL-XL and B) NF κ B gene expression in MCF-10F, Alpha3, Alpha5 and Tumor2 cell lines measured by RT-qPCR. β -Actin was used as an endogenous control gene. Bars represent the mean \pm S.E.M. of three independent experiments; ** p <0.01 vs. controls.

tumor cells. We found that pamidronate treatment significantly decreased gene expression of *c-Ha-ras* (p <0.01), *p53* (p <0.01), and *Serpin-1* (p <0.05) below control levels in the Tumor2 cell line, but not in the MCF-10F, Alpha3 or Alpha5 cell lines (Figure 3A-C).

Caveolin is a specialized lipid raft on the plasma membrane found in mesenchymal cells. The Caveolin family consists of three members, Caveolin-1 (Cav-1), Cav-2, and Cav-3. Cav-1 is widely expressed in various tissues. Previous studies demonstrated an essential role of Caveolin in a number of human diseases including cancer [10]. *In vitro* studies have shown that both stromal and epithelial Cav-1 play protective roles against mammary hyperplasia and tumorigenesis in breast cancer [11, 12]. Recently, both epithelial and stromal Caveolin expression have been measured in breast cancer patients to determine prognosis [13, 14]. We also found that expression of the Cav-1 gene was decreased by pamidronate treatment in Tumor2 (p <0.05), but not in the MCF-10F, Alpha3 or Alpha5 cell lines (Figure 3D).

Finally, the effect of pamidronate (10 μ M for 48 hours) on apoptosis was analyzed by flow cytometry (7-AAD/Annexin V staining) in MCF-10F, Alpha5 and Tumor2 cell lines. Results indicated that pamidronate treatment increased the number of apoptotic cells in Alpha5 (10.4%) and Tumor2 (14.5%) in comparison to the control MCF-10F cell lines (6.4%) as seen in Figure 4. The mechanism of apoptosis seems to be induced by affecting *Bcl-xL* and *NF κ B* gene expression since they were also reduced in Tumor2 (Figure 5). NF κ B is a family of 5 transcriptional factors including p65 (Rel-A), which is recognized as a key positive regulator of cancer cell proliferation and survival via its ability to transcriptionally activate many pro-survival and anti-apoptotic genes, including *Bcl-xL* [15, 16]. It can be concluded that pamidronate had a direct antitumor and apoptotic effect in a breast cancer model transformed by low doses of alpha particles and estrogen *in vitro*, and may be a valuable drug for therapeutic use by targeting *Rho-A* gene expression.

Grant support FONDECYT #1120006 (GMC) and MINEDUC-UTA (GMC).

References

1. Calaf GM and Hei TK Establishment of a radiation- and estrogen-induced breast cancer. *Carcinogenesis* 21: 769-776, 2000.
2. Riebeling C, Forsea A-M, Raisova M, Orfanos CE, Geilen CC. The bisphosphonate pamidronate induces apoptosis in human melanoma cells *in vitro*. *Br J Cancer* 87: 366-371, 2002.
3. Wada K, Fukui K, Sawai Y, Imanaka K, Kiso S, Tamura S, and Hayashi N. Pamidronate induced anti-proliferative, apoptotic, and anti-migratory effects in hepatocellular carcinoma. *J Hepatology* 44: 142, 2006.
4. Zhang PL, Lun M, Siegelmann-Sanieli N, Blasick TH, and Brown RE. Pamidronate resistance and associated low ras levels in breast cancer cells. A role for combinatorial therapy. *Annals Clinical & Lab Science* 34 (3): 263, 2004.
5. Zhang P L, Quiery A T, Blasick T H, and Brown R E. Morphoproteomic expression of H-ras (p21ras) correlates with serum monoclonal immunoglobulin reduction in multiple myeloma patients following pamidronate treatment. *Annals Clinical and Lab Science* 37: 34-38, 2007.
6. Ridley AJ, Hall A. The small GTP-binding protein rho regulates the assembly of focal adhesions and actin stress fibers in response to growth factors. *Cell* 70: 389-399, 1992.
7. Ridley AJ, Paterson HF, Johnston CL, Diekmann D and Hall A. The small GTP-binding protein rac regulates growth factor-induced membrane ruffling *Cell* 70: 401-410, 1992.
8. Lane DP. Cancer. p53, guardian of the genome. *Nature* 358 (6381): 15-16, 1992.
9. Congote L F, Temmel N. The C-terminal 26-residue peptide of serpin A1 stimulates proliferation of breast and liver cancer cells: role of protein kinase C and CD47. *FEBS Letters* 576: 343-347, 2004.
10. Hnasko R, Lisanti MP. The biology of caveolae: lessons from caveolin knockout mice and implications for human disease. *Mol Interv* 3: 445-464, 2003.
11. Williams TM, Sotgia F, Lee H, Hassan G, Di VD, Bonuccelli G, et al. Stromal and epithelial caveolin-1 both confer a protective effect against mammary hyperplasia and tumorigenesis: caveolin-1 antagonizes cyclin D1 function in mammary epithelial cells. *Am J Pathol* 169: 1784-1801, 2006.
12. Liedtke C, Kersting C, Burger H, Kiesel L, Wulfing P. Caveolin-1 expression in benign and malignant lesions of the breast. *World J Surg Oncol* 5: 110, 2007.
13. Witkiewicz AK, Dasgupta A, Sammons S, Er O, Potoczek MB, Guiles F, et al. Loss of stromal caveolin-1 expression predicts poor clinical outcome

in triple negative and basal-like breast cancers. *Cancer Biol Ther* 10: 135-143, 2010.

14. Qian N, Ueno T, Kawaguchi-Sakita N, Kawashima M, Yoshida N, Mikami Y, et al. Prognostic significance of tumor/stromal caveolin-1 expression in breast cancer patients. *Cancer Sci* 102: 1590-1596, 2011.
15. Sethi G, Ahn KS, Aggarwal BB. Targeting nuclear

factor-kappa B activation pathway by thymoquinone: role in suppression of antiapoptotic gene products and enhancement of apoptosis. *Mol Cancer Res* 6: 1059-1070, 2008.

16. Dolcet X, Llobet D, Pallares J, Matias-Guiu X. NF-kB in development and progression of human cancer. *Virchows Arch* 446: 475-482, 2005. ■

High Dose Gamma Radiation and the Human Endothelial Barrier: Collapse of Live Vessels

Preety Sharma and Peter Grabham

The sensitivity and damage of tumor vasculature is crucial in regulating tumor responses to radiotherapy. Fractionated gamma radiotherapy (2 Gy fractions) is well known to actually increase tumor vasculature and confound treatment by causing the secretion of vascular endothelial growth factor (VEGF). However, with the recent surge in the application of high-dose per fraction radiotherapy using stereotactic radiosurgery (SRS) of brain tumors and treatment of extra cranial tumors with stereotactic body radiation therapy (SBRT), the response of tumor vasculature to higher doses is now more relevant. The effects of these higher doses can be utilized along with other anti-angiogenic drugs to inhibit tumor vasculature much more effectively. It is therefore important to elucidate the effects of high dose irradiation alone on vascular structure and functionality for effective use of SRS or SBRT together with other agents. The following study by *in vitro* tissue culture techniques aims to characterize the vascular changes in normal human endothelial 2D and 3D microvessel structure and survival at gamma radiation doses relevant for the treatment outcomes of high dose therapy (HRT) such as SRS or SBRT.

Human endothelial umbilical vein cells (HUVEC) cultured as 2D monolayers and in 3D endothelial microvessels (as described previously in [1]) were exposed to selective single doses of gamma radiation (0 Gy, 8 Gy, 16 Gy, and 24 Gy). We first followed the transendothelial electrical resistance (TEER) across the endothelial barrier to gain an insight into the events following irradiation in real time. The effect of gamma radiation on TEER is shown in Figure 1. All doses caused an early dip in resistance at 3 hours. This

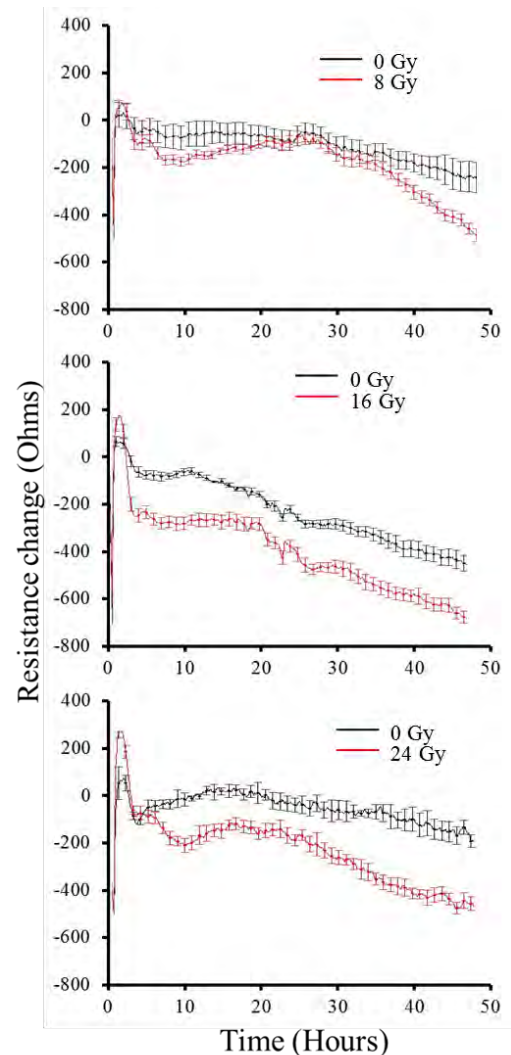


Figure 1. Effect of Gamma radiation on trans-endothelial electrical resistance. TEER across HUVEC monolayers after irradiation with different doses. Irradiated monolayers (red curves) are shown with matched controls (black curve) up to 48 hours post irradiation with different doses (as shown). A decrease in resistance was observed first at 3h post irradiation which corresponds to the uncoupling of PECAM-1 [1] a further drop in resistance was seen at ~10 h post radiation for all doses. This radiation induced resistance change was recovered in cells exposed to 8 Gy but not in cells exposed to 16 Gy and 24 Gy. Error bars = \pm SEM.

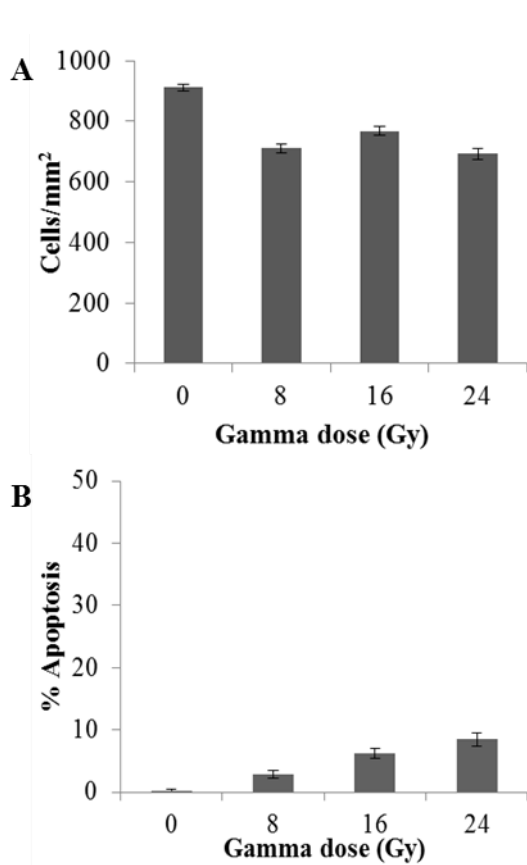
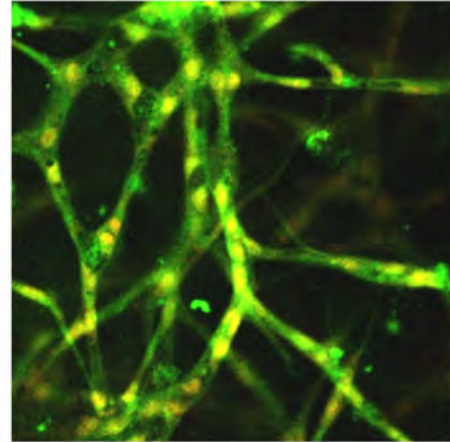


Figure 2. 2D cell count and 3D vessel cell apoptotic death at 48 hours post irradiation. A. Cell number in 2D monolayers in response to Gamma dose. Cell loss was observed starting at the 8Gy dose but did not increase significantly at higher doses B. 3D vessel cell apoptosis in response to gamma doses by TUNEL assay. An increase in the apoptosis was observed but remained at less than 10% with doses up to 24 Gy Gamma rays. Error bars = \pm SEM.

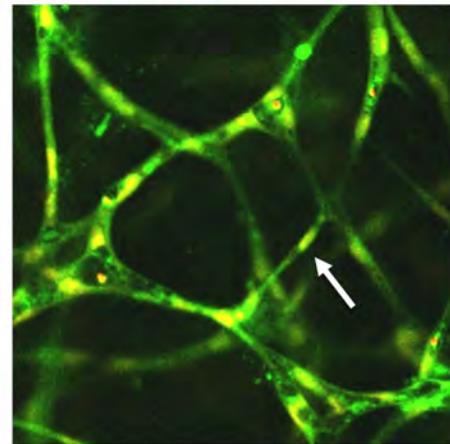
corresponds to the uncoupling of the cell adhesion molecule - PECAM-1 [2]. Later effects included a longer term reduction in TEER. A dose of 8 Gy gamma rays caused a longer dip in TEER at ~10 hours. This dip in resistance corresponded to a decrease of about 200 ohms that was recovered by about 24 hours post irradiation. The resistance stayed close to the control (0 Gy) for another 10 hours before declining. A similar dip in resistance was also present at ~ 10 hours for 16 Gy and 24 Gy and this corresponded to about 200-250 ohms difference. However, at these doses this drop in the resistance remained significantly lower than the controls up to 50 hours after exposure. This change in resistance at 48 hours post radiation did not correspond with the loss of staining of the cell adhesion protein PECAM and adherens junction structural protein ZO1 at cell junctions (not shown) except at the highest dose of 24 Gy.

A 15-25% cell loss in 2D cultures occurred starting at the dose of 8 Gy, although this did not increase significantly at higher doses (Figure 2A). However, only about 2-8% of the cell loss could be attributed to apoptosis in the 3D vessel models even at 24 Gy (Figure

A Control



B 16Gy Gamma



C

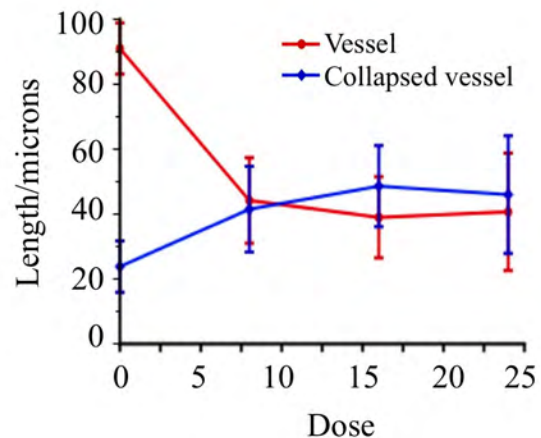


Figure 3. Effect of gamma rays on 3D vessel models. Vessel models were grown for 7 days to maturity then exposed to a dose range of gamma rays and stained for all proteins (green) and with propidium iodide (red). A. Control cultures show vessel models as tubular structures. B. 48 hours after exposure to 16 Gy gamma rays some of the vessels have collapsed around the nuclei (arrow). C. Quantification of the collapse based on the thickness of the vessels. Full vessels decrease at 8 Gy and collapsed vessels increase at the same dose although there is no further increase in collapse at 16 and 24 Gy.

2B), it should be noted here that the cells are cultured in the presence of VEGF and FGF which are known to inhibit apoptosis. This extent of apoptosis is therefore probably not the cause of TEER changes and cell loss at 8 Gy and 16 Gy, even though these doses are within the range of the doses used in SRS and SBRT. These results indicate that there are effects on the human vasculature at doses lower than those required for cell death by apoptosis. The doses used in stereotactic radiotherapy are therefore causing damage to the endothelium without killing cells.

To gain an insight into what is happening to the vasculature, we assayed for the morphological effects of a dose range of gamma rays on the 3D microvessels. Figure 3 shows the results of this study. We observed a phenomenon whereby the vessels collapsed starting at 8 Gy but without a dose response up to 24 Gy. Vessels are collapsing before there is appreciable loss of cells by apoptosis. Collapsed vessels contain cells in which the nucleus does not contain fragmented and condensed

DNA. These results indicate that there is more than one type of response of vessels to these doses of gamma rays and that stereotactic radiotherapy is able to cause damage to the vasculature before the onset of cell death. Harnessing this effect by coordinating treatment with agents such as VEGF inhibitors and Notch inhibitors is a promising direction for the inhibition of tumor vasculature during SRS and SBRT.

References

1. Sharma P, Templin T, Grabham P. Short term effects of gamma radiation on endothelial barrier function: uncoupling of PECAM-1. *Microvascular research*. 2013;86:11-20. Epub 2012/12/12.
2. Grabham P, Hu B, Sharma P, Geard C. Effects of ionizing radiation on three-dimensional human vessel models: differential effects according to radiation quality and cellular development. *Radiation research*. 2011;175(1):21-8. Epub 2010/12/24. ■

RAD9 Silencing Suppresses Prostatosphere Formation

Constantinos G. Broustas and Howard B. Lieberman

Introduction

Prostate cancer is the most prevalent non-cutaneous type of cancer in men. Radical prostatectomy is the main treatment option for localized primary prostate tumors, followed by androgen-deprivation treatment (ADT) for tumors that pose greater risk for the patient. Eventually, ADT will lead to castration-resistant prostate cancer, which is difficult to manage. In prostate cancer, it has been proposed that cancer stem-like cells are responsible for the initiation and progression of this cancer [1]. Furthermore, cancer stem cells (CSCs) have been implicated in the failure of chemotherapy and radiotherapy [2]. Prostate CSCs have lost expression of androgen receptor and have acquired aggressive characteristics, such as activation of survival pathways (e.g. PI3K/Akt) [3], increased expression of anti-apoptotic molecules (e.g. Bcl-2) [4], and an efficient DNA repair system [5]. Importantly, prostate cancer patients who receive ADT demonstrate an increased prostate cancer stem/progenitor stem population [4]. Thus, targeting the cancer stem cells in a prostate tumor may provide positive therapeutic intervention for patients with advanced prostate cancer.

Cancer cell lines harbor stem-like cells, and therefore can be used as *in vitro* models to study CSC biology. By using a combination of cell surface markers, such as CD44 and CD133, or the activity of aldehyde

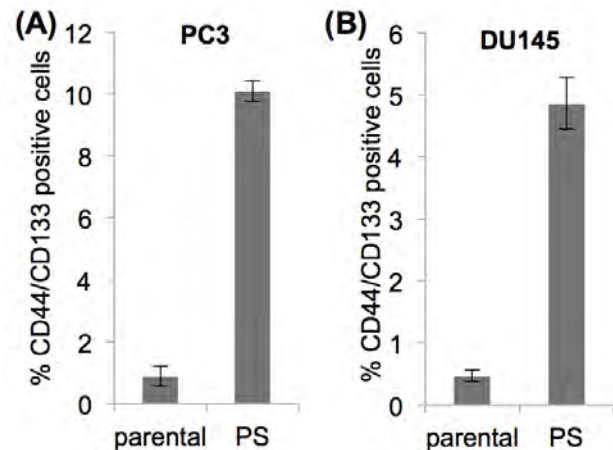


Figure 1. Enrichment of cancer stem cells under prostatosphere-forming conditions. Flow cytometry analysis shows enrichment of the CD44⁺/CD133⁺ populations under sphere-forming conditions, compared with monolayer conditions for PC3 (A) and DU145 (B) cells. Shown is mean ± SD from three (DU145) or four (PC3) independent experiments. PS; prostatospheres.

dehydrogenase, prostate CSCs can be successfully isolated by flow cytometry [6]. The number of CSCs in a cancer cell line is very small (usually less than 1%). However, CSCs can be propagated under anchorage-independent conditions in selective growth medium that

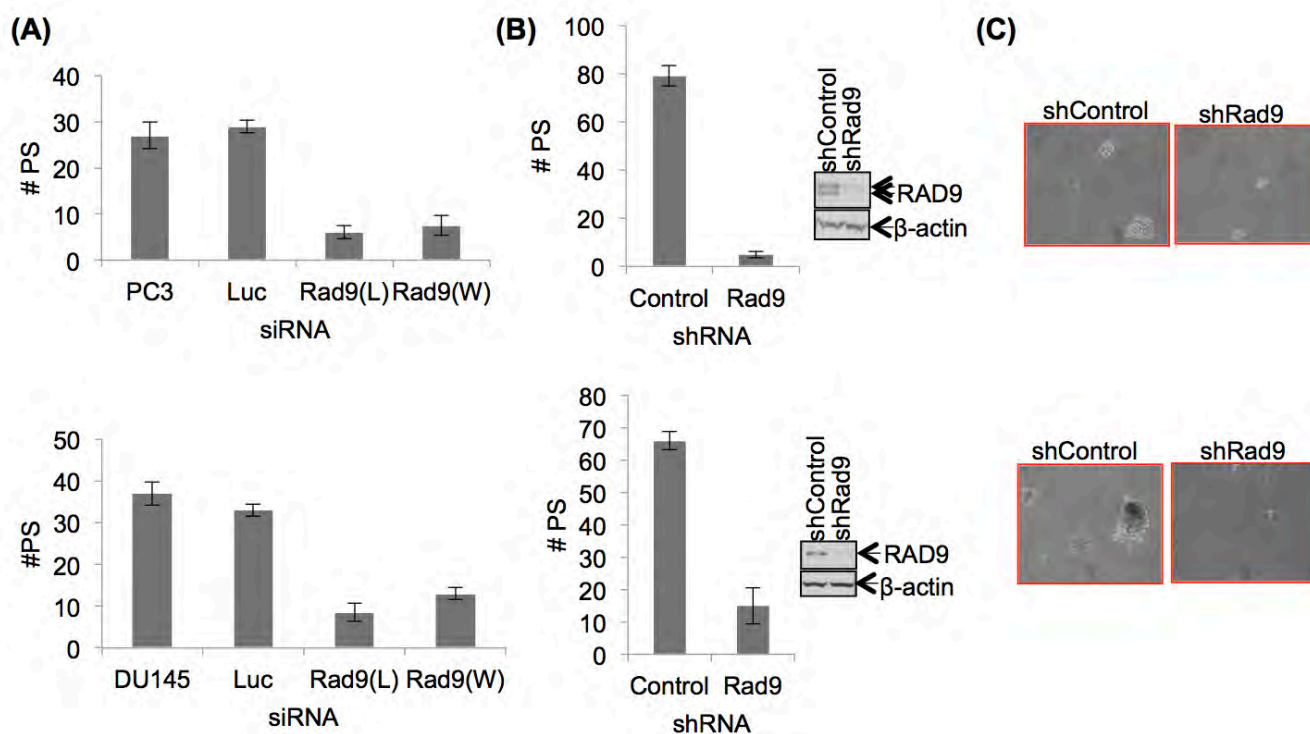


Figure 2. Targeting RAD9 in prostate cancer cells reduces prostatosphere formation. (A) PC3 (upper) or DU145 (lower) cells transiently transfected with two non-overlapping Rad9 siRNAs (L and W) were allowed to form prostatospheres for 7 days and subsequently counted. Shown as mean \pm SD ($n=3$). (B) PC3 (upper) and DU145 (lower) cells stably expressing an insertless vector (shControl) or shRAD9 were grown under sphere-forming conditions and prostatospheres were counted after 7 days. Shown as mean \pm SD ($n=3$). Western blot analysis confirmed RAD9 knockdown in shRAD9 clones. (C) Photographs of representative prostatospheres.

lacks serum. Stem cells can survive and generate spheres (called prostatospheres in the case of prostate cells), which can be passaged indefinitely. In contrast, non-CSCs are incapable of forming spheres under these conditions. Therefore, this sphere-forming assay is used to enrich for CSCs in the total population of cancer cells.

RAD9 plays important functions in mediating prostate cancer [7, 8]. In this study, we sought to examine the role of RAD9 in survival of prostate CSCs. To begin to address this role, we describe here the impact of RAD9 knockdown on cancer stem cell sphere formation.

Results

In our previous studies, we correlated levels of endogenous RAD9 with a number of *in vitro* tumor characteristics, such as cell migration, invasion, and anchorage-independent growth, which can predict metastatic behavior *in vivo* [8]. In that report, we showed that DU145 cells stably expressing a shRNA against RAD9 were unable to support growth in a soft-agar colony assay.

We used sphere-formation to enrich for CSCs from DU145 and PC3 human prostate cancer cells. Fluorescence activated cell sorting (FACS) analysis using a combination of the surface markers CD44 and CD133 revealed that the percentages of CSCs in cells growing under serum as monolayers were $0.89 \pm 0.31\%$ ($n=4$; PC3) and $0.47 \pm 0.09\%$ ($n=3$; DU145). However, FACS

analysis of cells grown as prostatospheres showed that the percentage had increased to $10.1 \pm 0.33\%$ ($n=4$) and $4.86 \pm 0.41\%$ ($n=3$) for PC3 and DU145 cells, respectively (Fig. 1). In addition, analysis of CSC-specific marker genes (e.g. *OCT3/4*, *NANOG*, and *SOX2*) revealed enrichment in prostatospheres from 2.5- to 5-fold in DU145 and PC3 cells (not shown).

Next, we sought to determine whether RAD9 knockdown had an impact on sphere formation. For this purpose we cultured PC3 and DU145 cells expressing normal or reduced levels of endogenous RAD9 under sphere-forming conditions. Transient downregulation of RAD9 using two independent siRNAs (Fig. 2A) or a clone stably expressing shRAD9 (Fig. 2B) demonstrated a dramatic effect on the ability of the cells to form prostatospheres. Specifically, PC3 or DU145 cells with normal levels of RAD9 formed 5-fold more prostatospheres than cells with transient RAD9 knockdown. Likewise, in stable cell cultures, shControl cells generated 15.5-fold (PC3) and 4.5-fold (DU145) more prostatospheres than cells with silenced RAD9. RAD9 knockdown levels were confirmed by immunoblotting after transient (not shown) and stable (Fig. 2B, right panels) transfections. Photographs of representative prostatospheres are shown (Fig. 2C).

Finally, we measured RAD9 levels in the DU145/shRAD9 cells that had formed prostatospheres. For this purpose, the few surviving prostatospheres from

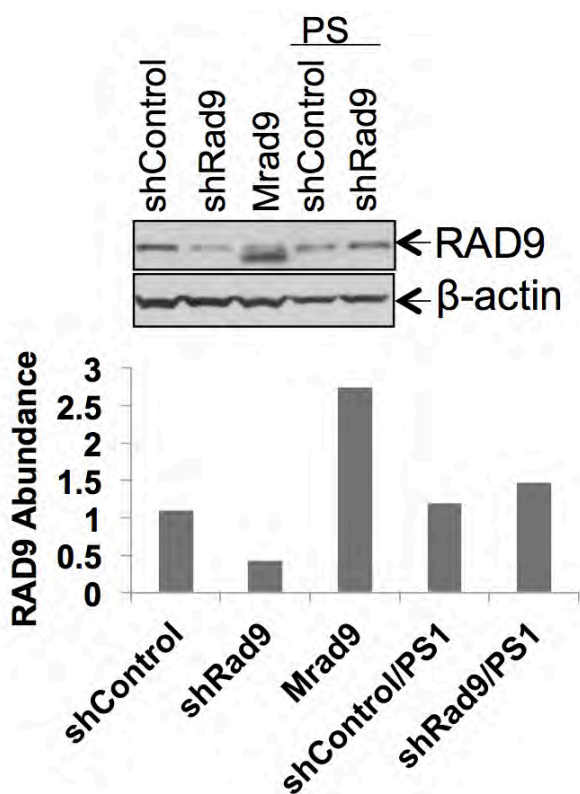


Figure 3. Surviving prostatospheres in DU145/shRAD9 cells have re-expressed RAD9. Upper panel, abundance of RAD9 protein in DU145 cells expressing shControl, shRAD9, or shRAD9 and ectopically expressing Mrad9 as well, grown either as adherent cells or recovered from prostatospheres and grown in serum-containing medium as monolayers. Lower panel, quantitation of the western blot protein bands. PS1; first generation of prostatospheres.

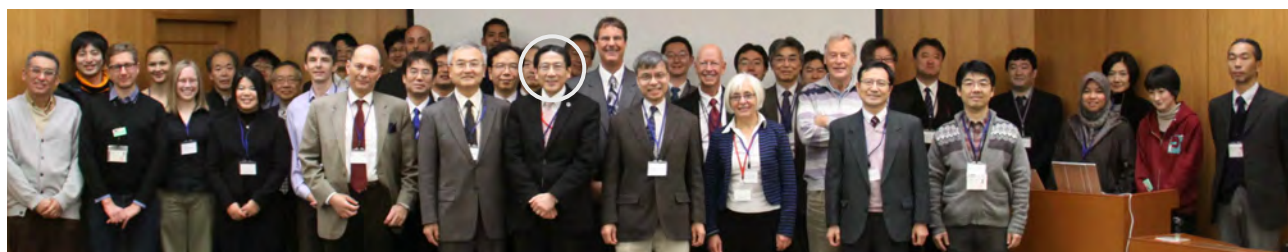
DU145/shRAD9 cells were recovered, and the cells were dissociated and plated under normal cell culture conditions. We compared RAD9 protein levels in prostatosphere-derived shControl and shRAD9 DU145 cells with parental DU145 cells, expressing shControl, shRAD9, or shRAD9 with ectopic mouse MRad9, which had been propagated as monolayers. Western blot analysis showed that RAD9 levels in DU145/shRAD9 cells, which formed prostatospheres, had increased by more than 3-fold compared to RAD9 levels in DU145/shRAD9 cells maintained as adherent cells, and reached the levels of RAD9 typical of shControl cells (Fig. 3). These results support the idea that RAD9 is required for prostatosphere formation.

Conclusions

Our present study suggests that RAD9 is necessary for prostatosphere formation. Elucidation of the mechanism by which RAD9 regulates the maintenance and survival of prostate CSCs will be the objective of future studies. Deciphering this pathway may provide opportunities to specifically target the CSC population therapeutically for treatment of prostate cancer patients.

References

1. Pfeiffer MJ, Schalken JA. (2010). Stem cell characteristics in prostate cancer cell lines. *Eur Urol.* 57(2):246-54.
2. Bao S, Wu Q, McLendon RE, Hao Y, Shi Q, Hjelmeland AB, Dewhirst MW, Bigner DD, Rich JN. (2006). Glioma stem cells promote radioresistance by preferential activation of the DNA damage response. *Nature.* 444(7120):756-60.
3. Dubrovskaya A, Kim S, Salamone RJ, Walker JR, Maira SM, García-Echeverría C, Schultz PG, Reddy VA. (2010). The role of PTEN/Akt/PI3K signaling in the maintenance and viability of prostate cancer stem-like cell populations. *Proc Natl Acad Sci U S A.* 106(1):268-73.
4. Lee SO, Ma Z, Yeh CR, Luo J, Lin TH, Lai KP, Yamashita S, Liang L, Tian J, Li L, Jiang Q, Huang CK, Niu Y, Yeh S, Chang C. (2013). New therapy targeting differential androgen receptor signaling in prostate cancer stem/progenitor vs. non-stem/progenitor cells. *J Mol Cell Biol.* 5(1):14-26.
5. Skvortsova I, Skvortsov S, Stasyk T, Raju U, Popper BA, Schiestl B, von Guggenberg E, Neher A, Bonn GK, Huber LA, Lukas P. (2008). Intracellular signaling pathways regulating radioresistance of human prostate carcinoma cells. *Proteomics.* 8(21):4521-33.
6. Maitland NJ, Collins AT. (2008). Prostate cancer stem cells: a new target for therapy. *J Clin Oncol.* 26(17):2862-70.
7. Zhu A, Zhang CX, Lieberman HB. (2008). Rad9 has a functional role in human prostate carcinogenesis. *Cancer Res.* 68(5):1267-74.
8. Broustas CG, Zhu A, Lieberman HB. (2012). Rad9 protein contributes to prostate tumor progression by promoting cell migration and anoikis resistance. *J Biol Chem* 287(49):41324-41333. ■



Tom Hei at the National Institute of Radiological Sciences International Open Laboratory Second Term Progress Meeting in Chiba, Japan.

RAD9 Modulates Secretion of the Tissue Inhibitors of Metalloproteinases (TIMP) in Prostate Cancer Cells

Constantinos G. Broustas and Howard B. Lieberman

Introduction

Tissue inhibitors of metalloproteinases (TIMP) comprise a family of four proteins (TIMP1, TIMP2, TIMP3, and TIMP4) that naturally suppress matrix metalloproteinase (MMP) activity, thereby controlling extracellular matrix remodeling and availability of bioactive cytokines and growth factors [1]. In addition to their MMP inhibitory activity, TIMPs have multiple functions that can be MMP-independent and affect cell growth, apoptosis, differentiation and metastasis [1]. Of the four TIMPs, TIMP1 and TIMP2 are the best studied in the context of cancer initiation and metastasis. TIMP2 is considered to have tumor-suppressive properties, and TIMP1 is believed to promote tumorigenesis.

TIMP1 displays growth-promoting properties in a wide variety of cell types, including cancer cells [2]. TIMP1 interacts with CD63 and integrin β 1 (ITGB1), thus increasing FAK/Akt and ERK1/2 signaling and cell proliferation [2]. Furthermore, TIMP1 suppresses apoptosis in cancer cells by maintaining elevated expression of anti-apoptotic BCL-XL and BCL2 proteins, or by promoting the phosphorylation and inactivation of BAD in tumor cells [2]. Moreover, TIMP1 interaction with ITGB1 confers anoikis resistance to melanoma cells [3]. Finally, high levels of TIMP1 protect cancer cells from the deleterious effects of diverse challenges, including serum deprivation and γ -radiation [4].

Changes in TIMP1 expression levels have been associated with various types of cancer, including prostate cancer. Serum TIMP1 levels are elevated in prostate cancer patients compared to men without cancer [5]. Furthermore, patients with castration-resistant prostate cancer have significantly higher serum TIMP1 levels compared with patients showing hormone-sensitive disease. Elevated circulating TIMP1 levels are associated with neuroendocrine differentiation in castration resistant prostate cancer [6].

TIMP2 is generally considered tumor-suppressive. Like TIMP1, TIMP2 also binds to ITGB1, but, unlike it, TIMP2 inhibits the function of ITGB1 and abrogates tumor associated angiogenesis and suppresses metastasis *in vivo* [7]. This action of TIMP2 is MMP-independent.

In human prostate cancer cells, TIMP2 expression is frequently lost due to gene promoter methylation, which, in turn, contributes to tumor cell invasion [8]. Forced expression of TIMP2 in human lung cancer cells inhibits cell migration and invasion *in vitro*, while it blocks angiogenesis and induces apoptosis *in vivo* [9].

In this study, we used two human prostate cancer cell lines that stably express *RAD9* shRNA to evaluate expression of TIMP1 and TIMP2 in cell lysates and in conditioned media.

Results

We have shown previously that *RAD9* has a functional role in human prostate tumorigenesis and is associated with metastasis [10]. Furthermore, *RAD9* affects a number of *in vitro* characteristics of metastasis, such as cell motility, invasion, anoikis resistance, and anchorage-independent growth, as well as activation of tumor promoting signaling pathways, specifically ITGB1 expression and Akt activation [11].

As matrix metalloproteinases and their inhibitors are intimately involved in the process of tumor invasion, we analyzed expression levels of MMP2, MMP9, MMP8, and the inhibitors TIMP1 and TIMP2 in cell lysates and conditioned media. Although we observed no appreciable changes in the levels of MMPs, the abundance of TIMP1 and TIMP2 proteins in both the whole cell lysates, and the conditioned medium, was changed relative to *RAD9* levels.

RAD9 silencing causes decreased levels of TIMP1 in PC3 human prostate cancer cells.

We examined expression of TIMP1 and TIMP2 in PC3 cells. We observed that, unlike for DU145 cells (see below), TIMP1 and TIMP2 proteins were detected in both the whole cell lysates and the conditioned media from PC3 cells. Stable knock down of *RAD9* in PC3 cells (two clones) resulted in a dramatic reduction in TIMP1 protein levels in both the cell lysates and the conditioned medium (Fig. 1A). In contrast, TIMP2 protein levels did not change.

We also performed quantitative RT-PCR to examine mRNA levels of *TIMP1* in PC3 parental cells, or PC3 that stably express an insertless retroviral vector (sh*Control*) or sh*RAD9* (clone 1), and the results were normalized against expression of glyceraldehyde-3-phosphate dehydrogenase (*GAPDH*) mRNA. As shown in Fig. 1B, the *TIMP1* mRNA level in sh*RAD9* cells was reduced by approximately 80% compared with *TIMP1* mRNA from either parental or sh*Control* PC3 cells. Finally, besides decreased levels of TIMP1, *TIMP2* mRNA levels were increased in PC3/sh*RAD9* cells (not shown), although this increase did not translate into increased protein abundance in the cell lysates or the conditioned medium (Fig. 1A).

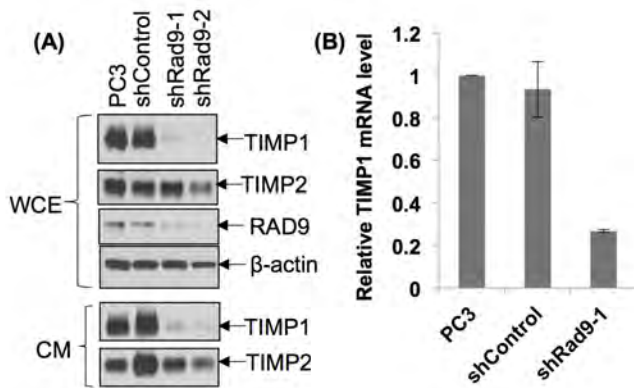


Figure 1. Depletion of *Rad9* in PC3 cells reduces TIMP1 protein abundance. (A) PC3 cells stably expressing Control or RAD9 (two clones) shRNA were assayed for TIMP1 and TIMP2 protein levels in cell lysates and conditioned media. RAD9 levels and β -actin (loading control) were immunodetected in the cell lysates. (B) Quantitative RT-PCR using RNA isolated from PC3/parental, PC3/shControl, and PC3/shRAD9-1. TIMP1 mRNA level was normalized against GAPDH mRNA abundance. CM: conditioned media; WCE: whole cell extracts.

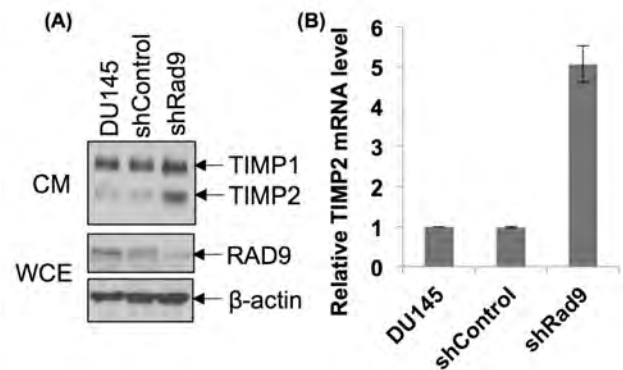


Figure 2. Depletion of *Rad9* in DU145 cells increases TIMP2 protein abundance. (A) DU145 cells stably expressing Control or RAD9 shRNA were assayed for TIMP1 and TIMP2 protein levels in the conditioned media. RAD9 levels and β -actin (loading control) were immunodetected in the cell lysates. (B) Quantitative RT-PCR using RNA isolated from DU145/parental, DU145/shControl, and DU145/shRAD9. TIMP2 mRNA level was normalized against GAPDH mRNA abundance. CM: conditioned media; WCE: whole cell extracts.

Targeted reduction of endogenous RAD9 levels in DU145 human prostate cancer cells causes increased levels of TIMP2.

We also examined expression of TIMP1 and TIMP2 in DU145 cells. TIMP2 protein levels were very low and only detected in the conditioned medium from DU145 cells, whereas the protein was barely detectable in the cell lysates. When RAD9 expression was suppressed by shRNA, however, there was a substantial increase in the levels of secreted TIMP2 (Fig. 2A). In contrast, TIMP1 levels did not change appreciably in the conditioned medium in these cells.

We carried out quantitative RT-PCR to examine mRNA levels of *TIMP2* in DU145 parental cell lines, or DU145 that stably express an insertless retroviral vector or *shRAD9* and the results were normalized against expression of *GAPDH* mRNA. As shown in Fig. 2B, the *TIMP2* mRNA level was increased approximately 5-fold compared with levels of *TIMP2* mRNA from either parental or *shControl* DU145 cells.

Conclusions

We provide *in vitro* evidence that supports the association of RAD9 with TIMP1 and TIMP2 in PC3 and DU145 prostate cancer cell lines. Silencing of RAD9 increases tumor-suppressive TIMP2 levels in DU145 cells, whereas RAD9 downregulation in PC3 cells results in reduction of tumor-promoting TIMP1 levels. RAD9 controls expression of these proteins at both the mRNA and protein levels. Future studies will determine (1) how RAD9 controls TIMP1 and TIMP2 gene expression, and (2) what is the contribution of TIMP1 and TIMP2 to RAD9-induced cell motility and invasion, as well as anoikis resistance.

References

1. Stetler-Stevenson WG. (2008). Tissue inhibitors of metalloproteinases in cell signaling: metalloproteinase-independent biological activities. *Sci Signal.* 1(27):re6.
2. Ries C. (2014). Cytokine functions of TIMP1. *Cell Mol Life Sci.* 71(4):659-72.
3. Toricelli M, Melo FH, Peres GB, Silva DC, Jasiulionis MG. (2013). Timp1 interacts with beta-1 integrin and CD63 along melanoma genesis and confers anoikis resistance by activating PI3-K signaling pathway independently of Akt phosphorylation. *Mol Cancer* 12:22.
4. Gilbert LA, Hemann MT. (2010). DNA damage-mediated induction of a chemoresistant niche. *Cell.* 143(3):355-66.
5. Gong Y, Scott E, Lu R, Xu Y, Oh WK, Yu Q. (2013). TIMP1 promotes accumulation of cancer associated fibroblasts and cancer progression. *PLoS One.* 8(10):e77366.
6. Gong Y, Chippada-Venkata UD, Galsky MD, Huang J, Oh WK. (2015). Elevated circulating tissue inhibitor of metalloproteinase 1 (TIMP1) levels are associated with neuroendocrine differentiation in castration resistant prostate cancer. *Prostate.* doi: 10.1002/pros.22945.
7. Seo DW, Li H, Guedez L, Wingfield PT, Diaz T, Salloum R, Wei BY, Stetler-Stevenson WG. (2003). TIMP2 mediated inhibition of angiogenesis: an MMP-independent mechanism. *Cell.* 114(2):171-80.
8. Hsu CH, Peng KL, Kang ML, Chen YR, Yang YC, Tsai CH, Chu CS, Jeng YM, Chen YT, Lin FM,

- Huang HD, Lu YY, Teng YC, Lin ST, Lin RK, Tang FM, Lee SB, Hsu HM, Yu JC, Hsiao PW, Juan LJ. (2012). TET1 suppresses cancer invasion by activating the tissue inhibitors of metalloproteinases. *Cell Rep.* 2(3):568-79.
9. Bourbouli D, Han H, Jensen-Taubman S, Gavil N, Isaac B, Wei B, Neckers L, Stetler-Stevenson WG. (2013). TIMP2 modulates cancer cell transcriptional profile and enhances E-cadherin / beta-catenin

complex expression in A549 lung cancer cells. *Oncotarget.* 4(1):163-73.

10. Zhu A, Zhang CX, Lieberman HB. (2008). Rad9 has a functional role in human prostate carcinogenesis. *Cancer Res.* 68(5):1267-74.
11. Broustas CG, Zhu A, Lieberman HB. (2012). Rad9 protein contributes to prostate tumor progression by promoting cell migration and anoikis resistance. *J Biol Chem* 287(49):41324-41333. ■

RAD9 Enhances Base Excision Repair by Regulating Neil1 Glycosylase

Sunil K. Panigrahi, Kevin M. Hopkins, and Howard B. Lieberman

Introduction

Base excision repair (BER) is an evolutionarily conserved process that mends a wide range of nucleotide alterations, including abasic sites [1]. BER is initiated by a DNA glycosylase, a small monomeric protein that removes damaged nitrogenous bases by catalyzing hydrolysis of the N-glycosidic bond [2]. Mammalian DNA glycosylases are classified into two families: 1) Fpg/Nei, and 2) Nth. In mammals, three Fpg/Nei family members have been identified, namely NEIL1, NEIL2 and NEIL3 [3]. NEIL1 and NEIL2 are well-characterized biochemically. Both are bi-functional enzymes that incise damaged DNA by β , δ -elimination, and also are involved in an APE1-independent BER pathway [4]. NEIL3 is a mono-functional enzyme and has only β -elimination incision activity [5]. NEIL1 prefers duplex DNA structures whereas both NEIL2 and NEIL3 prefer single stranded DNA or forks as substrate [3]. NEIL1 interacts with many DNA replication proteins and is involved in removal of DNA lesions during replication [4, 6, 7]. However, NEIL2 participates in transcription-coupled repair due to its preference for single stranded DNA and interaction with RNA polymerase II, along with many transcription factors [8]. As compared to NEIL2 and NEIL3, NEIL1 recognizes a wide variety of lesions and is responsible for repairing a diverse set of DNA modifications, including base oxidation and apurination.

The RAD9-HUS1-RAD1 (9-1-1) heterotrimeric protein complex is loaded onto chromatin by the RAD17-Replication factor C (RFC) clamp loader when DNA damage is incurred [9]. RAD9 is a multi-functional protein that interacts with several DNA repair proteins either as part of 9-1-1 or independently [10]. Unlike RAD1 or HUS1, RAD9 can also function as a transcriptional activator for specific downstream target genes [11]. Furthermore, RAD9 participates in most DNA

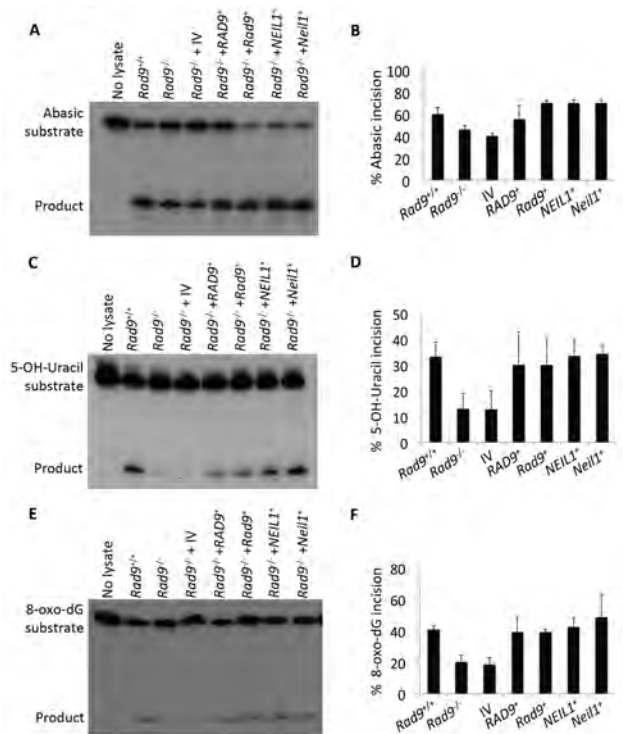


Figure 1. Glycosylase activity on different substrates in extracts from mES cells with varying Rad9 and Neil1 status. Glycosylase activity (incision) was measured by an *in vitro* assay using a 24-mer oligo substrate containing either abasic (A, B), 5-OH-Uracil (C, D) or 8-oxo-dG (E, F) modifications, coupled with extracts from mES cells, either Rad9^{+/+}, Rad9^{-/-}, or the latter with insertless pCMV6-AC-DDK-His vector (IV), or ectopically expressing RAD9⁺, Rad9⁺, NEIL1⁺, or Neil1⁺. Panels A, C, E: *in vitro* incision assay showing 24-mer oligo substrate and 10-mer product. Average percent incision from three independent experiments shown in panels B, D, F; error bars, standard deviation.

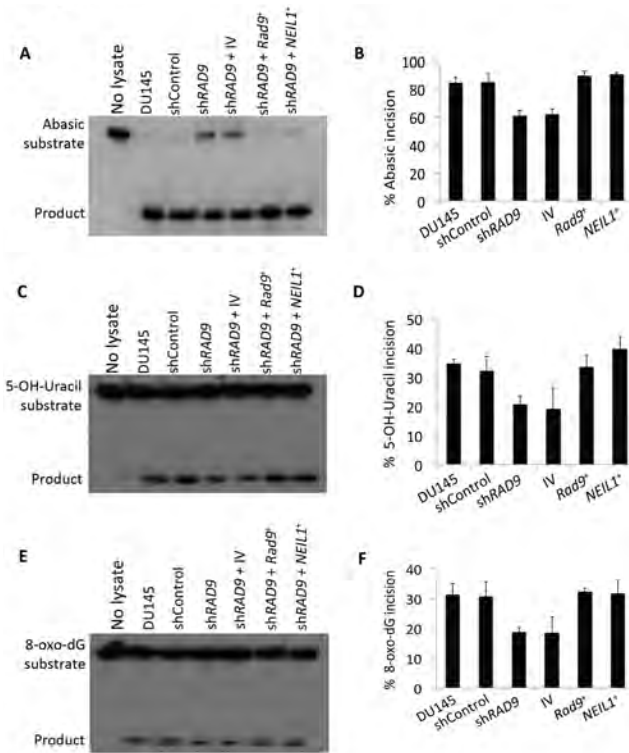


Figure 2. DU145 cells lacking RAD9 have less efficient glycosylase activity. Glycosylase activity (incision) was measured by an *in vitro* assay using a 24-mer oligo containing either abasic (A, B), 5-OH-Uracil (C, D) or 8-oxo-dG (E, F) modifications, coupled with extracts from parental DU145 cells or those with shControl or shRAD9, and the latter with insertless pCMV6-AC-DDK-His vector (IV), or ectopically expressing Rad9⁺ or NEIL1⁺. Denatured polyacrylamide gels showing *in vitro* incision assay (A, C, E); 24-mer is substrate and the 10-mer is product. Average percent incision of substrate from three independent experiments is illustrated (B, D, F); error bars represent standard deviation.

repair mechanisms, including BER [12], nucleotide excision repair [13], mismatch repair [14] and homologous recombination repair [15]. For BER, the 9-1-1 complex, and also RAD9, independently interact with the NEIL1 protein, resulting in the stimulation of NEIL1 activity [16].

In a previous report [17], we demonstrated that Rad9 is required for Neil1 protein stability in mouse ES cells, whereas it regulates NEIL1 expression at the transcriptional level by promoter binding in human prostate cancer cells. RAD9 deficient cells are sensitive to UV and menadione. Herein we provide evidence that NEIL1 glycosylase/lyase activity is lowered in RAD9 deficient cells, and is restored by ectopic expression of either RAD9 or NEIL1.

Results

Glycosylase activity (incision) on oligonucleotides containing single base modifications in mES and DU145 whole cell extracts. We reported before that RAD9 is responsible for NEIL1 regulation, and cells with reduced levels of either protein are more sensitive to several DNA

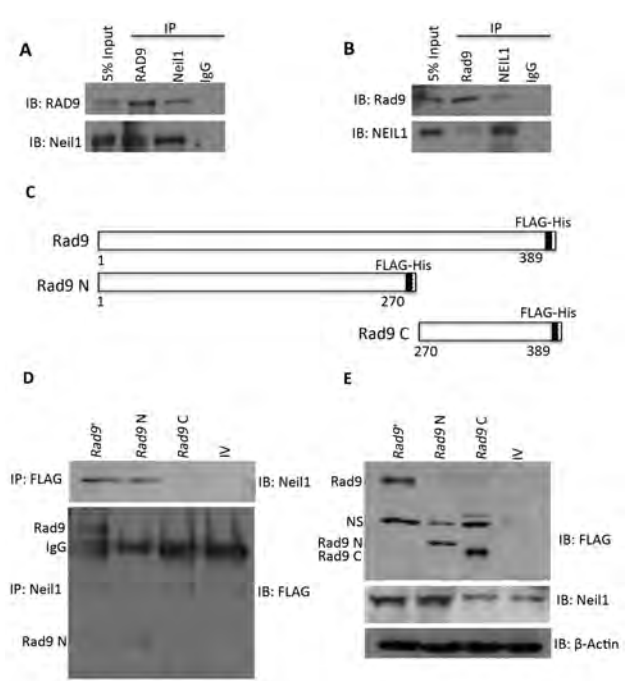


Figure 3. Deletion analysis used to determine the region of mouse Rad9 protein involved in Rad9-Neil1 binding. (A) Ectopically expressed RAD9 and endogenous Neil1 were immunoprecipitated from Rad9^{-/-} mES cells individually and tested for binding to the other. (B) Same as A, but in DU145-shRAD9 cells ectopically expressing FLAG-Rad9 (C) Graphic depiction of amino acids encoded by inherent or truncated Rad9 cloned into pCMV6-AC-DDK-His vector; numbers represent the amino acid positions. Rad9, full length; Rad9 N, amino-end fragment; Rad9 C, carboxy-end fragment. (D) Interaction of intact or deletion mutants of Rad9 to Neil1, shown by immunoprecipitation either with anti-FLAG (upper panel) or anti-Neil1 (lower panel) antibody. (E) Immunoblot showing abundance of Rad9 and Neil1 proteins in whole cell extracts from IP experiments in panel B. β-Actin was used as a loading control. Rad9 N, amino-terminal fragment; Rad9 C, carboxy-terminal fragment; NS, non-specific; IP, Immunoprecipitation; IB, Immunoblot.

damaging agents, relative to controls. We next tested whether, as predicted, glycosylase activity is reduced in RAD9 deficient cells. We performed an *in vitro* incision assay using extracts from various cell lines and a double stranded 24-mer oligonucleotide substrate, with any of the following modifications (abasic/apurinic, 5-OH-Uracil and 8-oxo-dG) at position 10. Incision activity on the substrates with an abasic site (Figure 1A, B), 5-OH-Uracil (Figure 1C, D), or 8-oxo-dG (Figure 1E, F) is lower in Rad9^{-/-} mES cells, compared to the Rad9^{+/+} control. Ectopically expressing RAD9/Rad9 or NEIL1/Neil1 restored incision activity to the Rad9^{-/-} mES cell extracts. Pooling the data from three independent trials, we observed that mES cells lacking Rad9 showed a 25% decrease in abasic site incision, a 60% decrease in 5-OH-Uracil site incision, and a 50% decrease in 8-oxo-dG site incision (Figure 1B, D, F, respectively). A similar pattern of incision activity was also demonstrated in DU145 cell extracts with different RAD9/Rad9 or NEIL1 expression

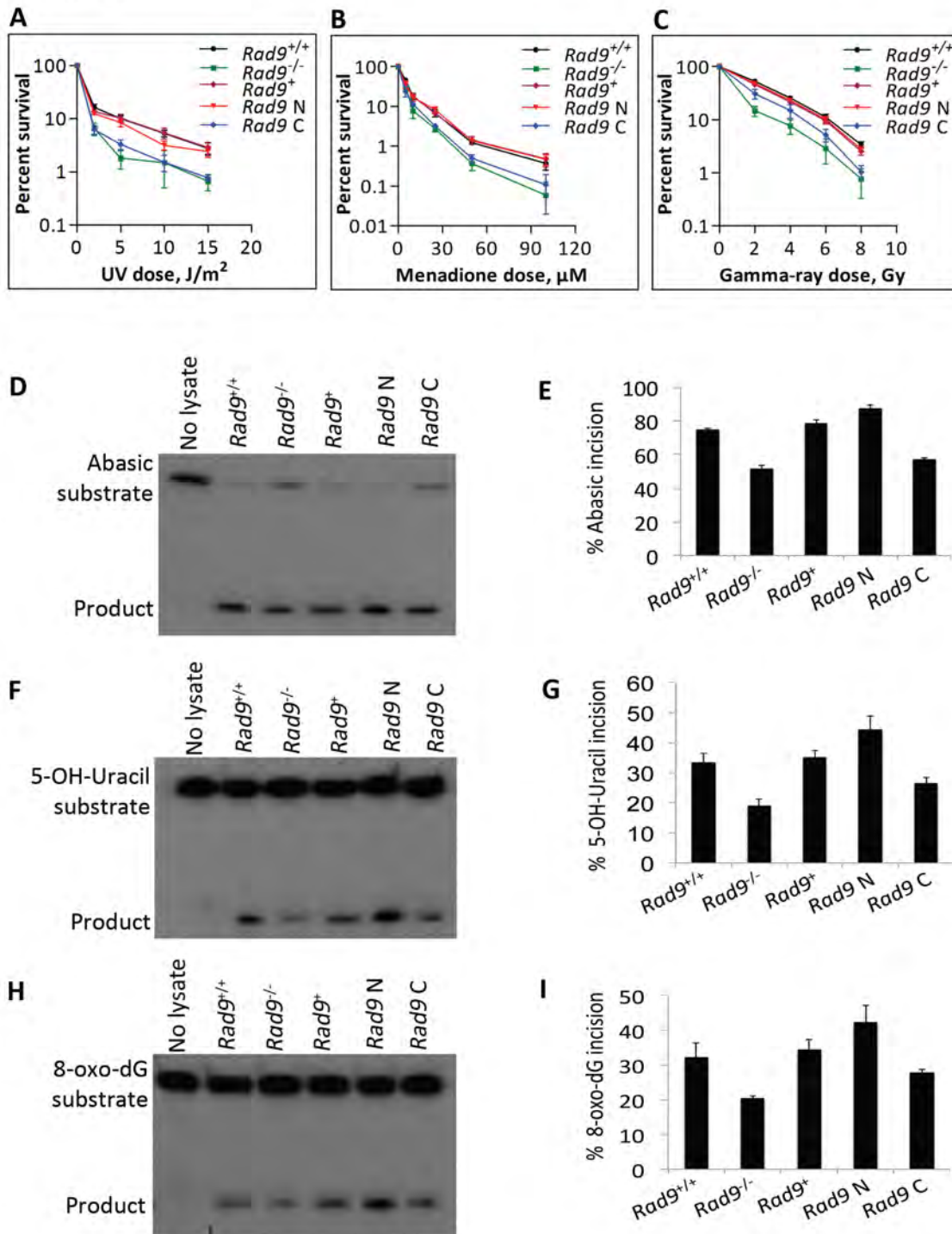


Figure 4. The N-terminal region of Rad9 is important for conferring DNA damage resistance and efficient glycosylase activity to mES cells. Cell survival after exposure to (A) 254 nm UV light, (B) menadione, and (C) gamma rays. Cells: mES cells bearing Rad9^{+/+}, Rad9^{-/-}, and the latter ectopically expressing Rad9⁺, Rad9^N or Rad9^C. Points are the average of three independent trials, each with duplicate dishes; error bars represent standard deviation. Glycosylase activity (incision) was measured by an in vitro assay using a 24-mer oligo substrate containing either abasic (D, E), 5-OH-Uracil (F, G) or 8-oxo-dG (H, I) modifications in extracts from Rad9^{+/+} or Rad9^{-/-} mES cells or the latter containing Rad9⁺, Rad9^N or Rad9^C. Panels D, F, H; denatured polyacrylamide gel showing in vitro incision of the 24-mer substrate and the resulting 10-mer product. The average percent incision of substrate from three independent experiments is shown in panels E, G and I. Error bars, standard deviation.

levels (Figure 2). DU145 cells expressing shRNA against RAD9 showed a 29% decrease in incision at the abasic site, a 60% decrease at 5-OH-Uracil, and a 43% decrease at 8-oxo-dG, relative to controls (Figure 2B, D, F,

respectively). These results suggest that the absence of Rad9/RAD9 causes a reduction in Neil1/NEIL1 protein levels and that leads to defective BER, as well as enhanced sensitivity to certain DNA damaging agents.

N terminal region of Rad9 interacts with Neil1. NEIL1 is known to interact with the RAD9-HUS1-RAD1 complex, as well as with each component individually [16]. The cross species interactions of NEIL1-Rad9 and Neil1-RAD9 were further demonstrated by co-immunoprecipitation (Figure 3A, B). A stronger interaction was observed in mES cells as compared to DU145 cells, suggesting that the mouse cells might contain some additional factors needed for enhancing this interaction. It was reported that the C-terminal region of NEIL1 is involved in RAD9-NEIL1 binding [16], and another study revealed that it is involved in intramolecular interactions that promote NEIL1 stability [18]. Therefore, we sought to identify the region of Rad9 involved in this interaction. We ectopically expressed full-length mouse *Rad9* (*Rad9*⁺), as well as the N-terminal encoding 1-270 aa (*Rad9* N), and the C-terminal encoding 270-389 aa (*Rad9* C) in *Rad9*^{-/-} mES cells such that each had a FLAG and His tag at its C-terminal end (Figure 3C). By immunoprecipitation, either with anti-FLAG M2 beads or anti-Neil1 antibody, we found that both *Rad9*⁺ and *Rad9* N, but not *Rad9* C, are engaged in the *Rad9*-Neil1 interaction (Figure 3D). Next, we asked whether this interaction has any effect on Neil1 stability and sensitivity of cells to DNA damaging agents. A 60% decrease in Neil1 protein level was observed in cells bearing *Rad9* C, compared to those having *Rad9*⁺ or *Rad9* N (Figure 3E). As assessed by colony formation, cells producing *Rad9* N, relative to those containing *Rad9* C, are more resistant to UV (Figure 4A), menadione (Figure 4B) and gamma rays (Figure 4C), and nearly equal to wild-type control levels. Using an *in vitro* incision assay coupled with substrates bearing abasic (Figure 4D, E), 5-OH-Uracil (Figure 4F, G), or 8-oxo-dG (Figure 4H, I) sites, we demonstrated that cells expressing *Rad9* N have higher activity than those with *Rad9*⁺ or *Rad9* C (Figure 4D, F, H). By densitometry quantitation of gel bands from three independent trials and calculating the averages, we found a greater increase in incision activity in *Rad9* N bearing *Rad9*^{-/-} cells, relative to those with *Rad9*⁺, or the *Rad9*^{+/+} cells (14% at the abasic site, 33% at 5-OH-Uracil, 27% at 8-oxo-dG substrates; Figure 4E, G, I). Cells expressing *Rad9* C showed a much more modest increase in incision activity relative to *Rad9*^{-/-} cells.

Conclusion

In summary, we show that RAD9 deficiency increases sensitivity of mammalian cells to a variety of DNA damaging agents, and ectopic expression of RAD9 or NEIL1 restored resistance. This is correlated with the *in vitro* glycosylase/lyase activity seen in the above cells. These results indicate that RAD9 participates in the base excision repair pathway not only by interacting with NEIL1 but also by regulating NEIL1 protein abundance. It is important to define these mechanisms in more detail, and how they coordinate with other functions of RAD9 in cell cycle checkpoint control and apoptosis, as the cellular response to DNA damage is critical for determining

whether carcinogenesis or other deleterious events will ensue.

References

- Wallace, S.S. (2014) Base excision repair: a critical player in many games. *DNA Repair (Amst)*, **19**, 14-26.
- Wallace, S.S. (2013) DNA glycosylases search for and remove oxidized DNA bases. *Environ Mol Mutagen*, **54**, 691-704.
- Liu, M., Doublet, S. and Wallace, S.S. (2013) Neil3, the final frontier for the DNA glycosylases that recognize oxidative damage. *Mutat Res*, **743-744**, 4-11.
- Wiederhold, L., Leppard, J.B., Kedar, P., Karimi-Busheri, F., Rasouli-Nia, A., Weinfeld, M., Tomkinson, A.E., Izumi, T., Prasad, R., Wilson, S.H. *et al.* (2004) AP endonuclease-independent DNA base excision repair in human cells. *Mol Cell*, **15**, 209-220.
- Krokeide, S.Z., Laerdahl, J.K., Salah, M., Luna, L., Cederkvist, F.H., Fleming, A.M., Burrows, C.J., Dalhus, B. and Bjoras, M. (2013) Human NEIL3 is mainly a monofunctional DNA glycosylase removing spiroimindiohydantoin and guanidinohydantoin. *DNA Repair (Amst)*, **12**, 1159-1164.
- Theriot, C.A., Hegde, M.L., Hazra, T.K. and Mitra, S. (2010) RPA physically interacts with the human DNA glycosylase NEIL1 to regulate excision of oxidative DNA base damage in primer-template structures. *DNA Repair (Amst)*, **9**, 643-652.
- Hegde, M.L., Theriot, C.A., Das, A., Hegde, P.M., Guo, Z., Gary, R.K., Hazra, T.K., Shen, B. and Mitra, S. (2008) Physical and functional interaction between human oxidized base-specific DNA glycosylase NEIL1 and flap endonuclease 1. *J Biol Chem*, **283**, 27028-27037.
- Banerjee, D., Mandal, S.M., Das, A., Hegde, M.L., Das, S., Bhakat, K.K., Boldogh, I., Sarkar, P.S., Mitra, S. and Hazra, T.K. (2011) Preferential repair of oxidized base damage in the transcribed genes of mammalian cells. *J Biol Chem*, **286**, 6006-6016.
- Parrilla-Castellar, E.R., Arlander, S.J. and Karnitz, L. (2004) Dial 9-1-1 for DNA damage: the Rad9-Hus1-Rad1 (9-1-1) clamp complex. *DNA Repair (Amst)*, **3**, 1009-1014.
- Broustas, C.G. and Lieberman, H.B. (2012) Contributions of Rad9 to tumorigenesis. *J Cell Biochem*, **113**, 742-751.
- Lieberman, H.B. and Yin, Y. (2004) A novel function for human Rad9 protein as a transcriptional activator of gene expression. *Cell Cycle*, **3**, 1008-1010.
- Wang, W., Brandt, P., Rossi, M.L., Lindsey-Boltz, L., Podust, V., Fanning, E., Sancar, A. and Bambara, R.A. (2004) The human Rad9-Rad1-Hus1 checkpoint

- complex stimulates flap endonuclease 1. *Proc Natl Acad Sci U S A*, **101**, 16762-16767.
13. Li, T., Wang, Z., Zhao, Y., He, W., An, L., Liu, S., Liu, Y., Wang, H. and Hang, H. (2013) Checkpoint protein Rad9 plays an important role in nucleotide excision repair. *DNA Repair (Amst)*, **12**, 284-292.
 14. He, W., Zhao, Y., Zhang, C., An, L., Hu, Z., Liu, Y., Han, L., Bi, L., Xie, Z., Xue, P. *et al.* (2008) Rad9 plays an important role in DNA mismatch repair through physical interaction with MLH1. *Nucleic Acids Res*, **36**, 6406-6417.
 15. Pandita, R.K., Sharma, G.G., Laszlo, A., Hopkins, K.M., Davey, S., Chakhparonian, M., Gupta, A., Wellinger, R.J., Zhang, J., Powell, S.N. *et al.* (2006) Mammalian Rad9 plays a role in telomere stability, S- and G2-phase-specific cell survival, and homologous recombinational repair. *Mol Cell Biol*, **26**, 1850-1864.
 16. Guan, X., Bai, H., Shi, G., Theriot, C.A., Hazra, T.K., Mitra, S. and Lu, A.L. (2007) The human checkpoint sensor Rad9-Rad1-Hus1 interacts with and stimulates NEIL1 glycosylase. *Nucleic Acids Res*, **35**, 2463-2472.
 17. Panigrahi SK, Hopkins KM, and Lieberman HB. (2014) Regulation of Neil1 Expression by Rad9 is Context Dependent. *Center for Radiological Research 2013 Annual Report*. pp. 33-35.
 18. Hegde, M.L., Tsutakawa, S.E., Hegde, P.M., Holthausen, L.M., Li, J., Oezguen, N., Hilser, V.J., Tainer, J.A. and Mitra, S. (2013) The disordered C-terminal domain of human DNA glycosylase NEIL1 contributes to its stability via intramolecular interactions. *J Mol Biol*, **425**, 2359-2371. ■

Effects of BET Bromodomain Inhibitor JQ1 on Radiosensitivity of Prostate Cancer Cell Lines

Enyuan Shang, Hongning Zhou, and Tom Hei

Cancer is one of the most devastating diseases. In the search for the next generation of drugs to treat cancer, epigenetic regulatory machineries are emerging as new targets. Based on their effects on epigenetic modifications, the epigenetic regulatory proteins can be divided into three groups: epigenetic writers that add epigenetic modifications, erasers that remove the modifications, and readers that interpret the epigenetic code.

BET (Bromodomain and Extra Terminal domain) bromodomain-containing proteins [1] are epigenetic readers, which interact with sequence specific transcription factors, the mediator complex, RNA polymerase II, transcription elongation factors, chromatin remodeling complexes, and acetylated histones to form super enhancers around genes essential for specialized cellular function or cell identity [2, 3]. BET proteins are characterized by the presence of double bromodomains in the N-terminal end, which bind acetyl lysines in histones and transcription factors, and a region of homology at the carboxy-terminal end referred to as the ET domain. There are four members of the BET family in humans, BRD2, BRD3, BRD4, and BRDT, and they serve various essential cellular functions. For example, BRD4 regulates the self-renewal ability and pluripotency of embryonic stem cells through forming super enhancers around core stem cell genes such as OCT4 [4]; while in endothelial

cells, BRD4 interacts with NF- κ B during inflammation initiation to form super enhancers to drive canonical genes of the inflammatory response [5]. The super-enhancer is a new concept introduced to describe chromatin regions that are extraordinarily large and are densely occupied by multiple core transcription factors that determine cell identities [2, 6]. It has been proposed that a set of core transcription factors establish a self-enhancing gene expression circuit through forming super-enhancers on their own genes and other cell type specific genes to determine cell identity [2, 4]. BET family members have been found as key cofactors in these super-enhancers [4, 6].

BET bromodomain proteins are also involved in the maintenance of cancer cells identities. It has been proposed that cancer cells' identities are determined by super-enhancer networks [2]. Recently, a group of small molecules that can disrupt the interaction between BET bromodomains and acetyl lysines in transcription factors and histones, the so-called BET bromodomain inhibitors, have been discovered. Using these BET bromodomain inhibitors as tools, it is confirmed that BET proteins have critical roles in the proliferation and survival of a broad spectrum of cancer types [3], for example, castration-resistant prostate cancer [7], basal-like breast cancer [8], melanoma [9], and glioblastoma [10]. This group of small

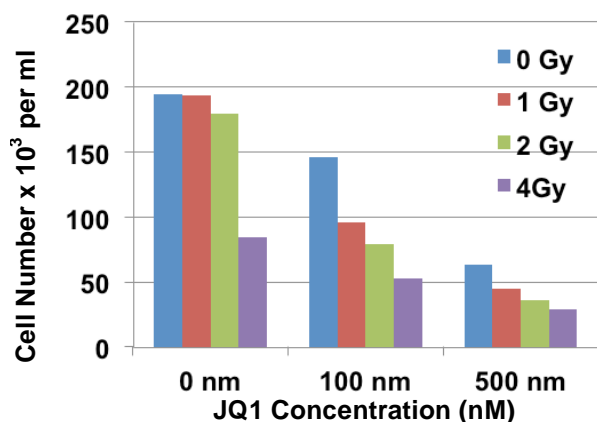


Figure 1. LNCaP cells treated with JQ1 in combination with X-ray irradiation.

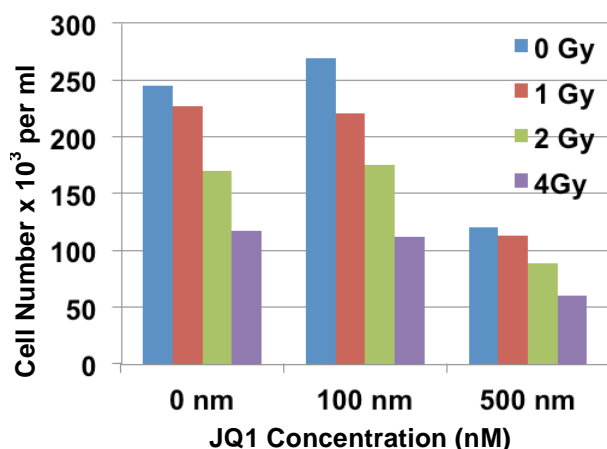


Figure 2. PC3 cells treated with JQ1 in combination with X-ray irradiation.

molecules has the potential to become the next generation of drugs for cancer treatment. For high-risk breast and prostate cancer patients, radiation therapy is often combined with chemotherapy as adjuvant treatment. To test whether these BET bromodomain inhibitors can synergize with radiation to suppress cancer cell growth, we treated prostate cancer cell lines LNCaP and PC3 with JQ1, one of the first of these inhibitors discovered, in combination with X-rays and found that JQ1 has additive effects with radiation in suppressing proliferation of these cell lines (Figure 1 and Figure 2).

The cells were plated at 3×10^4 /ml one day before X-ray irradiation. We first added JQ1 into the culture media at 100 nm and 500 nm concentrations. Four hours later,

the cells were irradiated at doses of 1 Gy, 2 Gy, and 4 Gy. The cells were cultured for four days with the drug remaining in the media and then the cell numbers were counted. Figure 1 shows that JQ1 treatment and X-ray radiation have an additive effect in LNCaP cells: a single 4 Gy X-ray irradiation reduced cell proliferation by half, when combined with 500 nm JQ1, it further reduced the cell number more than 50%. Figure 2 shows a similar effect in PC3 cells, in which JQ1 is less effective. At 100 nm concentration, no difference in radiation response was observed between control and JQ1-treated PC3 cells.

References

1. Florence, B. and D.V. Faller, *You bet-cha: a novel family of transcriptional regulators*. Front Biosci, 2001. **6**: p. D1008-18.
2. Hnisz, D., et al., *Super-enhancers in the control of cell identity and disease*. Cell, 2013. **155**(4): p. 934-47.
3. Shi, J. and C.R. Vakoc, *The mechanisms behind the therapeutic activity of BET bromodomain inhibition*. Mol Cell, 2014. **54**(5): p. 728-36.
4. Whyte, W.A., et al., *Master transcription factors and mediator establish super-enhancers at key cell identity genes*. Cell, 2013. **153**(2): p. 307-19.
5. Brown, J.D., et al., *NF-kappaB Directs Dynamic Super Enhancer Formation in Inflammation and Atherogenesis*. Mol Cell, 2014. **56**(2): p. 219-31.
6. Di Micco, R., et al., *Control of embryonic stem cell identity by BRD4-dependent transcriptional elongation of super-enhancer-associated pluripotency genes*. Cell Rep, 2014. **9**(1): p. 234-47.
7. Asangani, I.A., et al., *Therapeutic targeting of BET bromodomain proteins in castration-resistant prostate cancer*. Nature, 2014. **510**(7504): p. 278-82.
8. Shi, J., et al., *Disrupting the interaction of BRD4 with diacetylated Twist suppresses tumorigenesis in basal-like breast cancer*. Cancer Cell, 2014. **25**(2): p. 210-25.
9. Segura, M.F., et al., *BRD4 sustains melanoma proliferation and represents a new target for epigenetic therapy*. Cancer Res, 2013. **73**(20): p. 6264-76.
10. Pastori, C., et al., *BET bromodomain proteins are required for glioblastoma cell proliferation*. Epigenetics, 2014. **9**(4): p. 611-20. ■

Knockdown of DNA Repair Gene Expression in Mouse Embryonic Stem Cells Proficient or Deficient in mRad9

Li Wang, Kevin M. Hopkins, and Howard B. Lieberman

The maintenance of genome stability is a fundamental aspect of all life. In order to maintain stability, a significant percentage of genomes encode DNA repair, cell cycle checkpoint and other DNA damage tolerance proteins that act in multiple complexes and interrelated pathways. Rad9 is required for maintaining genome stability. Rad9 possesses a C-terminal tail that is

phosphorylated constitutively, and the protein participates in multiple cell cycle phase checkpoints, apoptosis, and DNA repair, including base excision repair, nucleotide excision repair, homologous recombination repair and mismatch repair. The checkpoint sliding clamp heterotrimeric Rad9/Hus1/Rad1 (9-1-1) complex acts as a versatile scaffold in the coordinated recruitment of

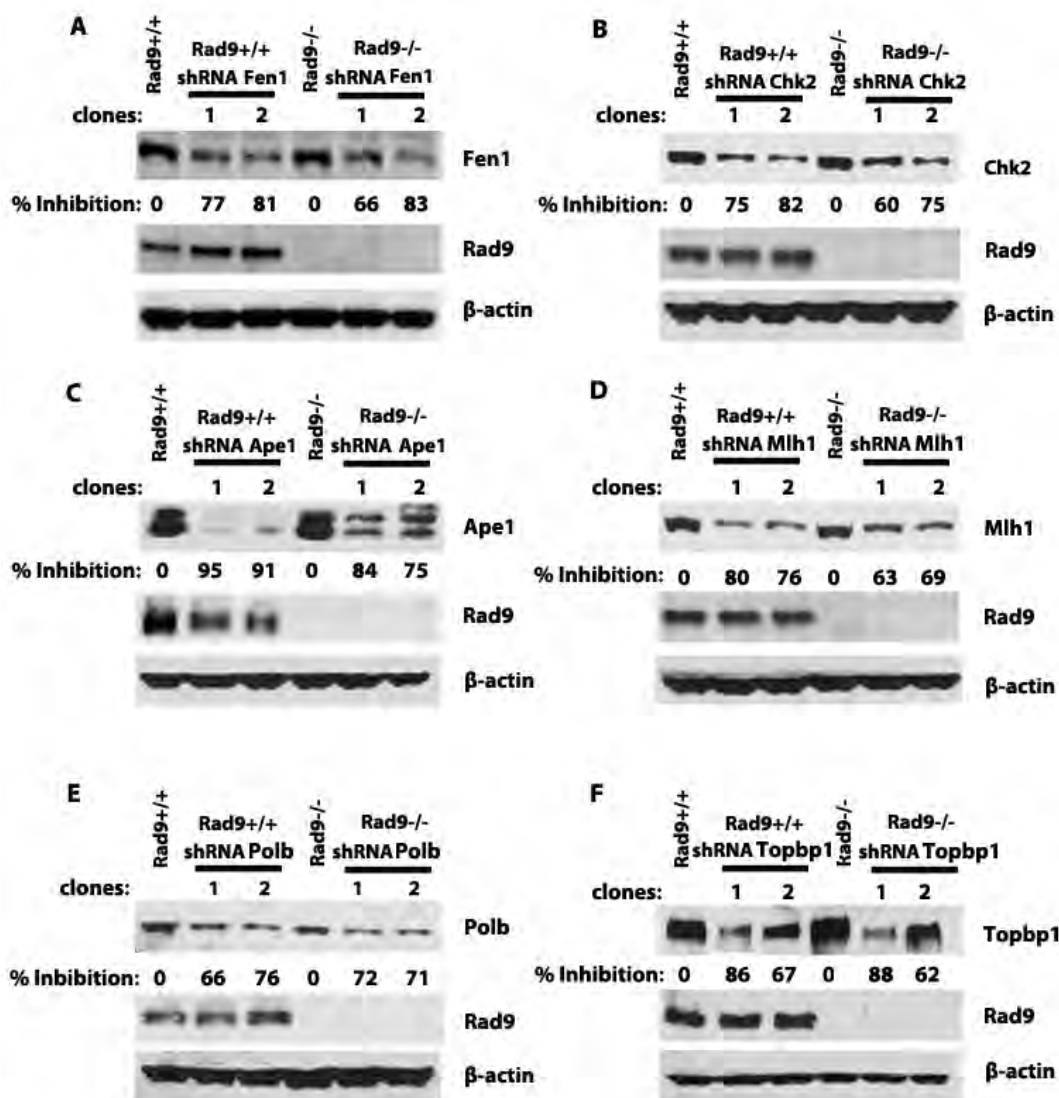


Figure 1. Western blot analysis of DNA repair proteins in mouse embryonic stem cells proficient or deficient in Rad9 were stably transfected with target shRNA or vector control. Lanes 1 and 4 were transfected with control shRNA, lanes 2, 3, 5, and 6 are stable clones transfected with specific DNA repair gene shRNA. Western blot analysis was performed using antibodies against Rad9 and β-actin as well as A) Fen1 B) Chk2 C) Ape1 D) Mlh1 E) Polb F) Topbp1. Image J was used to quantify the level of protein after knockdown. % Inhibition indicates the percentage of knockdown found for the shRNA target gene relative to β-actin levels and untreated control cells.

proteins involved in DNA replication, cell cycle checkpoint control, and DNA repair. Despite the tremendous progress that has been made in deciphering the biochemical functions of the 9–1–1 complex and the in-depth understanding of the signals that lead to the loading of 9–1–1 onto DNA, as well as demonstration that Rad9 interacts with many DNA repair related proteins, the biochemical function and details of the interactions between Rad9 and Rad9-binding proteins in DNA repair are still unclear.

In this study, we have individually established Fen1, Chk2, Ape1, Mlh1, Polb or Topbp1 short hairpin RNA (shRNA) stable cell lines to knock down respective expression of the genes in mouse ES cells either proficient or null for mRad9. Wild type or null mRad9 ES cells stably transfected with a specific shRNA for these

genes or control shRNA were established as follows: selectable expression vectors corresponding to each of the target genes or nontarget control was obtained (Sigma-Aldrich), transfected into ES or null mRad9 ES cells, then puromycin-resistant clones expressing the target shRNA were selected. The target protein and Rad9 levels were analyzed by western blotting; β -actin served as a loading control (Figure 1).

In continuing studies, stable cell lines will be treated with DNA damaging agents to test for any differences between the mRad9 deleted cells and the double deficient cells with regard to cell survival and other DNA damage response parameters. These studies will assess, via an epistasis-like approach, whether Rad9 interacts functionally with any of the DNA damage response proteins to promote cell survival. ■

Expression and Purification of the hRAD9(1-272 aa) Flag -hHUS1-hRAD1 Protein Complex

Li Wang and Howard B. Lieberman

DNA damage is a common event and can lead to mutation or deletion within chromosomal DNA, which may cause cancer, or cellular or organismic death. Cellular DNA damage activates cell cycle checkpoints, leading to a delay or arrest in cell cycle progression to prevent replication and the induction of further DNA damage. This allows for repair and prevention of the transmission of damaged or incompletely replicated chromosomes to progeny. Previous studies have demonstrated that Rad9, Hus1, and Rad1 can bind as a heterotrimeric complex (9-1-1), which resembles a PCNA-like sliding clamp and plays dual roles in cell cycle checkpoint activation and DNA repair in eukaryotic cells. The Rad9-Rad1-Hus1 complex is specifically loaded at the junction between duplex DNA and single-stranded DNA coated by multiple copies of the ssDNA binding complex RPA [1]. The DNA-bound 9-1-1 complex then facilitates ATR-mediated phosphorylation and activation of Chk1, a protein kinase that regulates S-phase progression, G2/M arrest, and replication fork stabilization. In addition to its role in checkpoint activation, much evidence suggests that the 9-1-1 complex also participates in DNA repair. The N-terminal region of Rad9 (1–270 amino acids) is essential for sensing DNA damage by forming a complex with Hus1 and Rad1. Electrophoretic mobility shift assay (EMSA) showed that full length 9–1–1 failed to interact with linear duplex DNA. However, the 9^{1–272}–1–1 complex with truncated Rad9 (residues 1–272) did form a stable

complex with duplex DNA [2]. Based on this information, we co-expressed and purified a truncated hRAD9 (residues 1–272), full-length hRAD1, and full-length hHUS1, which are able to form a heterotrimer. The complex will be used to characterize biochemical functions in vitro.

We made the heterotrimeric proteins as follows. Recombinant baculoviruses encoding Flag-tagged hRAD9(1-272aa) and untagged hHUS1 and hRAD1 were generated using the Bac-to-Bac expression system (Life Technologies, Inc.). The coding region of hRAD9(1-272aa) was PCR amplified and ligated into BamHI and XhoI linearized pFasBac baculoviral transfer vector. hHUS1 cDNA was excised out of pZeo-hHUS1 plasmid as a BamHI-EcoRI fragment before inserting into BamHI and EcoRI linearized pFasBac baculoviral transfer vector. The coding region of hRAD1 was PCR amplified and ligated into BamHI and EcoRI linearized pFasBac baculoviral transfer vector. All cloned PCR products were confirmed by sequencing. Transfer vectors were then transformed into DH10Bac *E. coli* and selected for recombination between the transfer vector and the bacterial bacmid plasmid using an in-plate β -galactosidase assay. Recombined bacmids were transfected into Sf9 cells using CellFectin reagent and viral supernatants were harvested after 3 days. hRAD9, hHUS1, and hRAD1 protein abundance was verified by immunoblotting cell lysates from infected Sf9 cells.

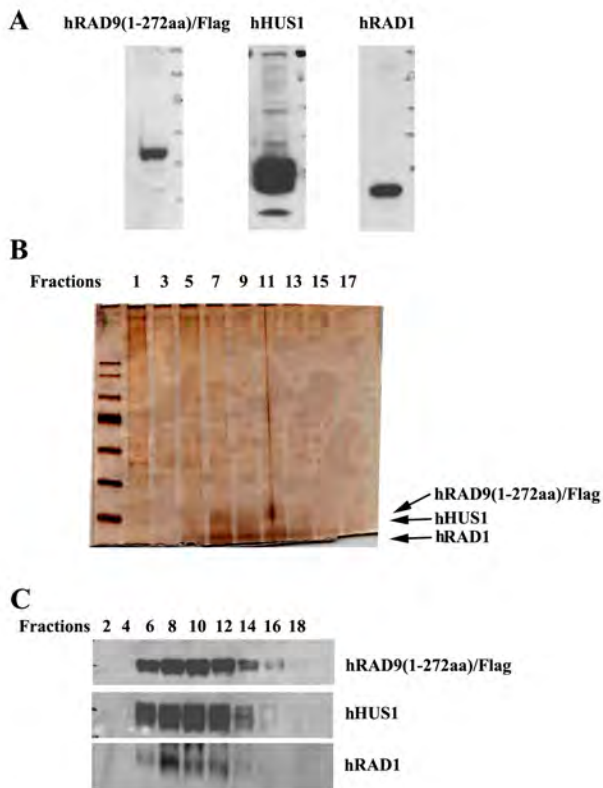


Figure 1. Co-expression and purification of the hRAD9(1-272aa)/Flag-hHUS1-hRAD1 complex. A) Analysis of ectopically expressed hRAD9(1-272aa)/Flag-hHUS1-hRAD1 complex in Sf9 cells. Approximately 20 μ g of whole Sf9 cell extract expressing hRAD9(1-272aa)/Flag-hHUS1-hRAD1 was analyzed by immunoblotting using either anti-Flag, hHUS1, or hRAD1 rabbit polyclonal antibodies. B) Silver-stained gel of Flag affinity purified hRAD9(1-272aa)-hHUS1-hRAD1 complex fraction. C) Purified fractions were collected and analyzed by Western blotting with either anti-Flag, hHUS1, or hRAD1 antibodies.

Protein purification was performed essentially as described previously [3]. The recombinant hRAD9(1-272 aa) Flag-hHUS1-hRAD1 complex was expressed in Sf9 cells, which were lysed in homogenization buffer and then centrifuged for 5 min at 2500g at 4°C. Pelleted nuclei were resuspended and allowed to lyse in nuclei buffer on ice for 30 min. Nuclear extracts were cleared by centrifugation at 18000g for 10 min at 4°C. Western blotting was used to detect target protein expression (Figure 1A). hRAD9(1-272 aa) Flag-hHUS1-hRAD1 complexes were purified by incubating nuclear extracts with anti-Flag M2 affinity gel overnight at 4°C. The beads were loaded onto a column and washed extensively with 0.15 M KCl, followed by a wash with 0.3M KCl. Bound proteins were eluted with Flag peptide. Silver staining (Figure 1B) and Western blot analysis (Figure 1C) were used to check purification.

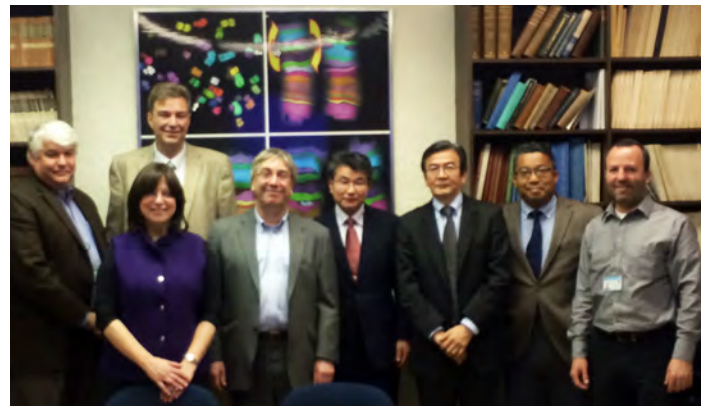
Future work will focus on characterizing the complex in more detail.

Reference

1. Majka, J., Binz, S.K., Wold, M.S., and Burgers, P.M. (2006). Replication protein A directs loading of the DNA damage checkpoint clamp to 50-DNA junctions. *J. Biol. Chem.* (2006) **281**: 27855–27861.
2. Sun Young Sohn and Yunje Cho. Crystal Structure of the Human Rad9–Hus1–Rad1 Clamp. *J. Mol. Biol.* (2009) **390**: 490–502.
3. Berkovits BD, Wang L, Guarnieri P, Wolgemuth DJ. The testis-specific double bromodomain-containing protein BRDT forms a complex with multiple spliceosome components and is required for mRNA splicing and 3'-UTR truncation in round spermatids. *Nucleic Acids Res.* (2012) **40(15)**: 7162-75. ■



Members of the CRR Advisory Council on the RARAF tour. L to R: Chip Cameron, Paul Locke, David Brenner, C.J. DeSantis, Eric Goldstone, Alan Jakimo, Gareth Roberts, and Gerald Chan.



Representatives from Ushio UV lamp manufacturer meet with David Brenner (fourth from left) and Alan Bigelow (far right)..

Regulation of Death in Human Melanoma Cells Carrying Stem Cell Biomarkers: Apoptosis versus Necroptosis

Vladimir N. Ivanov and Tom K. Hei

Significant progress has been made during the last 15 years in new molecular targeted therapies for treatment of advanced cancers, including melanomas. There are several dominant genetic alterations during melanoma carcinogenesis: i) *BRAF* and *NRAS* gene mutations [1-3], found in nearly 50%-60% and 20% of melanomas, respectively; ii) deletion of the *CDKN2A* locus, which encodes two tumor suppressor proteins, p16^{INK4a} and p14^{ARF}, was found in up to 50% of melanomas [4]; iii) deletion or mutation of *PTEN*, an endogenous inhibitor of PI3K-AKT, was found in 20% of melanomas [5]; iv) finally, mutations of *TP53* were found in 19% of melanomas [6]. Small molecule inhibitors, such as vemurafenib, suppress permanently active mutated *BRAF*, resulting in the arrest of proliferation and the

subsequent death of melanoma cells [1, 7]. A complementary approach to improve the survival of patients with metastatic melanoma is based on the usage of immune-stimulating monoclonal antibodies, which suppress endogenous inhibitors of the immune response: ipilimumab that blocks CTLA-4 [8] and nivolumab that blocks the PD-1 receptor [9]. Unfortunately, tumor relapse frequently follows within several months after treatment with specific molecule inhibitors or after immunostimulation [10, 11].

The existence of melanoma initiating cells or “melanoma stem cells” has also been suggested for this type of cancer [12, 13]. However, it still remains a controversial theory [14, 15] due to a strong variation in

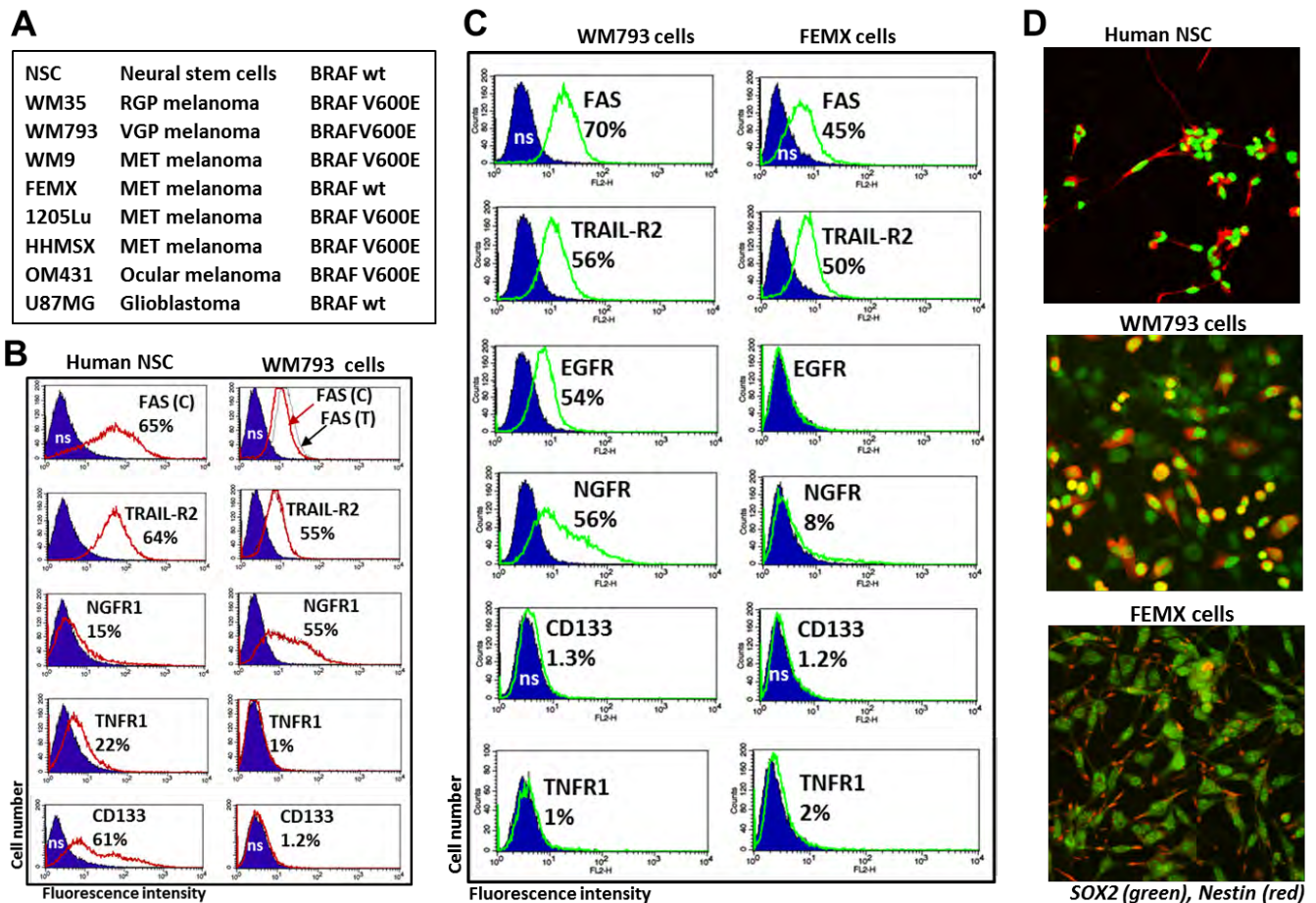


Figure 1. Comparison of stem cell surface biomarkers, death receptors, and pluripotency markers for neural stem cells (NSC) and human melanomas. (A) State of *BRAF* (wild type and mutated) in radial growth phase (RGP), vertical growth phase (VGP) and metastatic (MET) human melanomas. (B and C) Surface expression of death receptors (FAS, TRAIL-R2 and TNFR1), melanoma stem cells markers (NGFR1 and CD133), and EGFR in NSC, WM793 melanoma and FEMX melanoma cells. (D) Confocal images of NSC, WM793 and FEMX after staining of SOX2, a pluripotency marker, and Nestin, an early neuroprogenitor marker.

the percentage of cancer initiating cells in different melanoma lines and patient's samples, in addition to uncertainty in the specificity of stem cell biomarkers. Melanoma initiating cells could be identified via expression of different biomarkers such as CD133, ABCB5, NGFR, SOX10, CD20 and some others [16-19]. However, there is no final consensus on this subject. Therefore, further elucidation of molecular mechanisms underlying the regulation of melanocyte stem cells (melanoblasts) and their possible linkage with the melanoma initiating cells are especially important for the development of novel therapeutic strategies for melanocyte malignancy.

Progression and development of cancer, including melanoma, are tightly linked with the regulation of cell death. Programmed death of normal and cancer cells is executed via two main mechanisms, apoptosis and programmed necrosis (or necroptosis), which are modulated by numerous genetic, epigenetic and metabolic regulators (including misfolded protein stress,

macroautophagy and mitophagy) that finally result in positive or negative effects on survival of normal and cancer cells. The significance of the induction of apoptosis (in its two forms, the exogenous death ligand/death receptor-dependent and the endogenous mitochondria-dependent death signaling pathways) to cure cancer is well established [6, 20-22], while a role for regulated necrosis [23, 24] in cancer cells is still unknown since it is not completely investigated. In the present study, we used several human melanoma cell lines from the subsequent phases of melanoma development (radial growth phase, vertical growth phase and metastatic phase) [25], to compare: i) the presence of neural and cancer stem cell biomarkers, as well as the death receptors DR5 and FAS in adherent and spheroid cultures of melanoma cells; ii) the frequency and efficiency of the induction of cell death via apoptosis and necroptosis.

We used eight well-characterized melanoma cell lines (Fig. 1A) that were isolated from different phases of melanoma progression [26, 27] with established BRAF

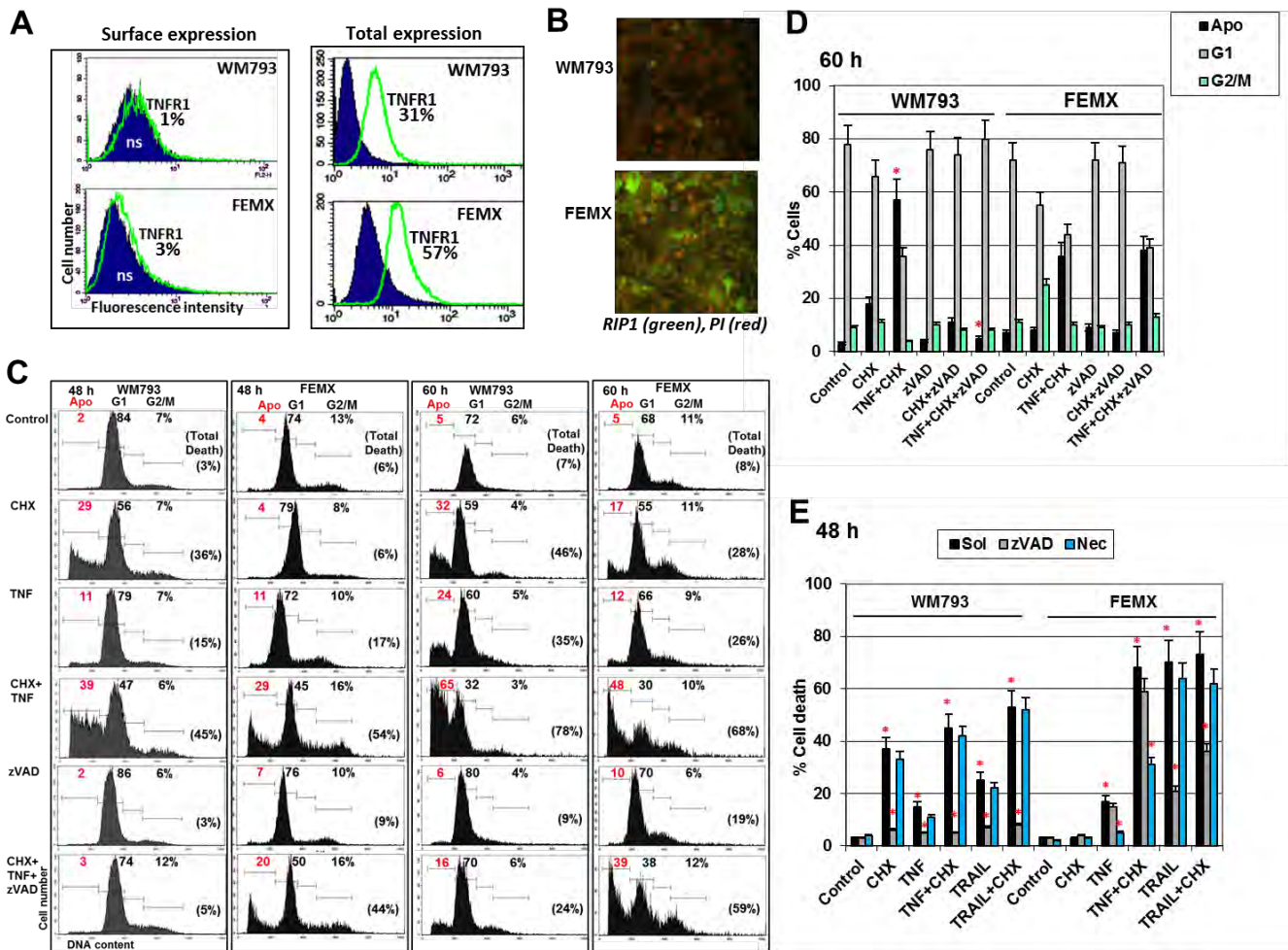


Figure 2. Induction of apoptosis and necroptosis among human melanomas. (A) Surface and total expression of TNFR1 in WM793 and FEMX melanoma cells. (B) Confocal analysis of RIP1 expression in melanoma cells. (C and D) Cell cycle-apoptosis analysis of WM793 and FEMX cells after PI staining of DNA and FACS assay. Cells were treated as indicated for 48 or 60h in the absence or presence of zVAD (40 μM). (E) Total cell death levels were determined using Trypan blue staining and light microscopy. Cells were treated in the absence or presence of zVAD, a caspase inhibitor, or Necrostatin (Nec, 50 μM), a RIP1 inhibitor. Stars indicate a significant difference (p<0.05).

status [28, 29]. Embryonic neural stem cells (NSC), which are in close relation to neural crest stem cells (NCSC), the ancestors of melanoblasts, have been used as reference cells expressing high levels of master regulators of pluripotency, such as SOX2 and NANOG, and stem cell biomarkers, CD133 and NGFR (Fig. 1B and C). Most NSC are positive for FAS and TRAIL-R2/DR5 (Fig. 1B) that could be involved in the initiation of death signaling cascades and, alternatively, under specific circumstances in protective signaling in cancer stem cells [30]. All eight melanoma lines exhibited high protein expression levels of SOX2, with preferential nuclear and perinuclear localization (Fig. 1D and data not shown). However, Nestin, an early neuroprogenitor marker, was almost completely absent in WM35 radial growth phase (RGP) melanoma cells and was present in approximately 40% of WM793 vertical growth phase (VGP) melanoma cells (Fig. 1D). All metastatic melanoma lines used in the current study exhibited high Nestin expression. (Fig. 1D and data not shown).

Besides high levels of SOX2, pronounced levels of NANOG protein expression were also detected in these cell lines. Variable levels of other important transcription factors, such as NF- κ B (total and active phosphorylated forms) and STAT3, as well signaling kinases MAPK p38, ERK1/2 and AKT (total and active forms) were revealed by Western blot assay (data not shown). NGFR, a lineage marker of neural crest stem/progenitor cells and melanoma initiated cells [16], was expressed on the surface of a vast majority of WM793 (VGP) and metastatic WM9 cells, but was revealed only at low levels in NSC and FEMX cells (Fig. 1B and C). In contrast, CD133, a potential marker for several types of cancer stem cells, was present at high surface levels in a majority of NSC, modestly on the WM35 surface and as a minor subpopulation (only 1%) with low surface levels in WM793 and FEMX cells (Fig. 1C). Similarly, TNFR1 demonstrated intermediate levels of surface expression in NSC, while this receptor was poorly detectable on the surface of melanoma lines (Fig. 2C). After cell permeabilization with 0.5% NP40, however, high intracellular levels of TNFR1 and other receptors, including CD133 and NGFR, were revealed in WM793 and FEMX cells (Fig. 2A and data not shown).

To determine the extent of the induction of apoptosis and total cell death in WM793 and FEMX melanoma cells after treatment with death ligands (TRAIL, FASL or TNF α), we used several approaches: i) Annexin-V-FITC+PI staining of control and treated cells 18 h after exposure to the indicated inhibitors followed by flow cytometry (data not shown); ii) cell cycle-apoptosis analysis of PI stained nuclei 48 h after treatment followed by flow cytometry (Fig. 2C and D); and iii) detection of levels of total death using Trypan blue staining and light microscopy (Fig. 2E). The pan-caspase inhibitor zVAD (40 μ M) and Necrostatin-1 (40 μ M), an inhibitor of RIP1 were used to further confirm the involvement of caspase-dependent apoptotic signaling pathways.

TRAIL in combination with cyclohexamide (CHX) effectively induced TRAIL/DR5-mediated apoptosis and upregulated total death levels in both WM793 and FEMX cells, due to evident surface expression of DR5/TRAIL-R2 (Fig. 2E). Similarly, FasL and CHX induced well pronounced apoptosis in both melanoma lines (data not shown). Caspase-3-mediated cleavage of PARP-1 was detected after TRAIL- and FasL-induced apoptosis in both lines.

We previously observed efficient induction of both apoptosis and necroptosis by TNF α +CHX in NSC, which possess high surface expression of TNFR1/2. However, TNFR surface expression was detected at low levels in most melanoma lines. In contrast, total intracellular levels of TNFR1 (after permeabilization of the plasma membrane) in WM793 and FEMX cells were relatively high (Fig. 2A). Both melanoma lines expressed RIP1, with the highest levels in FEMX (Fig. 2B). Cell cycle-apoptosis analysis demonstrated substantial levels of TNF+CHX induced cell death in both WM793 and FEMX melanoma cells. Although the presence of zVAD completely prevented this induced cell death in WM793 cells, it had essentially no effect on TNF+CHX induced cell death in FEMX cells (Figs. 2C and D). Conversely, Necrostatin-1 (40 μ M), an inhibitor of RIP1 kinase activity and necroptosis, substantially downregulated levels of total death induced by the combination of TNF+CHX in FEMX, but not in WM793 cells (Fig. 2E). This indicated the induction of necroptosis by TNF+CHX in FEMX metastatic melanoma cells.

Additional analysis of melanoma lines confirmed TNF-mediated death via necroptosis for ocular melanoma OM431. In general, apoptotic pathways of cell death were prevalent among melanoma cells. However, the existence of the necroptotic pathway in this cancer type provides an additional opportunity for treatment of melanomas.

References

1. Davies H, Bignell GR, Cox C, Stephens P, Edkins S, Clegg S, Teague J, Woffendin H, Garnett MJ, Bottomley W, Davis N, Dicks E, Ewing R, Floyd Y, Gray K, Hall S, Hawes R, Hughes J, Kosmidou V, Menzies A, Mould C, Parker A, Stevens C, Watt S, Hooper S, Wilson R, Jayatilake H, Gusterson BA, Cooper C, Shipley J, Hargrave D, Pritchard-Jones K, Maitland N, Chenevix-Trench G, Riggins GJ, Bigner DD, Palmieri G, Cossu A, Flanagan A, Nicholson A, Ho JW, Leung SY, Yuen ST, Weber BL, Seigler HF, Darrow TL, Paterson H, Marais R, Marshall CJ, Wooster R, Stratton MR, Futreal PA (2002) Mutations of the BRAF gene in human cancer. *Nature* 417: 949-954
2. Pollock PM, Harper UL, Hansen KS, Yudt LM, Stark M, Robbins CM, Moses TY, Hostetter G, Wagner U, Kakareka J, Salem G, Pohida T, Heenan P, Duray P, Kallioniemi O, Hayward NK, Trent JM, Meltzer PS

- (2003) High frequency of BRAF mutations in nevi. *Nat Genet* 33: 19-20. DOI 10.1038/ng1054
3. Tsao H, Goel V, Wu H, Yang G, Haluska FG (2004) Genetic interaction between NRAS and BRAF mutations and PTEN/MMAC1 inactivation in melanoma. *J Invest Dermatol* 122: 337-341. DOI 22243 [pii]
 4. Curtin JA, Fridlyand J, Kageshita T, Patel HN, Busam KJ, Kutzner H, Cho KH, Aiba S, Brocker EB, LeBoit PE, Pinkel D, Bastian BC (2005) Distinct sets of genetic alterations in melanoma. *N Engl J Med* 353: 2135-2147. DOI 10.1056/NEJMoa050092
 5. Tsao H, Zhang X, Fowlkes K, Haluska FG (2000) Relative reciprocity of NRAS and PTEN/MMAC1 alterations in cutaneous melanoma cell lines. *Cancer Res* 60: 1800-1804
 6. Hodis E, Watson IR, Kryukov GV, Arold ST, Imielinski M, Theurillat JP, Nickerson E, Auclair D, Li L, Place C, Dicara D, Ramos AH, Lawrence MS, Cibulskis K, Sivachenko A, Voet D, Saksena G, Stransky N, Onofrio RC, Winckler W, Ardlie K, Wagle N, Wargo J, Chong K, Morton DL, Stemke-Hale K, Chen G, Noble M, Meyerson M, Ladbury JE, Davies MA, Gershenwald JE, Wagner SN, Hoon DS, Schadendorf D, Lander ES, Gabriel SB, Getz G, Garraway LA, Chin L (2012) A landscape of driver mutations in melanoma. *Cell* 150: 251-263. DOI 10.1016/j.cell.2012.06.024
 7. Vultur A, Villanueva J, Herlyn M (2011) Targeting BRAF in Advanced Melanoma: A First Step toward Manageable Disease. *Clinical Cancer Research* 17: 1658-1663. DOI 10.1158/1078-0432.ccr-10-0174
 8. Lipson EJ, Drake CG (2011) Ipilimumab: an anti-CTLA-4 antibody for metastatic melanoma. *Clin Cancer Res* 17: 6958-6962. DOI 10.1158/1078-0432.CCR-11-1595
 9. Wolchok JD, Kluger H, Callahan MK, Postow MA, Rizvi NA, Lesokhin AM, Segal NH, Ariyan CE, Gordon RA, Reed K, Burke MM, Caldwell A, Kronenberg SA, Agunwamba BU, Zhang X, Lowy I, Inzunza HD, Feely W, Horak CE, Hong Q, Korman AJ, Wigginton JM, Gupta A, Sznol M (2013) Nivolumab plus ipilimumab in advanced melanoma. *N Engl J Med* 369: 122-133. DOI 10.1056/NEJMoa1302369
 10. Chapman PB, Hauschild A, Robert C, Haanen JB, Ascierto P, Larkin J, Dummer R, Garbe C, Testori A, Maio M, Hogg D, Lorigan P, Lebbe C, Jouary T, Schadendorf D, Ribas A, O'Day SJ, Sosman JA, Kirkwood JM, Eggermont AM, Dreno B, Nolop K, Li J, Nelson B, Hou J, Lee RJ, Flaherty KT, McArthur AG (2011) Improved survival with vemurafenib in melanoma with BRAF V600E mutation. *N Engl J Med* 364: 2507-2516. DOI 10.1056/NEJMoa1103782
 11. Flaherty KT, Puzanov I, Kim KB, Ribas A, McArthur GA, Sosman JA, O'Dwyer PJ, Lee RJ, Grippo JF, Nolop K, Chapman PB (2010) Inhibition of mutated, activated BRAF in metastatic melanoma. *N Engl J Med* 363: 809-819. DOI 10.1056/NEJMoa1002011
 12. Smalley KS, Herlyn M (2009) Integrating tumor-initiating cells into the paradigm for melanoma targeted therapy. *Int J Cancer* 124: 1245-1250. DOI 10.1002/ijc.24129
 13. Schatton T, Murphy GF, Frank NY, Yamaura K, Waaga-Gasser AM, Gasser M, Zhan Q, Jordan S, Duncan LM, Weishaupt C, Fuhlbrigge RC, Kupper TS, Sayegh MH, Frank MH (2008) Identification of cells initiating human melanomas. *Nature* 451: 345-349. DOI 10.1038/nature06489
 14. Quintana E, Shackleton M, Sabel MS, Fullen DR, Johnson TM, Morrison SJ (2008) Efficient tumour formation by single human melanoma cells. *Nature* 456: 593-598. DOI 10.1038/nature07567
 15. Held MA, Curley DP, Dankort D, McMahon M, Muthusamy V, Bosenberg MW (2010) Characterization of melanoma cells capable of propagating tumors from a single cell. *Cancer Res* 70: 388-397. DOI 10.1158/0008-5472.CAN-09-2153
 16. Boiko AD, Razorenova OV, van de Rijn M, Swetter SM, Johnson DL, Ly DP, Butler PD, Yang GP, Joshua B, Kaplan MJ, Longaker MT, Weissman IL (2010) Human melanoma-initiating cells express neural crest nerve growth factor receptor CD271. *Nature* 466: 133-137. DOI 10.1038/nature09161
 17. Lang D, Mascarenhas JB, Shea CR (2013) Melanocytes, melanocyte stem cells, and melanoma stem cells. *Clinics in dermatology* 31: 166-178. DOI 10.1016/j.clindermatol.2012.08.014
 18. Murphy GF, Wilson BJ, Girouard SD, Frank NY, Frank MH (2014) Stem cells and targeted approaches to melanoma cure. *Molecular aspects of medicine* 39C: 33-49. DOI 10.1016/j.mam.2013.10.003
 19. Redmer T, Welte Y, Behrens D, Fichtner I, Przybilla D, Wruck W, Yaspo ML, Lehrach H, Schafer R, Regenbrecht CR (2014) The nerve growth factor receptor CD271 is crucial to maintain tumorigenicity and stem-like properties of melanoma cells. *PLoS One* 9: e92596. DOI 10.1371/journal.pone.0092596
 20. Ashkenazi A, Herbst RS (2008) To kill a tumor cell: the potential of proapoptotic receptor agonists. *J Clin Invest* 118: 1979-1990
 21. Jin Z, El-Deiry WS (2005) Overview of cell death signaling pathways. *Cancer Biol Ther* 4: 139-163
 22. Hanahan D, Weinberg RA (2011) Hallmarks of cancer: the next generation. *Cell* 144: 646-674. DOI 10.1016/j.cell.2011.02.013
 23. Degterev A, Hitomi J, Gemscheid M, Ch'en IL, Korkina O, Teng X, Abbott D, Cuny GD, Yuan C, Wagner G, Hedrick SM, Gerber SA, Lugovskoy A, Yuan J (2008) Identification of RIP1 kinase as a specific cellular target of necrostatins. *Nature*

- chemical biology 4: 313-321. DOI 10.1038/nchembio.83
24. Vandenameele P, Galluzzi L, Vanden Berghe T, Kroemer G (2010) Molecular mechanisms of necroptosis: an ordered cellular explosion. *Nat Rev Mol Cell Biol* 11: 700-714. DOI 10.1038/nrm2970
 25. Vultur A, Herlyn M (2013) SnapShot: melanoma. *Cancer Cell* 23: 706-706 e701. DOI 10.1016/j.ccr.2013.05.001
 26. Satyamoorthy K, DeJesus E, Linnenbach AJ, Kraj B, Kornreich DL, Rendle S, Elder DE, Herlyn M (1997) Melanoma cell lines from different stages of progression and their biological and molecular analyses. *Melanoma Res* 7 Suppl 2: S35-42
 27. Myklebust AT, Helseth A, Breistol K, Hall WA, Fodstad O (1994) Nude rat models for human tumor metastasis to CNS. Procedures for intracarotid delivery of cancer cells and drugs. *J Neurooncol* 21: 215-224
 28. Haass NK, Sproesser K, Nguyen TK, Contractor R, Medina CA, Nathanson KL, Herlyn M, Smalley KS (2008) The mitogen-activated protein/extracellular signal-regulated kinase kinase inhibitor AZD6244 (ARRY-142886) induces growth arrest in melanoma cells and tumor regression when combined with docetaxel. *Clin Cancer Res* 14: 230-239. DOI 14/1/230 [pii]10.1158/1078-0432.CCR-07-1440
 29. Krasilnikov M, Ivanov VN, Dong J, Ronai Z (2003) ERK and PI3K negatively regulate STAT-transcriptional activities in human melanoma cells: implications towards sensitization to apoptosis. *Oncogene* 22: 4092-4101
 30. Peter ME, Legembre P, Barnhart BC (2005) Does CD95 have tumor promoting activities? *Biochim Biophys Acta* 1755: 25-36 ■



Top (l to r): Tom Hei on the Silk Road after attending the International Symposium on DNA Repair and Space Radiation in Lanzhou, China; Tom Hei receiving his appointment plaque of an adjunct chair professorship from Vice-President Xiong of Soochow University in Suzhou, China. Bottom (l to r): Jingsong Yuan (who will join our faculty next year) and Tom Hei; The Hei and Lieberman lab Christmas luncheon – a tradition for more than twenty years.

High-Dose and Fractionation Effects in Stereotactic Radiation Therapy: Analysis of Tumor Control Data from 2,965 Patients

Igor Shuryak, David J. Carlson^a, J. Martin Brown^b, and David J. Brenner

Stereotactic radiosurgery (SRS) and stereotactic body radiotherapy (SBRT), also known as stereotactic ablative radiotherapy (SABR), are becoming increasingly accepted [1]. The spatial accuracy of dose delivery using these techniques (hereafter referred to as stereotactic radiotherapy, SRT) allows substantial dose escalation to the tumor [1]. Two aspects of SRT response require clarification: First, are tumoricidal mechanisms at high-doses/fraction the same as at lower doses? Second, does single high-dose treatment confer added advantage for tumor control (TCP), vs. multiple fractions?

As radiation dose increases, the mechanistic basis of the linear quadratic (LQ) model becomes less clear [2].

Some investigators argue that tumor eradication by large doses/fraction is dominated by distinct biological

phenomena (e.g. damage to the tumor vasculature) that are qualitatively different from those operating at lower doses, and are not accounted for by the LQ model [3]. By contrast, others argue [4] that SRT effectiveness is sufficiently explained by increased tumor doses, which destroy tumors largely through the same mechanisms that operate at lower doses.

Attempts to incorporate potential distinct tumoricidal mechanisms that operate at high doses into quantitative formalisms produced the Linear Quadratic Linear (LQL) [5], Universal Survival Curve (USC) [6], and Pade Linear

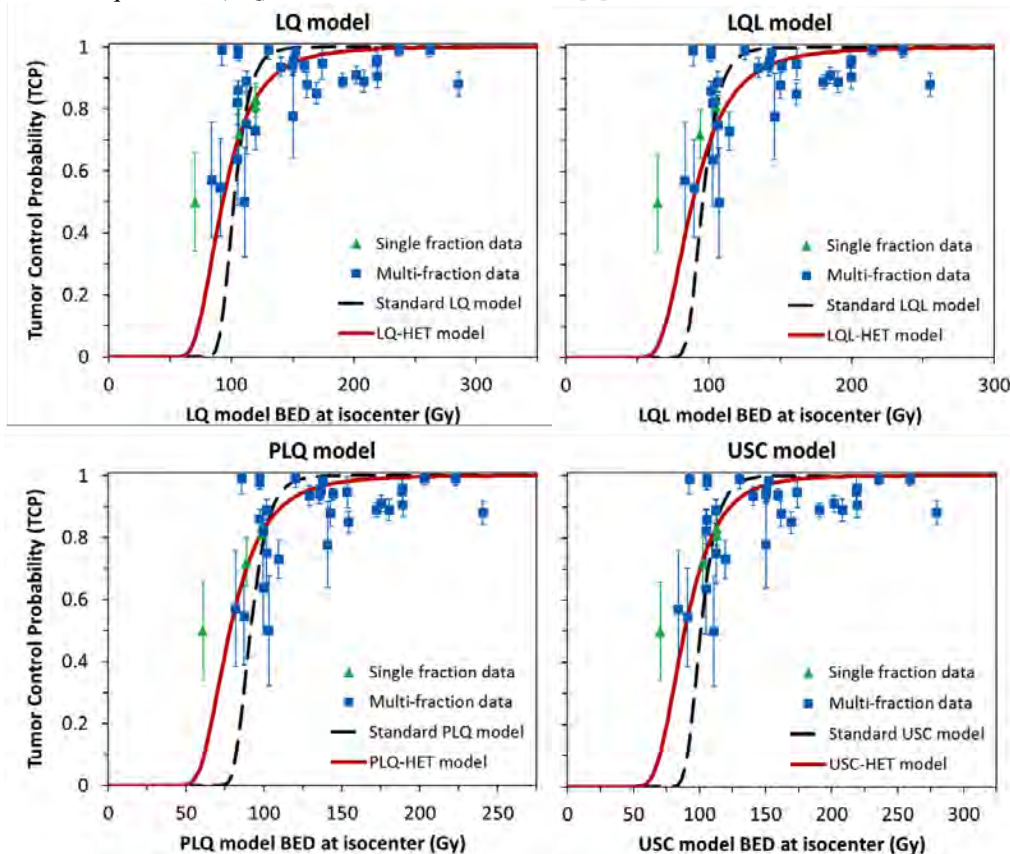


Figure 1. Best fits to data on early-stage NSCLC from the standard LQ model, the model with heterogeneous radiosensitivity (LQ-HET), and from the LQL, PLQ and USC models. In this and the following figures, error bars represent standard errors.

^aDepartment of Therapeutic Radiology, Yale University School of Medicine, New Haven, CT.

^bDepartment of Radiation Oncology, Stanford University School of Medicine, Stanford, CA.

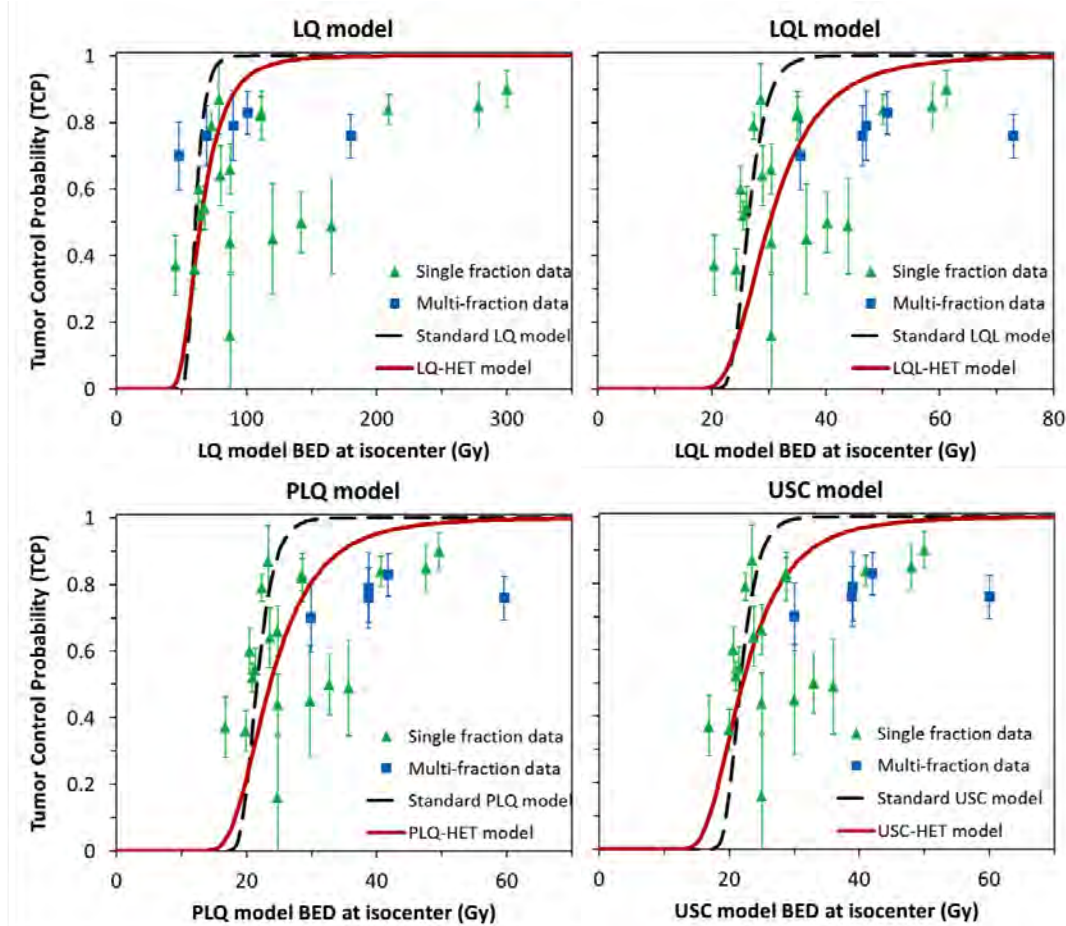


Figure 2. Best fits to data on brain metastases from the standard LQ model, the model with heterogeneous radiosensitivity (LQ-HET), and from the LQL, PLQ and USC models.

Quadratic (PLQ) [7] models. These formalisms reduce (effectively linearize) the dose response for the logarithm of tumor cell survival ($\ln[S]$) at high doses by adding one or more extra parameters to the LQ model.

Radiation response within a tumor is likely to be heterogeneous due to differences in oxygenation state, cell cycle phase, and/or cell phenotype (e.g. cancer “stem cell” vs. “non-stem cell”). Consistently with this picture, models with heterogeneous tumor cell radiosensitivity [8] often describe clinical data from conventionally fractionated radiotherapy better than models with homogeneous radiosensitivity.

We hypothesize that: (1) most of the observed changes in the TCP dose response shape at high doses/fraction vs lower doses/fraction can be explained by heterogeneous tumor radiosensitivity, rather than by distinct tumoricidal mechanisms that operate at high vs low doses; (2) consequently, single high-dose treatment will not confer added biological advantage for TCP, vs. multiple fractions. To test this hypothesis, we have used a large set of published TCP data for lung tumors and brain metastases treated with modern SRT.

We analyzed published TCP data from 2,965 SRT patients for lung tumors (Fig. 1) or brain metastases (Fig. 2), with wide ranges of doses and fraction numbers. We used: a) linear-quadratic (LQ) models, which assume the same mechanisms at all doses, and b) alternative models

incorporating extra terms for different mechanisms at high doses. Versions with homogeneous or heterogeneous tumor cell radiosensitivity were used for each model.

Ranking of models by relative goodness of fit, taking into account sample size and parameter number, was based on the Akaike information criterion with sample size correction (AICc), which has gained widespread popularity for this purpose [9]. For ranking non-linear models, AICc is preferable to methods that rely on reduced Chi-squared or R-squared [10]. Another useful property of AICc is that more than two models can be compared simultaneously, without the need for models to be “nested” or to belong to the same class. The model that has the lowest AICc value among those being compared is the best-fitting model, and those models that have AICc ≥ 6 units higher than the best-fitting model have much poorer support from the data.

The strengths of our study include: (1) use of a large amount of clinical data (from 2,965 SRT-treated patients); (2) use of multiple radiobiological models, some of which (LQ with homogeneous or heterogeneous radiosensitivity) assume that the same tumoricidal mechanisms determine TCP at all doses and fraction numbers, whereas others (LQL, USC, PLQ) explicitly account for potential high-dose-specific tumoricidal mechanisms; and (3) use of a robust criterion (AICc) to compare support from the data for each of these models. The main weaknesses (which are inherent in most similar analyses) involve: (1) fitting

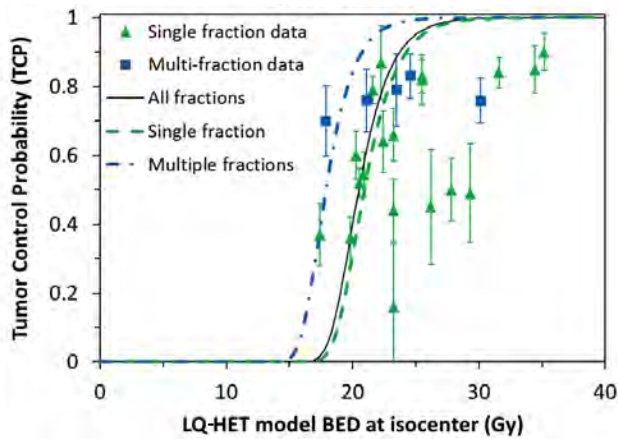


Figure 3. Best fits of the model with heterogeneous radiosensitivity (LQ-HET) to data on brain metastases treated with single-fraction vs. multiple-fraction SRT.

summary data vs. individual-patient data; and (2) oversimplification of tumor radiation response by not accounting for effects of tumor size and stage, time after SRT when TCP was reported, patient age and sex, calendar year and institution-specific factors, and many other potential effects. However, because these weaknesses are the same for all considered models, relative comparison of model fit quality can provide insight into how well (or how poorly) each model captures the main features of tumor response to SRT.

We can draw the following main conclusions:

First, at the high doses per fraction used in SRT, the effects of heterogeneous radiosensitivity dominate the relatively subtle differences between dose response shapes produced by different radiobiological models. In other words, accounting for variability in radiosensitivity is more important for describing the SRT TCP data, than adjusting the details of cell survival curve shape at high doses by terms that attempt to account for hypothetical high dose-specific tumoricidal mechanisms.

Second, among all tested formalisms with heterogeneous radiosensitivity, only the simplest one – the LQ-HET model – consistently produced biologically-plausible parameter estimates. Analysis of the data with this model suggested that there was no evidence that single-fraction SRT produces better tumor control than multi-fraction regimens (Fig. 3). Instead, multi-fraction brain SRT was predicted to produce slightly better TCPs than single-fraction treatments. These conclusions are consistent with expected effects on hypoxic tumors, where fractionation allows tumor reoxygenation between fractions.

Consequently, when heterogeneous tumor cell radiosensitivity (which becomes particularly important at high doses per fraction) is accounted for, the TCP data from modern SRT can be reasonably described by models that assume that the same tumoricidal mechanisms determine TCP at all doses and fraction numbers.

Consequently, the use of such models remains a clinically successful and mechanistically plausible approach for guiding radiotherapy design. In contrast, the addition of terms that attempt to account for hypothetical high dose-specific tumoricidal mechanisms makes the models overly flexible, which often results in biologically unrealistic parameter estimates.

In summary, this analysis suggests that model fit to SRT TCP data is dramatically improved by accounting for heterogeneous radiosensitivity, whereas additional parameters that modify the dose response at high doses have a much smaller effect.

References

1. Hadziahmetovic M, Loo BW, Timmerman RD, et al. Stereotactic body radiation therapy (stereotactic ablative radiotherapy) for stage I non-small cell lung cancer--updates of radiobiology, techniques, and clinical outcomes. *Discov Med* 2010;9:411-7.
2. Kirkpatrick JP, Brenner DJ, Orton CG. Point/Counterpoint. The linear-quadratic model is inappropriate to model high dose per fraction effects in radiosurgery. *Med Phys* 2009;36:3381-4.
3. Kirkpatrick JP, Meyer JJ, Marks LB. The linear-quadratic model is inappropriate to model high dose per fraction effects in radiosurgery. *Semin Radiat Oncol* 2008;18:240-3.
4. Brown JM, Brenner DJ, Carlson DJ. Dose escalation, not "new biology," can account for the efficacy of stereotactic body radiation therapy with non-small cell lung cancer. *Int J Radiat Oncol Biol Phys* 2013;85:1159-60.
5. Guerrero M, Carlone M. Mechanistic formulation of a lineal-quadratic-linear (LQL) model: split-dose experiments and exponentially decaying sources. *Med Phys* 2010;37:4173-81.
6. Park C, Papiez L, Zhang S, Story M, Timmerman RD. Universal survival curve and single fraction equivalent dose: useful tools in understanding potency of ablative radiotherapy. *Int J Radiat Oncol Biol Phys* 2008;70:847-52.
7. Belkic D. Parametric analysis of time signals and spectra from perspectives of quantum physics and chemistry. *Adv Quant Chem* 2011;61:145-260.
8. Carlone MC, Warkentin B, Stavrev P, Fallone BG. Fundamental form of a population TCP model in the limit of large heterogeneity. *Med Phys* 2006;33:1634-42.
9. Burnham KP, Anderson DR. Model selection and multi-model inference: a practical information-theoretic approach: Springer; 2002
10. Andrae R, Schulze-Hartung T, Melchior P. Dos and don'ts of reduced chi-squared. arXiv preprint arXiv:10123754 2010. ■

Far UVC (~200 nm) as a Safe and Low-cost Tool for Reducing Surgical Site Infections: In Vivo Studies

Manuela Buananno, Alan W. Bigelow, Gerhard Randers-Pehrson, Henry M. Spotnitz^a, and David J. Brenner

Introduction

It has been estimated that up to 10% of clean surgeries in the US result in surgical site infections (SSI) [1]. The annual number of deaths attributed to SSI has been estimated at 8,200, with annual patient hospital costs between \$3 and \$10 billion [2].

Despite improvements in operating room practices, the increasing number of SSI are attributable to antibiotic-resistant pathogens such as methicillin-resistant *S. aureus* (MRSA), one of the leading causes of SSI in community hospitals.

UV radiation is an effective approach to inactivating bacteria. However, it is a human health hazard, being both carcinogenic and cataractogenic. To address this issue, we have used novel excimer lamps (excilamps) that produce a broad high-intensity beam of single-wavelength UV radiation of ~ 200 nm. Because UV radiations of different wavelengths have different abilities to penetrate into cells, the lower the wavelength, the less penetrating the radiation. Therefore, while far-UVC wavelengths can penetrate and kill bacteria, they cannot penetrate either the human stratum corneum (the outer dead-cell skin layer), nor the ocular cornea, nor even the cytoplasm of individual human cells.

Our preliminary *in vitro* studies [3] in human cells and a human skin tissue model have shown that while far-UVC wavelengths are approximately as efficient as conventional UV in inactivating drug-resistant bacteria (in particular MRSA), they do not produce biological damage in human cells compared to conventional UV.

In the context of reducing SSI in clinical practice, the next logical step is to assess the safety of the excilamps and their efficacy in reducing SSI in *in vivo* models. To investigate the safety of the krypton-bromine (KrBr) excilamp (207 nm), hairless mice were exposed for 8 h to a total fluence of 150 mJ/cm². Mice exposed to the same fluence (delivered in 2.5 h) from a conventional germicidal lamp (254 nm) were used as positive controls; sham-irradiated mice were handled in parallel. Forty-eight hours after exposure, mouse dorsal skin was collected and fixed for analysis. Figure 1 shows the 20 x view of mouse dorsal skin tissue stained with hematoxylin and eosin. Compared to sham-exposed mice (Fig. 1A), exposure to conventional UV resulted in a 2.5-fold

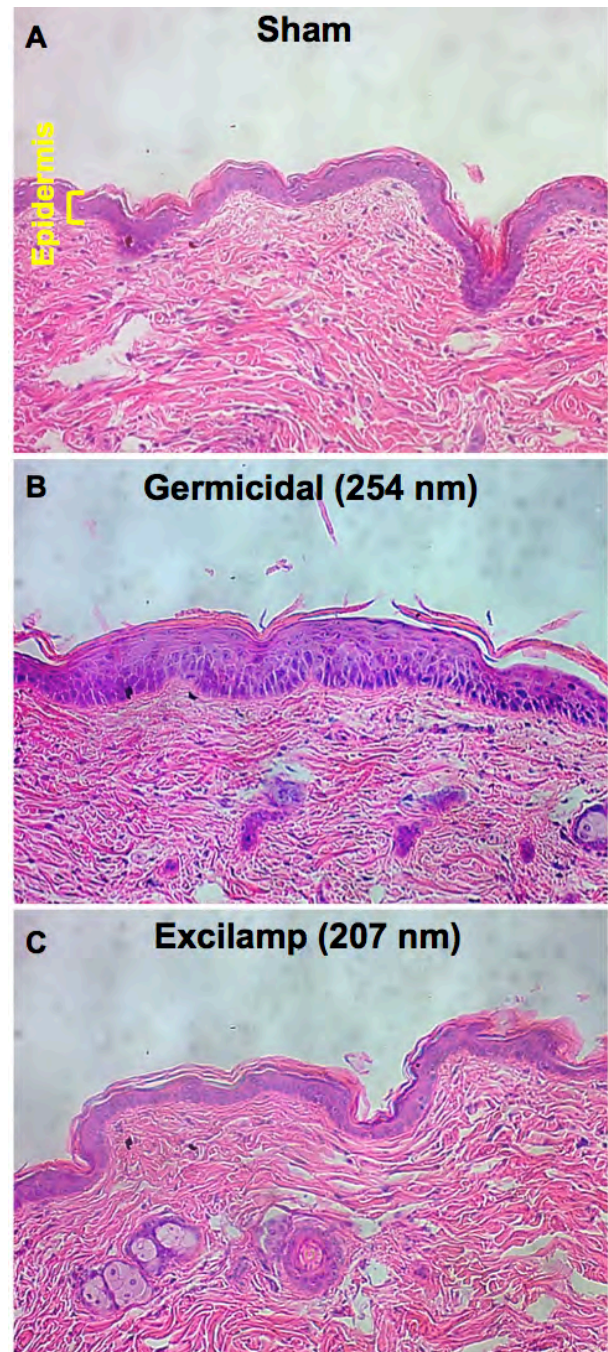


Figure 1. Hematoxylin and eosin stain of dorsal skin of hairless mice. Mice were A) sham-irradiated or exposed to 150 mJ/cm² generated by B) a germicidal lamp (254 nm) and delivered in 2.5 h or C) a 207-nm excilamp and delivered in 8 h. 48 h after, skin exposed to the excilamp appeared similar to sham-exposed skin. In contrast, germicidal lamp induced an increase in epidermal thickness.

^aDepartment of Surgery, Columbia University Medical Center.

increase ($P = 0.02$) in epidermal thickness (Fig. 1B). In contrast, the epidermal thickness of skin of mice exposed to UV generated by the 207 nm excilamp was similar to control (Fig. 1C).

We also measured the percentage of epidermal cells with cyclobutane pyrimidine dimers (CPDs), the most abundant pre-mutagenic DNA lesions induced by

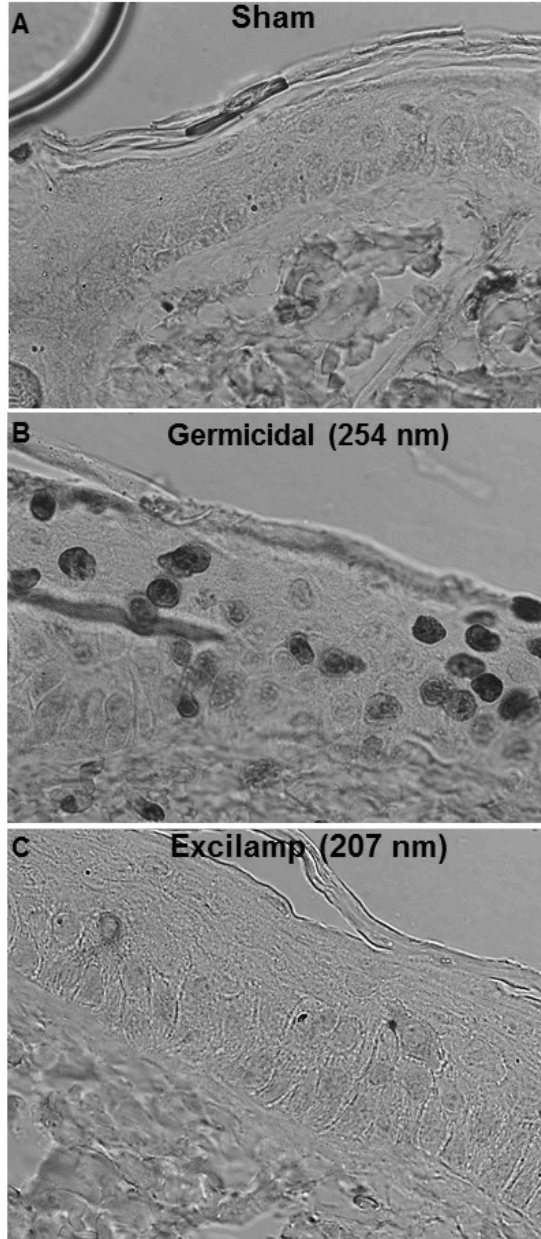


Figure 2. Immunohistochemical analysis of cyclobutane pyrimidine dimers (appearing as black nuclei) in the epidermis of mice that were A) sham-irradiated or exposed to 150 mJ/cm^2 generated by B) a germicidal lamp (254 nm) and delivered in 2.5 h or C) a 207-nm excilamp and delivered in 8 h. Relative to control, 48 h after exposure, the germicidal lamp induced a drastic increase in the percentage of epidermal cells carrying DNA photodamage. No statistically significant increase of photodamage was measured in epidermal cells of mice exposed to the excilamp.

exposure to UV light, and which appear as black nuclei in Figure 2 (60 x view). Relative to sham-exposed skin (Fig. 2A), exposure to a germicidal lamp induced CPDs ($57.5 \pm 2.1 \%$ vs. $2.6 \pm 0.5 \%$ in controls) (Fig. 2B). In contrast, no statistically significant increase in DNA photodamage relative to control was induced in mice exposed to the 207 nm excilamp ($3.5 \pm 0.8\%$ vs. $2.6 \pm 0.5 \%$ in controls; $P > 0.1$) (Fig. 2C).

Similar safety studies will be carried out in a porcine model, while ongoing studies aim at establishing the efficacy of the excilamps for SSI reduction in mice and porcine wound-infection models. Finally, current studies are aimed at investigating the efficacy of the excilamps to inactivate surface- and airborne-viruses.

In conclusion, we propose that far-UVC radiations have all the anti-microbial advantages of conventional UV lamps, but without the safety hazards.

References

1. Barie, P.S. and S.R. Eachempati, *Surgical site infections*. Surg Clin North Am, 2005. **85**(6): p. 1115-35, viii-ix.
2. Klevens, R.M., et al., *Estimating health care-associated infections and deaths in U.S. hospitals, 2002*. Public Health Rep, 2007. **122**(2): p. 160-6.
3. Buonanno, M., et al., *207-nm UV light - a promising tool for safe low-cost reduction of surgical site infections. I: in vitro studies*. PLoS One, 2013. **8**(10): p. e76968. ■



Sasha Lyulko and Manuela Buonanno.

Determining Key Pathways Sensitizing Lung Cancer to Combined Chemoradiation Therapy by Exploiting Synthetic Lethal Relationships in an RNAi High-throughput Screen

Kunal R. Chaudhary^a and Simon Cheng^a

Introduction

Lung cancer is known to be the most common cancer and the leading cause of cancer-related death in men and women worldwide. Platinum-based concurrent chemoradiation (CRT) remains the standard treatment for patients with locally advanced, stage III non-small cell lung cancer (NSCLC) [1]. Despite treatment advances, patient outcomes remain dismal and overall survival at 5 years is only 15%, stressing the need to improve treatment [2]. Novel treatment options and predictive biomarkers to improve upon the outcome and reduce the toxicity of our current treatment paradigms are sorely needed. The resistance mechanisms for concurrent chemoradiation therapy are poorly studied.

Cancer stem cells have been proposed to be the driver for many cancers including lung cancer, and also may be responsible for therapy resistance. We sought therefore to identify therapy resistance pathways in lung cancer by

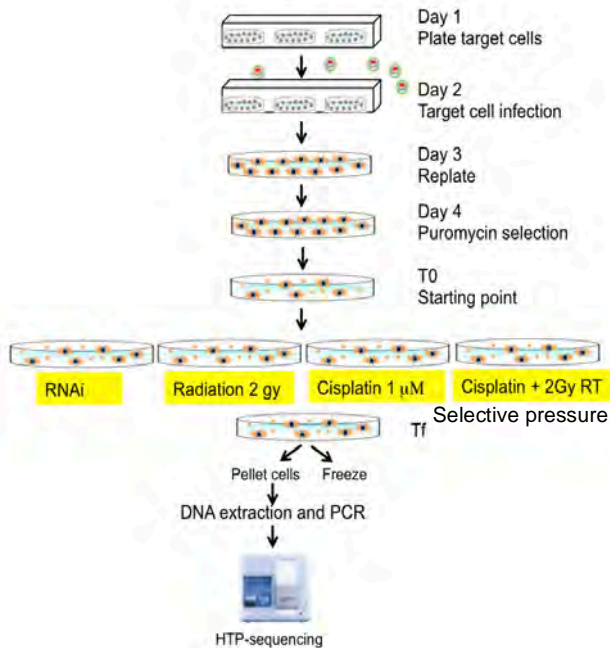


Figure 1. Experimental design describing whole genome high-throughput RNAi screening of PC9 cells.

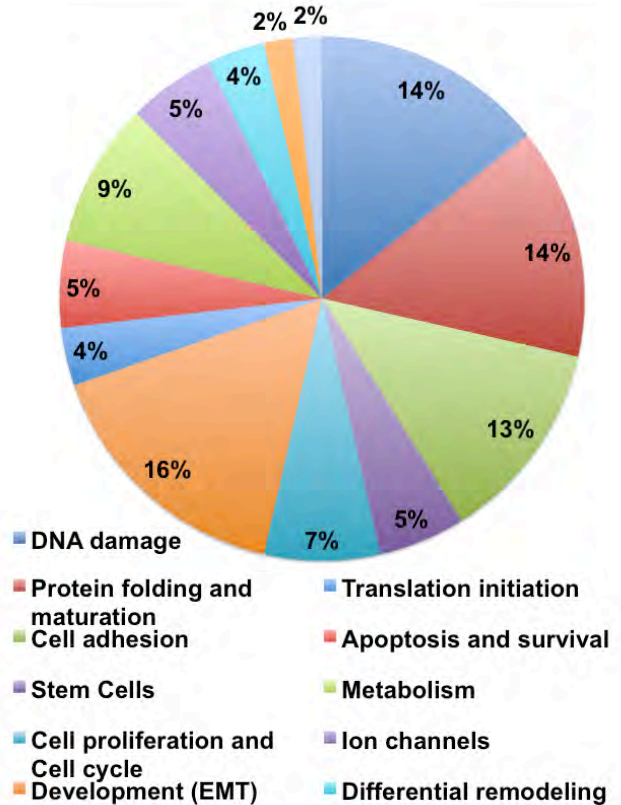


Figure 2. Pie Chart of major pathways represented by depleted RNAi species after treatment of PC9 cells with combined cisplatin and radiation compared to the control group.

using RNA interference (RNAi) [3]. Our overall hypothesis is that the identification of acquired resistance pathways and synergistic targets for platinum-radiation therapy will lead to improved treatments and patient selection. One effective approach would be to identify and down regulate resistance-causing genes in tumors using small interfering RNAs (siRNAs) to increase the sensitivity of tumor cells to chemotherapeutic challenge.

Experimental overview and Results

To identify novel genes that modulate the response to platinum chemotherapy and radiation therapy we have performed a genome-wide RNAi high-throughput screen testing a shRNA viral library containing approx. 60,000 individual shRNAs on a human lung adenocarcinoma cell

^aDepartment of Radiation Oncology, Columbia University Medical Center.

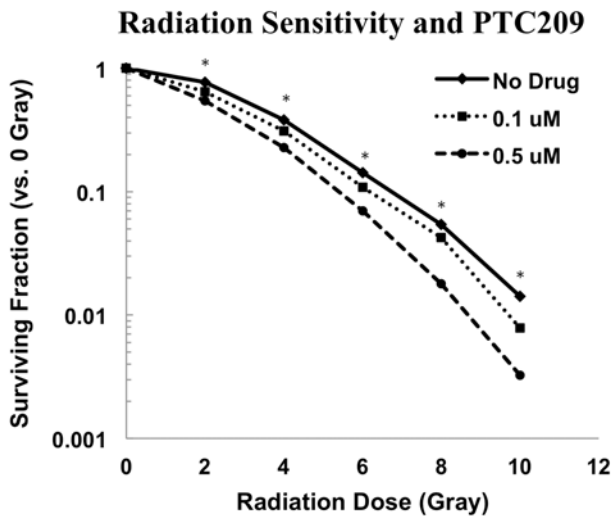


Figure 3. Cell survival assay determining sensitization of PC9 cells to radiation after Bmi1 inhibitor treatment. Each point represents the mean of five technical replicates; data are expressed as mean \pm s.e.m. ‘*’ indicates $P < 0.05$.

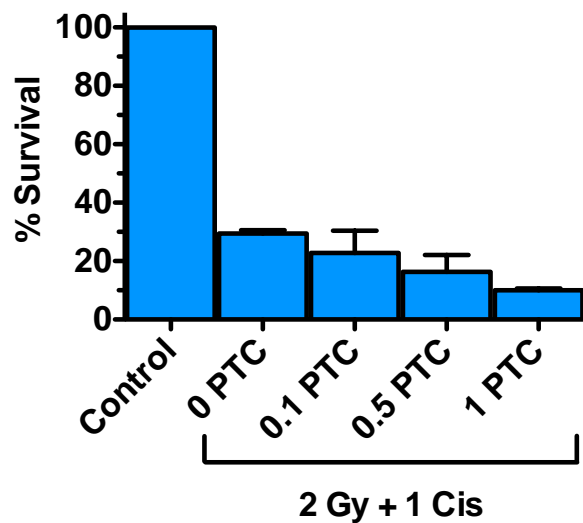


Figure 4. Colonogenic survival of PC9 cells 9 days after 2 Gy irradiation in the presence of 1 μ M cisplatin (Cis) and PTC-209. Results (mean and SD of 3 independent experiments) are expressed as percent of non-irradiated controls.

line (PC9) [4]. After two weeks of cisplatin and/or radiation treatment of PC9 cells with shRNA and controls, depleted versus enriched shRNAs were

identified through library sequencing (Fig.1). We hypothesized that depleted shRNAs in the treated versus control cells might represent genes whose function is crucial for resistance to therapy-induced cell death.

From the cisplatin and radiation screen, analysis of the top 100 potential hits (depleted shRNAs) interestingly showed several cancer stem cell markers including Sox, Lrg6, and members of the Hedgehog signaling pathway Patched and Bmi1 (Fig.2) [5]. We further determined the effects of Bmi1 on therapy resistance using survival assays with PC9 cells treated with Bmi1 inhibitor PTC-09. MTT cell survival and clonogenic assays were performed by treating PC9 cells with PTC-09 in triplicate and then treating the cells with increasing doses of cisplatin (0.1, 1 and 10 μ M) or X-ray radiation (2, 4 and 6 Gy). Significantly decreased cell survival following cisplatin or radiation was observed in PTC-09 treated PC9 cells compared to controls (Fig. 3). Further clonogenic assay of PC9 cells treated with 2 Gy X-rays plus 1 μ m cisplatin and increasing doses of PTC-09 showed significant decreases in the ability of cells to form colonies compared to controls (Fig.4).

Conclusions

By performing an unbiased genome-wide RNAi screen for therapeutic resistance, we have successfully identified and validated a target in the cancer stem cell pathways. We are further evaluating the effect of Bmi1 using a CRISPR knock out model.

References

1. Olaussen, K.A., et al., DNA repair by ERCC1 in non-small-cell lung cancer and cisplatin-based adjuvant chemotherapy. *N Engl J Med*, 2006. **355**(10): p. 983-91.
2. Kobayashi, S., et al., EGFR mutation and resistance of non-small-cell lung cancer to gefitinib. *N Engl J Med*, 2005. **352**(8): p. 786-92.
3. Cheng, H., et al., PARP inhibition selectively increases sensitivity to cisplatin in ERCC1-low non-small cell lung cancer cells. *Carcinogenesis*, 2013.
4. Silva, J.M., et al., Profiling essential genes in human mammary cells by multiplex RNAi screening. *Science*, 2008. **319**(5863): p. 617-20.
5. Kreso, A., et al., Self-renewal as a therapeutic target in human colorectal cancer. *Nat Med*, 2014. **20**(1): p. 29-36. ■

Anatomically Accurate Mouse Phantoms for Radiation Dosimetry Studies

David Welch, Andrew Harken, Gerhard Randers-Pehrson, and David J. Brenner

Radiation biology experiments often utilize mice as test animals because the well-known genetic similarities within a strain provide an excellent model system for analysis. Accurate radiation dosimetry is crucial to correctly interpret the results of such experiments. However, determining the precise dose delivered to each region within test animals is difficult to accomplish due to their intricate anatomy and the associated complex physics phenomena. Density inhomogeneity within a mouse, associated with lung and bone regions for example, complicates organ dose and dosimetry assessment [1, 2]. In order to better understand absorbed dose in such situations, we have developed a physical mouse phantom, which closely mimics the internal and overall anatomical features of a mouse.

Methods

The phantoms are constructed using a method similar to that of Winslow et al. [3] where slices are processed individually and then assembled to create an entire phantom. The mouse phantoms contain regions of tissue equivalent material, bone equivalent material, and lung equivalent material, which were chosen to mimic the physical properties of each region, such as density and attenuation coefficients. Precision computer controlled micro-milling techniques are used to replicate anatomical features down to approximately 400 μm .

The phantom design was based on the Digimouse atlas [4], which used CT scan data to create an organ segmented model. The organ segmented data were processed with MATLAB to isolate planes which would be replicated in 2 mm thick slabs of tissue equivalent plastic. The images of each plane were processed and converted into GCode, which can be read by a computer controlled micro-milling machine. Starting with a solid piece of tissue equivalent plastic, areas for insertion of bone and lung equivalent material, as well as the region for alignment rod insertion, were removed using an end mill run at 25,000 RPM with a feed rate of 300 mm/min. The total machining time for a phantom is approximately 12 hours.

Upon completion of the machining steps, the bone areas were filled with an epoxy-based mixture and the lung regions were filled with a urethane-based mixture. The fully cured slices were then assembled into a completed phantom using 1/16" diameter tissue equivalent rods. The total time required to complete a mouse was approximately 4 days, but much of the time is either automated machining or curing time.



Figure 1. The two constructed mouse phantoms, one made with coronal slices (top) and one with axial slices (bottom), are shown completely assembled. The coronal sliced phantom is made of nine slices and the axial sliced phantom contains 40 slices. Slices are held in place by two tissue-equivalent supporting rods running perpendicular to the slice plane.

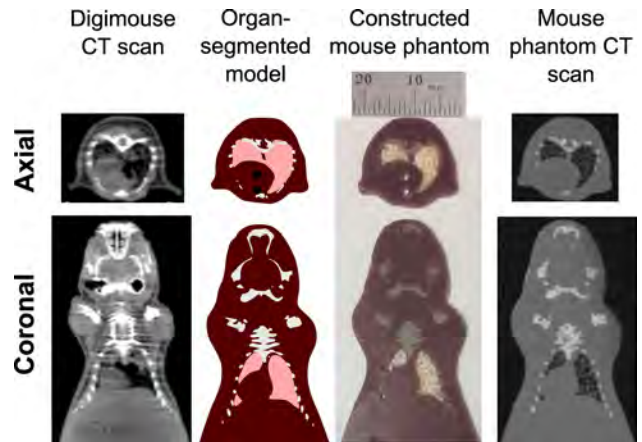


Figure 2. The progression from CT scan of a mouse, to an organ-segmented digital model, to constructed phantom, to verification by CT scan is exhibited for representative slices in both the axial and coronal planes.

Results

Two completed mouse phantoms are shown in Figure 1, one made with coronal slices and the other with axial slices. Example slices from each of the phantoms are shown in Figure 2. The photograph of the slices from the phantom exhibits regions of bone and lung in the appropriate positions within tissue equivalent plastic. The precision milling allowed for intricate details to be

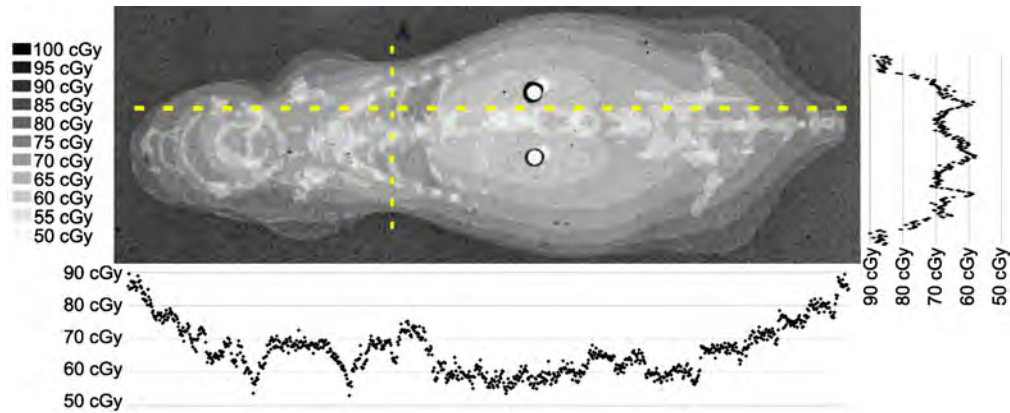


Figure 3. The grayscale dose map obtained from the radiographic film shows variations in absorbed dose across the coronal phantom when exposed to a nominal 70 cGy pulmonary dose of 100 kVp x-rays. Plots of the dose profile along the dashed lines are aligned with their position in the dose map.

replicated while also ensuring their exact positioning within the phantom.

To demonstrate the phantom as a useful tool, the completed mouse phantom was tested for use in dosimetry measurements using Gafchromic radiographic films (Ashland, Covington, KY). Specifically, Gafchromic EBT3 film was used for testing. The film has a total thickness of 280 μm made up of a 30 μm active region with a 125 μm polyester base coating on either side. For demonstration purposes, the EBT3 film was placed between the third and fourth coronal slice counting from the ventral side (6 mm from the bottom of the phantom); the remaining six coronal slices were located above the film. A Westinghouse x-ray machine, operating at 100 kVp and 10 mA without added filtration, was used to irradiate the phantom and film to a nominal 70 cGy pulmonary dose of x-rays at a distance of 50 cm and a rate of 38.7 cGy/min as determined using a Victoreen R-meter. The x-ray source and phantom were oriented to irradiate from the dorsal side, thus the film was perpendicular to the x-ray source. The result of radiographic film dosimetry with the constructed mouse phantoms is shown in Figure 3. The grayscale dose map

shows the various doses of 100 kVp x-rays received across an entire coronal slice of the phantom. The high resolution of the film allows for various dose profiles to be acquired; profiles that pass through the lung region of the mouse phantom are shown in the figure to illustrate this capability.

References

1. Chow, James CL, et al. "Dosimetric variation due to the photon beam energy in the small-animal irradiation: A Monte Carlo study." *Medical physics* 37.10 (2010): 5322-5329.
2. Bazalova, Magdalena, and Edward E. Graves. "The importance of tissue segmentation for dose calculations for kilovoltage radiation therapy." *Medical physics* 38.6 (2011): 3039-3049.
3. Winslow, James Frederick, et al. "Construction of anthropomorphic phantoms for use in dosimetry studies." *Journal of Applied Clinical Medical Physics* 10.3 (2009).
4. Dogdas, Belma, et al. "Digimouse: a 3D whole body mouse atlas from CT and cryosection data." *Physics in medicine and biology* 52.3 (2007): 577. ■



L to R: Tom Hei and Andrew Einstein; Charles Geard and Peter Grabham; David Brenner.

First Irradiations with a Novel Capillary Irradiator

Guy Garty, Helen C. Turner, Maria Taveras, and David J. Brenner

We have developed an innovative automated high-throughput system, the RABIT (Rapid Automated Biodosimetry Tool [1]), for measuring yields of γ -H2AX foci in lymphocytes, using fingerstick-based blood samples and an in-situ multi-well plate platform. In addition to its primary role in triage following a radiological event, a secondary use of the RABIT is to allow performance of epidemiologic studies [2] on radiation sensitivity. We describe here the first irradiations using a compact irradiator, which we have developed for incorporation into the RABIT, allowing rapid, repeatable irradiations of capillary blood samples.

Irradiator Design

The Irradiator, shown in Fig. 1, consists of two 100mCi $^{90}\text{Sr}/^{90}\text{Y}$ sealed disk sources (Eckert & Zeigler, Germany). The sources are placed opposite each other with a 1 cm gap providing a uniform dose field. The tight geometry allows the use of a relatively weak β -emitter, which in turn minimizes the required shielding. Previously, we have tested the dosimetry [4] and showed that the irradiator provides a dose rate of up to 0.35 Gy/sec within a well confined region between the sources.

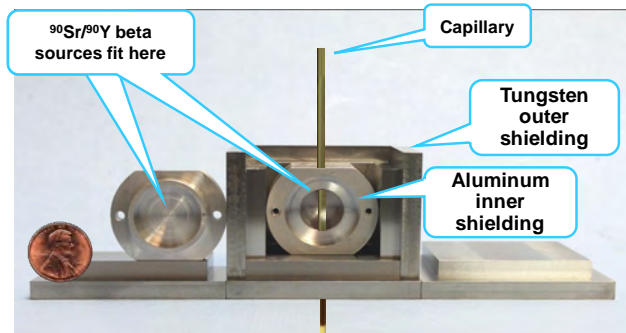


Figure 1. Assembly photo of the irradiator module. The measured dose rate profile is shown at left with a peak of 0.35 Gy/sec.

In the orientation shown in Fig. 1, capillaries can be dipped into the irradiator using the existing capillary gripper of the RABIT [1]. To support testing of the irradiator, independent of the RABIT, we have built a standalone capillary loading mechanism [5], whereby the capillaries pass through it horizontally, similar to the orientation shown in Fig. 2. A programmable linear actuator [5] allows capillaries to be irradiated in one of two modes:

Slow mode: The capillaries are passed, at a constant linear velocity between 0.6 to 200 mm/sec, through the irradiation zone, uniformly irradiating the whole capillary.

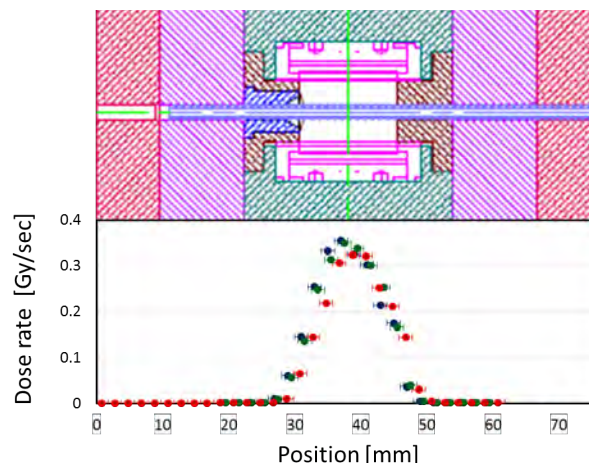


Figure 2. The measured dose rate profile (red, green, and blue symbols represent three independent measurement runs), shown below the irradiator design drawing.

Accelerated mode: The capillary is loaded rapidly such that a segment of the capillary, containing whole blood or an isolated lymphocyte band is brought into the irradiation region (40 mm in Fig. 2), paused for between 2.5 and 20 seconds and rapidly pushed out of the irradiator. In this mode only a 20 mm segment of the capillary is irradiated with the rest of the sample receiving a negligible dose.

Gamma H2AX Analysis

Following informed consent, peripheral blood samples were collected by venipuncture from a healthy human volunteer into a heparinized Vacutainer tube. Thirty μl of blood were pipetted into each capillary tube prefilled with lymphocyte separation medium. Each blood-filled capillary was sealed using Hemato-SealTM tube sealing compound and transported to the irradiator.

Following irradiation, the samples were left at room temperature for an hour to allow the formation of γ -H2AX foci. Either before or after irradiation, the blood samples were spun at 3750 RPM to isolate a lymphocyte band at the interface between the blood plasma and separation medium.

The irradiated lymphocyte band was released into a disposable glass centrifuge tube containing ~ 5 ml fresh RPMI 1640 medium and mixed. Lymphocytes from 3-4 capillaries irradiated to the same dose were merged at this stage. The lymphocytes were pelleted and resuspended in 0.5 ml fresh RPMI. Lymphocytes were spun onto slides and fixed using 2% paraformaldehyde. ■

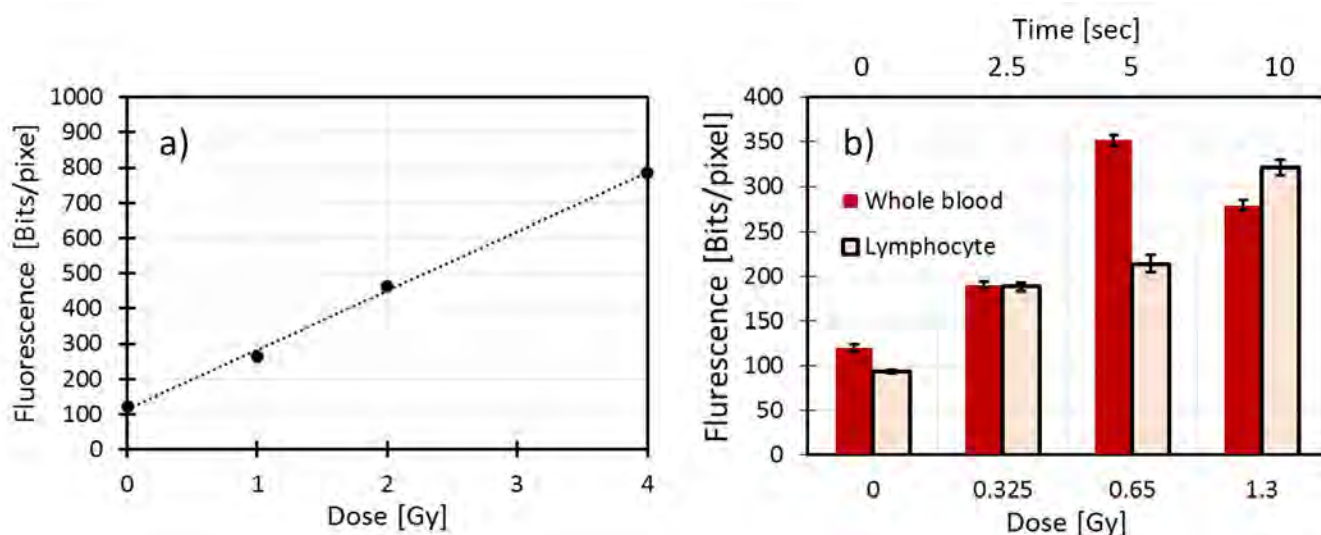


Figure 3. γ -H2AX yields using a) slow mode and b) accelerated mode.

For the γ -H2AX assay, the lymphocytes were permeabilized in 0.5% Triton X for 10 minutes at room temperature and washed three times with 5-minute PBS washes. The cells were blocked with 3% bovine serum albumin (BSA) for 30 minutes and exposed to a rabbit polyclonal γ -H2AX primary antibody (1:750 dilution). After three 10-minute PBS washes, the cells were exposed to an Alexa Fluor[®] 488 goat anti-rabbit secondary antibody (1:1000) for 50 minutes. The cells were washed, and mounted using Vectashield containing DAPI and sealed with a glass coverslip. The slides were imaged using the RABiT imaging system. For each condition tested, 169 40x fields of view, covering an area of about 4 mm x 4 mm and containing a total of 500-2500 cells, were captured and analyzed [3].

Fig. 3 shows the results of the γ -H2AX yields for the two irradiation modes. As expected, the deposited dose is inversely proportional to the velocity with which a sample passes through the radiation field as seen by the linear curve in Fig. 3a.

However, the slow irradiation mode is not really practical for use in the high-throughput RABiT workstation. First of all, it is rather slow. The minimal stroke required for transferring a capillary through the irradiator is >150 mm. At 0.6 mm/sec (2 Gy) this corresponds to over 4 minutes per capillary. Secondly this type of protocol cannot be easily automated as the capillary needs to be released on one side of the irradiator and recaptured on the other side. The RABiT system is better suited for insertion and retraction (without release) of the capillary.

A more efficient method for irradiating a short lymphocyte band within a longer capillary is to rapidly push the capillary into the source holder to the point where the lymphocyte band is centered on the source, pause for the required time, and then either push or retract

the capillary rapidly out of the source holder. This results in irradiation times that are roughly 3-4 times faster. This accelerated irradiation mode is demonstrated in Fig. 3b. Once again a good dose response is observed with much faster irradiation times. To irradiate capillaries to 2 Gy in the accelerated mode, a pause of 15 sec is required, resulting in a throughput of over 200 capillaries/h.

In summary, we have developed a rapid capillary irradiator to allow use of the RABiT biodosimetry workstation as a tool for performing epidemiological DNA-repair capacity studies. As expected, γ -H2AX induction yields were linear with the delivered dose. Depending on the required dose, a throughput of a few hundreds of capillaries per hour is attainable.

References

1. Garty, G., et al., The RABiT: A Rapid Automated Biodosimetry Tool For Radiological Triage II. Technological Developments International Journal of Radiation Biology, 2011. **87**(8): pp. 776-790.
2. Sharma, P.M., et al., High throughput measurement of γ -H2AX DSB repair kinetics in a healthy human population PLoS One 2015, in press.
3. Turner, H.C., et al., Adapting the γ -H2AX assay for Automated Processing in Human Lymphocytes. 1. Technological Aspects. Radiation Research, 2011. **175**(3): p. 282-290.
4. Garty, G., Marino, S., and Brenner, D.J., Mapping the dose profile in a capillary irradiator based on ⁹⁰Sr sealed sources. CRR Annual Report, 2013. p.67.
5. Garty, G., Xu, Y., and Brenner, D.J., A capillary irradiator based on sealed ⁹⁰Sr sources. CRR Annual Report 2012: pp. 87-88. ■

Accelerator-Based Biological Irradiation Facility Simulating Neutron Exposure from an Improvised Nuclear Device

Yanping Xu, Gerhard Randers-Pehrson, Stephen A. Marino, Guy Garty, Andrew Harken, and David J. Brenner

Several scenarios of large-scale radiological events include the use of an improvised nuclear device (IND) that may produce a significant neutron component with prompt radiation exposure [1]. Specifically, the prompt radiation from this type of detonation would be qualitatively similar to that of the gun-type 15 kT device exploded over Hiroshima [2]. In order to assess the significance of the neutron exposure in this type of scenario, a new broad-energy neutron irradiator was designed [3] and built at the Radiological Research Accelerator Facility (RARAF).

This accelerator-driven neutron irradiator provides a neutron beam with energies from 0.2 MeV to 9 MeV that mimic the evaluated energy spectrum produced in the detonation of the atomic bomb at Hiroshima at about 1.5 km distance from ground zero [2]. The neutron radiation spectrum is produced by a mixed beam composed of 5 MeV atomic and molecular ions of hydrogen and deuterium that is used to bombard a thick beryllium (Be) target. The beam composition in the present setup is approximately a 1:2 ratio of protons to deuterons. However, to enable the study of other scenarios, the shape of the neutron spectrum can be modified by adjusting the ratio of protons to deuterons.

The neutron spectrum (Figure 1) was evaluated by making measurements with a proton-recoil proportional counter [5] and a liquid scintillator detector [6], which respond to the broad spectrum of neutrons produced by the accelerator-based neutron target system. The measured proton recoil spectra were unfolded using a standard technique [7, 8].

The dosimetry for the irradiations was performed using a custom tissue-equivalent (TE) gas ionization chamber, placed at the same position where the samples would be during the irradiation. This chamber measures the total dose in the mixed neutron and γ -ray field. To evaluate the ratio of neutron and γ doses, gamma-ray dosimetry was performed separately by replacing the ionization chamber with a compensated Geiger-Mueller dosimeter, which has a very low neutron response. It was seen that the ratio of neutron to γ dose is approximately 4:1.

In order to account for possible variations in dose rate during irradiations, a second TE gas ionization chamber is placed in a fixed location directly in front of the neutron target and used as a monitor. All measurements are made

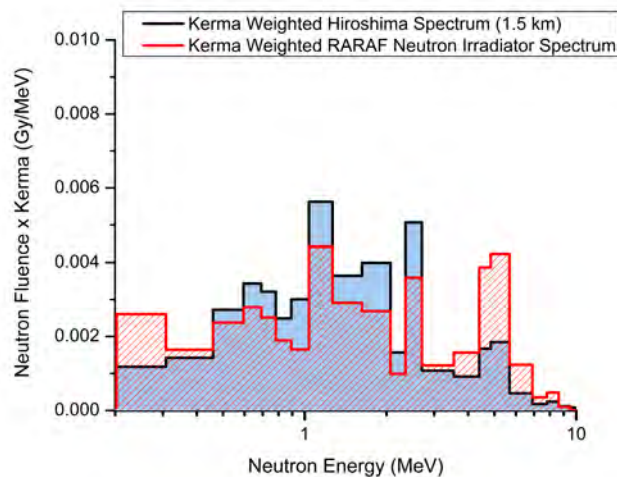


Figure 1. A comparison of the kerma-weighted neutron spectrum generated at RARAF (hashed) with the one at 1.5 km from Hiroshima ground zero (gray).

relative to the signal from the monitor, which is used to determine the dose during irradiation. The neutron dose rate yield at the sample position is $\sim 8.6 \times 10^{-2}$ Gy/hr/uA. The neutron dose rate is $\sim 79\%$ of the total dose rate and the γ -ray dose rate is $\sim 21\%$ of the total dose rate. During the irradiation, the beam current was tuned to and kept at about 17.5 uA, resulting in a neutron dose rate of ~ 1.5 Gy/hr.

Irradiation setup

Due to the requirement for a mixed hydrogen/deuterium beam, the irradiation facility was set up using an un-deflected (zero degree angle) beam line at RARAF. A water cooling chamber cooled the Be target by impinging water onto its copper backing plate. A vertical Ferris wheel-like fixture (Figure 2) was used to hold the customized sample holder tubes (for either blood or mice) arrayed around the Be target. The sample tubes were mounted to rods on the wheel with a constant horizontal orientation at a distance of 190 mm from the center of the target. The sample holders for both mice and ex-vivo irradiation of blood are standard 50 ml conical centrifuge tubes (BD, Franklin Lakes, NJ), which were modified to allow mounting on the wheel. The tubes used for blood irradiations were fitted with a customized cap, designed to hold a 4 ml Vacutainer tube (BD) centered within the conical tube. The tubes used for mouse irradiations were fitted with a cap that allows the tail to pass through and were perforated to make breathing

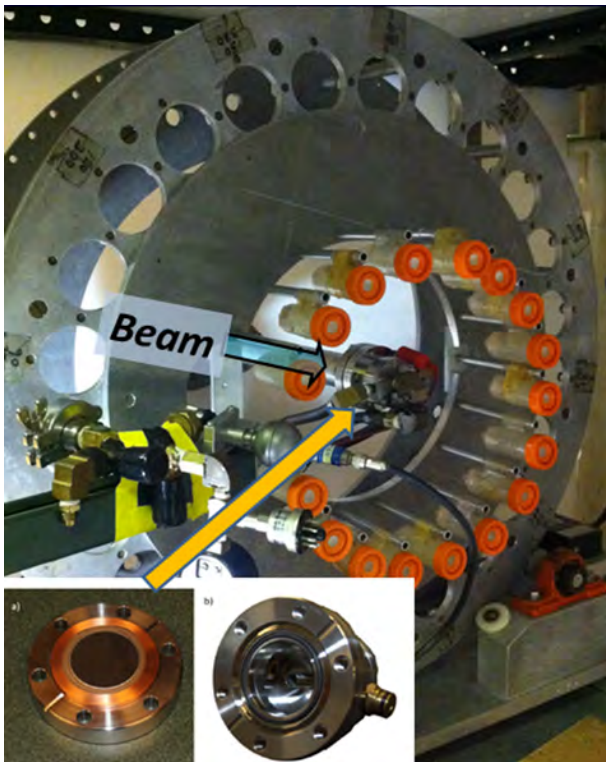


Figure 2. Target and sample fixture. Bottom left, Be target; bottom right, cooling chamber.

holes. As the neutron dose is not azimuthally uniform, the fixture rotates up to 18 samples about the beam axis, providing a more uniform dose. Additionally, the sample tubes were flipped front to back halfway through the irradiation.

For pure photon exposures, a 250 kVp Westinghouse Coronado x-ray machine, which is within 15 m of the neutron target station, was used. This proximity allows for future mixed-field studies, where each sample may be immediately transported to the x-ray machine and irradiated after neutron exposure, with a time gap between the neutron and the photon irradiations of less than 5 min.

Summary

An accelerator-based, broad-energy-range neutron irradiator has been constructed at RARAF. A mixed beam of atomic and molecular deuterons and protons, accelerated to 5 MeV, impinges on a thick beryllium target and the resultant neutron spectrum is the sum of the spectra from the ${}^9\text{Be}(d,n){}^{10}\text{B}$ reaction (higher-energy neutrons) and the ${}^9\text{Be}(p,n){}^9\text{B}$ reaction (lower-energy neutrons). The neutron energy spectrum is manipulated by adjusting the ratio of protons and deuterons to mimic the neutron spectrum expected from an IND exposure, providing an exposure source appropriate for medical triage and biodosimetry studies. Specifically, it mimics the Hiroshima gun-type bomb spectrum at a relevant

distance from the epicenter (1.5 km) and is significantly different from a standard reactor fission spectrum, because the bomb spectrum changes as the neutrons are transported through air. The neutron spectrum of this irradiator was measured and is verified comparable with the Hiroshima bomb spectrum at 1.5 km. About 79% of the radiation dose is from neutrons and 21% is from γ rays.

References

1. Homeland Security Council, National Planning Scenarios (Final Version 21.3). 2006.
2. Egbert SD, Kerr GD, Cullings HM, DS02 fluence spectra for neutrons and gamma rays at Hiroshima and Nagasaki with fluence-to-kerma coefficients and transmission factors for sample measurements. *Radiat Environ Biophys* 2007; 46, 311-25.
3. Xu Y, Garty G, Marino SA, Massey TN, Randers-Pehrson G, Johnson GW, et al., Novel neutron sources at the Radiological Research Accelerator Facility. *Journal of Instrumentation* 2012; 7, C03031.
4. Xu Y, Randers-Pehrson G, Marino S, Garty G, Brenner D, Broad Energy Range Neutron Spectroscopy with a Liquid Scintillator and a Proportional Counter: Application to a Neutron Spectrum Similar to that from an Improvised Nuclear Device. *Nuclear Instruments and Methods in Physics Research Section A: Accelerators, Spectrometers, Detectors and Associated Equipment* 2015; Submitted.
5. Tagziria H, Hansen W, Neutron spectrometry in mixed fields: proportional counter spectrometers. *Radiation Protection Dosimetry* 2003; 107, 73-93.
6. Klein H, Neutron spectrometry in mixed fields: NE213/BC501A liquid scintillation spectrometers. *Radiation Protection Dosimetry* 2003; 107, 95-109.
7. Pozzi SA, Flaska M, Enqvist A, Pázsit I, Monte Carlo and analytical models of neutron detection with organic scintillation detectors. *Nuclear Instruments and Methods in Physics Research Section A: Accelerators, Spectrometers, Detectors and Associated Equipment* 2007; 582, 629-37.
8. Reginatto M, Goldhagen P, Neumann S, Spectrum unfolding, sensitivity analysis and propagation of uncertainties with the maximum entropy deconvolution code MAXED. *Nucl Instr Meth A* 2002; 476, 242-46.
9. Verbinski VV, Burrus WR, Love TA, Zobel W, Hill NW, Textor R, Calibration of an organic scintillator for neutron spectrometry. *Nucl Instr Meth* 1968; 65, 8-25. ■

Depletion and Recovery Kinetics of Long-term and Short-term Hematopoietic Stem Cells in C57BL/6 Mice Irradiated with γ -rays

Erik F. Young and Lubomir B. Smilenov

An important indicator for the acute effects of radiation and for biodosimetry is the depletion and recovery kinetics of nucleated blood cells. It is well known that an insult to the hematopoietic system will generate effects that are not limited in scope to hematologic endpoints. There is an interrelationship between the correct function of the hematopoietic system and other organ systems. Systemic infections and mortality are known to accompany the reduction of peripheral blood cell counts that result from radiation exposure [1, 2]. Circulating leukocyte counts form the basis for current clinical assessment and triage of irradiated human patients and the depletion and recovery kinetics of these circulating cells form the basis for the HEMODOSE dosimetry application currently available via the Internet.

Comparative studies using mouse models have been employed extensively for obtaining data on the response to radiation in the range of doses that are lower than the LD50 [3,4]. Interestingly, such studies lack precise analysis of the depletion and recovery kinetics of the bone marrow hematopoietic stem cell (HSCs) populations at longer time points after irradiation. This is a critical compartment within the mouse, which is directly responsible for the recovery and replenishment of circulating nucleated cells in the blood. The goal of this study is to acquire data on the depletion and recovery kinetics of both long term HSCs (LT-HSCs) and short term HSCs (ST-HSCs) that can be used for radiation risk assessment, radiation biodosimetry, and experimental planning.

Toward this goal, we monitored depletion and recovery kinetics of HSCs in C57BL/6 mice for up to a month after irradiation with different doses of γ -rays and here we present the results from this study. There are two populations of HSC in the mouse bone marrow [5]. The first of these is the LT-HSCs that have the ability to confer long-term reconstitution of all lineages of the hematopoietic system to a lethally irradiated mouse and subsequent secondary recipients. The second population is the ST-HSC, which arises from LT-HSCs but has more limited self-renewal capacity and cannot be considered truly pluripotent. While it is true that ST-HSCs can mediate recovery of lethally irradiated recipients for up to several months after transplantation, ST-HSCs are not capable of further hematopoiesis in subsequent secondary recipients. Monitoring the depletion and recovery

kinetics of these two cell types in response to radiation will give us important information on the effect of radiation on the hematopoietic system and specifically on its capacity to recover from radiation insults.

Methods

All animal husbandry and experimental procedures were conducted in accordance with applicable federal and state guidelines and approved by the Institutional Animal Care and Use Committees of Columbia University Medical Center. Eight-week-old male C57BL/6 mice (Charles River, LD50/30 of 7.00 Gy) were irradiated with doses of 1, 3 and 6 Gy γ -rays. Bone marrow was collected at 1, 2, 7, 14, and 30 days after the irradiation. The bone marrow counts were determined using 6-color staining that includes antibodies against mouse Sca1, c-Kit, Flt3, CD34, Il-7R α and anti-lineage cocktail. The distribution of subpopulations was determined using a multicolor LSRII flow cytometer. Two mice per condition were used.

Results and discussion

C57BL/6 mice are used extensively in radiation studies but surprisingly there are no data on the status of

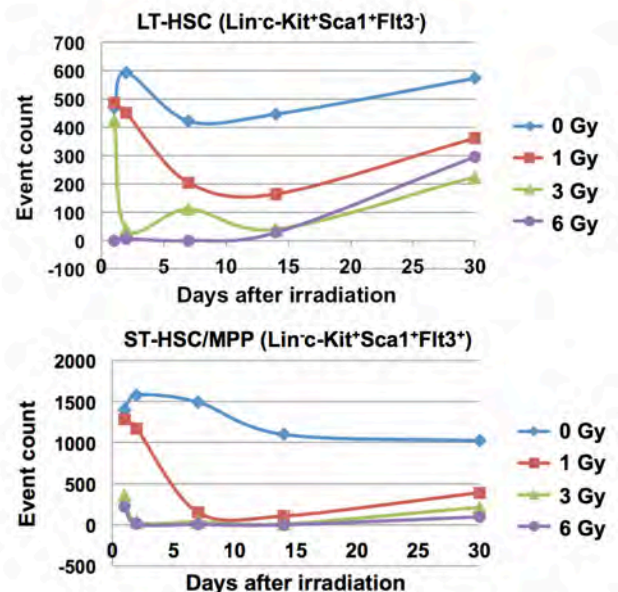


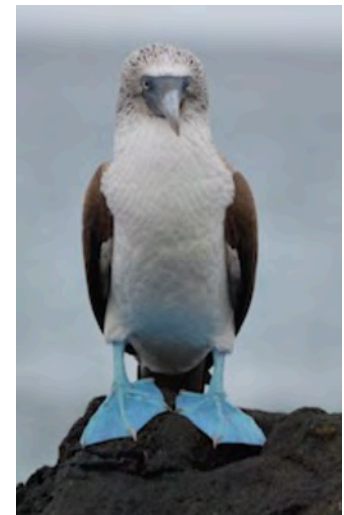
Figure 1. Post-irradiation depletion and recovery kinetics of long term (top) and short term (bottom) hematopoietic stem cells of C57BL/6 mice.

their HSCs after irradiation. The goal of this work is to acquire data on the depletion and recovery kinetics of both LT-HSCs and ST-HSCs that can be used in radiation studies. The results of the experiments (Fig. 1) show a rapid decrease in the numbers of both cell types for doses of 3 Gy and 6 Gy. 1 Gy of γ -radiation leads to 50% reduction of the LT-HSC counts 7 days after irradiation. The recovery process starts around 15 days after irradiation, with the LT-HSCs reaching 50-70% of the initial counts after another two weeks. ST-HSCs are replenished by the proliferative activity of LT-HSCs and correspondingly we see a delay in their recovery. We failed to observe a complete recovery of HSCs 30 days after irradiation irrespective of the dose. The overall conclusion from this study is that the mouse hematopoietic system is sufficiently robust to recover from high doses of radiation that approach the LD50. In a three-week period after irradiation, circulating leukocytes (commonly assessed in several biodosimetry modalities) will be generated from an incompletely recovered hematopoietic apparatus. The genomics, metabolomics and epigenetic characteristics of leukocytes sourced from

a hematopoietic system at equilibrium versus one that is undergoing active reconstitution and replenishment-associated expansion could be different. Such differences could be the source of noise, or of new dosimetry-competent markers for future use. Irrespective of these potential differences, the quantity of material available from circulating nuclear cells in the blood will be reduced. Taken together, these points illustrate the need for extra care in analyzing mice that are subject to irradiation with doses of 1 Gy and higher.

References

1. Dainiak, N., et al., Disaster Med Public Health Prep, 2011. **5**(3): p. 202-12.
2. Brook, I., et al., Mil Med, 2002. **167**(2 Suppl): p. 105-6.
3. Maks, C.J., et al., Radiat Res, 2011. **176**(2): p. 170-6.
4. Pecaut, M.J., G.A. Nelson, and D.S. Gridley, In Vivo, 2001. **15**(3): p. 195-208.
5. Liu, L., et al., PLoS One, 2012. **7**(2): e31300. ■



*Top (l to r): Howard Lieberman following in the footsteps of Darwin with a Galapagos Tortoise; Sea Lion.
Bottom (l to r): Iguana; Darwin's Finch; Blue-footed Booby.*

Automated FISH on the RABiT System

Mikhail Repin, Sergey Pampou^a, Helen C. Turner, Guy Garty, and David J. Brenner

Traditional cytogenetic assays are generally considered low throughput due to sample preparation using large volumes of reagents in individual flasks and tubes, and image analysis of large areas of individual microscope slides. The RABiT (Rapid Automated Biodosimetry Tool) was developed in the Center for Radiological Research to increase the speed of radiation dose estimation using different biological dosimetry assays [1, 2]. In the USA there are many commercial high-throughput biotech robotic systems that can potentially be used with RABiT protocols for cytogenetic (micronucleus and dicentric) assays [3].

We proposed the combined use of plates and tubes in racks compatible with ANSI/SLAS microplate formats to enable the use of commercial robotic systems for next generation high-throughput radiation biomarker analysis [3]. By introducing these platforms, we simplified the task of automation of high-throughput sample preparation for cytogenetic-based biodosimetry assays on preexisting commercial biotech robotic systems, such as cell::explorer (Perkin Elmer, USA), which is available for use at the Columbia Genome Center (Fig. 1).

The fluorescence *in situ* hybridization (FISH) technique has become a powerful tool in chromosome analysis including the dicentric assay using telomere and centromere probes, and MBAND-FISH analysis that simplifies the task of automated image analysis (see also publications of Garty *et al.* and Bigelow *et al.* in this annual report) [4-6]. We developed a FISH protocol for multistep fluorescent *in situ* hybridization with PNA centromere/telomere probes to run on the same RABiT system that is used for cytogenetic sample preparation in 96-well imaging plates (Fig. 2).

The newly developed protocol allows preparation of cytogenetic samples with FISH-labelling of chromosomes (Fig. 3) on the automated RABiT system without using specialized cytogenetics systems (e.g. automated hybridization station, automated station for metaphase preparations, automated station for work with glass coverslips, auto-stainer station).

In summary, we have demonstrated that universal biotech robotic systems and microplate formats can be used successfully for all stages of high-throughput preparation of cytogenetic samples and FISH, from blood collection into microtubes to image analysis, without using specialized cytogenetics stations.



Figure 1. Common scheme of the automated cytogenetics-based biodosimetry assay.

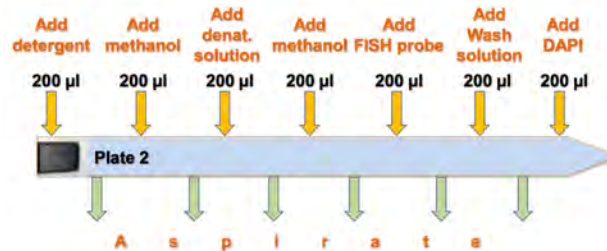


Figure 2. The scheme of the RABiT program for fluorescent *in situ* hybridization on dicentric assay samples in a 96-well imaging plate.

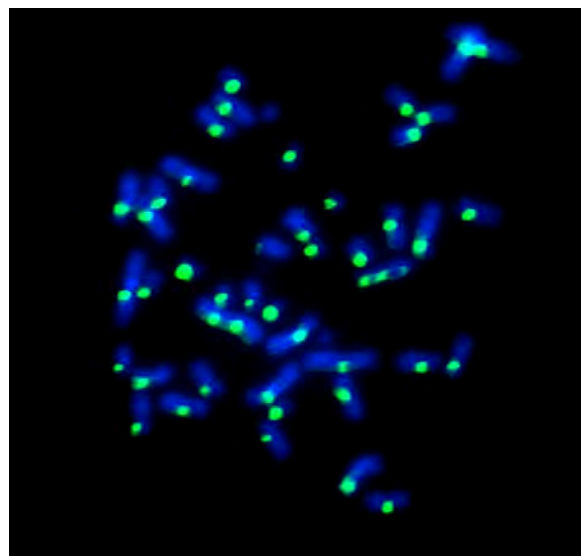


Figure 3. Centromere-labeled chromosomes of human lymphocytes prepared from 20 µl of irradiated (4.0 Gy, ¹³⁷Cs γ-rays) peripheral blood in a 96-well plate with an optically clear bottom on the cell::explorer robotic system.

^aDepartment of Systems Biology, Columbia University Medical Center.

References

1. Garty, G., et al., *The RABIT: a rapid automated biodosimetry tool for radiological triage*. Health Phys, 2010. **98**(2): p. 209-17.
2. Turner, H.C., et al., *Adapting the γ -H2AX Assay for Automated Processing in Human Lymphocytes. 1. Technological Aspects*. Radiation research, 2010. **175**(3): p. 282-290.
3. Repin, M., et al., *Next Generation Platforms for High-Throughput Biodosimetry*. Radiat Prot Dosimetry, 2014.
4. Shi, L., et al., *A modified system for analyzing ionizing radiation-induced chromosome abnormalities*. Radiat Res, 2012. **177**(5): p. 533-8.
5. Cartwright, I.M., M.D. Genet, and T.A. Kato, *A simple and rapid fluorescence in situ hybridization microwave protocol for reliable dicentric chromosome analysis*. J Radiat Res, 2013. **54**(2): p. 344-8.
6. Durm, M., et al., *Fast-FISH technique for rapid, simultaneous labeling of all human centromeres*. Cytometry, 1998. **31**(3): p. 153-62. ■

Automated Scoring of Dicentric Chromosomes

Guy Garty, Mikhail Repin, and David J. Brenner

For many decades, the dicentric chromosome assay has been the “gold standard” for radiation biodosimetry, because ionizing radiation is fairly specific for inducing dicentric chromosomes. It has been used in every major radiological incident over the past 30 years, including Fukushima [1]. Historically, this assay is based on morphologic image analysis of Giemsa [2] or DAPI [3] stained metaphase spreads, which have defied useful rapid automation, due to issues of background, shape variation, and chromosome overlap [4]. Thus, in practice the dicentric assay remains either fully manual or, at best, semi-automated. Using these standard approaches, the highest throughput that can be achieved by a single lab without full automation is <80 samples per day [5, 6], and even national and international laboratory networks are expected to have throughputs of only a few hundred samples per day [7-9].

In the Center for Radiological Research, we introduced next generation biodosimetry platforms, which utilize tubes in racks and plates with ANSI/SLAS microplate format [10, 11]. This allows automation of the

process of dicentric assay sample preparation on biotech robotic systems in a high-throughput manner – 96 samples simultaneously. In parallel with developing robotic sample handling protocols and a dedicated imaging system, we have been investigating algorithms for dicentric identification and scoring.

Several approaches to automated morphometric detection of dicentric chromosomes are available. However, they are computationally difficult, requiring parallel computing to achieve any reasonable throughput [3]. An alternative technique under development by us and others [12] is the use of FISH probes specific for centromeres and telomeres of all human chromosomes. In this case, dicentric detection becomes relatively easy; one needs to score the chromosomes with 0, 1 or 2 bright centromeric spots as shown in Fig. 1a.

To perform this analysis we have modified the RABiT image analysis software to perform dicentric analysis as follows:

- The background-subtracted DAPI image is binarized

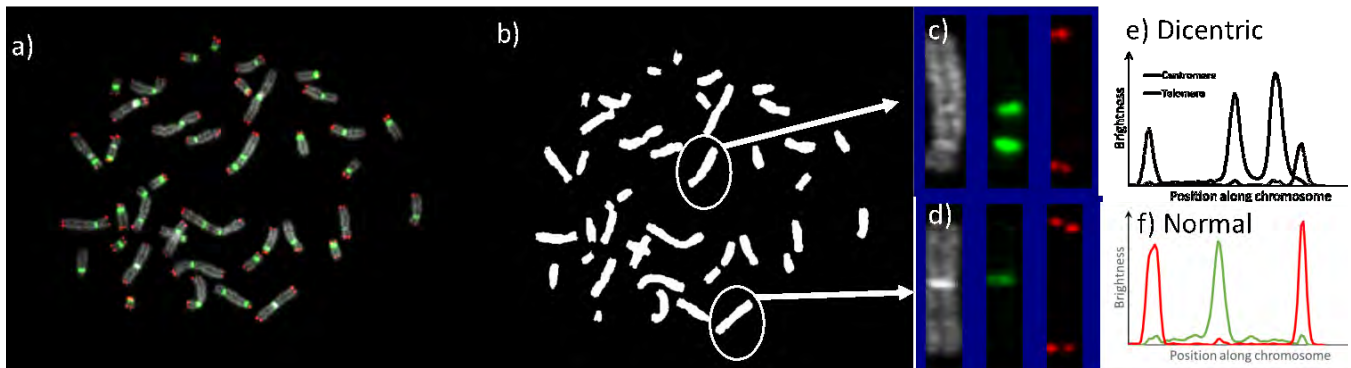


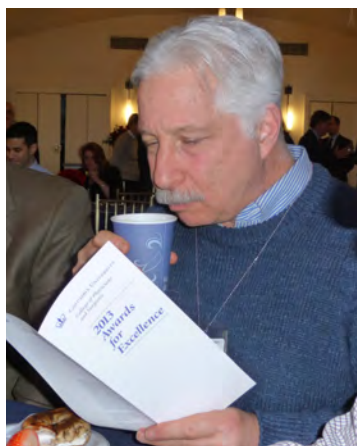
Figure 1. Example of Dicentric analysis using FISH probes. a) Chromosomes are stained with a centromeric probe (green) and telemetric probe (red) and counterstained with DAPI (gray). b) The chromosomes are identified from the DAPI channel. c) and d) show cropped images of a c) dicentric and d) normal chromosome. The intensity profile along each of the chromosomes is shown in e) and f).

using an adaptive threshold algorithm, which assigns each pixel a value of 1 if its value is larger than pixels in a 99x99 pixel neighborhood and zero otherwise (see Fig. 1b).

- Chromosomes are located as Binary Large Objects (BLOBs) [13]. BLOBs within a size range of 1-50 μm^2 and having an aspect ratio greater than 2 are selected for further analysis.
- The area of each BLOB is extracted from the probe images (Fig. 1c, d) and the brightness is integrated across the long axis, generating a trace of the brightness of both probes along the chromosome (Fig. 1e, f). Brightness maxima exceeding designated thresholds are located for each trace and the full-width at half maximum (FWHM) about each selected maximum identifies the bounds for that probe.
- Chromosomes are scored as acentric, dicentric or normal based on the number of spots detected.

References

1. Lee, J.K., et al., Cytogenetic biodosimetry for Fukushima travelers after the nuclear power plant accident: no evidence of enhanced yield of dicentrics. *Journal of Radiation Research*, 2012. **53**(6): p. 876-881.
2. Romm, H., et al., Automatic scoring of dicentric chromosomes as a tool in large scale radiation accidents. *Mutat Res*, 2013. **756**(1-2): p. 174-83.
3. Rogan, P.K., et al., Automating dicentric chromosome detection from cytogenetic biodosimetry data. *Radiation Protection Dosimetry*, 2014. **159**(1-4): p. 95-104.
4. Bayley, R., et al., Radiation dosimetry by automatic image analysis of dicentric chromosomes. *Mutat Res*, 1991. **253**(3): p. 223-35.
5. Martin, P.R., et al., Sample Tracking in an Automated Cytogenetic Biodosimetry Laboratory for Radiation Mass Casualties. *Radiat Meas*, 2007. **42**(6-7): p. 1119-1124.
6. Vaurijoux, A., et al., Strategy for population triage based on dicentric analysis. *Radiat Res*, 2009. **171**(5): p. 541-8.
7. Blakely, W.F., et al., WHO 1st consultation on the development of a global biodosimetry laboratories network for radiation emergencies (BioDoseNet). *Radiat Res*, 2009. **171**(1): p. 127-39.
8. IAEA, IAEA Response Assistance Network Incident and Emergency Center: EPR-RANET Technical Document. 2006, International Atomic Energy Agency: Vienna.
9. Miller, S.M., et al., Canadian Cytogenetic Emergency network (CEN) for biological dosimetry following radiological/nuclear accidents. *Int J Radiat Biol*, 2007. **83**(7): p. 471-7.
10. Repin, M., et al., Next generation platforms for high-throughput biodosimetry. *Radiation Protection Dosimetry*, 2014. **159**(1-4): p. 105-110.
11. Repin, M., et al., The use of biotech robots for high-throughput preparation of biodosimetry samples, in *CRR Annual Report 2013, 2014*. pp. 81-82.
12. M'kacher, R., et al., New tool for biological dosimetry: Reevaluation and automation of the gold standard method following telomere and centromere staining. *Mutation Research/Fundamental and Molecular Mechanisms of Mutagenesis*, 2014. **770**(0): p. 45-53.
13. Suzuki, S. and K. Abe, Topological structural analysis of digitized binary images by border following. *Computer Vision, Graphics, and Image Processing*, 1985. **29**(3): p. 396. ■



L to R: Christine Hellweg; Howard Lieberman; J.D. Knotts, Sally Amundson, and Norman Kleiman.

Development of an Automated High-throughput System for Detection of Intrachromosomal Rearrangements

Alan W. Bigelow, Guy Garty, Adayabalam S. Balajee, Yanping Xu, Charles R. Geard, and David J. Brenner

The multicolor band (mBAND) fluorescence in situ hybridization [1] assay is a well-accepted cytogenetic technique for detecting intrachromosomal rearrangements [2, 3]. Intrachromosomal rearrangements are routinely detected by mBAND, a refined fluorescence in situ hybridization (FISH) technique that uses overlapping fragments of human chromosome-specific DNA labeled with five different fluorochromes in varying combinations [1, 2]. Alterations in the spatial ordering of colored fragments along the entire chromosome length either with or without the involvement of centromeres can be detected by visual examination. Conventional scoring, however, is a manual process with a rate of about 100-150 metaphase spreads per day per person.

Imaging and manual scoring of mBAND preparations is labor-intensive, as it involves a careful inspection of a two-dimensional image of the painted chromosome. Furthermore, different degrees of chromosome condensation affect the relative width/length of each of the colored fragments. Since intrachromosomal rearrangements are less frequent than interchromosomal rearrangements, rapid imaging and analysis using an automated system may prove to be a distinct advantage. With this objective, an automated high throughput mBAND system with rapid imaging and analysis algorithms was developed at the Center for High-Throughput Minimally Invasive Radiation Biodosimetry (Center for Radiological Research, Columbia University Medical Center) for rapid imaging and automated scoring to extend and enhance the functionality of the Rapid Automated Biodosimetry Tool (RABiT) for large scale analysis of human samples in a triage scenario [4, 5]. The name RABiT-BAND has been coined for the integration of RABiT with an automated mBAND-based assay.

Imaging System

The imaging system comprises an automated routine for acquiring multicolor images on a custom-designed, epi-illumination fluorescence microscope; a schematic diagram for this system is shown in Fig. 1.

Each multicolor image of an mBAND chromosome is a combination of an image series representing each of the fluorophores used in the technique: DAPI, DEAC, FITC, Texas Red, Spectrum Orange, and Cy5. DAPI stains the entire DNA of all the chromosomes while the other 5 fluorophores mark specific regions along the length of the chromosome to be banded. The automated image-acquisition routine manages: the wavelength of a switchable excitation light source, the position of fast

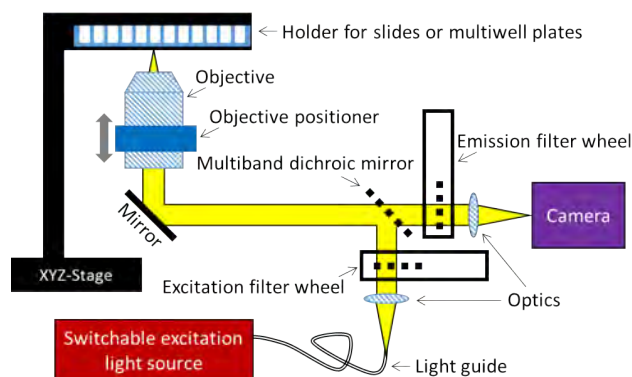


Figure 1. Schematic of the light path and components of the RABiT-BAND system.

excitation and emission filter wheels, and the exposure parameters for the camera. The specifications on the custom multiband dichroic mirror and the sets of excitation and emission filters have been optimized for the mBAND assay. High-resolution images are acquired using a 60X 1.49 NA oil-immersion objective. The sample holder can accommodate up to four sample slides or a multiwell plate and is manipulated by a mechanical stage. Fine focusing is achieved using a precision objective positioner. Sample positioning and image acquisition are managed through computer control routines designed in-house.

Automated mBAND Scoring

Two approaches are available on our system for mBAND image processing. One approach involves a MATLAB image processing program that was written in-house to produce a pseudocolor mBAND image through the following steps: 1) cropping mBAND chromosomes from an image of metaphase chromosomes, 2) removing background signal, 3) normalizing gray scale values, 4) setting thresholds for binary images, and 5) solving for the pseudocolor banding pattern using color-ratio analysis. Bands in these pseudocolor images correspond to the regions of 11 probe combinations along the length of the chromosome. While this two-dimensional approach is the conventional form of mBAND image processing, it involves a significant effort by the user to set threshold levels to produce binary images for the fluorophores that will result in consistent multicolor mBAND images.

To achieve automated high throughput image processing and scoring, a routine was devised to bypass production of two-dimensional pseudocolor renditions of mBAND samples. More efficiently, analysis of the

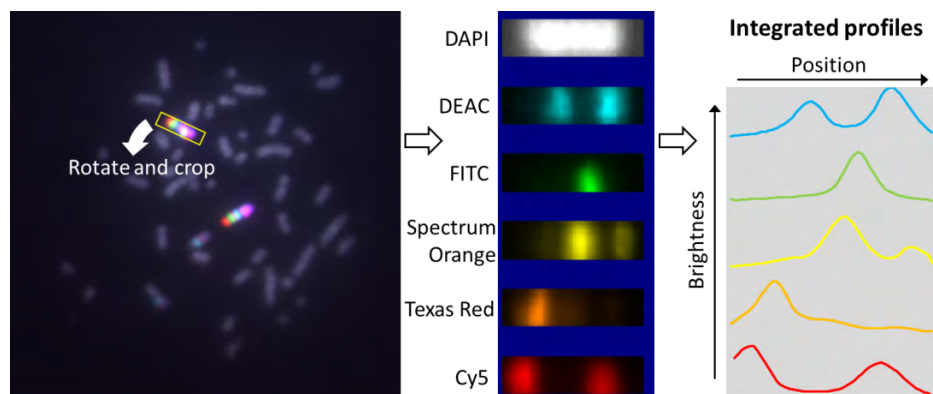


Figure 2. Fundamental aspects of the automated RABiT-BAND image analysis algorithm displayed from left to right: 6-color composite image to capture a chromosome 5 sample in a metaphase spread; cropped image series of probes across that chromosome 5 sample; and integrated profiles across that chromosome 5 sample for probes DEAC (blue), FITC (green), Spectrum Orange (yellow), Texas Red (orange) and Cy5 (red).

images is performed by locating the stained chromosome, and integrating the brightness of each probe along the length of the chromosome, as depicted in Fig. 2. This produces a probe distribution for each probe along a single chromosome. In this mode, the probe distributions along a particular chromosome are compared with chromosome-specific scoring criteria to determine any chromosome rearrangements.

The current image analysis algorithm, implemented in OpenCV, is as follows. The background-subtracted DAPI image is binarized using an adaptive threshold algorithm which assigns each pixel a value of 1 if its value is larger than that of pixels in a 99x99 pixel neighborhood and zero otherwise. Chromosomes are then located as Binary Large Objects (BLOBs), using the algorithm of Suzuki and Abe [6]. BLOBs within a size range of 100-5000 pixels (1-50 μm^2) and having an aspect ratio greater than 2 are selected for further analysis.

The area of each BLOB is extracted from the probe images and the brightness is integrated across the long axis, generating a trace of the brightness of all five probes along the chromosome (see Fig. 2). Brightness maxima exceeding designated thresholds are located for each trace and the full-width at half maximum (FWHM) about each selected maximum identifies the bounds for that probe. Each combination of probes along the length of the chromosome is assigned a character, generating a string corresponding to that chromosome's trace. The string is then compacted by removing duplicate consecutive characters and isolated characters, forming a string corresponding to the chromosome's band structure. The string is then compared with the solution for an intact chromosome to score whether or not there is a rearrangement of the chromosome structure, such as in a pericentric or paracentric inversion. The algorithm recognizes a complete reversal of the string as a healthy chromosome. In the data shown here we have used the standard Chromosome 5 probe set resulting in the string PXHAEDFBSQU or its reverse (UQSBFDEAHXP), depending on the chromosome orientation. Probe sets for different chromosomes would naturally result in a different string, which would need to be determined before use.

In terms of throughput, the system described here is capable of acquiring and analyzing several metaphases per minute, requiring roughly 10 sec per metaphase for image acquisition and, after the algorithm recognizes a metaphase, 3 sec per metaphase for analysis.

Experiment

RABiT-BAND represents an automated version of the standard mBAND [2] assay for detecting chromosomal inversions. Of relevance here is that chromosomal inversions have been considered to be specific markers of high-LET (e.g. neutron) exposure [3]. In the mBAND assay [2] Fluorescent In-Situ Hybridization (FISH) is used to "barcode" a given chromosome with different-color fluorochromes.

In this work, the goal was to assess both our new automated high-throughput detection system and the utility of inversions as a biomarker to separately assess the neutron component in a mixed neutron-photon field. In practice, the standard mBAND analysis technique used in epidemiological studies [7] is relatively laborious and time-consuming, and currently not appropriate for high-throughput analysis. However, with the development of RABiT-BAND, to measure intrachromosomal aberrations with high throughput, it is a reasonable hypothesis that this approach will provide an automated high-throughput methodology suitable for separating out the neutron component in a mixed neutron-photon field.

Whole blood from healthy volunteers was irradiated using neutron doses resulting from a mixed proton/deuteron beam impinging on a thick beryllium target to simulate neutron spectra from an improvised nuclear device [8]. The whole blood cultures were set up with PHA and harvested after 72 h of culture including a colcemid treatment (0.1 $\mu\text{g}/\text{ml}$) for the last 18 h. The mBAND procedure, as described by MetaSystems [1, 2, 9], was used for labeling chromosome 5. The samples were analyzed with our new automated high-throughput RABiT-BAND system and also using a commercial MetaSystems mBAND system.

Our automated RABiT-BAND scoring system detected consistent patterns in undamaged chromosomes, and was successful at detecting paracentric inversions induced by our first IND-simulated neutron exposures.

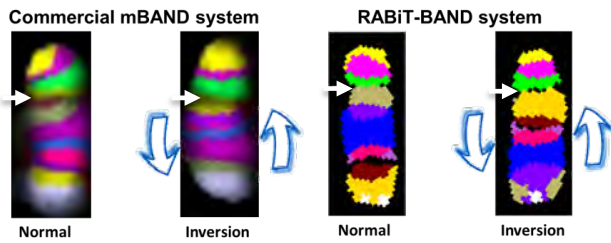


Figure 3. Processed images of a specific chromosome 5 pair showing a paracentric inversion, obtained from a commercial mBAND system and also from our RABiT-BAND system using automated scoring software. The paracentric inversion in this neutron-irradiated sample is seen as a reversal of the banding pattern along the long arm of the chromosome. The small white arrows denote the position of the centromere.

Fig. 3 shows an example of a paracentric inversion that was detected by both the commercial system and by our RABiT-BAND system. While Fig. 3 depicts 2D-image results from a neutron-irradiated lymphocyte, the corresponding 1D character-string result is PXHAEDFBSQU for the normal chromosome 5, and PXHQSBFDEAU for the chromosome 5 expressing a paracentric inversion (underlined segment) along the long arm of the chromosome.

References

1. I. Chudoba, A. Plesch, T. Lörch, J. Lemke, U. Claussen, and G. Senger, "High resolution multicolor-banding: a new technique for refined FISH analysis of human chromosomes," *Cytogenetic and Genome Research* **84**, 156-160 (1999).
2. I. Chudoba, G. Hickmann, T. Friedrich, A. Jauch, P. Kozlowski, and G. Senger, "mBAND: a high resolution multicolor banding technique for the detection of complex intrachromosomal aberrations," *Cytogenetic and Genome Research* **104**, 390-393 (2004).
3. M. Hada, Y. Zhang, A. Feiveson, F. A. Cucinotta, and H. Wu, "Association of inter- and intrachromosomal exchanges with the distribution of low- and high-LET radiation-induced breaks in chromosomes," *Radiation research* **176**, 25-37 (2011).
4. A. Salerno, J. Zhang, A. Bhatla, O. V. Lyulko, J. Nie, A. Dutta, G. Garty, N. Simaan, G. Randers-Pehrson, Y. L. Yao, and D. J. Brenner, "Design Considerations for a Minimally Invasive High-Throughput Automation System for Radiation Biodosimetry," *Automation Science and Engineering*, 2007. CASE 2007. IEEE International Conference on, 846-852 (2007).
5. G. Garty, Y. Chen, H. C. Turner, J. Zhang, O. V. Lyulko, A. Bertucci, Y. Xu, H. Wang, N. Simaan, G. Randers-Pehrson, Y. Lawrence Yao, and D. J. Brenner, "The RABiT: A Rapid Automated Biodosimetry Tool for radiological triage. II. Technological developments," *International Journal of Radiation Biology* **87**, 776-790 (2011).
6. S. Suzuki and K. Abe, "Topological structural analysis of digitized binary images by border following," *Computer Vision, Graphics, and Image Processing* **29**, 396 (1985).
7. M. P. Hande, T. V. Azizova, C. R. Geard, L. E. Burak, C. R. Mitchell, V. F. Khokhryakov, E. K. Vasilenko, and D. J. Brenner, "Past exposure to densely ionizing radiation leaves a unique permanent signature in the genome," *American journal of human genetics* **72**, 1162-1170 (2003).
8. Y. Xu, G. Garty, S. A. Marino, T. N. Massey, G. Randers-Pehrson, G. W. Johnson, and D. J. Brenner, "Novel neutron sources at the Radiological Research Accelerator Facility," *Journal of instrumentation : an IOP and SISSA journal* **7**, C03031 (2012).
9. G. Senger, J. Ragoussis, J. Trowsdale, and D. Sheer, "Fine mapping of the human MHC class II region within chromosome band 6p21 and evaluation of probe ordering using interphase fluorescence in situ hybridization," *Cytogenetics and cell genetics* **64**, 49-53 (1993). ■



L to R: Peter Grabham; Norman Kleiman, Igor Shuryak, and Vladimir Ivanov; David Cuniberti.



Analysis of Partial Body Irradiation using γ -H2AX Foci

Guy Garty, Manuela Buonanno, and David J. Brenner

Early development of assays for the Rapid Automated Biodosimetry Tool (RABiT) has focused on uniform irradiations; we have validated the RABiT's performance both on blood from healthy volunteers irradiated ex-vivo [1], and on blood from total body irradiation patients. This scenario, while very useful for testing and validation of assays, is not a realistic model of most types of exposure.

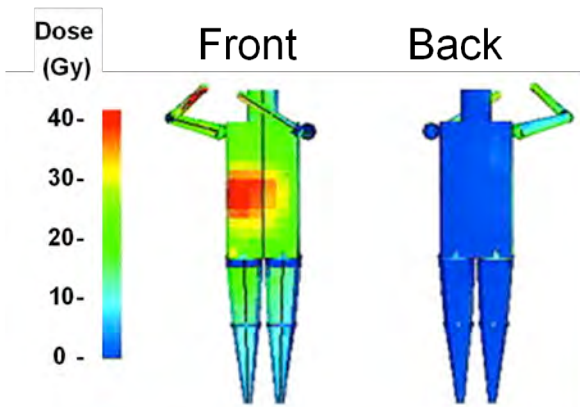


Figure 1. Simulated γ -ray dose distribution in worker A in the Tokai-Mura criticality accident.

As an example, Fig. 1 shows the actual dose received by worker A in the Tokai-Mura criticality accident [2]. The maximal local dose was about 40 Gy of γ -rays and 20 Gy of neutrons. This dose is five times higher than the averaged whole-body dose of neutrons and three times higher than that of γ -rays, which would be obtained from standard biodosimetry. This heterogeneous dose distribution indeed resulted in a much better description of the clinical outcomes than the original uniform dose estimate [2].

In an improvised nuclear device scenario, it is expected that most individuals will be indoors during the detonation [3] and will be partially shielded by structural materials. Even those outside are likely to be shielded from direct radiation by buildings.

In a radiological dispersal device scenario, on the other hand, the bulk of the radioactive material is aerosolized [3]. In this case most of the exposure will be due to inhaled radionuclides. Different possible radionuclides will accumulate in different organs. For example $^{137}\text{CsCl}$, being extremely soluble, is absorbed rapidly from the lungs and the digestive tract, distributing uniformly amongst the skeletal muscle, skin, lung and

kidney [4]. $^{238}\text{PuO}_2$, on the other hand, is insoluble and will remain in the lungs providing localized irradiation [5].

In such cases, it would be medically more useful to report the fraction of the body irradiated and the dose absorbed in that fraction, rather than the total body average, which is currently reported.

As the RABiT measures radiation effects in circulating blood lymphocytes, an acute partial body irradiation will result in a fraction of the lymphocytes (roughly equal to the mass fraction of the body irradiated) expressing marked radiation effects, with the remaining fraction expressing background or close to background levels. This will be manifest in an over dispersed distribution of damage amongst the lymphocytes.

The fraction of irradiated lymphocytes and dose delivered to them is currently determined based on Dolphin's contaminated Poisson method [6]. In this method, used routinely in partial body irradiation dosimetry [6-8], the distribution of micronuclei is assumed to be due to a subpopulation of exposed lymphocytes, whose number of micronuclei is Poisson distributed (with an average yield, Y , of micronuclei) while the remaining, unexposed, lymphocytes have no micronuclei.

We present here adaptation of this method to γ -H2AX yields and first tests using hemi-body irradiation of mice

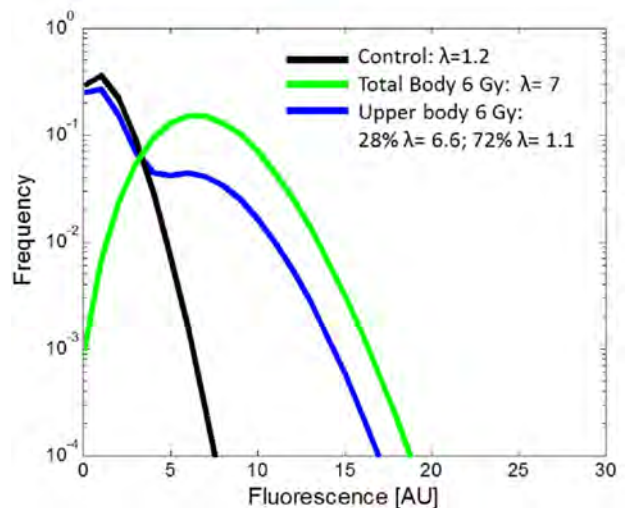


Figure 2. Double Poisson fit to the γ -H2AX yields for mouse upper body irradiation (blue). The fit results for total body irradiation (green) and control (black) are also shown for comparison.

[9]. Specifically, we have performed partial body irradiations of mice using lead shielding (irradiating roughly above or below the diaphragm).

Gamma-H2AX analysis as performed by us [10] results in a continuous fluorescence value for each cell scored. These values were binned to form a histogram and fit to either a single or double Poisson distribution. Fig. 2 shows the fit results for upper body irradiations (blue), controls (black) and total body irradiations (green). The controls are well described by a single Poisson distribution with a parameter $\lambda=1.2$. The total body irradiations with $\lambda=7$. The upper body irradiation can be reconstructed as a mixture of 28% of the total body distribution and 72% of the control. This would indicate that in this experiment roughly a third of the mouse's blood was irradiated.

References

1. Turner, H.C., et al., Adaptation of the γ -H2AX assay for automated processing in human lymphocytes. *Radiation Research*, Submitted.
2. Endo, A. and Y. Yamaguchi, Analysis of Dose Distribution for Heavily Exposed Workers in the First Critically Accident in Japan. *Radiation Research*, 2003. **159**(4): p. 535-542.
3. Homeland Security Council, National Planning Scenarios (Final Version 21.3). 2006: Washington DC.
4. Stara, J.F. and R.G. Thomas, *The Tissue Distribution and Excretion of Cesium-137 Following Inhalation*, A.E. Comission, Editor. 1963, Lovelace Foundation for Medical Education and Research: Albuquerque, NM.
5. Kathren, R.L., et al., Distribution of Plutonium and Americium in Human Lungs and Lymph Nodes and Relationship to Smoking Status. *Radiat Prot Dosimetry*, 1993. **48**(4): p. 307-315.
6. Szluńska, M., A. Edwards, and D. Lloyd, "Statistical Methods for Biological Dosimetry", in *Chromosomal Alterations*. 2007. p. 351-370.
7. Barquintero, J.F., et al., Biological dosimetry in simulated in vitro partial irradiations. *International Journal of Radiation Biology*, 1997. **71**(4): p. 435-440.
8. Senthamizhchelvan, S., et al., Biodosimetry using micronucleus assay in acute partial body therapeutic irradiation. *Physica Medica*, 2009. **25**(2): p. 82-87.
9. Ponnaiya B., J. Perrier, L. Smilenov, and D.J. Brenner, Assaying Hematopoietic Responses of Mice Following Partial Body Irradiation. CRR Annual Report 2014, 2015, pp.88-89.
10. Turner, H.C., et al., Adapting the γ -H2AX assay for Automated Processing in Human Lymphocytes. 1. Technological Aspects. *Radiation Research*, 2011. **175**(3): p. 282-290. ■

γ -H2AX Kinetic Profile in Mouse Lymphocytes Exposed to the Internal Emitters Cesium-137 and Strontium-90

Helen C. Turner, Igor Shuryak, Waylon Weber^a, Melanie Doyle-Eisele^a, Raymond Guilmette^a, Dunstana Melo^a, Sally A. Amundson, and David J. Brenner

Introduction

In the event of an accidental or terrorist radiological incident, the release of radionuclides to the environment is a major concern for both acute and chronic exposures. Radioactive isotopes of Cesium-137 (¹³⁷Cs) and Strontium-90 (⁹⁰Sr), produced by nuclear fission, are considered to be the most dangerous radionuclides released into the environment in terms of their high radioactivity, long-lived effects (physical half-lives of about 30 years) and the ease in which they are taken up

into the food chain [1-3]. In the present study we have developed two mouse models for a) chronic relatively uniform whole-body irradiation using intraperitoneally injected, systemically distributed ¹³⁷CsCl as a radiation source and b) chronic non uniform low-LET radiation resulting from parenterally administered liquid soluble ⁹⁰SrCl₂. Based on known biokinetics for ¹³⁷CsCl and ⁹⁰SrCl₂ [4-7], a single injection dose was calculated to produce accumulated total-body doses of up to 10 Gy over 30 days of protracted ¹³⁷CsCl exposure and for ⁹⁰SrCl₂, skeletal doses were calculated over two dose ranges, a lower dose range from 0 to 5 Gy and a much

^aLovelace Biomedical and Environmental Research Institute, Lovelace Respiratory Research Institute, Albuquerque, NM .

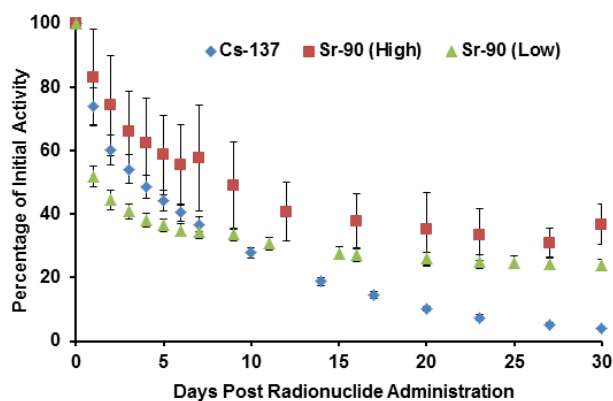


Figure 1. Retention profiles for ¹³⁷CsCl and ⁹⁰Sr.

higher dose range up to approximately 49 Gy over a similar 30 day period.

To evaluate the ionizing radiation-induced DNA damage effects in peripheral mouse blood lymphocytes, we used the established biodosimetry biomarker γ -H2AX and indirect immunofluorescence protocols [8-10] to measure the induction and repair of nuclear DNA double strand breaks (DSBs). To assess the DNA DSB repair capacity in the mouse lymphocytes, total nuclear γ -H2AX fluorescent yields were measured at five specific time points over a 30 day study period following the administration of liquid soluble ¹³⁷CsCl and ⁹⁰SrCl₂. The radionuclide doses as a function of time post exposure were verified by real-time dosimetry. Presented are the *in vivo* γ -H2AX kinetics patterns for each radionuclide.

Study Design and Dosimetry

The irradiations were performed at the Lovelace Respiratory Research Institute. For the Cesium-137 study, male C57BL/6 mice were injected intraperitoneally (IP) with a single 8.0 ± 0.3 MBq dose ¹³⁷CsCl solution in a volume of 50 μ l. For the Strontium-90 study, animals were administered intravenously (IV) by tail vein injection with 1.55 MBq (high dose) and 200 ± 0.3 kBq (low dose) ^{85/90}SrCl₂ solution in a volume of 50 μ L. The ¹³⁷Cs and ⁹⁰Sr whole-body retention profile measurements *in vivo* were obtained by serial counting for each mouse using the LBERI *in vivo* photon counting system, consisting of a single 5" diameter Phoswich (dual NaI(Tl) – CsI(Tl) detector) and associated pulse height analysis electronics.

To convert the empirical ¹³⁷Cs and ⁹⁰Sr retention data into radiation absorbed dose, the software RATDOSE

Table 1. Summary of the total body doses (Gy) at specific time points measured over the 30-day study period.

DAY	Cs-137 (Gy \pm SD)	DAY	Sr-90 (High) (Gy \pm SD)	DAY	Sr-90 (low) (Gy \pm SD)
2	1.95 \pm 0.11	4	11.4 \pm 2.03	4	1.19 \pm 0.1
3	2.7 \pm 0.37	7	20 \pm 1.85	7	1.81 \pm 0.12
5	4.14 \pm 0.35	9	28.5 \pm 4.14	9	2.12 \pm 0.32
20	9.46 \pm 0.41	23	49.4 \pm 11.21	25	4.76 \pm 0.39
30	9.91 \pm 1.2	30	49.4 \pm 11.95	30	5.25 \pm 0.74

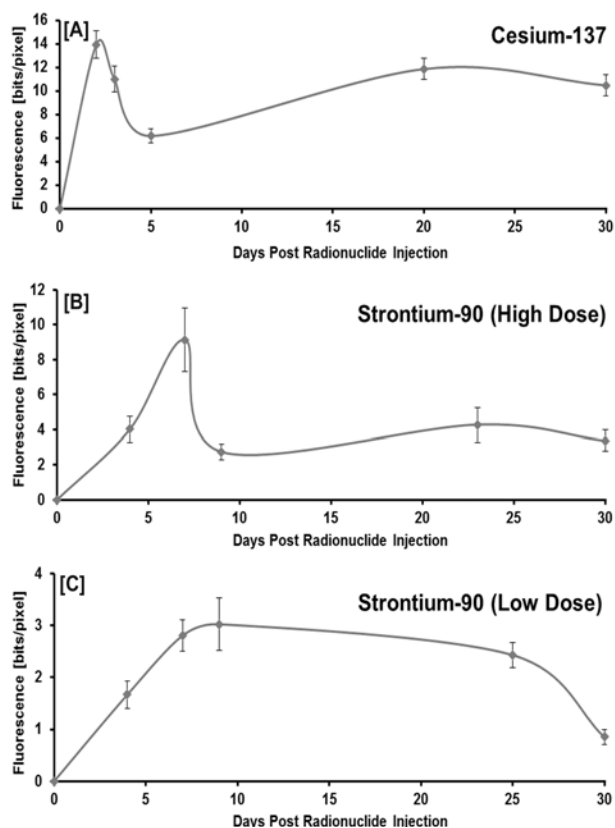


Figure 2. Response pattern of γ -H2AX yields in peripheral blood mouse lymphocytes resulting from long-term internal exposures to ¹³⁷Cs (Panel A), ⁹⁰Sr high dose (Panel B) and ⁹⁰Sr low dose (Panel C). The data presented show the mean γ -H2AX yields \pm SEM over 30 day study period.

[11] was used. Since the biological distribution of ¹³⁷Cs is relatively uniform throughout the body, only the whole-body dose was calculated and used for this study. To determine the biokinetics of injected ⁹⁰Sr in mice, for ⁹⁰Sr/⁹⁰Y dosimetry modeling, the experimental design relied on the use of absorbed radiation dose to bone as the relevant dose metric. Figure 1 shows the whole-body counting data normalized to the amount of ¹³⁷Cs and ⁹⁰Sr present in each animal on Day 0 following isotope injection and Table 1 shows the accumulated total body doses (Gy) calculated at specific time points (days) over the 30 day study period.

The biokinetic and dosimetric modelling showed that within the first week, more than 60% of the initial ¹³⁷CsCl dose (8.0 ± 0.3 MBq) and low dose ⁹⁰SrCl₂ (200 ± 0.3 kBq) have been excreted, whereas $\sim 60\%$ remained after injection of high dose ⁹⁰SrCl₂ (1.55 MBq). By Day 30, 96% of ¹³⁷Cs had been excreted, whereas 37% and 24% remained in the skeleton for ⁹⁰Sr (high dose) and ⁹⁰Sr (low dose), respectively.

γ -H2AX Kinetic Profile

Gamma H2AX foci were detected by indirect immunostaining using a primary rabbit polyclonal antibody (#ab2893; Abcam Inc., Cambridge, MA) and quantified by the fluorescence intensity (arbitrary units);

bits/pixel) [10]. Figure 2, shows the mean (\pm SEM) total γ -H2AX fluorescence yields as a function of elapsed time post injection of each radionuclide. In Excel, a line was created to pass through each of the five data points. The mean γ -H2AX fluorescence for the non-irradiated lymphocytes was 0.6 ± 0.13 .

The γ -H2AX kinetic profile for ^{137}Cs exposure (Fig. 2, Panel A), indicated that the γ -H2AX yields peaked by Day 2 (total body dose = 1.95 Gy) followed by a rapid decline in γ -H2AX frequency by Day 5 (total body dose = 4.14 Gy), after which time there is a gradual increase in the γ -H2AX frequency up to 30 Days. As the rate of accumulation of the ^{137}Cs isotope decreased, the apparent lack of dose response for the formation of γ -H2AX suggests that the rate of γ -H2AX disappearance is not dependent on dose rate. The results also show that there is a significant γ -H2AX signal 4 weeks after initial exposure. The γ -H2AX kinetic profile pattern after exposure to ^{90}Sr (high dose) was similar to that of ^{137}Cs , apart from the fact that peak lymphocyte DNA DSB levels were observed at Day 7 after which the γ -H2AX frequency rapidly decreased (Fig. 2, Panel B). By Day 23 (total skeletal dose = 49.4 Gy), γ -H2AX yields appear to have recovered to levels reflected at Day 4. In contrast, the ^{90}Sr (low dose) total γ -H2AX fluorescence levels continued to increase up to Day 9, after which time the γ -H2AX expression levels are maintained through to Day 25 (Fig. 2, Panel C), suggesting that there is a similar rate of induction and repair of DSBs.

Application of a mechanistic mathematical biophysical model to the data (analyses ongoing) assumes that the γ -H2AX signal is first observed in mature lymphocytes such that the initial decline in the γ -H2AX frequency is due to the radiation-induced death of differentiated mature lymphocyte cells. As time increases, a new peak of γ -H2AX fluorescence is produced in new lymphocytes, which were produced from radiation-damaged stem and/or progenitor cells.

Conclusions

The γ -H2AX assay provides a strong signal for several weeks after the start of an internal emitter exposure. This is in contrast to γ -H2AX signal measured after acute exposures, which is typically undetectable after ~24-48 hours. The results suggest a complex interplay between changing dose, dose rate, and the biokinetics of cell death and the production of new lymphocytes.

References

1. Whicker FW (1983) Radionuclide transport processes in terrestrial ecosystems. *Radiat Res* 94: 135-150.
2. Stather JW (2000) Risk of radiation-induced cancer at low doses and low dose rates. *Med J Aust* 172: 352.
3. Bertho JM, Louiba S, Faure MC, Tourlonias E, Stefani J, et al. (2010) Biodistribution of (^{137}Cs) in a mouse model of chronic contamination by ingestion and effects on the hematopoietic system. *Radiat Environ Biophys* 49: 239-248.
4. Fujita M, Iwamoto J, Kondo M (1966) Comparative metabolism of cesium and potassium in mammals--interspecies correlation between body weight and equilibrium level. *Health Phys* 12: 1237-1247.
5. Stara JF, Nelson NS, Della Rosa RJ, Bustad LK (1971) Comparative metabolism of radionuclides in mammals: a review. *Health Phys* 20: 113-137.
6. Stara JF, Thomas RG (1963) The Tissue Distribution and Excretion of Cesium-137 Following Inhalation-Preliminary Data for Rats. Lf-4. *Fission Prod Inhal Proj* 84: 1-21.
7. Varga LP, Sztanyik LB, Ronai E, Bodo K, Brucher E, et al. (1994) Mobilization of radioactive strontium from mouse and rat using dicarboxylic acid derivatives of cryptand (2.2). *Int J Radiat Biol* 66: 399-405.
8. Rogakou EP, Pilch DR, Orr AH, Ivanova VS, Bonner WM (1998) DNA double-stranded breaks induce histone H2AX phosphorylation on serine 139. *J Biol Chem* 273: 5858-5868.
9. Rothkamm K, Horn S (2009) gamma-H2AX as protein biomarker for radiation exposure. *Ann Ist Super Sanita* 45: 265-271.
10. Turner HC, Shuryak I, Taveras M, Bertucci A, Perrier JR, et al. (2015) Effect of Dose Rate on Residual gamma-H2AX Levels and Frequency of Micronuclei in X-Irradiated Mouse Lymphocytes. *Radiat Res* 183: 315-324.
11. Miller G, Bertelli L, Klare K, Weber W, Doyle-Eisele M, et al. (2012) Software for empirical building of biokinetic models for normal and decorporation-affected data. *Health Phys* 103: 484-494. ■



L to R: Helen Turner, Kunal Chaudhary, and Constantinos Broustas; Cui-Xia Kuan; Charles Geard

Assaying Hematopoietic Responses of Mice Following Partial Body Irradiation

Brian Ponnaiya, Jay Perrier, Lubomir Smilenov, and David J. Brenner

An efficient and effective response to a large-scale radiological event will require high throughput biodosimetry methods. Towards this end, the RABiT (Rapid Automated Biodosimetry Tool) has been designed and built to score micronuclei or γ -H2AX fluorescence in lymphocytes derived from a single drop of blood. Early development and validation of RABiT assays focused on uniform irradiations [1-3]. However, in the event of a radiological event, it is likely that a vast majority of the exposures will not be uniform, with exposed individuals being partially shielded by interposed objects. To determine the utility of the RABiT micronuclei assay in such scenarios, a mouse model was used to simulate partial body exposures.

Either the upper or lower bodies of seven-week-old male C57BL/6 mice were partially shielded using a lead partial-body shield, and the unshielded regions were x-irradiated to doses of 6 or 12.5 Gy using the XRAD 320 x-ray machine. Twenty-four hours post-irradiation, mice were euthanized by CO₂ inhalation and blood was drawn by cardiac puncture and processed using standard RABiT protocols to examine the incidences of micronuclei in either mononuclear or binucleate cells. The results are presented in Figures 1 and 2.

At day 1, frequencies of micronuclei in binucleate cells in all irradiated animals were significantly higher than those of controls (Figure 1), but lower than those observed in the total body irradiated mice. These elevations in micronucleus yields in response to partial body irradiations did not appear to be dose dependent at this time point.

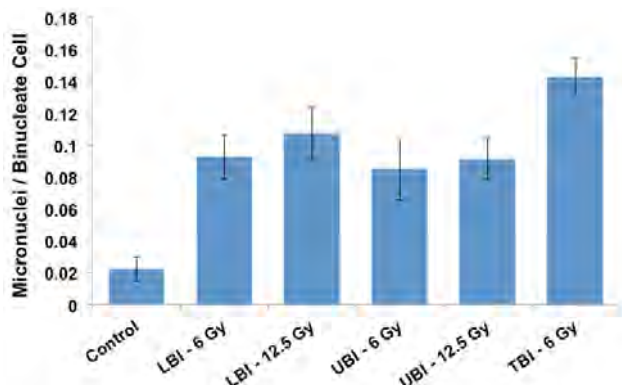


Fig. 1. Micronuclei per binuclear cell in partial body irradiated C57BL/6 mice on day 1 post irradiation, mean \pm SD (n=6), LBI-low body irradiated, UBI-upper body irradiated, TBI – total body irradiated.

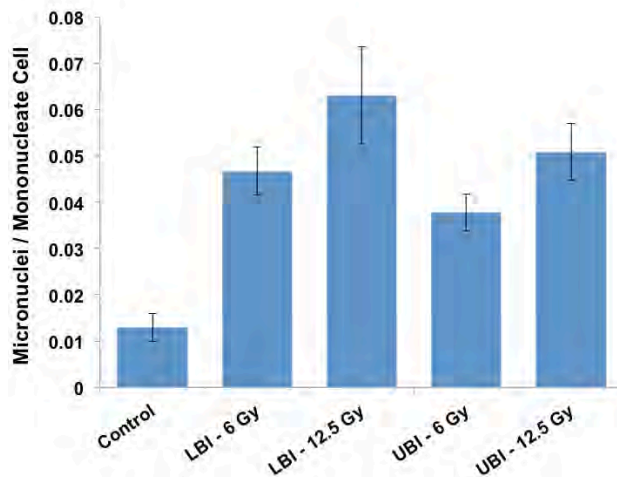


Fig. 2. Micronuclei per mononuclear cell in partial body irradiated C57BL/6 mice 24 hours post irradiation mean \pm SD (n=6), LBI-low body irradiated, UBI-upper body irradiated.

Micronucleus yields in mononuclear cells were also significantly elevated when compared to controls (Figure 2). Interestingly, here it appears that there is a dose dependence in yields of micronuclei. In addition, there seems to be a difference in frequencies depending on which region of the body was irradiated, with lower body irradiations producing higher micronuclei frequencies than upper body irradiations at similar doses.

In summary, it appears that micronucleus assays can be useful in distinguishing partial body from total body irradiations at a given dose. In addition, a new and potentially important observation is the significant differences in micronucleus yields observed between lower and upper body partial exposures.

References

1. Lyulko OV, Garty G, Randers-Pehrson G, Turner HC, Szolc B, Brenner DJ. Fast image analysis for the micronucleus assay in a fully automated high-throughput biodosimetry system. *Radiation Research*. 2014; 181(2):146-61. PMID: PMC4011502.
2. Garty G, Chen Y, Turner HC, Zhang J, Lyulko OV, Bertucci A, Xu Y, Wang H, Simaan N, Randers-Pehrson G, Lawrence Yao Y, Brenner DJ. The RABiT: a rapid automated biodosimetry tool for radiological triage. II. Technological developments. *International Journal of Radiation Biology*. 2011; 87(8):776-90. PMID: PMC3176460.

3. Chen Y, Zhang J, Wang H, Garty G, Xu Y, Lyulko OV, Turner HC, Randers-Pehrson G, Simaan N, Yao YL, Brenner DJ. Design and Preliminary Validation of a Rapid Automated Biodosimetry Tool for High

Throughput Radiological Triage. Proceedings of the ASME Design Engineering Technical Conferences 2009; 3:61-7. PMID: PMC3024000. ■

Whole Blood Immunoassay Using Gamma-H2AX Phosphorylation with Minimal Sample Preparation

Erik F. Young, Matthew L. Johnston^a, and Kenneth L. Shepard^d

Introduction

High throughput minimally invasive biodosimetry involves the handling of large numbers of specimens. In an effort to increase sample throughput and mitigate the need for highly trained operators, several strategies have been successfully developed for the automation of a dosimetric assay. Strategies include automation of image processing for microscopy-based foci-counting techniques, as well as morphological cell selection and automatic scoring [1-2]. Robotic systems have been developed for automated sample processing, including cell fixation and staining, to significantly increase assay throughput and decrease required human interaction [3-4]. Sample preparation can be simplified through flow cytometry-based γ H2AX quantification, which does not require cell fixation and further decreases assay turnaround time [5]. All of these techniques successfully increase throughput and decrease sample processing time. However, the requirement for complex optical hardware or significant robotic sample preparation limit the utility of these approaches for point-of-care radiation biodosimetry.

In this work, a simplified enzyme-linked immunosorbent assay (ELISA) is developed to provide γ H2AX-based radiation dose assessment from a small volume of minimally prepared sample. The ELISA relies on direct antibody-based detection of cellular proteins from sample lysate immobilized on a solid substrate. The γ H2AX response is quantified per sample, instead of measured on a per cell basis as in previous whole-cell staining and flow-cytometry techniques. This method eliminates cell fixation and staining, and non-specific immobilization of cellular proteins obviates initial filtration of samples. Through a focus on simplified sample preparation, omitting filtering and centrifugation processes typically required in γ H2AX assays, we aim to eliminate much of the instrumentation and expertise needed for existing biodosimetry techniques, thus increasing portability.

Using this γ H2AX immunoassay, we find that a linear proportionality between received radiation dose and phosphorylation of H2AX is measured from simple cell lysates of cultured cells and ex vivo irradiated human whole blood. The γ H2AX ELISA described here employs a small sample volume and minimal sample preparation, which make it ideally suited for future adaptation to portable platforms. After further development, it may be

especially suitable for triage-level point-of-care dose assessment after radiation exposure.

Whole blood Lysis

Human blood was collected from consenting volunteers under approved IRB protocols in EDTA containing Vacutainer™ tubes (BD Biosciences, Franklin Lakes, NJ) to prevent clotting. Each de-identified blood sample was split into aliquots ranging from 25 μ L to 200 μ L, depending on the anticipated range of experiments, and stored for irradiation and incubation in 1.5 mL eppendorf tubes (Fisher Scientific, Pittsburgh, PA). These aliquots were subject to irradiation or sham treatment. At prescribed times after irradiation or sham treatment, whole blood lysates were made by supplementing the existing volume of blood with protease-inhibitor supplemented RIPA buffer in an optimized ratio (RIPA: blood). The resulting lysates were then used in ELISA experiments.

ELISA

Lysates were diluted in a 100 mM sodium carbonate/bicarbonate coating buffer (pH 9.6) and added to 96 well microtiter plates (Nunc Maxisorp, Rochester, NY) then incubated overnight at 4°C. Adsorbed lysates were blocked by addition of a blocking buffer comprised of 0.05% Tween 20 (Sigma-Aldrich, St. Louis, MO) in phosphate buffered saline (PBS-T) supplemented with 1% (w/v) bovine serum albumin (Sigma-Aldrich, St. Louis, MO). Wells were blocked for two hours at room temperature. After blocking, wells were washed with PBS-T before addition of primary monoclonal antibody against phosphorylated H2AX (ab22551, Abcam, Cambridge, MA) for two hours at room temperature and

^aDepartment of Electrical Engineering, Columbia University.

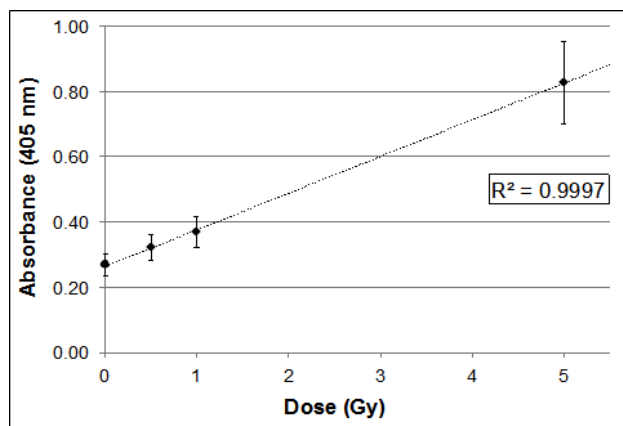


Figure 1. Quantitation of absorbed radiation dose in *ex vivo* irradiated human blood samples. Whole blood was drawn from five consenting adult donors and irradiated with gamma ray doses of 0.5 Gy, 1 Gy, and 5 Gy and processed alongside a sham-irradiated sample. Whole blood was incubated after irradiation for 1 h, after which each sample was lysed by the addition of RIPA buffer. Lysates were interrogated for γ H2AX formation using a custom ELISA protocol. The mean absorbance measured from all five donors is reported here and demonstrates a linear relationship with radiation dose with a correlation exceeding $R^2=0.999$. Error bars represent one standard deviation of mean absorbance across the five donors.

subsequently washed with PBS-T. Wells were then probed with a secondary horseradish peroxidase conjugated anti-mouse antibody (Jackson ImmunoResearch, West Grove, PA) for 1 h at room temperature, followed by three washes in PBS-T. Detection of the bound secondary antibody was performed with a chromogenic substrate solution of 1 mM 2,2'-azino-bis(3-ethylbenzothiazoline-6-sulphonic acid) (ABTS, Sigma-Aldrich, St. Louis, MO) in 70 mM citrate-phosphate buffer (pH 4.2) immediately following the addition of 1 μ L of 30% hydrogen peroxide per milliliter of substrate solution. Absorbance at 405 nm was read and recorded with a Multiskan FC Microplate Photometer (Thermo Fisher Scientific, Waltham, MA).

Results

De-identified blood samples from five human donors were each split into multiple volumes and subjected to gamma irradiation at the specified dose or sham treatment of 0-5 Gy, incubated at 37 °C, and lysed using RIPA buffer before being stored at -80 °C for further analysis. No additional sample preparation was performed. Each sample lysate was interrogated in triplicate using the γ H2AX assay, and the mean absorbance value for each donor and dose was used to assess biological variation among the five human donors. The result obtained is representative of 50 independent experiments. The developed assay resulted in a linear dose response curve with high correlation ($R^2=0.9997$, Fig. 1). This provides an initial exploration of biological variability among multiple human donors using the ELISA approach we have developed.

Discussion

We report the refinement of a straightforward whole blood immunoassay competent to report H2AX phosphorylation in response to ionizing radiation. Our results demonstrate the ability to measure a highly correlated linear relationship between radiation dose and phosphorylation of H2AX in a small volume of minimally prepared sample lysate. The assay has proven to be functionally competent in several other biological systems (Johnston et al in press). At 1 h after exposure, the assay can resolve radiation dose into 1 Gy bins in the 0-5 Gy range using human samples. This resolving power is sufficient for clinical triage during a nuclear emergency response scenario [6]. Our testing suggests that this window may extend up to 6 h after exposure, although extended time course experiments using lysed whole blood are not feasible, as whole blood lysis *in vitro* causes confounding DNA damage during extended incubation [7]. Future refinements in the context of this simplified assay have the strong potential to function in point-of-care triage use in emergency response scenarios.

This work was supported by NIH-NIAID U19 AI067773, and NSF SBIR Phase I grant number 1314228.

References

1. Roche-Lefèvre S, Mandina T, Voisin P, Gaëtan G, Ernesto J, Mesa G, Valente M, Bonnesoeur P, Garcia O, Voisin P, Roy L (2010) Quantification of gamma-H2AX Foci in Human Lymphocytes: A Method for Biological Dosimetry After Ionizing Radiation Exposure. *Radiat Res* 174(2): 185-194.
2. Valente M, Voisin P, Laloi P, Roy L, Roch-Lefèvre S (2011) Automated Gamma-H2AX Focus Scoring Method For Human Lymphocytes After Ionizing Radiation Exposure. *Radiat Meas* 46(9): 871-876.
3. Chen Y, Zhang J, Wang H, Simaan N, Yao YL (2010) Development of a robotically-based automated biodosimetry tool for high-throughput radiological triage. *Int. J. Biomechanics and Biomedical Robotics* 1(2): 115-125.
4. Garty G, Chen Y, Salerno A, et al. (2010) The RABiT: A Rapid Automated Biodosimetry Tool for Radiological Triage. *Health Phys* 98(2): 209-217.
5. Muslimovic A, Ismail IH, Gao Y, Hammarsten O (2008) An Optimized Method for Measurement of gamma-H2AX in Blood Mononuclear and Cultured Cells. *Nat Protoc* 3(7): 1187-1193.
6. Blakely WF, Carr Z, Chin-May M, et al. (2009) WHO 1st Consultation on the Development of a Global Biodosimetry Laboratories Network for Radiation Emergencies. *Radiat Res* 171(1): 127-39.
7. Narayanan S, O'Donovan MR, Duthie SJ (2001) Lysis of whole blood *in vitro* causes DNA strand breaks in human lymphocytes. *Mutagenesis* 16(6): 455-459. ■

Human Pattern of Radiation-induced Gene Expression Restored in Humanized Mice

Sally A. Amundson, Shanaz A. Gandhi, Mashkura Chowdhury, Erik Young, and Lubomir B. Smilenov

Introduction

While studies in irradiated humans would be ideal for development of radiation biodosimetry, such studies are limited largely to cancer patients undergoing radiotherapy. This approach has several drawbacks, including the use of cancer patients, whose responses to radiation might not be representative of the healthy population, potential confounding by chemotherapy or other treatments, and the restriction of the study to the prescribed dose and fractionation regimens. Non-human primate studies are a possible alternative, but their cost precludes systematic studies, making them more useful for validation than for earlier-stage systematic investigations.

In our development of a gene expression approach to radiation biodosimetry, we have made extensive use of an alternative approach, the *ex vivo* irradiation of human peripheral blood from healthy donors. This model is very convenient and flexible, but it also has limitations. For instance, the expression of some genes alters as a function of time the blood is held in tissue culture conditions. The tissue culture environment also lacks signaling from other irradiated tissues and cells that would interact with the blood cells *in vivo*. It is therefore necessary to use this model in concert with an *in vivo* model, such as mice.

Although mice have been used widely as an *in vivo* irradiation model for the development of advanced biodosimetry approaches, we have noted that many genes do not respond to radiation exposure in the same way in mice and humans. A striking example of this was the finding that a subset of p53-regulated genes that are up regulated in response to both *in vivo* and *ex vivo* radiation exposure in humans were significantly down regulated in response to radiation in the commonly used C57BL/6 mouse strain [1]. Many genes have been found to respond to radiation in one species but not the other, just as many genes respond differently to irradiation *in vivo* and *ex vivo*, complicating the development of gene expression signatures for radiation biodosimetry.

One possible approach to mitigate these experimental difficulties may be the hematopoietically humanized mouse model (Hu-NSG) [2], which combines the advantages of *ex-vivo* irradiated blood model and mouse models. In short, immunodeficient NSG mice can be transplanted with human hematopoietic stem cells (HSCs), resulting in long-term engraftment. This essentially results in a mouse with a human immune system. The advantages of this mouse model include long

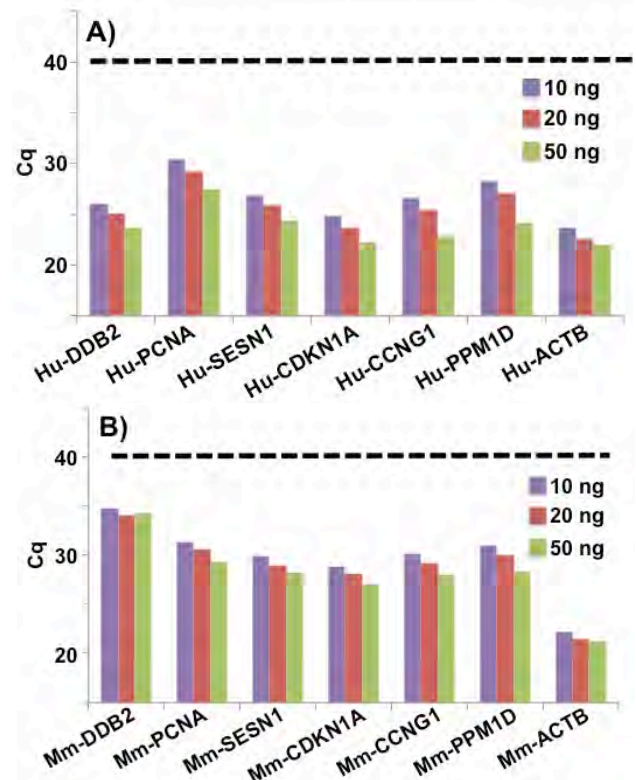


Figure 1 A) Human Taqman® assays were run in duplicate 40-cycle amplification reactions using 10ng, 20ng and 50ng cDNA, and Cq values were determined. The bars show the Cq for various input amounts of human cDNA for the seven assays tested. The same human assays were also tested in parallel with the same amounts of cDNA of mouse origin, resulting in a Cq>40 in all reactions (dashed line), indicating no amplification. B) The results of the equivalent test for mouse Taqman® assays (prefix Mm) are plotted for mouse cDNA input. Again, there was no amplification in any reaction when human cDNA was used as input (Cq>40, dashed line).

lifespan (>100 weeks), low frequency of lymphomas, and high engraftment of human hematopoietic stem cells. Numerous transplant studies have demonstrated that transplantation of human CD34⁺ cells, leads to the development of human hematopoietic progenitor and differentiated cells in the mouse bone marrow, spleen and thymus, culminating in a functional immune system. However, the model lacks appropriate human MHC (major histocompatibility complex) molecules for T cell selection, as well as specific cytokines required for human

cell development, resulting in predominantly naïve B cells in the peripheral blood. The Hu-NSG model has been used in various fields, including cancer biology, viral infection and pathobiology, liver disease, immune response, and ageing of the hematopoietic system. The Hu-NSG model could potentially allow detailed long-term studies of the response of human hematopoietic cells to diverse radiation exposure scenarios in an *in-vivo* environment, making it attractive for the development of radiation biodosimetry. We have performed pilot studies testing the potential of this model for gene expression studies of radiation response.

Generation of humanized mice

We have established the hematopoietically humanized mouse model in our laboratory [3], successfully generating over a hundred humanized mice using tail vein injection with human CD34⁺ cells. Our engraftment efficiency (percentage of mice with human cells in the peripheral blood at 12 weeks after injection) is 92%. The frequency of mice with more than 50% human cells is 85%.

Gene expression by qRT-PCR

As an initial test of the Hu-NSG mouse to see if it could provide an *in vivo* irradiation model with human-like gene expression patterns, we exposed 3 each of Hu-NSG, NSG, and C57BL/6 mice to 0 or 2 Gy of X-rays. We similarly *ex-vivo* irradiated (0 or 2 Gy X-rays) blood from 3 human donors using our standard protocols, and extracted RNA from all mouse and human samples 24 h after exposure, and prepared cDNA from human and mouse total RNA.

Prior to measuring the gene expression responses in blood from the humanized mice, we used increasing amounts of input cDNA (10, 20 or 50 ng per reaction) to test TaqMan® real-time PCR (qRT-PCR) assays for several genes of interest to ensure they showed no cross-species reactivity. As expected, all human assays showed lower detection thresholds (Cq values) with increasing input amounts of human cDNA, but no signal from mouse cDNA in any of the 40-cycle amplification reactions (Fig. 1A). Similarly, the mouse assays (Fig. 1B) showed lower detection thresholds with increasing input of mouse cDNA, and no signal with human cDNA after 40 cycles (Cq > 40).

We next confirmed that *CDKN1A* and *CCNG1* showed similar up-regulation in all irradiated samples (*ex-vivo* irradiated human blood and *in-vivo* irradiated humanized mice as measured with human assays, and all *in-vivo* irradiated mice as measured with mouse assays) as expected from our previous studies. We finally measured expression levels of four genes that were up-regulated in human blood exposed *ex vivo* [4] and in total body irradiated patients [5], but that are unresponsive or down-regulated in irradiated mice. These genes followed the human expression pattern, showing up-regulation in *in-vivo* irradiated humanized mice as measured with human, but not mouse, assays (Fig. 2). This recapitulation of the

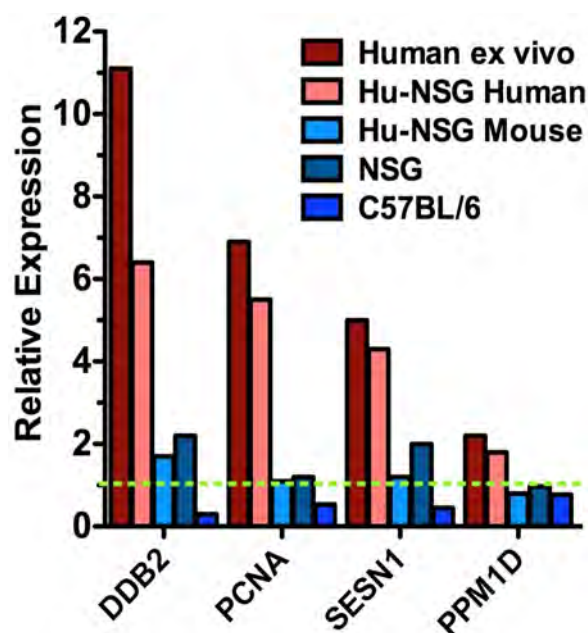


Figure 2. Gene induction by 2 Gy x rays relative to unexposed control levels (dashed line) in human blood or blood from humanized mice measured using human qRT-PCR assays (red bars) and in blood from Hu-NSG, non-humanized NSG, or C57BL/6 mice measured using mouse qRT-PCR assays (blue bars).

human pattern of gene expression in the *in-vivo* irradiated humanized mice supports the use of this model as a powerful tool enabling gene expression profiling of human cells irradiated in an *in-vivo* environment using diverse radiation modalities for biodosimetry development.

References

1. Amundson SA, Ming L, and Paul S (2012) Divergent gene expression responses to radiation in human and murine exposure models. *Center for Radiological Research Annual Report 2011*, pp. 74-76.
2. Shultz LD, Brehm MA, Garcia-Martinez JV, Greiner DL (2012) Humanized mice for immune system investigation: progress, promise and challenges. *Nature Reviews Immunology*. **12**: 786-98 PMID: PMC3749872.
3. Young E, and Smilenov L (2013) Generation of humanized mice for radiation studies. *Center for Radiological Research Annual Report 2012*, pp.79-81.
4. Paul S and Amundson SA (2008) Development of gene expression signatures for practical radiation biodosimetry. *Int J Radiat Oncol Biol Phys* **71**: 1236-1244. PMID: PMC2478639.
5. Paul S, Barker CA, Turner HC, McLane A, Wolden SL and Amundson SA (2011) Prediction of In Vivo Radiation Dose Status in Radiotherapy Patients using Ex Vivo and In Vivo Gene Expression Signatures. *Radiat Res* **175**: 257-265. PMID: PMC3134561. ■

Gene Expression Effects of Neutron Irradiation on Human Whole Blood

Shanaz A. Ghandhi, Yanping Xu, Guy Garty, Lubomir B. Smilenov, and Sally A. Amundson

Introduction

Radiation biodosimetry of individuals exposed after radiological accidents or events, such as detonation of an improvised nuclear device (IND), is an important aspect of triage for immediate treatment and also for health risk assessment in the long term. The neutron component of radiation in such an event would contribute to the dose with potentially different effects on the biological response of cells and molecules. We studied the effect of neutron radiation on human and mouse blood cells, using a new RARAF exposure facility for IND-spectrum neutron irradiation [1].

Methods

Human blood from three healthy donors was exposed *ex vivo* to 0, 0.25, 0.5, 1.0 or 1.5 Gy IND-spectrum neutron radiation at a dose rate of approximately 1.25 cGy/min. For comparison, aliquots of the same blood samples were also irradiated *ex vivo* with 1, 2 or 4 Gy X rays. The blood was then cultured with an equal volume of RPMI1640 medium supplemented with 10% heat-inactivated fetal calf serum. After 24 h, RNA was isolated and a panel of radiation response genes selected based on results from previous studies with *ex vivo* irradiated human blood [2] was measured for expression changes by quantitative RT-PCR (qRT-PCR) using Taqman™ probes. All gene expression results are presented as mean relative induction or repression of mRNA levels using *ACTB* as the endogenous control gene.

Results

We analyzed gene expression using qRT-PCR and the results are summarized as heat-maps (Figure 1) representing the changes in gene expression with colors ranging from green to red (see scale). The samples (columns) are arranged in order of increasing radiation dose of neutrons (left) and X-rays (right). A comparison of the mRNA response by these two types of radiation suggested that there were three broad patterns of gene expression; group I, in which genes were induced by up to 0.5 Gy Neutron radiation but not by higher doses; group II, in which genes showed a similar dose response pattern to both X-ray and neutron irradiation; and group III, in which genes that showed increasing fold-changes with dose by X ray, peaked at 0.5 Gy neutrons. Cluster I genes that increased expression with increasing X rays, but appeared to peak at 0.5 Gy neutrons included *IL1A*, *MMP1*, *IL6* and other genes associated with cell death and inflammatory response. Genes in cluster II included

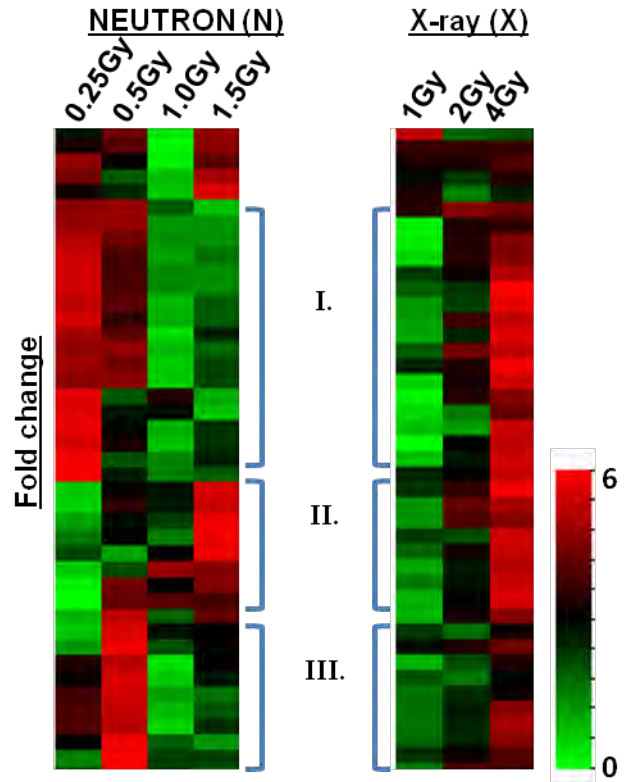


Figure 1. Heatmaps of 24h post-irradiation gene expression ratios as measured by qRT-PCR, normalizing to *ACTB* expression. Each column (dose) represents the average of 3 independent donors, each row represents an individual gene, shown in the same order for both neutrons and X rays.

radiation response genes such as the TP53-regulated *FDXR*, *GDF15*, *GADD45A* and *DDB2* that responded with increasing dose of both neutrons and X rays.

The X-ray doses for this study were selected as equitoxic to the neutron doses, for which the RBE was expected to be around 4. We compared relative fold induction of genes by neutron and X-ray at these theoretically equivalent doses (0.25 Gy neutron and 1 Gy X-ray; 0.5 Gy neutron and 2 Gy X-ray; and 1 Gy neutron and 4 Gy X-ray), to test the prediction of an RBE of 4. Most genes did not respond as expected based on a simple RBE value and only 10% of the genes showed an equivalent effect on gene expression across all dose-pairs. 40% of the genes had higher fold changes by neutron exposure at 0.25 Gy than the equivalent 1 Gy dose of X-ray; 58% of the genes showed lower fold-changes by neutron radiation at 1 Gy than the equivalent 4 Gy X-ray dose. The differences in response of these genes to

radiation type and dose suggest a complex biological response of human blood cells to neutron irradiation that is distinct from the response to X-rays and warrants further studies.

References

1. Xu Y, Garty G, Marino SA, Massey TN, Randers-Pehrson G, Johnson GW, and Brenner DJ (2012)

Novel neutron sources at the Radiological Research Accelerator Facility. *J Instrum* 7: C03031. PMC3337765.

2. Paul S and Amundson SA (2008) Development of gene expression signatures for practical radiation biodosimetry. *Int J Radiat Oncol Biol Phys* 71: 1236-1244. PMC2478639. ■

Correlation of Radiation-induced Micronuclei and Radiosensitivity among Inbred Mouse Strains

Brian Ponnaiya, Jay Perrier, and David J. Brenner

It is clear that different individuals can respond differently to exactly the same dose radiation exposure. Consequently, after a large-scale radiological event such as an Improvised Nuclear Device, in which tens of thousands of individuals would be exposed to high doses, it would be highly advantageous to be able to triage individuals based on their potential individual sensitivity to acute radiation syndromes, as well as based on their dose.

Apart from known factors such as age, weight, and diabetic status, variations in individual acute sensitivity to radiation exposure can come from two basic sources: a) genetic differences, and b) stochastic differences. Among inbred mouse strains, the role of genetic differences as an important determinant of acute radiosensitivity has long been established [1, 2]. However, despite much study, these insights have not turned into usable biomarkers of acute (early) radiosensitivity. Here we present results of a study to examine the links between our RABiT assays and variations in acute radiation sensitivity.

To examine the correlation between the induction of micronuclei and LD₅₀ values of three mouse strains with varying radiosensitivities, BALB/c, C57BL/6 and CD2F1 mice (LD_{50/30} values of 6.55, 8 and 9.025 Gy respectively) were irradiated with either 2 or 4 Gy x-rays (whole body irradiation). One day after irradiation animals were euthanized with carbon dioxide and blood was drawn by cardiac puncture. Samples were put in culture and processed for expression of micronuclei in binucleated cells using standard RABiT protocols [3, 4].

Data for yields of micronuclei in binucleate cells at 1 day post-irradiation are presented in Figure 1. As can be seen, background yields of micronuclei in BALB/c mice (the strain with the lowest LD_{50/30} value) were significantly higher than those of C57BL/6 and CD2F1 mice (intermediated and higher LD₅₀ values respectively). This trend was seen to extend to the irradiated samples as well; following irradiation with 2 Gy, BALB/c mice had higher yields of micronuclei (0.07 micronuclei per binucleate) than did similarly treated C57BL/6 and CD2F1 mice (0.04 and 0.05 micronuclei per cell respectively). Similar trends were also observed in animals irradiated with 4 Gy. Interestingly, while frequencies of micronuclei in control C57BL/6 mice (0.016 micronuclei per binucleate) were significantly higher than those of control CD2F1 animals (0.01 per cell), there were no significant differences between the two strains after exposure to 2 and 4 Gy.

In conclusion, statistically significant differences were found between radiation-induced micronucleus yields in blood from different strains of mice, and these differences were inversely related to each strain's LD_{50/30} values, indicating that this RABiT biomarker has the potential to be predictive of radiation sensitivity to acute injury.

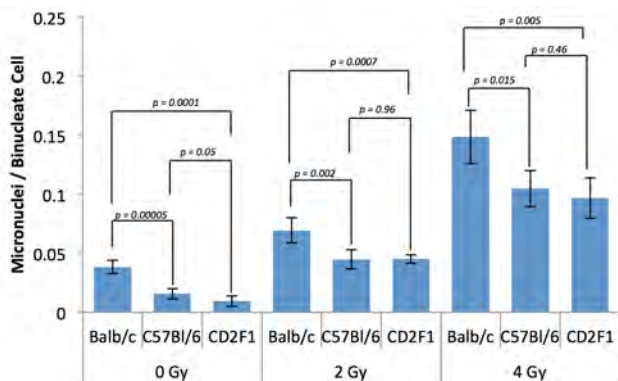


Figure 1. Micronucleus frequencies in binucleated cells 24 hours post-irradiation, Mean ±SD (n=6).

References

1. Storer JB. Effect of aging and radiation in mice of different genotypes. *Birth Defects Original Article Series*. 1978; 14(1):55-70.
2. Yuhas JM, Storer JB. On mouse strain differences in radiation resistance: hematopoietic death and the endogenous colony-forming unit. *Radiation Research*. 1969; 39(3):608-22.
3. Turner HC, Sharma P, Perrier JR, Bertucci A, Smilenov L, Johnson G, Taveras M, Brenner DJ, Garty G. The RABiT: high-throughput technology for assessing global DSB repair. *Radiation and Environmental Biophysics*. 2014; 53(2):265-72. PMID: PMC3999265.
4. Garty G, Chen Y, Turner HC, Zhang J, Lyulko OV, Bertucci A, Xu Y, Wang H, Simaan N, Randers-Pehrson G, Lawrence Yao Y, Brenner DJ. The RABiT: a rapid automated biosimetry tool for radiological triage. II. Technological developments. *International Journal of Radiation Biology*. 2011; 87(8):776-90. PMID: PMC3176460. ■



*Top row (l to r): Steve Marino, Lisa Herr; Howard Lieberman, Shanaz Ghandhi; Gerhard Randers-Pehrson, Sally Amundson.
 Second row (l to r): Cheng-Shie Wu, Steve Marino; Eric Hall, David Brenner; Noah Lugo, Angela Lugo, Noellie Lugo.
 Third Row (l to r): David Brenner, Tom Hei, Margaret Zhu.
 Bottom row (l to r): Howard Lieberman; Helen Turner.*

THE RADIOLOGICAL RESEARCH ACCELERATOR FACILITY

An NIH-Supported Resource Center

WWW.RARAF.ORG

Director: David J. Brenner, Ph.D., D.Sc.

Associate Director: Gerhard Randers-Pehrson, Ph.D.

Manager: Stephen A. Marino, M.S.

Research Using RARAF

The “bystander” effect - the response of cells that are not directly irradiated but are in close contact with, nearby, or only in the presence of irradiated cells - has been the focus for many of the biological studies at RARAF over the past two decades. Both the Microbeam and the Track Segment Facilities continue to be utilized in various investigations of this response to radiation exposure. The number of biological experiments investigating the mechanism(s) by which the effect is transmitted increased slightly this year compared with last year, with newer experiments continuing to use the Microbeam Facility to examine damage to sub-nuclear structures (e.g., mitochondria, telomeres, and specific

chromosomes) and other radiation effects. Research into bystander effects *in vivo* continued this past year with irradiations of the ears of mice.

Experiments

Listed in Table I are the experiments performed using the RARAF Singletron between January 1 and December 31, 2013 and the number of shifts each was run in this period. Fractional shifts are assigned when experimental time is shared among several users (e.g., track segment experiments) or when experiments run for significantly more or less than an 8-hour shift. Use of the accelerator for experiments was 27% of the regularly scheduled time (40 hours per week), up slightly from 23% last year.

Table I. Experiments Run at RARAF January 1 - December 31, 2014

Exp No.	Experimenter	Institution	Exp. Type	Title of Experiment	Shifts Run
110	Tom K. Hei	CRR	Biol.	Identification of molecular signals of alpha particle-induced bystander mutagenesis	37.5
112	Yigal Horowitz	Ben Gurion Univ.	Phys.	TLD track separation and distinction testing for dosimetry	5.0
113	Alexandra Miller	AFRRI	Biol.	Role of alpha particle radiation in depleted uranium-induced cellular effects	2.5
128	Mark Axelrod	Landauer, Inc.	Phys.	Testing of new radiation detector formulations	4.5
153	Howard Lieberman	CRR	Biol.	The role of Rad9 in mediating global gene expression in directly irradiated and bystander cells	2.5
163	Lubomir Smilenov	CRR	Biol.	Bystander effects in the hairless mouse ear	3.0
164	Lubomir Smilenov	CRR	Biol.	Mouse irradiation using IND spectrum neutrons	2.0
165	Helen Turner	CRR	Biol.	Mouse/blood irradiation using IND spectrum neutrons	1.0
169	Vincent LiCata	LSU	Biol.	The denatured states of a thermophilic versus a mesophilic DNA polymerase after charged particle irradiation	1.5
170	Ciaran Morrison	National Univ. of Ireland	Biol.	Live cell imaging of centrosome kinetics following microbeam irradiation	1.5
173	Ekaterina Dadachova	Albert Einstein College of Medicine	Biol.	Comparison of fungal cell susceptibility to external alpha particle beam radiation versus alpha particles delivered by ²¹³ Bi-labeled antibody	2.0
174	Gordana Vunjak-Novakovic	Columbia University	Biol.	Micro proton induced x-ray emission of bone/cartilage grown on artificial scaffolds	3.0

Sixteen different experiments were run during the year. Four experiments were undertaken by members of the CRR, supported by grants from the National Institutes of Health (NIH), the National Cancer Institute (NCI), the National Institute of Allergies and Infectious Diseases (NIAID) and the National Institute of Biomedical Imaging and Bioengineering (NIBIB). Twelve experiments were performed by external users, supported by grants and awards from the Department of Energy (DoE), the Department of Defense (DoD), the NIH, the National Aeronautics and Space Administration (NASA), the National Science Foundation (NSF), the National Cancer Institute (NCI), the Economic Community Cooperation Programme, and internal funding from the Georgetown University Department of Radiation Medicine. Brief descriptions of these experiments follow.

A group led by Tom Hei of the CRR continued experiments investigating the effects of cytoplasmic irradiation and the radiation-induced bystander effect (Exp. 110). Using the Microbeam Facility, Jinhua Wu investigated mechanisms by which cytoplasmic stimuli modulate mitochondrial dynamics and functions in human small airway epithelial cells (SAECs). Their recent studies have shown that mitochondrial fragmentation induced by targeted cytoplasmic irradiation of human SAECs is mediated by up-regulation of dynamin-regulated protein 1 (DRP1), a mitochondrial fission protein. To further explore the role of mitochondria in modulating the biological activities of high-LET radiation, autophagy in SAECs was examined. Autophagy was observed as early as 30 minutes after cytoplasmic irradiation with 10 alpha particles and peaked at 4 hours based on LC3B punctae formation (Fig. 1). Sequestration of free radicals by DMSO abolished the induction of LC3B punctae formation, suggesting that activation of autophagy is free radical dependent. Autophagy led to an increase of γ -H2AX foci that was dramatically reduced by chloroquine (CQ) or 3-methyladenine (3-MA), which are known inhibitors for autophagy. The DRP1 inhibitor mdivi-1 also significantly reduced autophagy, indicating that it plays a key role in activation of autophagy. DRP1 knockout HCT116 cells

showed little or no autophagy after cytoplasmic irradiation, further confirming its role in autophagy induction. DRP1-dependent up-regulation of autophagy-initiating protein beclin-1 was also observed. Finally, a sustained activation of ERK was detected, suggesting potential involvement of the non-canonical MEK/ERK pathway in regulating autophagy in cytoplasmic irradiated cells.

Yigal Horowitz returned this year to continue his study of TLD dosimetry. The current experiment looks at the effects of track density on read out accuracy of TLD dosimeters. This work was performed on the Track Segment facility, delivering ^4He ion (alpha) doses of several kGy to produce very high track density. The TLDs were returned to Yigal in Israel for study and development of plans for further experiments.

Alexandra Miller of the Armed Forces Radiobiological Research Institute (AFFRI) continued studies using the Track Segment Facility to evaluate depleted uranium (DU) radiation-induced carcinogenesis and other late effects using *in vitro* models and to test safe and efficacious medical countermeasures (Exp. 113). One objective of this study has been to determine if phenylbutyrate (PB), a histone deacetylase inhibitor and epigenetic effector, can mitigate neoplastic cell transformation induced by different qualities of radiation, and if so, to identify which adverse epigenetic mechanisms are involved in carcinogenesis and potentially reversed by PB. This also would be of interest for Space missions and alpha particle exposures from accidental releases. Track segment irradiations with ^4He ions were performed on human small airway epithelial cells (SAECs) and growth rate, transformation, and genomic instability were quantified. Irradiation of SAECs overcame contact inhibition and caused an increase in transformation frequency and induction of gene amplification, i.e., genomic instability. Treatment with PB following irradiation resulted in a significant suppression of transformation frequency and gene amplification. Studies are ongoing to evaluate the impact of PB treatment on changes in DNA methylation caused by irradiation with ^4He ions.

In a second part of the Miller study, rodent bone marrow stromal cells were irradiated and co-cultured with unirradiated hematopoietic progenitor cells (FDC-P1). The FDC-P1 cells were monitored for the ability to grow in agar to assess neoplastic transformation. The data have demonstrated that co-culturing irradiated bone marrow stromal cells with FDC-P1 cells causes an increase in neoplastic transformation of FDC-P1 cells that involves the process of cell-cell communication. Additional mechanistic studies have shown that antioxidant processes are also involved in the non-targeted effect in FDC-P1 cells. Further studies with this model are ongoing evaluating involvement of non-targeted effects in multiple exposures at low doses (5 cGy).

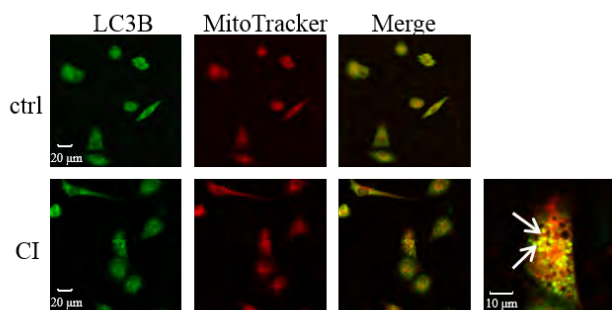


Figure 1. Mitophagy and non-selective autophagy mediated by cytoplasmic irradiation. Co-localization of autophagosome (LC3B labeled in green) and mitochondria (MitoTrackerRed) after cytoplasmic irradiation (4 hr). ctrl, control. CI, cytoplasmically irradiated.

Mark Axelrod from Landauer, Inc. continued to collaborate with our team in the development of dosimetry tools. The experiment this year was determining the dose response of new, proprietary film and chip dosimeters developed by Landauer. The work used our track segment facility to deliver proton and ^4He ion irradiations with different LET values ranging from 10 keV/ μm up to 125 keV/ μm to verify the range of sensitivity to particle irradiation of these dosimeters. Landauer is performing irradiations with gamma and x rays for comparison to our particle irradiations. The ultimate goal is for Landauer to be able to provide discriminated particle/EM dose characterization from a single film badge.

Howard Lieberman, Shanaz Ghandhi, Sunil Panigrahi, and Kevin Hopkins continued investigations of the effects of Rad9 on radiation-induced changes in gene expression in human cells directly irradiated or as bystanders (Exp. 153). Using shRNA against RAD9, the expression of RAD9 was knocked down in the human prostate cancer cell line DU145. The RAD9 knocked-down DU145 cells were seeded onto double-ring “strip” dishes (described above) and irradiated with ^4He ions using the Track Segment Facility. Both irradiated and bystander cells were of the same type and the signaling was through cell-to-cell contact and also through factors released into the medium.

Additional irradiations were made using spacer dishes in which cells were plated on Mylar glued to a stainless steel ring and the ring was inserted into a standard track segment dish so that the cells on the ring were not in direct contact with the cells irradiated on the dish. In these experiments, the DU145 cells were irradiated, WPMY1 or prSMC cells were the bystander cells, and signaling was only possible through molecules secreted by the irradiated cells. After irradiation, bystander response was measured by the micronucleus assay. An increase in micronucleus count was observed in the RAD9 knockdown cells as compared to the parental cells, supporting a role for RAD9 in the radiation-induced bystander effect. Future studies will investigate the mechanisms involved in this process.

Lubomir Smilenov and Manuela Buonanno of the CRR are examining the bystander effect *in vivo*, irradiating mouse ears using the Microbeam Facility (Exp. 163). A special fixture has been designed and constructed in the CRR machine shop to position anesthetized mice so that a region on one ear can be irradiated with the microbeam, with the other ear serving as a control. The mouse ear has an average thickness of 250 μm . A 3 MeV proton beam with a range of $\sim 134 \mu\text{m}$ was defocused to a diameter of $\sim 35 \mu\text{m}$ and scanned in a line a few mm long in order to irradiate a large number of cells. At chosen times after irradiation, mice were sacrificed and a punch of the ear was collected. Tissues were then fixed, paraffin-embedded and cut in 5- μm sections perpendicular to the direction of the charged particle

beam. As expected, cells in the epidermal layer opposite to the γH2AX -positive region, well beyond where the beam penetrated, did not exhibit foci. The average width spanned by γH2AX -positive cells exceeded 150 μm , however, significantly larger than the proton beam width. These results suggest that microbeam proton irradiation induced DNA damage in bystander cells *in vivo*. Ongoing experiments aim at investigating the kinetics of DNA repair focus formation and apoptosis in microbeam-irradiated ears. Further, the biological effects of smaller-diameter proton microbeams will be investigated.

Lubomir Smilenov and Helen Turner both made use of our new improvised nuclear device (IND)-spectrum neutron irradiation system to study the effects of IND-spectrum neutrons on mice and human blood samples. This work was supported by the Columbia Center for Medical Countermeasures against Radiation (CMCR) for the development of biodosimetry approaches for a radiological event. Human blood samples were given up to 2 Gy of IND-spectrum neutron dose or 4 Gy of x rays using the Westinghouse orthovoltage x-ray system. Mice were irradiated with up to 2 Gy of neutrons, and comparison mice were given up to 4 Gy of x rays. Some mice were also given 1 Gy of neutrons and then an additional dose of x-ray to simulate a mixed field. The mice were sacrificed and blood was collected and scored for micronucleus and γH2AX foci to determine dose response. The results for this initial study will guide the future irradiations for the complete study of neutron exposures by the CMCR.

Vincent LiCata of Louisiana State University has continued his investigation into whether proteins from radiation resistant organisms are radiation resistant in isolation. This project examines homologous DNA binding proteins from organisms that live under very different conditions, one being the extremely radiation-resistant bacterium *Deinococcus radiodurans*. Protein stability and function are assayed at different radiation doses to determine whether the DNA polymerase (and eventually other isolated proteins) from *D. radiodurans* are better able to withstand radiation exposure than are homologous proteins from non-radiation resistant organisms. In this study, the protein is spread evenly under a cover slip and irradiated using the Track Segment facility to doses of 5 and 10 kGy and then analyzed for fragmentation and DNA end rejoining capacity.

Ciaran Morrison of the National University of Ireland, in collaboration with Brian Ponnaiya, continued a study probing the mechanisms involved in unscheduled centrosome duplication after exposure to ionizing radiation at defined nuclear sites using the Microbeam Facility. Experiments using DT40 chicken lymphocytes were conducted to test the ability of the cells to adhere to a substrate, and to assess the viability of these cells over the time span proposed for the experiments (48 h). Cells were seeded onto poly L-lysine-coated 60 mm dishes and imaged for irradiation on the microbeam endstation.

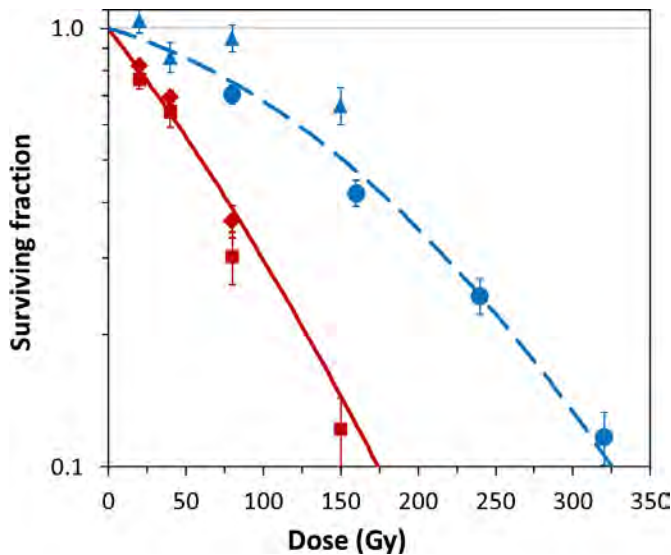


Figure 2. *C. neoformans* clonogenic survival curves for external-beam α -particles (red symbols and line) and γ -rays (blue symbols and line). Different symbol shapes of each color represent independent repeat experiments. Curves represent best-fit linear-quadratic dose responses, and error bars are 95% confidence intervals.

Ekaterina Dadachova at the Albert Einstein College of Medicine has been developing radioimmunotherapy (RIT) for treatment of *Cryptococcus neoformans* infections using ^{213}Bi -labeled antibodies specific to the cryptococcal capsule. She is performing a comparison of fungal cell susceptibility to external α -particle beam radiation versus α particles delivered by the bismuth-labeled antibodies (Exp. 173). Fungi grown to stationary phase in defined minimal medium were suspended in solution. As for other experiments, the solution was formed into a thin layer with a known uniform thickness under a cover slip. The fungi were irradiated with doses of 1 to 80 Gy of $125\text{ keV}/\mu\text{m}$ ^4He ions. Results so far (Fig. 2) indicate that: a) *C. neoformans* is more sensitive to external beam α particles than to external γ rays; b) α particles delivered by the capsule-binding antibodies may be more cytotoxic to the *C. neoformans* cells than external beam α particles.

In addition to these experiments that use ionizing radiation, the ultraviolet (UV) microspot is being used by Kimara Targoff in the Division of Pediatric Medicine of Columbia University as an irradiation modality to observe the consequences of the ablation of single cells in the developing embryonic zebrafish heart (Exp. 162). Unlike the charged particle microbeams, the UV microspot only produces damage in the focal spot (approximately $1\ \mu\text{m}$ diameter, $1.5\ \mu\text{m}$ long), thus producing minimal effect elsewhere along the beam path. Cardiomyocytes in the ventricles of the hearts of zebrafish embryos are transfected with red fluorescent protein (RFP). The exposure protocol involves imaging cells on the top ventricular surface of the heart, where the incident laser first transits the ventricle, in live embryos 52 hours post fertilization and identifying individual cell nuclei as

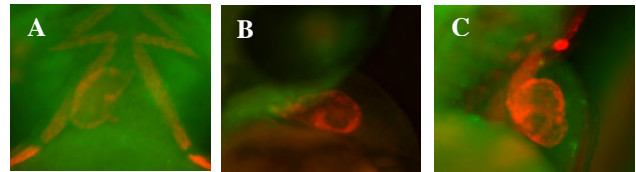


Figure 3. Lateral views of control (panel A) and 4 and 24 hours post-UV irradiated (panels B and C respectively) Zebrafish embryos following immunostaining for Caspase 3 (green) and MF20 (red). MF20 was used to visualize the ventricles.

targets. Each cellular target exposure is a sequence of three co-planar UV microspot scans over a $17.5 \times 17.5\ \mu\text{m}^2$ area about each cell nucleus. The incident laser wavelength is tuned to 700 nm (350 nm during two-photon absorption) and the total exposure energy per cell is 27 mJ, corresponding to 18 mW exposure power during the 1.5 s exposure time. Consequences of UV microspot damage are monitored by live imaging (Fig. 3), in situ hybridization, and immunostaining.

Development of Facilities

Development continued on a number of extensions of our irradiation facilities and capabilities for imaging and irradiating biological specimens:

- Focused particle microbeams
- Focused x-ray microbeam
- Neutron microbeam
- IND spectrum neutron source
- Advanced imaging systems
- Targeting and manipulation of cells
- New cell analysis tools
- Small animal systems

Focused particle microbeams

The electrostatically focused microbeam was consistently operated with a 1-2 μm diameter beam and 0.5 μm when called for by a particular experiment. We have continued the process of performing a test run of the microbeam system on the evening preceding an irradiation day. These test runs have become a vital point of development for new techniques and training of operators for the microbeam system.

The Super-Microbeam development continued with the design and purchase of the super conducting solenoid magnet from Cryomagnetics, Inc. We will be taking delivery of the magnet in 2015 and installing it during the summer. The construction of the scanning Stimulated Emission Depletion (sSTED) super resolution microscope extension was begun with the purchasing of the required optical components. The interface of the sSTED development with the multi-photon microscope was begun with a low power alignment laser with the full 2 W continuous wave (CW) laser to be purchased in mid-2015.

The permanent magnet microbeam (PMM) was used as a secondary charged particle microbeam endstation for

the development of our Flow and Shoot (FAST) microfluidics irradiation system and the capillary electrophoresis (CE) system. The PMM has all of the irradiation capabilities of the electrostatic microbeam except the sub-micron beam spot size.

Focused x-ray microbeam

The x-ray microbeam uses characteristic Ti K α x rays (4.5 keV) generated by proton-induced x-ray emission (PIXE). PIXE produces a nearly monochromatic x-ray source (extremely low bremsstrahlung) of the characteristic target x-ray energy. This allows these x-rays to be focused using a Fresnel zone plate to a spot size of 5 μ m from a proton beam size of ~50 μ m in diameter.

The x-ray microbeam is stationed at a dedicated horizontal beamline at RARAF with the x-ray beam focused up in the vertical direction with the same microscope and stage geometry used in the charged particle microbeam systems, allowing for easy intercomparison between the microbeam types.

Neutron microbeam

The neutron microbeam at RARAF is the world's first neutron microbeam that can irradiate single cells. Incident protons near the reaction threshold (1.881 MeV) of the ${}^7\text{Li}(p,n){}^7\text{Be}$ reaction generate neutrons that are severely forward coned in the laboratory frame of reference. By placing the target cells close to the lithium target it is possible to limit this cone to a single cell target. The Neutron microbeam uses a proton beam at 1.886 MeV focused to 10 μ m on the lithium target. This results in a neutron spot size at the cell targets of 36 μ m diameter with neutron energies ranging from 10-50 keV and a dose rate of 27 mGy/min.

The neutron microbeam is located in the accelerator bay at RARAF on a dedicated horizontal beam line. The proton beam is focused using a single quadrupole quadruplet with the spot size measured using an ionization counter and a knife-edge occlusion measurement. The center of the proton beam, visualized using a thin scintillator, is the center of the neutron beam. The proton beam measurements are made with a thin

Havar metal window, which is exchanged with the lithium target for diagnostics.

The neutron spot size is measured using CR-39 track-etch plastic coated with a thin layer of lithium carbonate heavily enriched with ${}^6\text{Li}$. The neutrons interact with the ${}^6\text{Li}$ through the ${}^6\text{Li}(p,\alpha){}^3\text{H}$ reaction, producing energetic α and ${}^3\text{H}$ recoils that are easily observable as pits in the etched CR-39 using a microscope.

IND-spectrum neutron source

The IND-spectrum irradiator, based on the neutron energy spectrum of the Hiroshima bomb, was completed in the past year and irradiations have begun for both whole blood (Fig. 4) and small animals.

This fast neutron irradiation source was designed to generate the neutron spectrum seen from the "Little Boy" atomic bomb at Hiroshima at 1.5 km from ground zero. This field is generated through the reactions ${}^9\text{Be}(d,n){}^{10}\text{B}$ and ${}^9\text{Be}(p,n){}^9\text{B}$ using a mixed beam of monoatomic, diatomic and triatomic protons and deuterons. The RARAF Singletron uses a gas mixture of hydrogen to deuterium of 1:2, which feeds into the radio frequency plasma ion source. This irradiator is on the 0° beam line, as any bending of the beam to get to a target would separate the six different beams, preventing generation of the spectrum.

The neutron spectrum was verified using two proton recoil detection systems. A 2" diameter 2" thick liquid scintillator for energies >1 MeV and a 1.5" diameter spherical gas proportional counter with 3 atmospheres of hydrogen gas for <1 MeV. Using MCNPX-PoliMi Monte Carlo simulations to calculate the exact response functions of the detectors, it is possible to reconstruct the spectrum from the readout of the detectors in the neutron field.

The dose rate has been calibrated to deliver 0.25 Gy of neutrons in 10 minutes (with a gamma-ray contribution of an additional 15%). This dose rate allows the delivery of 1 Gy in less than 1 hour and provides the opportunity to rotate animals or other samples to achieve dose symmetry.

Advanced imaging systems

We continue to develop new techniques to obtain two- and three-dimensional images of cells, reduce UV exposure, and improve resolution.

Real-time imaging

Short-term effects that happen within seconds up to the first few minutes after irradiation set the stage for later effects. Real-time imaging and observation of the short-term responses will give insight to experimenters into their end points. Techniques have been developed using our EMCCD camera and our fast switching SOLA LED light source to acquire images with several frames per second to observe the short-term effects of irradiation on a timescale of minutes to hours following irradiation.

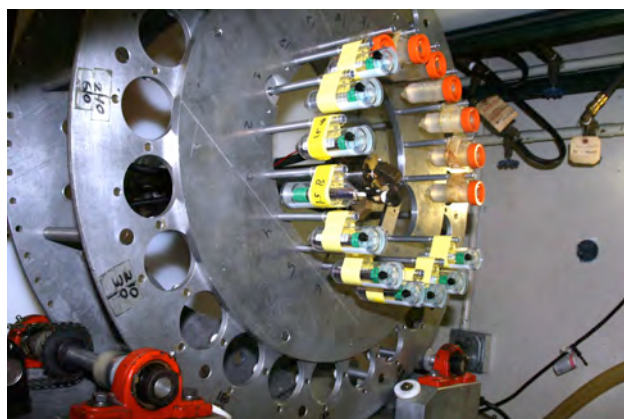


Figure 4. Irradiation of blood samples at the Hiroshima spectrum neutron source

Multi-photon microscope with the UV microspot

The multi-photon microscope was developed several years ago and integrated with the charged particle microbeam irradiator. This microscope, through the long wavelength incident laser, allows in-depth imaging of 3D tissues and small animals, such as *c. elegans* and zebrafish embryos. This is achieved using the sectioning capability of the multi-photon effect, in which the photon density increases to generate constructive interference producing a 3D voxel of photons with half the original incident wavelength and twice the energy, which can locally excite fluorophores and/or produce other fluorescent effects (e.g. auto fluorescence and second-harmonic generation). This 3D voxel is then scanned through a single layer and stepped through the sample using the nanoprecision z-stage, generating a stack of 3D slices of the sample, which are reconstructed into 3D images.

By increasing the intensity of the laser, there can be a 3 photon interference at the area of constructive interference, resulting in a voxel of UV light with a third of the incident wavelength (and three times the energy). This is how we produce our UV microspot. The UV microspot can be used to induce damage within a 3D target. This UV microspot is currently being used to irradiate developing zebrafish embryo ventricles with Dr. Targoff (see above).

STED

We are developing a Stimulated Emission Depletion (STED) super resolution microscope system with optical resolution of 70 nm in combination with our super microbeam to achieve compatibility between imaging resolution and beam spot size. The STED system at RARAF builds off the multi-photon microscope using it as the primary excitation laser. A second CW laser is added in parallel with the multi-photon laser. Using polarization optics, the second laser projects a donut shaped point spread function around the excitation spot of the multi-photon system. With proper selection of the second laser wavelength and sufficient intensity, the second laser will deplete the fluorescent states around the excitation spot allowing fluorescence to be produced only from the center of the donut, which will be reduced to nanometer sizes.

We have already shown that it is possible to perform STED imaging on live cells using a water immersion lens and the STED super resolution microscope at Dr. Liao's Lab in the Mechanical Engineering Department. This system, while not optimized for water immersion optics, gave a resolution of <100 nm.

We have completed the design of the STED system for RARAF and have begun purchasing the required optics. A small, low powered alignment laser with the correct wavelength was purchased to allow the construction and alignment of the STED system without the safety hazard presented by the higher power laser, which will be purchased in 2015.

Targeting and manipulation of cells

We have the capability to fabricate microfluidic devices in hard plastics, such as acrylic, and soft plastics, such as polydimethylsiloxane (PDMS). The micro-milling machine installed at RARAF has software to produce parts designed using the Solid Works computer-aided design (CAD) program. This system has been used to manufacture the single-cell dispenser and the microfluidics chips for the cell sorter and microFACS systems (described below). Several new microfluidic systems are being developed to target, manipulate and analyze cells.

FAST

The Flow And Shoot (FAST) microfluidic irradiation system has continued in development. This system flows non-adherent cells, such as lymphocytes, through a microfluidic channel over the microbeam window where the Point and Shoot magnetic deflector tracks, targets and irradiates the cells as they pass the beam location.

The current design is for a PDMS microfluidic chip with a 200 μm wide by 20 μm deep channel to be vacuum coupled to the microbeam exit window. The channel is thin enough for particles to pass completely through the chip and into the gas ionization counter mounted on the microscope objective. The channel is imaged with 10's of frames per second for cell imaging, locating and tracking for inputs to the Point and Shoot irradiator. We have increased the analysis speed of this process and can track cells with flow rates up to 2 cm/second. The tracking prediction accuracy of the system is within 1.5 μm of the actual new position of the cells 95% of the time.

Cell dispenser

Development of the automated cell dispenser has continued with further study of the electrical properties of the fluid channels, geometry of the detection elements and the design of the output channels to assist in the flow characteristics of the dispensing pulse. The basic design is cells flowing in a polymethyl methacrylate (PMMA) microfluidic channel approach a T intersection of channels. Immediately before the intersection are parallel electrodes that sense the cell by the change in the impedance of the fluid in the channel. When a cell is detected, a speed determination is made from the detection signal and a pulse is sent through the intersecting channel to dispense the cell out of the chip.

Work has been performed looking at the conductivity of the cell medium with the geometry of the impedance electrodes for detection of cells. This work continues with the optimal spacing of the electrodes for the media and flow rates to be determined ultimately by the throughput needs in terms of number of cells/minute.

The original design of the dispenser with a long delay output channel demonstrated that the dispenser with the sensor technology worked as theorized. The dispensing channel has been shortened and several designs are being tested for dispensing droplet size control and accuracy of

dispensing. These design changes are required for optimization and integration into our other microfluidic devices.

MicroFACS

Development of the microfluidic Fluorescence-Activated Cells Sorting (microFACS) system has continued to combine flow cytometry and sorting with our other microfluidic irradiation and dispensing technologies.

The microFACS system uses Dean vortex, drift flow focusing to entrain the samples into a sheath flow focused column for flow cytometry detection in the main channel. The sample is illuminated with a laser through fiber optic coupling, with the fluorescent output also detected through fiber optic coupling. The combination of fiber optics and microfluidics will allow for the microFACS to be coupled to the other microfluidic systems in close proximity to the microbeam endstations.

The primary development on the microFACS was the modeling using COMSOL Multiphysics (Fig. 5) and construction of different introduction arcs for the drift flow focusing. Longer input arcs allow for slow flow on the output channel without loss of focusing. The current design has a 180° arc with an output flow rate of 5 cm/sec. Ultimately, matching this speed to that of the FAST (currently 2 cm/sec) will allow for an integrated microfluidic sorting and irradiation system.

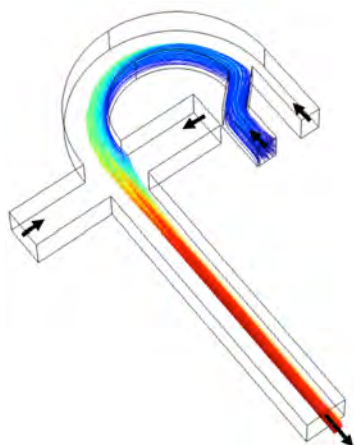


Figure 5. COMSOL model showing the Dean flow focusing of the sample input. The color of the trajectories corresponds to the velocity: slower (blue) to faster (red). The arrows denote flow directions. The column diameter at the exit is 60 μm .

AMOEBA

Our Automated Microbeam Observation Environment for Biological Analysis (AMOEBA) is an automated system for precise regulation and control of environmental conditions for biological samples before, during, and after microbeam irradiations. The AMOEBA system will establish, maintain and change culture conditions (e.g. temperature, pH, pCO₂, drug concentrations) as required by our microbeam users. This system will have automated feedback, fluid-flow control

systems for all of the needed parameters through a distributed electronics control package.

The AMOEBA is being designed in two comparable systems: the standard AMOEBA for dish based microbeam experiments and the μ AMOEBA for microfluidics based irradiation experiments. Initial testing has verified that we can control temperature (37 ± 1 °C) and pH over long periods with minimal feedback circuitry. We have begun using these basic controls for monitoring cell kinetics involving DNA repair, cell-cycle progression and chromosomal domain dynamics.

New cell analysis tools

CE-LIF

We have begun the construction of our Capillary Electrophoresis – Laser Induced Fluorescence (CE-LIF) system to provide our users with the capability of measuring reactive oxygen species within individual cells immediately after irradiation. The nanoliter input volumes make this system ideal for single-cell, small-scale biochemical analysis.

The basic idea of CE is to take advantage of two superimposed flow modalities experienced by the analytes in a long, thin fused silica capillary: (1) Electrophoretic flow, responsible for separating the analytes of lysed cells by charge and Stokes radius; (2) Electroosmotic flow, which drives the buffer and analytes (regardless of polarity) toward the detector. The electroosmotic flow is much stronger than the electrophoretic flow, ensuring that all analytes will reach the detector. Coupled to CE, laser-induced fluorescence (LIF) provides highly sensitive detection, particularly for brightly fluorescent molecules.

Preliminary studies with our collaborator, Dr. Jonathan Sweedler from the University of Illinois (Urbana-Champaign) has demonstrated that single cell CE-LIF has sufficient sensitivity to measure radiation relevant endpoints (e.g. glutathione levels and oxidation of redox-sensitive dyes, such as DHR-123). These preliminary studies are guiding the development of the CE-LIF system for sensitivity at the RARAF Microbeam Facility.

Single-cell Raman spectroscopy

We plan a unique coupling of Raman spectroscopy with a microbeam irradiator to provide non-invasive, label-free identification and assessment of the distribution of bio- molecules and chemicals within a single cell in real time. Raman will allow for the determination of conformational changes to biomolecules resulting from radiation damage in live single cells in culture or 3D tissues before, during and after irradiation. This will be the first real-time coupling of Raman spectroscopy in conjunction with a microbeam irradiator.

The Raman spectroscopy system to be integrated with our Microbeam Facility will be a Renishaw InVia Raman spectroscopy system. An identical system is available in the Electrical Engineering Department on the Columbia

University main campus, where we have acquire preliminary data and demonstrated the ability of the system to acquire data using water immersion optics. With this system, we have successfully measured the Raman spectrum of single cells in 3D full-thickness human skin models (MatTek Corp.).

Small animal systems – Transgenic mouse model

For many years now, investigations of radiation-induced bystander effects have been conducted in cell cultures and 3-D systems *in vitro*. The next logical step was to develop and implement microbeam irradiation protocols to study effects in living organisms. We have now developed a mouse ear model for *in vivo* bystander studies. With an average thickness of 250-300 μm , this model can be used to investigate radiation-induced bystander effects with a 3-MeV proton microbeam having a range of 134 μm .

Using gentle suction, the ear of an anesthetized mouse is flattened onto the underside of a flat plate of a custom-made holder. The flattened mouse ear is then placed over the microbeam port and cells along a line of the ear are irradiated with the proton microbeam. At chosen times after irradiation, mice are sacrificed and a punch of the ear is collected. Tissues are then fixed, paraffin-embedded and cut in 5- μm sections perpendicularly to the direction of the line of irradiation. The sections are then analyzed for biological endpoints (i.e., formation of repair protein foci, apoptosis) as a function of the distance from the irradiated line.

Using γH2AX focus formation assessed by immunohistochemical analysis as an endpoint, we found that proton irradiation induced γH2AX foci *in vivo* relative to controls. As expected, keratinocytes positive for γH2AX foci were observed in only one of the two epidermal layers of the mouse ear. Cells in the epidermal layer opposite to the irradiated γH2AX positive region did not exhibit foci. Assuming that the nuclei of mouse keratinocytes are 9-11 μm in diameter, a larger number of cells than expected showed foci. In a particular experiment, although the irradiated line was ~ 35 μm wide, the average width spanned by γH2AX -positive cells exceeded 150 μm . These results suggest that microbeam proton irradiation induced DNA damage in bystander cells *in vivo*.

Singletron Utilization and Operation

Table II summarizes accelerator usage for the past year. The nominal Singletron availability is one 8-hour shift per weekday (~ 248 days per year), however the accelerator is frequently run well into the evening, often on weekends, and occasionally 24 hours a day for experiments or development. Total use for experiments and development this year was 50% of the regularly available day shifts.

Accelerator use for radiobiology and associated dosimetry was about 22% more than last year and about 2/3 the average for the last 5 years. About 71% of the use

for all experiments was for charged particle microbeam irradiations, 21% for track segment irradiations, and 8% for neutron irradiations. Approximately 25% of the experiment time was for studies proposed by external users, and 75% was for internal users.

On-line facility development and testing was about 29% of the available time, primarily for development and testing of the neutron microbeam and the IND neutron spectrum system, and for testing the charged particle microbeam prior to scheduled irradiations. This was about 15% less than the average for the last five years and about the same as last year due to an emphasis on development not requiring accelerator use.

The accelerator was opened once this year to replace the source bottle after 16 months of use.

Table II. Accelerator Use, January 1 - December 31, 2014
Normally Scheduled Shifts

Radiobiology and associated dosimetry	27%
Radiological physics and chemistry	4%
On-line facility development and testing	29%
Microbeam Training Course	1%
Safety system	2%
Accelerator-related repairs/maintenance	5%
Other repairs and maintenance	1%
Off-line facility development	55%

Training

REU

Since 2004 we have participated in the Research Experiences for Undergraduates (REU) project in collaboration with the Columbia University Physics Department. This is a very selective program that attracts highly talented participants. For 9-10 weeks during the summer each student attends lectures by members of different research groups at Nevis Laboratories, works on a research project, and presents oral and written reports on his or her progress at the end of the program. Among other activities, the students attend a seminar about and take a tour of RARAF.

This year, Steven Harrellson from Missouri State University participated in the program and worked with Alan Bigelow on the study of radiation effects on hemoglobin in human blood analyzed using Raman spectroscopy.

Microbeam Training Course

The fourth annual RARAF microbeam training course “Single-Cell Microbeams: Theory and Practice” was

given May 19-21, 2014. There were nine students, which is about the largest number we can reasonably handle.

Dr. Marcelo Vazquez of Loma Linda University Medical Center continued his service as Course Director. He has had significant experience from his prior employment at the NASA Space Radiation Laboratory (NSRL) at Brookhaven National Laboratory (BNL) where he helped establish the first NASA Space Radiation Summer School and ran the course for three years.

The microbeam training course was publicized by e-mail notifications using the contact lists for the previous courses and the 2012 Microbeam Workshop and by announcements on the RARAF and the EURADOS web sites.

Applicants and Students

- We received 16 applications. The prospective students were from the U.S, Europe and Asia and, as in the previous courses, covered a wide range of educational levels.
- The nine applicants selected for the course are listed in Table III and shown in Fig. 6.
- As before, candidate selection was made by the RARAF Local Executive Committee, with scores applied based on a set of predetermined criteria.

Course

DAY 1:

- Followed essentially the same format as the first two courses, and featured a guest lecture by Dr. Eduoard Azzam from Rutgers University.
- As before, a live demonstration was given of the immediate production of a focus in cells with GFP-tagged XRCC1 protein using the charged particle microbeam.

- The day ended with a session on the planning and experimental design of microbeam irradiations.

DAY 2:

- Followed the format of last year with demonstrations, hands-on activities (Fig. 6), and intense debriefings.
- In addition, the students were tasked with designing an experiment based on their own scientific interest using knowledge obtained during the course to create a RARAF beam time request proposal.

DAY 3:

- Followed the format of the previous years, with lectures and group discussions and an in-depth tour of the x-ray, and neutron microbeams and the UV microspot.
- The lectures were followed by an intense discussion on user/facility interfacing.
- The students made presentations of their individual or team beam-time proposals for review and critique by the instructors.
- The course ended with an informal closing ceremony and the delivery of a certificate of completion to each student.

Each student took home a notebook containing copies of all the slides from the lectures as well as the instructions for all the physics and biology procedures that were demonstrated and that they had performed.

A virtual course created from the lectures and demonstrations from the past two years is described under “Dissemination” below. A paper on the design of and our experience with the training course was also published this year.

Table III. Students for the third RARAF Microbeam Training Course.

<i>Name</i>	<i>Position</i>	<i>Affiliation</i>
<i>Daniel Adjei</i>	Ph.D. Student	Dept. of Physics, King’s College, London
<i>Alisa Kobayashi</i>	Technical Staff Member	Research Development and Support Center, National Institute of Radiological Sciences, Japan
<i>Nicolas Colangelo</i>	MD/Ph. D. student	Rutgers University – New Jersey Medical School
<i>Ruqun Wu</i>	Primary Research Experimenter	Institute of Modern Physics, Chinese Academy of Sciences
<i>Jörgen Elqvist</i>	Researcher	Medical Radiation Physics/Lund Bioimaging Center, Lund University
<i>Maurizia Di Paolo</i>	Fellowship Researcher	University of L’Aquila
<i>Hakim Belmouaddine</i>	Ph.D. Student	Radiation Sciences and Biomedical Imaging, Univ. of Sherbrooke, Quebec, Canada
<i>Pia Fredericia</i>	Ph.D. student	Center for Nuclear Technologies, DTU Risø, Roskilde, Denmark
<i>Velauthapillai Nivethan</i>	Research Assistant	Institute of Medical Science, University of Toronto

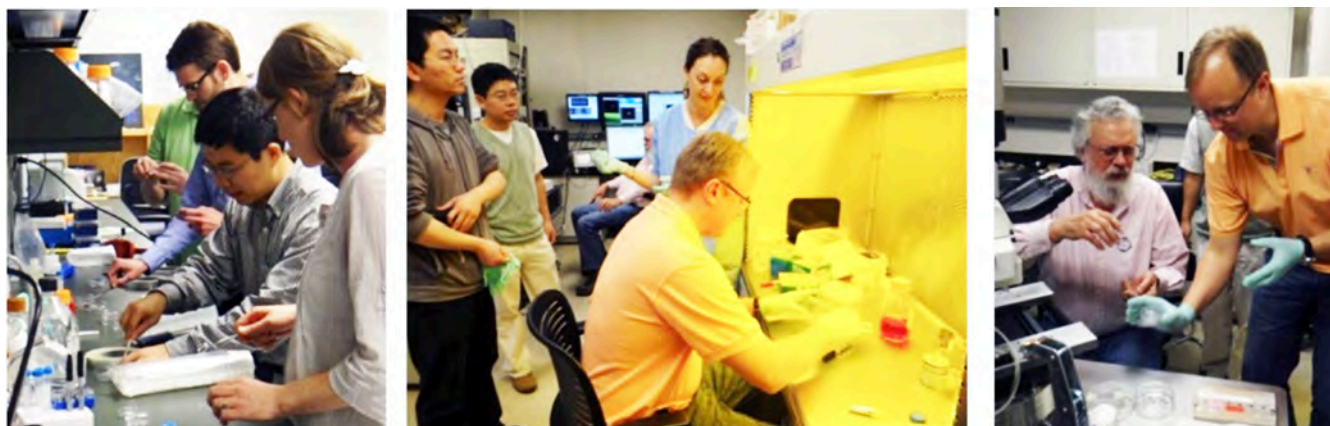


Figure 6. Microbeam Training Course students engaging in hands-on training.

Group Training

In addition to training individuals at RARAF, staff members also participate in training courses presented at other facilities as a means of introducing microbeam concepts and experiments to a broader audience. As for the past two years, Gerhard Randers-Pehrson lectured on “High/low LET microbeams” at the NASA Space Radiation Summer School, Brookhaven National Laboratory, Upton, NY, on June 11, 2014.

Dissemination

Web site

A new RARAF website design was created in 2013 to provide clear and effective presentation and improve access to content. Functional menus (including a home page rotating-picture menu) were designed to make navigation through the content easy and interesting, with a hierarchical structure from general information, suitable for a general or non-science audience, to more detailed technical content.

The site contains information on microbeams in general, as well as detailed technical information on our various microbeams; *in-vitro* and *in-vivo* endpoints that we use; details of available on-line and off-line imaging capabilities; microfluidic systems we are developing; other charged particle and neutron irradiation facilities available at RARAF; our on-line training course materials; publication lists; information on RARAF contacts and directions to the facility. The site is periodically updated to include new irradiation facilities, cell handling and analysis capabilities, publications and other information.

Virtual training course

We have developed an on-line virtual microbeam training course, based on the three-day microbeam training courses. This on-line course was designed to give interested physicists and biologists who could not attend in person a thorough introduction to microbeam technology.

The goal of the online course, as for the face-to-face course, is to facilitate a better understanding of how microbeams work, what experiments can be performed using a microbeam, why these experiments are of biological interest, and how to design / perform these experiments.

The on-line curriculum material consists of audio podcasts and the same handouts that the face-to-face students received. The audio of each podcast is synched with the accompanying PowerPoint slides (viewable on a video iPod, tablet, PC or Mac, or smart phone), as well as a PDF version of the slides. High-resolution video (720p, with audio) was also used to document demonstrations of all aspects of a microbeam experiment, from making microbeam dishes to irradiating cells and performing online analyses. After extensive editing, this resulted in about 4½ hours of video footage. Additional material is added to the on-line course for new course presentations or lecturers.

The on-line training course can be accessed through the RARAF YouTube channel (<http://www.youtube.com/user/RARAFcourses>), or through the RARAF website (www.RARAF.com). The videos can be viewed on any Internet-enabled device supporting YouTube format.

Tours

In addition to training students, tours of the Facility (Fig. 7) provide a general introduction to the research performed at RARAF and the irradiation facilities that are available. This year we gave tours to more than 30 scientists, students, and members of the public.

As an example, eleven high school seniors who had been offered priority admission to Columbia as physics majors, some of whom were Columbia I. I. Rabi Scholarship winners, toured RARAF in April along with Dr. John Parsons from the Physics Department at Nevis Labs.



Figure 7. Dr. Harken giving a tour for a group from Shanghai Jiao Tong University.

Personnel

The Director of RARAF is Dr. David Brenner, the Director of the Center for Radiological Research (CRR). The accelerator facility is operated by Dr. Gerhard Randers-Pehrson, the Associate Director of RARAF.

Dr. Charles Geard, a Senior Biologist Emeritus, continues to visit RARAF frequently lending his considerable expertise.

Dr. Brian Ponnaiya, an Associate Research Scientist, is the biology advisor for RARAF. He collaborates with many of the external users and coordinates with the CRR, where he spends about half his time.

Dr. Alan Bigelow, an Associate Research Scientist, developed the multiphoton microscopy system, which includes the UV microspot irradiation facility, and is working on the development of the Raman spectroscopy and AMOEBA systems.

Dr. Guy Garty, an Associate Professor, developed the Flow and Shoot (FAST) system and is developing the CE-LIF system. He spends about half his time working on Project 1 of the CRR National Institute of Allergy and Infectious Diseases (NIAID) project, for which he is the project manager.

Dr. Andrew Harken, an Associate Research Scientist, is responsible for the x-ray microbeam. He is also working on the imaging of cells without stain using a highly sensitive EMCCD camera, the STED system for extremely high-resolution spectroscopy, and the microFACS system.

Dr. Yanping Xu, an Associate Research Scientist, is developing the neutron microbeam. He is also developing the accelerator-generated IND-spectrum neutron source.

Dr. Manuela Buonanno, a Postdoctoral Fellow in radiation biology, collaborates with many of our external users and performs the assays for the mouse ear microbeam irradiations.

Dr. David Welch, a Postdoctoral Fellow, is responsible for the development of new microfluidic tools and interfaces for microfluidic irradiation tools. His expertise in microfluidics has been of considerable assistance in the development of our microfluidics applications.

RECENT PUBLICATIONS OF WORK PERFORMED AT RARAF

1. Brenner DJ, Vazquez M, Buonanno M, Amundson SA, Bigelow AW, Garty G, Harken AD, Hei TK, Marino SA, Ponnaiya B, Randers-Pehrson G, Xu Y (2014) Integrated interdisciplinary training in the radiological sciences. *Br. J. Radiol* **87**: 20130779.
2. Ghandhi SA, Ponnaiya B, Panigrahi SK, Hopkins KM, Cui Q, Hei TK, Amundson SA, and Lieberman HB (2014) RAD9 deficiency enhances radiation induced bystander DNA damage and transcriptomal response. *Radiat Oncol* **9**: 206.
3. Halm BM, Franke AA, Lai JF, Turner HC, Brenner DJ, Zohrabian VM, Dimauro R (2014) γ -H2AX foci are increased in lymphocytes in vivo in young children 1 h after very low-dose X-irradiation: a pilot study. *Pediatr Radiol*. **44(10)**: 1310-1317.
4. Lyulko OV, Garty G, Randers-Pehrson G, Turner HC, Szolc B, and Brenner DJ (2014) Fast image analysis for the micronucleus assay in a fully automated high-throughput biodosimetry system. *Radiat Res* **181**: 146-161..
5. Welch D and Christen JB (2014) Real-time feedback control of pH within microfluidics using integrated sensing and actuation. *Lab Chip*, **14**: 1191-1197. ■

Publications

- Balajee AS, Bertucci A, Taveras M, and Brenner DJ (2014) Multicolour FISH analysis of ionising radiation induced micronucleus formation in human lymphocytes. *Mutagenesis* **29**: 447-455. PMC4201842.
- Brenner DJ, Vazquez M, Buonanno M, Amundson SA, Bigelow AW, Garty G, Harken AD, Hei TK, Marino SA, Ponnaiya B, Randers-Pehrson G, and Xu Y (2014) Integrated interdisciplinary training in the radiological sciences. *Br J Radiol* **87**: 20130779. PMC4064543.
- Brenner DJ, Shuryak I, Jozsef G, Dewyngaert KJ, and Formenti SC (2014) Risk and risk reduction of major coronary events associated with contemporary breast radiotherapy. *JAMA Intern Med* **174**: 158-160.
- Brenner DJ (2014) What we know and what we don't know about cancer risks associated with radiation doses from radiological imaging. *Br J Radiol* **87**: 20130629. PMC4064597.
- Broustas CG, and Lieberman HB (2014) DNA damage response genes and the development of cancer metastasis. *Radiat Res* **181**: 111-130. PMC4064942.
- Broustas CG, and Lieberman HB (2014) RAD9 enhances radioresistance of human prostate cancer cells through regulation of ITGB1 protein levels. *Prostate* **74**: 1359-1370. PMC4142073.
- Brown JM, Carlson DJ, and Brenner DJ (2014) The tumor radiobiology of SRS and SBRT: are more than the 5 Rs involved? *Int J Radiat Oncol Biol Phys* **88**: 254-262. PMC3893711.
- Calaf GM, Balajee AS, Montalvo-Villagra MT, Leon M, Daniela NM, Álvarez RG, Roy D, Narayan G, and Abarca-Quinones J (2014) Vimentin and Notch as biomarkers for breast cancer progression. *Oncol Lett* **7(3)**: 721-727. PMC3919898.
- Calaf GM. (2014) Curcumin, oxidative stress and breast cancer, in *Cancer: Oxidative Stress and Dietary Antioxidants* (Preedy VR, ed). pp.159-69 Elsevier Academic Press Inc., London England.
- Ciaffardini F, Nicolai S, Caputo M, Canu G, Paccosi E, Costantino M, Frontini M, Balajee AS, and Proietti-De-Santis L (2014) The cockayne syndrome B protein is essential for neuronal differentiation and neuritogenesis. *Cell Death Dis* **5**: e1268. PMC4047889.
- Fazel R, Gerber TC, Balter S, Brenner DJ, Carr JJ, Cerqueira MD, Chen J, Einstein AJ, Krumholz HM, Mahesh M, McCollough CH, Min JK, Morin RL, Nallamothu BK, Nasir K, Redberg RF, and Shaw LJ (2014) Approaches to enhancing radiation safety in cardiovascular imaging: a scientific statement from the American Heart Association. *Circulation* **130**: 1730-1748.
- Ghandhi SA, Ponnaiya B, Panigrahi SK, Hopkins KM, Cui Q, Hei TK, Amundson SA, and Lieberman HB (2014) RAD9 deficiency enhances radiation induced bystander DNA damage and transcriptomal response. *Radiat Oncol* **9**: 206. PMC4261775.
- Gong X, Ivanov VN, Davidson MM, and Hei TK (2014) Tetramethylpyrazine (TMP) protects against sodium arsenite-induced nephrotoxicity by suppressing ROS production, mitochondrial dysfunction, pro-inflammatory signaling pathways and programmed cell death. *Arch Toxicol*. [Epub ahead of print]
- Goudarzi M, Weber W, Mak TD, Chung J, Doyle-Eisele M, Melo D, Brenner DJ, Guilmette RA, and Fornace AJ (2014) Development of urinary biomarkers for internal exposure by cesium-137 using a metabolomics approach in mice. *Radiat Res* **181**: 54-64. PMC4029349.
- Goudarzi M, Weber WM, Mak TD, Chung J, Doyle-Eisele M, Melo DR, Brenner DJ, Guilmette RA, and Fornace AJ (2014) Metabolomic and lipidomic analysis of serum from mice exposed to an internal emitter, Cesium-137, using a shotgun LC-MS approach. *J Proteome Res* [Epub ahead of print] PMC4286155.
- Goudarzi M, Mak TD, Chen C, Smilenov LB, Brenner DJ, and Fornace AJ (2014) The effect of low dose rate on metabolomic response to radiation in mice. *Radiat Environ Biophys* **53**: 645-657. PMC4206600.
- Halm BM, Franke AA, Lai JF, Turner HC, Brenner DJ, Zohrabian VM, and DiMauro R (2014) gamma-H2AX foci are increased in lymphocytes in vivo in young children 1 h after very low-dose X-irradiation: a pilot study. *Pediatr Radiol* **44**: 1310-1317. PMC4175172.
- Horowitz DP, Wang TJ, Wu CS, Feng W, Drassinower D, Lasala A, Pieniazek R, Cheng S, Connolly EP, and Lassman AB (2014) Fetal radiation monitoring and dose minimization during intensity modulated radiation therapy for glioblastoma in pregnancy. *J Neurooncol* **120**: 405-409.
- Hu W, Xu S, Yao B, Hong M, Wu X, Pei H, Chang L, Ding N, Gao X, Ye C, Wang J, Hei TK, and Zhou G (2014) MiR-663 inhibits radiation-induced bystander effects by targeting TGFB1 in a feedback mode. *RNA Biol* **11**: 1189-1198.

- Ivanov VN, and Hei TK (2014) A role for TRAIL/TRAIL-R2 in radiation-induced apoptosis and radiation-induced bystander response of human neural stem cells. *Apoptosis* **19**: 399-413. PMC3945673.
- Ivanov VN, and Hei TK (2014) Radiation-induced glioblastoma signaling cascade regulates viability, apoptosis and differentiation of neural stem cells (NSC). *Apoptosis* **19**: 1736-1754.
- Laiakis EC, Mak TD, Anizan S, Amundson SA, Barker CA, Wolden SL, Brenner DJ, and Fornace AJ, Jr (2014) Development of a Metabolomic Radiation Signature in Urine from Patients Undergoing Total Body Irradiation. *Radiat Res* **181**: 350-361. PMC4071158.
- Luo X, Suzuki M, Ghandhi SA, Amundson SA, and Boothman DA (2014) ATM Regulates Insulin-Like Growth Factor 1-Secretory Clusterin (IGF-1-sCLU) Expression that Protects Cells against Senescence. *PLoS One* **9**: e99983. PMC4061041.
- Lyulko OV, Garty G, Randers-Pehrson G, Turner HC, Szolc B, and Brenner DJ (2014) Fast image analysis for the micronucleus assay in a fully automated high-throughput biodosimetry system. *Radiat Res* **181**: 146-161. PMC4011502.
- Martinerie L, Manterola M, Chung SS, Panigrahi SK, Weisbach M, Vasileva A, Geng Y, Sicinski P, Wolgemuth DJ (2014) Mammalian E-type cyclins control chromosome pairing, telomere stability and CDK2 localization in male meiosis. *PLoS Genet* **10**(2): e1004165. PMC3937215.
- Ng J and Shuryak I (2014) Minimizing second cancer risk following radiotherapy: current perspectives. *Cancer Manag Res* **7**: 1-11.
- Paul S, and Amundson SA (2014) Differential effect of active smoking on gene expression in male and female smokers. *J Carcinog Mutagen* **5**: 198. PMC4303254.
- Paul S, Ghandhi SA, Weber W, Doyle-Eisele M, Melo D, Guilmette R, and Amundson SA (2014) Gene expression response of mice after a single dose of ¹³⁷CS as an internal emitter. *Radiat Res* **182**: 380-389. PMC4212697.
- Repin M, Turner HC, Garty G, and Brenner DJ (2014) Next generation platforms for high-throughput biodosimetry. *Radiat Prot Dosimetry* **159**: 105-110. PMC4067228.
- Rivas M, Rojas E, and Calaf GM (2014) Skin cancer risk affected by ultraviolet solar irradiance in Arica, Chile. *Oncol Lett* **7**(2): 483-486. PMC3881954.
- Roy D and Calaf GM (2014) Allelic loss at chromosome 11q13 alters FGF3 gene expression in a human breast cancer progression model. *Oncol Rep* **32**(6): 2445-52.
- Shuryak I, Bryan RA, Nosanchuk JD, and Dadachova E (2014) Mathematical modeling predicts enhanced growth of X-ray irradiated pigmented fungi. *PLoS One* **9**(1): e85561. PMCID: PMC3893251.
- Shuryak I, Lubin JH, and Brenner DJ (2014) Potential for adult-based epidemiological studies to characterize overall cancer risks associated with a lifetime of CT scans. *Radiat Res* **181**: 584-591. PMC4157352.
- Turner HC, Sharma P, Perrier JR, Bertucci A, Smilenov L, Johnson G, Taveras M, Brenner DJ, and Garty G (2014) The RABiT: high-throughput technology for assessing global DSB repair. *Radiat Environ Biophys* **53**: 265-272. PMC3999265.
- Wallner PE, Anscher MS, Barker CA, Bassetti M, Bristow RG, Cha YI, Dicker AP, Formenti SC, Graves EE, Hahn SM, Hei TK, Kimmelman AC, Kirsch DG, Kozak KR, Lawrence TS, Marples B, McBride WH, Mikkelsen RB, Park CC, Weidhaas JB, Zietman AL, and Steinberg M (2014) Current status and recommendations for the future of research, teaching, and testing in the biological sciences of radiation oncology: report of the American Society for Radiation Oncology Cancer Biology/Radiation Biology Task Force, executive summary. *Int J Radiat Oncol Biol Phys* **88**: 11-17.
- Welch D and Christen JB (2014) Real-time feedback control of pH within microfluidics using integrated sensing and actuation. *Lab Chip* **14**: 1191-1197.
- Xu Y, Zhang B, Messerli M, Randers-Pehrson G, Hei TK, and Brenner DJ (2014) Metabolic oxygen consumption measurement with a single-cell biosensor after particle microbeam irradiation. *Radiat Environ Biophys*. [epub ahead of print]
- Zepeda AB, Figueroa CA, Calaf GM and Farías JG. (2014) Male reproductive system and antioxidants in oxidative stress induced by hypobaric hypoxia. *Andrología* **46**(1): 1-8.
- Zepeda AB, Calaf GM, Figueroa CA, and Farías JG. (2014) Blueberries prevent the effect of intermittent hypobaric hypoxia in rat epididymis. *Andrología* **46**(7): 766-9.
- Zhang B, Davidson MM, and Hei TK (2014) Mitochondria regulate DNA damage and genomic instability induced by high LET radiation. *Life Sci Space Res (Amst)* **1**: 80-88. PMC4111269.
- Zhao Y, de Toledo SM, Hu G, Hei TK, and Azzam EI (2014) Connexins and cyclooxygenase-2 crosstalk in the expression of radiation-induced bystander effects. *Br J Cancer* **111**: 125-131. PMC4090739. ■